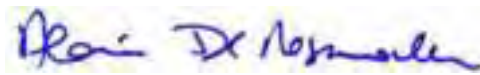


Jahresbericht 2015 der SCS Foundation

Stiftung der Schweizerischen Chemischen Gesellschaft

Bern, 05. Juli 2016



Dr. Alain De Mesmaeker
Präsident



David Spichiger
Geschäftsführer



Bilder: David Spichiger, Simeon Lüthi
Text: David Spichiger
Gestaltung: David Spichiger

Zwecks Lesefreundlichkeit wird die geschlechtliche Doppelformulierung weggelassen. Alle männlichen Formulierungen gelten sinngemäss auch für weibliche Personen.

SCS Foundation

c/o Schweizerische Chemische Gesellschaft
Haus der Akademien
Laupenstrasse 7, Postfach
3001 Bern
T: +41 31 306 92 92
info@scs-foundation.ch
www.scs-foundation.ch



Inhaltsverzeichnis

- 2** 2015 in Zahlen
- 3** Die SCS Foundation
- 5** Aktivitäten allgemeiner Fonds
- 8** Aktivitäten Alfred Werner Fonds
- 9** Partner und Gönner

Anhänge

- i. Revisionsbericht
- ii. Bilanz und Erfolgsrechnung
- iii. CHIMIA Bericht: Review Werner Scholarship winners 2013-2015
- iv. CHIMIA Bericht: Review SCS Fall Meeting 2015, inkl. Gewinner der ‚Best Oral & Best Poster Presentation Awards‘
- v. CHIMIA Issue 4/2016: Laureates Junior Prizes SCS Fall Meeting 2015

2015 in Zahlen

- 4** Anzahl unterstützte Projekte
- 10** Anzahl unterstützende Firmen
- 8** Anzahl Partner-Universitäten
- 222'750** Summe der Projekt-Vergabungen
- 316'750** Summe der Einnahmen
- +51'133** Bilanzerfolg
- 50'000** Stiftungskapital
- 100'394** Kapital Allgemeiner Fonds (Dez 15)
- 1'149'269** Kapital Werner Fonds (Dez 15)



Die SCS Foundation

Die SCS Foundation (SCS Stiftung, SCS Foundation) ist eine Stiftung gemäss Art. 80-89 ZGB, welche im Handelsregister des Kantons Bern eingetragen ist (CHE-114.458.707) und unter Aufsicht der Eidgenössischen Stiftungsaufsicht (Eidg. Departement des Innern, EDI), in Bern, agiert.

Die Stiftung wurde im Jahr 2008 gegründet und per 01.01.2014 mit der Stiftung für Stipendien auf dem Gebiete der Chemie (Werner Stiftung) fusioniert.

Ziel und Zweck der Stiftung

Zweck der Stiftung ist die Förderung und Unterstützung der Naturwissenschaften, im Besonderen in den Bereichen Chemie und Biochemie. Dazu gehört die Unterstützung von Wissenschaft, Forschung, Lehre, Ausbildung und Früherziehung durch Vorhaben, Massnahmen, Projekte und Werke aller Art. Der Stiftungszweck wird insbesondere verwirklicht durch entsprechende Finanzierungen, Ausschüttungen, Unterstützungsbeiträge, Vergabe von Stipendien, Preisverleihungen und durch alle weiteren Aktivitäten, die der Erreichung des Stiftungszweckes dienen. Die Stiftung verfolgt öffentliche bzw. gemeinnützige Zwecke und ist politisch und konfessionell neutral. Sie verfolgt keine kommerziellen Zwecke und erstrebt keinen Gewinn.

Organe der Stiftung

Stiftungsrat

Dem Stiftungsrat obliegen die strategische Führung der Stiftung und die Kontrolle über die Erfüllung des Stiftungszwecks.

Die Mitglieder des Stiftungsrats sind auch zuständig für die Äufnung der Fonds.

Mitglieder des Stiftungsrats mit Stimmrecht

- Prof. E. Peter Kündig, Präsident
Stiftungsrat (2010-2015)
- Prof. Peter Chen, Vizepräsident (seit 2011)
- Dr. Hans Peter Lüthi, Mitglied und Quästor
(seit 2011)
- David Spichiger, Geschäftsführer (seit 2011)
- Dr. Alain De Mesmaeker, Präsident elect (im SR seit 2015 und Präsident ab 2016)
- Prof. Georg Frater, Mitglied (2008-2015)
- Prof. Richard Ernst, Mitglied (2008-2016)
- Prof. Titus Jenny, Mitglied (seit 2015)
- Dr. Reto Naef, Mitglied (seit 2015)
- Prof. Lothar Helm, Mitglied (seit 2015)



Geschäftsstelle

Die Geschäftsführung der Stiftung wird von David Spichiger wahrgenommen, welcher auch die Geschäftsstelle der Schweizerischen Chemischen Gesellschaft (SCG) führt. Die Geschäftsstelle ist insbesondere für die Bereiche operative Finanzen, Kommunikation und Administration zuständig und agiert als Schnittstelle zur Eidgenössischen Stiftungsaufsicht des EDI.

Anlageausschuss

Der Anlageausschuss definiert die Anlagestrategie und legt diese dem Stiftungsrat zur Genehmigung vorzulegen. Mitglieder des Anlageausschusses sind:

- Dr. Hans Peter Lüthi (als Quästor ex-officio), ETH Zürich
- David Spichiger, Geschäftsführer SCS Foundation
- Simon Wyss, Privatbank von Graffenried, Bern (seit Oktober 2014)

Vergabeausschuss SCS Fonds

Der Vergabeausschuss des SCS Fonds definiert die Mittelvergabe aus dem allgemeinen Fonds der SCS Foundation. Die Mitglieder werden durch den Präsidenten und den Quästor der Stiftung sowie den Präsidenten der 5 Divisionen der Schweizerischen Chemischen Gesellschaft repräsentiert.

Vergabeausschuss Alfred Werner Fonds

Der Vergabeausschuss des Alfred Werner Fonds definiert die Mittelvergabe aus dem Alfred Werner Fonds und spricht Stipendien des Master's Student Scholarships Programm. Die Mitglieder werden durch die Donatorenfirmen sowie die Vertreter der Partneruniversitäten repräsentiert.

Rechnung

Das Rechnungswesen inklusive Jahresabschluss wird durch die Treuhand-Firma TREUA Baumgartner, Belp, wahrgenommen.

Revision

Als Revisor amtiert Peter Baumgartner von der Firma REVITREU Baumgartner, Muri b. Bern.



Aktivitäten Allgemeiner Fonds

Best Oral Presentation Award at the SCS Fall Meeting 2015 EPF Lausanne

The prize is given for the two best presentations of each parallel session. The main criteria are the scientific quality and originality of the research, plus the quality of the presentation.

Prizes for Winners

- cash contribution of CHF 500.00
- travel voucher of CHF 1'000.00 to attend an international conference.
- invitation to present the research in the laureates issue of CHIMIA. Value CHF 1'000.00

Prizes for Runners' up

- cash contribution of CHF 400.00

The prize was sponsored by Metrohm.

Winners 2015

Analytical Sciences

- 1st Riedo Andreas, University of Bern
- 2nd Cuartero Maria, University of Geneva

Catalysis Science & Engineering

- 1st Moser Maximilian, ETH Zurich
- 2nd Kopelent René, PSI Villigen

Computational Chemistry

- 1st Golze Dorothea, University of Zurich
- 2nd Petraglia Riccardo, EPF Lausanne

Inorganic & Coordination Chemistry

- 1st Bispinghoff Mark, ETH Zurich
- 2nd Buslov Ivan, EPF Lausanne

Medicinal Chemistry & Chemical Biology

- 1st: Nilforoushan Arman, ETH Zurich

Organic Chemistry:

- 1st Auth Johanna, University of Basel
- 2nd Piemontesi Cyril, EPF Lausanne

Physical Chemistry

- 1st Balmer Franziska, University of Bern
- 2nd Canet Estel, EPF Lausanne

Polymers, Colloids & Interfaces

- 1st Najer Adrian, University of Basel
- 2nd Vybornyi Mykhailo, University of Bern



Best Poster Presentation Award at the SCS Fall Meeting 2015 at University of Zürich

The prizes were given for the best posters of each parallel session. The main criteria are the scientific quality and originality of the research, plus the quality of the presentation.

Prize for Winners

- cash contribution of CHF 500.00
- travel voucher of CHF 750.00 to attend an international conference.
- invitation to present the research in the laureates issue of CHIMIA. Value CHF 1'000.00

Runners' up Prize

- cash contribution of CHF 300.00

The prize was sponsored by DSM.

Winners 2015

Analytical Sciences

- 1st Krismer Jasmin, ETH Zurich
- 2nd Patiny Luc, EPF Lausanne

Catalysis Science & Engineering

- 1st Stern Lucas Alexander, EPF Lausanne
- 2nd Olah Michael, University of Zurich,
Lari Giacomo Marco, ETH Zurich

Computational Chemistry

- 1st Knecht Stefan, ETH Zurich
- 2nd Das Akshaya Kumar, University of Basel

Inorganic & Coordination Chemistry

- 1st Cecot Giacomo, EPF Lausanne
- 2nd Szentkuti Alexander, University of Zurich,
Bünzli Andreas, University of Basel

Medicinal Chemistry

- 1st Urfer Matthias, University of Zurich
- 2nd Schwertz Geoffrey, ETH Zurich,
Goncharenko Kristina, University of Basel

Chemical Biology

- 1st Dumas, Anaëlle, University Paris-Sud
- 2nd Simonin Jonathan, University of Bern

Organic Chemistry

- 1st Heinz Christoph, EPF Lausanne
- 2nd Isenegger Patrick, University of Basel,
Engl Oliver Dieter, ETH Zurich

Physical Chemistry

- 1st Sassmannshausen Heiner, ETH Zurich
- 2nd Nançoz Christoph, University of Geneva,
Eberle Pascal, University of Basel

Polymers, Colloids & Interfaces

- 1st Albert Albert, PSI Villigen
- 2nd Scherz Léon F., ETH Zurich,
Matthieu André, University of Fribourg



Aktivitäten Alfred Werner Fonds

Das Alfred Werner Master's Student Scholarships Programm unterstützt Master Studenten der Studienrichtungen Chemie und Biochemie an Schweizer Universitäten oder Schweizer Technischen Hochschulen.

Der Fonds unterstützt jährlich 8-10 ausländische Top-Studenten mit einem einmaligen Beitrag von CHF 25'000, um ihnen ein Masters-Studium in der Schweiz zu ermöglichen.

Studienzeit 2013-2015

Im Jahr 2015 haben folgende, durch den Werner Fonds unterstützte Studenten ihren Masters-Abschluss erlangt:

- *Jelena Habjanic*, Croatia
University of Zurich
- *Amina Saleh*, Egypt
EPF Lausanne
- *Aleksander Salim*, Serbia
EPF Lausanne
- *Ani Baghdasaryan*, Armenia
University of Geneva

Studienzeit 2014-2016

Im Jahr 2014 wurden keine Stipendien gesprochen.

Studienzeit 2015-2017

Im Jahr 2015 hat der Werner Fonds folgende Studenten mit einem Stipendium unterstützt, die das Masterstudium im Herbst 2015 begonnen haben:

- *Cassandra Oji-Okora Ogadimma*, Nigeria
EPF Lausanne
- *Loren Ban*, Croatia,
ETH Zurich
- *Riccardo Tarchini*, Italy
ETH Zurich
- *UniGE: Ms Sarah Folliet*, France
University of Geneva
- *UniGE: Mr. Lluc Farrera*, Spain
University of Geneva
- *UniGE: Ms Yuting Feng*, China
University of Geneva
- *Mr Ali Tuna*, Turkey
University of Zurich

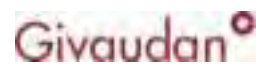


Partner und Gönner 2015

Gönner des SCS Fonds



Gönner des Alfred Werner Fonds



Thomas Baumgartner, Inhaber
Dipl. Wirtschaftsprüfer
Dipl. Experte in Rechnungslegung und Controlling

Peter Baumgartner, Partner
Dipl. Experte in Rechnungslegung und Controlling

REVITREU

Baumgartner + Revisionsunternehmung

Stiftungsrat der SCS-Foundation
c/o Schweizerische Chemische Gesellschaft
Laupenstrasse 7
3008 Bern

Gerzensee, 28. Juni 2016 TB/scR

Bericht der Revisionsstelle zur eingeschränkten Revision

An den Stiftungsrat

Als Revisionsstelle habe ich die Jahresrechnung (Bilanz, Erfolgsrechnung und Anhang) der SCS-Foundation für das Geschäftsjahr 2015 geprüft.

Für die Jahresrechnung ist der Stiftungsrat verantwortlich, während meine Aufgabe darin besteht, diese zu prüfen. Ich bestätige, dass ich die gesetzlichen Anforderungen hinsichtlich Zulassung und Unabhängigkeit erfülle.

Meine Revision erfolgte nach dem Schweizer Standard zur eingeschränkten Revision. Danach ist diese Revision so zu planen und durchzuführen, dass wesentliche Fehlaussagen in der Jahresrechnung erkannt werden. Eine eingeschränkte Revision umfasst hauptsächlich Befragungen und analytische Prüfungshandlungen sowie den Umständen angemessene Detailprüfungen der beim geprüften Unternehmen vorhandenen Unterlagen. Dagegen sind Prüfungen der betrieblichen Abläufe und des internen Kontrollsystems sowie Befragungen und weitere Prüfungshandlungen zur Aufdeckung deliktischer Handlungen oder anderer Gesetzesverstösse nicht Bestandteil dieser Revision.

Bei meiner Revision bin ich nicht auf Sachverhalte gestossen, aus denen ich schliessen müsste, dass die Jahresrechnung sowie der Antrag über die Verwendung des Bilanzgewinns nicht Gesetz und der Stiftungsurkunde entsprechen, sodass einer Genehmigung nichts im Wege steht. Die Stiftung ist durch die Steuerverwaltung des Kantons Bern mit Verfügung vom 11. November 2008 als gemeinnützige Stiftung von der Steuerpflicht befreit.

Mit freundlichen Grüssen

REVITREU Baumgartner
Leitender Revisor



T. Baumgartner
Revisionsexperte

Beilagen:

- Jahresrechnung (Bilanz, Erfolgsrechnung, Anhang)

Bezeichnung	31.12.2015	31.12.2014
Aktiven		
UMLAUFVERMÖGEN		
von Graffenried 206,697/01,01	318,892.37	165,206.30
Basler Kantonalbank 80 808.999.23	0.00	559,416.42
Wertschriften	386,762.32	0.00
Swisscanto AST Obligationen Schweiz	369,240.00	369,342.00
Swisscanto AST Obligationen Ausland	117,633.50	118,139.50
Verrechnungssteuer	16,324.40	13,615.45
Transitorische Aktiven	102,553.28	32,553.28
Total Umlaufvermögen	1,311,405.87	1,258,272.95
ANLAGEVERMÖGEN		
Darlehen SCG	0.00	10,000.00
Total Anlagevermögen	0.00	10,000.00
Total Aktiven	1,311,405.87	1,268,272.95
Passiven		
FREMDKAPITAL KURZFRISTIG		
Transitorische Passiven	-11,743.00	-19,743.00
Total Fremdkapital kurzfristig	-11,743.00	-19,743.00
EIGENKAPITAL		
Stiftungskapital	-50,000.00	-50,000.00
Kapital Fonds Balmer-Preis	0.00	-8,716.50
Kapital Allgemeiner Fonds	-103,337.95	-110,598.81
Kapital Werner Fonds	-1,095,192.00	-1,095,192.00
Total Eigenkapital	-1,248,529.95	-1,264,507.31
Passiven vor Reingewinn	-1,260,272.95	-1,284,250.31
Ergebnis	-51,132.92	15,977.36
Total Passiven	-1,311,405.87	-1,268,272.95

Detailübersicht
Erfolgsrechnung 1.1.2015 - 31.12.2015
Währung CHF

Bezeichnung	Saldo insgesamt	Verwaltung	Allgemeiner Fonds	Werner Fonds
Erfolgsrechnung				
Spenden	316,750.00		57,750.00	259,000.00
Verluste Forderungen	-10,000.00			-10,000.00
Verrechnung Verwaltung	16,453.89	16,453.89		
Total Spendeneingänge	323,203.89	16,453.89	57,750.00	249,000.00
Verleihung Awards	-47,750.00		-47,750.00	
Stipendienzusagen	-175,000.00			-175,000.00
Verrechnung Verwaltung	-16,453.89		-5,484.63	-10,969.26
Total Beiträge	-239,203.89	0.00	-53,234.63	-185,969.26
Reisespesen	-106.00		-106.00	
Sonstiger Personalaufwand	-116.00		-116.00	
Kostenverrechnung SCG	-11,497.50		-5,497.50	-6,000.00
Total Personalaufwand	-11,719.50	0.00	-5,719.50	-6,000.00
Verwaltungskosten	-520.00		-520.00	
Buchhaltung und Rechtsberatung	-8,921.40	-8,852.00	-69.40	
Informatikaufwand	-1,468.65		-820.65	-648.00
Werbung	-908.80			-908.80
Geschäftssessen	-660.90		-329.70	-331.20
Zinsaufwand	-134.98	-134.98		
Bank- und PC-Spesen	-2,769.15	-2,741.35		-27.80
Depotgebühren	-1,334.09	-400.00		-934.09
Wertschriftenaufwand	-2,522.00	-2,262.80		-259.20
Kursverluste aus Finanzanlagen	-9,981.93	-9,981.93		
Zinserträge	4.85			4.85
Wertschriftenertrag	8,069.45	7,919.15		150.30
Kursgewinne aus Finanzanlagen	0.02	0.02		
Total Übriger Betriebsaufwand	-21,147.58	-16,453.89	-1,739.75	-2,953.94
Ergebnis	51,132.92	0.00	-2,943.88	54,076.80



SCS
Foundation
Swiss Chemical
Society

SCS Foundation

News and Announcements
www.scs-foundation.ch

ALFRED WERNER FUND, MASTER'S STUDENT SCHOLARSHIPS



The Alfred Werner Fund of the SCS Foundation was established in 2014 and continues the initiatives and projects of the former foundation 'Stiftung für Stipendien auf dem Gebiete der Chemie', also known as the 'Werner Stiftung'. The SCS Foundation is very proud to provide this program in collaboration with the Swiss chemical and pharmaceutical industry.

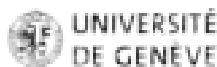
<https://scs-foundation.ch>

Alfred Werner Master's Student Scholarships

The program invites scholarship applications to carry out Master degree studies in Chemistry or Biochemistry at a Swiss University or Federal Institute of Technology.

The Foundation offers 8 to 10 scholarships of CHF 25'000 each as a one-time contribution to the cost of the Master study program. This opportunity targets students from foreign countries in the top 10% of their undergraduate programs. The goal of the program is to bring in young talents to Swiss Universities or FIT or to keep them after the BSc studies in Switzerland.

Partner Universities / Federal Institutes of Technology



The program is supported by



Winners of the Scholarships 2015–17

We are proud and happy to announce the winners of the Werner Scholarships 2015–17 and wish them all the best for their studies in Switzerland.

- EPFL: Ms **Cassandra Oji-Okora Ogadimma** (RU), BSc in chemical engineering and biotechnology, Lomonosov Moscow State University of fine chemical technologies, Russia
- ETHZ: Mr **Loren Ban** (HR), BSc in chemistry, Department of Chemistry, University of Zagreb, Croatia
- ETHZ: Mr. **Riccardo Tarchini** (IT), BSc in chemical engineering, Dipartimento di Scienza Applicata e Tecnologia, Politecnico di Torino, Italy
- UniGE: Ms **Sarah Folliet** (FR), BSc in chemistry, Department of Organic Chemistry, University of Geneva, Switzerland
- UniGE: Mr. **Lluc Farrera** (ES), BSc in chemistry, Facultat De Química, University of Barcelona, Spain
- UniGE: Ms **Yuting Feng** (CN), BSc in biochemistry, Department of Chemistry, McGill University, Montréal, QC, Canada
- UniZH: Mr **Ali Tuna** (TR), BSc in chemistry, Department of Biomedical Engineering, Istanbul University, Turkey

Winners of the Scholarships 2013–15

Two year ago the following four students received one of the Werner Scholarships and they all successfully finished the Master studies.

- UniGE: Ms **Ani Baghdasaryan** (AM), BSc at Yerevan State University, Armenia
- EPFL: Ms **Amina Saleh** (EG), BSc at American University in Cairo (AUC), Egypt
- UniZH: Ms **Jelena Habjanič** (HR), BSc at University of Zagreb, Croatia
- EPFL: Mr **Aleksandar Salim** (CS), BSc at University of Belgrade, Serbia

Summaries of the Master Theses

«Ligand exchange reactions on Au₃₈: selective arrangements of helical dithiolates»

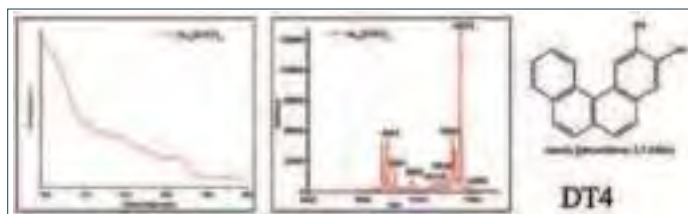


Ani Baghdasaryan
Nationality: Armenia
Bachelor at
Yerevan State University
Master at
University of Geneva
Master thesis supervisor:
Prof. Thomas Bürgi

The aim of this work was the analysis of the ligand exchange of a chiral but configurationally labile dithiolate ligand on chiral Au₃₈(2-PET)₂₄ cluster in order to elucidate whether the attachment to the chiral cluster stabilizes one enantiomer of the ligand.

Racemic and enantiopure Au₃₈(2-PET)₂₄ clusters and DT4 ligand were used for exchange reaction.

SEC, HPLC, TLC separation techniques were employed for obtaining pure samples. The products were analyzed using UV-vis and CD spectroscopy and MALDI-TOF mass spectrometry.

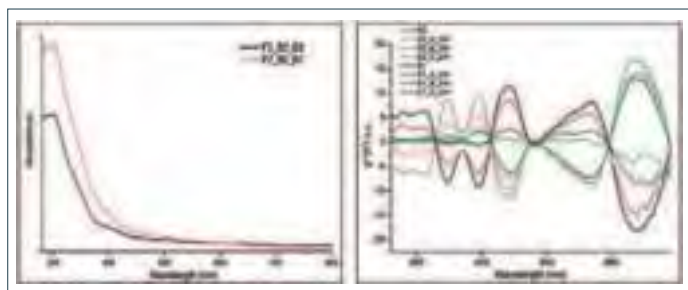


$Au_{38}(2-PET)_{24} + DT4$; 1:50 ratio

Ligand exchange reaction was run at 50 °C for 48 h.

TLC separation:

1. Band 1- $Au_{38}(2-PET)_{22}(DT4)$ one-exchange (10808 Da)
2. Band 2- $Au_{38}(2-PET)_{23}(DT4)$ monodentate bonded (10935 Da) products
3. UV-vis features disappear.



CD measurements of enantiopure samples

The mirror image signals at lower wavelengths become smoother and helical properties disappear.

Preparation of $Au_{38}(2-PET)_{24}$

Rac. $Au_{38}(2-PET)_{24}$ educts were prepared according to previously reported protocols.^[1,2] The UV-vis spectrum of clusters shows characteristic features at 480, 525 and 600-670 nm. The peak at 10793 Da in the mass spectrum belongs to the cluster.

Conclusions

- Ligand exchange reaction between $Au_{38}(2-PET)_{24}$, enantiopure clusters and DT4 ligand leads to the formation of $Au_{38}(2-PET)_{22}(DT4)$ and $Au_{38}(2-PET)_{23}(DT4)$
- UV-vis features at higher wavelengths disappear due to the distortion of the cluster structure;
- TLC method was successfully used for the separation of $Au_{38}(2-PET)_{24-x}(DT4)_x$ species;
- The introduction of ligand induces changes of the surface structure and promotes racemization.

[1] S. Knoppe, A. C. Dharmaratne, E. Schreiner, A. Dass, T. Bürgi, *J. Am. Chem. Soc.* **2010**, *132*, 16783.

[2] S. Knoppe, J. Boudon, I. Dolamic, A. Dass, T. Bürgi, *Anal. Chem.* **2011**, *83*, 5056.

Future plans

The obtained results were quite promising and encouraged us to improve the separation procedure. Moreover, the ligand exchange reaction with other chiral thiolate ligands will make an original contribution to the understanding of chiroptical properties of atomically precise gold nanoclusters.

«A fully printable mesoscopic scaffold with Indium Tin Oxide for hole-transporter-free semi-transparent perovskite solar cells »



Amina Saleh

Nationality: Egypt

Bachelor at

American University in Cairo (AUC)

Master at

École Polytechnique Fédérale de Lausanne (EPFL)

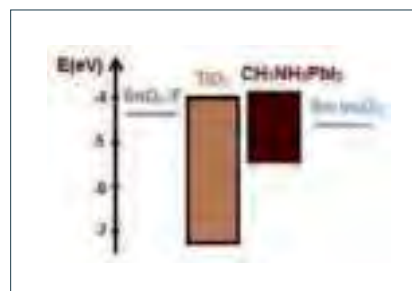
Master thesis supervisor:

Prof. Michael Grätzel

Perovskite solar cells are the most recently developed type of solar cells which have caught a lot of attention by scientists because of their promising photovoltaic performance that, in only a few years, surpassed all the alternative technologies based on solution-processed materials.^[1] Perovskites have the advantages of large absorption coefficient, high carrier mobility, direct band gap, as well as being formed from Earth-abundant materials.^[2]

However, a typical perovskite solar cell incorporates a hole transporting material (HTM) and gold, which are too expensive for scaling up. There are perovskite solar cells which are HTM-free but they cannot be used in tandem geometry, an architecture that combines different cells to boost the overall performance of the device. No HTM-free perovskite cells were reported to be semi-transparent in the infrared (IR) region of the spectrum, the condition required for their participation in tandem cells.

This work presents an HTM-free perovskite cell that could potentially be semi-transparent in the IR (for tandem cells) and/or in the visible region (for windows fabrication). Another advantage of the scaffold is its simplicity: a fully printable mesoporous structure consisting of a TiO_2 layer (for electrons' injection), a tin-doped indium oxide (ITO) layer (for holes' injection), and a layer of Al_2O_3 between them (to prevent recombination). No HTM or gold is needed. To push the accessibility of industrial scale-up further, infiltrating the perovskite solution with the inkjet printing technology was attempted.



The effect of varying the thickness of each of the layers on the photovoltaic performance was studied, as well as that of varying the concentration and the halide composition of the perovskite. A particular attention was given to understanding and decreasing the series resistance of the device. Fundamental characterizations such as measuring the optical properties of the scaffold (with and without perovskite) and the conductivity properties of the ITO were conducted.

[1] Editorial, *Nat. Mater.* **2014**, *13*, 837.

[2] A. Mei, X. Li, L. Liu, Z. Ku, T. Liu, Y. Rong, M. Xu, M. Hu, J. Chen, Y. Yang, M. Grätzel, H. Han, *Science* **2014**, *345*, 295.

«Towards the understanding of unique histidine-rich metallothioneins – protein production, characterization, and investigation of metal ion binding properties»



Jelena Habjanić

Nationality: *Croatian*

Bachelor at

University of Zagreb

Master at

University of Zürich

Master thesis supervisor:

PD Dr. Eva Freisinger

Metallothioneins (MTs) are a superfamily of cysteine-rich proteins with low molecular weight found in all phyla. The precise function of MTs is still a matter of debate, but it is assumed that they have a role in metal homeostasis, provide protection against metal toxicity, and have redox capabilities, hence can act against oxidative stress. The most widely studied MTs are the mammalian forms, and multiple three-dimensional structures are known. From bacteria, only the structure of the SmtA MT from *Synechococcus elongatus* has been explored. The structure of SmtA is unique as it shows several unexpected features for MTs that are absent in the mammalian forms such as a high percentage of secondary structural elements and the presence of aromatic amino acid residues. Most importantly, the structure of SmtA revealed for the first time that also histidine residues can act as metal ligands in MTs.^[1]

In my thesis I focused on novel MT sequences from the ubiquitous gram negative bacteria *Pseudomonas fluorescens*, which were shown to contain an unusually high number of histidine residues. These sequences can be divided into three groups distinctive by the length of the sequence, overall charge of the respective protein, and number of His residues. One representative of each group was successfully cloned, over-expressed, purified, and characterized. The investigation of the metal binding abilities of these novel MTs showed surprisingly different metal ion binding properties and mainly lower affinities to Zn^{II} than to Cd^{II}. Surprisingly, the latter finding is in contrast to the properties of SmtA despite the conserved Cys distribution pattern of all four proteins. The three *P. fluorescens* MTs can all bind up to four Cd^{II} ions, but the fourth metal ion is bound less tightly and easily released. Zn^{II} binding is highly dependent on the conditions but mass spectrometry reveals predominantly Zn₃ species.

The investigation of spectroscopic features of the novel MTs revealed several interesting, unexpected features previously not observed for MTs, the basis of which has to be further investigated. In addition, the influence of a long C-terminal Cys-free tail in one of the proteins with respect to the metal ion binding abilities was studied and showed no major effect. However, its influence on the binding kinetics and thermodynamic stability cannot be excluded and additional studies are necessary.

Preliminary NMR studies for the determination of the overall 3D structure showed promising results for two of the proteins in their Cd^{II}-bound form, but also here further efforts are needed to arrive at a final structure.

[1] C. A. Blindauer, M. D. Harrison, J. A. Parkinson, A. K. Robinson, J. S. Caavet, N. J. Robinson, P. J. Sadler, *PNAS* **2001**, 98, 9593.

Future plans

After finishing my master degree I have decided to immediately continue my education on the PhD level. I got a great opportunity to continue working on the project I started during my master program in the group of PD Dr. Eva Freisinger at University of

Zurich and I am looking forward to study these exciting new proteins on a deeper level.

«Contributions to Pd(0)-catalyzed C_{sp²}-H bond functionalization»



Aleksandar Salim

Nationality: *Serbia*

Bachelor at

University of Belgrade

Master at *EPFL*

Master thesis supervisor:

Prof. Nicolai Cramer

Recently, there has been extensive research in palladium-catalyzed C–H functionalization reactions. The aim of this work was the investigation of enantioselective Pd(0)-catalyzed C_{sp²}-H alkylation as a potential access to desired molecules. The work was performed in the Cramer group. The results will be published in due time.

Future plans

After graduation, I decided to stay at EPFL. I am currently doing a PhD in group of Prof. Kai Johnsson, working on the multidisciplinary project which aims to develop new fluorescent probes for live cell labeling of centrosome. After my PhD my plans are to pursue a career in science and further develop my scientific skills.

Submit to



www.eurjoc.org



**SCG**Schweizerische
Chemische
Gesellschaft**SSC**Soci t 
Suisse
de Chimie**SCS**Swiss
Chemical
Societywww.scg.ch

Society News and Announcements

REVIEW SCS FALL MEETING 2015

Dinner and Award Ceremonies 2015

On the occasion of the Fall Meeting Dinner Prof. E. Peter K ndig, SCS President, awarded the SCS Prize Winners 2015. More than 50 guests from academia and industry joined the dinner at the Restaurant 'Le Petit Manoir' in Morges on September 3, 2015, and paid homage to the prize winners.



Grammaticakis-Neumann Award:
Prof. Natalie Banerji, University
of Fribourg



KGF-SCS Industrial Investigator
Award: **Dr. Dietmar H glin**, BASF
Schweiz AG



KGF-SCS Senior Industrial Inves-
tigator Award: **Dr. Michelangelo
Scalone**, F. Hoffmann La Roche



KGF-SCS Distinguished Industrial
Investigator Award: **Dr. J rg Zim-
mermann**, Novartis Pharma AG



Sandmeyer Award: **Dr. Stefan Abele**, **Dr. Jacques-Alexis Funel** and
Dr. Gunther Schmidt from Actelion Pharmaceuticals Ltd, **Prof. Roger
Mart **, Hochschule f r Technik und Architektur Fribourg, **Dr. Christian
M ssner**, **Mischa Schwaninger**, Swissi Process Safety, a member of
T V S D Group.

The dinner also offered good opportunities to strengthen the interaction between academia and industry and to discuss interdisciplinary topics. The dinner brought together representatives of the Fall Meeting Sponsors and Session Supporters from companies as well as university representatives from all field of chemical sciences.

Conference with Plenary Lectures, Parallel Sessions and Poster Sessions

On September 4, 2015, the traditional SCS Fall Meeting took place at EPF Lausanne and attracted about 750 participants from industry and academia. With more than 520 scientific contributions the Fall Meeting offered again a fantastic possibility to meet experts and specialists and to discuss about their latest research. But it also offered the chance to widen the scientific knowledge and to connect to other thematic fields for joint-projects.

Session	Posters	Lectures
Plenary Session		3
Analytical Sciences	34	12
Catalysis Science & Engineering	61	12
Computational Chemistry	30	13
Inorganic Chemistry	65	12
Medicinal Chemistry & Chemical Biology	61	14
Organic Chemistry	64	14
Physical Chemistry	52	13
Polymers, Colloids & Interfaces	48	13
Total Contributions	415	106

University/Company	Posters	Lectures
EPF Lausanne	72	19
ETH Zurich	94	23
University of Basel	51	11
University of Bern	24	4
University of Fribourg	23	4
University of Geneva	42	11
University of Lausanne	5	
University of Neuchatel	5	
University of Zurich	40	8
EMPA D�bendorf	6	2
Paul Scherrer Institute, Villigen	18	1
FHNW, MuttENZ	1	
HES-SO, Fribourg/Valais	4	1
ZHAW, W�denswil	3	1
Non-Swiss University	19	7
Industry Switzerland	8	14
Total Contributions	415	106

For more details about presenters and titles of the given lectures and posters please see *CHIMIA 2015*, 69 (7–8), 447 ff.

All abstracts of the Fall Meeting 2015 are available on the website <http://scg.ch/fallmeeting/2015> or in the SCS Conference Tool on <http://chemistrycongresses.ch>.

I would like to take the opportunity to thank our Sponsors and Supporters:

General Sponsors: SCS Foundation, Qatar Environment & Energy Research Institute, EPF Lausanne, Swiss Academy of Sciences, Contact Group for Research Matters (KGF: BASF Schweiz AG, Novartis Pharma Schweiz AG, F. Hoffmann-La Roche AG, Syngenta Crop Protection AG)

Session Endowments: EPF Lausanne, School of Basic Sciences, Clariant International Ltd, Contact Group for Research Matters (KGF: BASF Schweiz AG, Novartis Pharma Schweiz AG, F. Hoffmann-La Roche AG, Syngenta Crop Protection AG), Actelion Ltd., Syngenta Crop Protection AG, Bruker BioSpin AG, Dow Europe GmbH.

Exhibitors: Advion Inc., Agilent Technologies Schweiz AG, Borer Chemie AG, Büchi Glas Uster, Büchi Lab Equipment AG, Chemie Brunschwig AG, Equilabo, IGZ Instruments AG, LOT Quantum Design, Merck Millipore Corp., Metrohm Schweiz AG, Perkin Elmer Inc., Setaram Instrumentation, TCI Europe N.V., Georg Thieme Verlag KG

Sponsors: Biazzi AG, Scientific Computing & Modelling NV (SCM), ChemistryViews

Winners of the Best Oral Presentation Award



The prizes were given for the two best presentations of each parallel session and Dr. Markus Tobler, CEO Metrohm Schweiz AG could award 15 young scientists for their excellent work.

Prizes for Winners

- cash contribution of CHF 500.00
- travel voucher of CHF 1'000.00 to attend an international conference.
- invitation to present the research in the laureates issue of CHIMIA.

Prizes for Runners-up

- cash contribution of CHF 400.00

Winners 2015

Analytical Sciences

- Winner: Andreas Riedo, University of Bern
- Runner up: Maria Cuartero, University of Geneva



Catalysis Science & Engineering

- Winner: Maximilian Moser, ETH Zurich
 - Runner up: René Kopelent, PSI Villigen
- Computational Chemistry
- Winner: Dorothea Golze, University of Zurich
 - Runner up: Riccardo Petraglia, EPF Lausanne
- Inorganic & Coordination Chemistry
- Winner: Mark Bispinghoff, ETH Zurich
 - Runner up: Ivan Buslov, EPF Lausanne
- Medicinal Chemistry & Chemical Biology
- Winner: Arman Nilforoushan, ETH Zurich
- Organic Chemistry:
- Winner: Johanna Auth, University of Basel
 - Runner up: Cyril Piemontesi, EPF Lausanne
- Physical Chemistry
- Winner: Franziska Balmer, University of Bern
 - Runner up: Estel Canet, EPF Lausanne
- Polymers, Colloids & Interfaces
- Winner: Adrian Najer, University of Basel
 - Runner up: Mykhailo Vybornyi, University of Bern

Winners of the Best Poster Presentation Award



The prizes were given for the two or three best posters of each session and Dr. Thomas Netscher, principal scientists at DSM, could award 24 young scientists for their excellent work.

Prizes for Winners

- cash contribution of CHF 500.00
- travel voucher of CHF 750.00 to attend an international conference.
- invitation to present the research in the laureates issue of CHIMIA.

Prizes for Runners-up

- cash contribution of CHF 300.00

Winners 2015

Analytical Sciences

- Winner: Jasmin Krismer, ETH Zurich
- Runner-up: Luc Patiny, EPF Lausanne

Catalysis Science & Engineering

- Winner: Lucas Alexander Stern, EPF Lausanne
- Runners-up: Michael Olah, University of Zurich, Giacomo Marco Lari, ETH Zurich

Computational Chemistry

- Winner: Stefan Knecht, ETH Zurich
- Runner-up: Akshaya Kumar Das, University of Basel



Inorganic & Coordination Chemistry

- Winner: Giacomo Cecot, EPF Lausanne
- Runners-up: Alexander Szentkuti, University of Zurich, Andreas Bünzli, University of Basel

Medicinal Chemistry

- Winner: Matthias Urfer, University of Zurich
- Runners-up: Geoffrey Schwertz, ETH Zurich, Kristina Goncharenko, University of Basel

Chemical Biology

- Winner: Anaëlle Dumas, University Paris-Sud
- Runner-up: Jonathan Simonin, University of Bern

Organic Chemistry

- Winner: Christoph Heinz, EPF Lausanne
- Runners-up: Patrick Isenegger, University of Basel, Oliver Dieter Engl, ETH Zurich

Physical Chemistry

- Winner: Heiner Sassmannshausen, ETH Zurich
- Runners-up: Christoph Nançoz, University of Geneva, Pascal Eberle, University of Basel

Polymers, Colloids & Interfaces

- Winner: Albert Albert, PSI Villigen
- Runners-up: Léon F. Scherz, ETH Zurich, André Matthieu, University of Fribourg



A special thank goes to **Prof. Sandrine Gerber** and her team from the EPF Lausanne who organized and chaired a perfect event and ensured a smoothly procedure throughout the whole day.

Visit the conference website's news section to see more photos of the event.

Outlook SCS Fall Meeting 2016

The next SCS Fall Meeting will take place at University of Zurich on September 15, 2016. The call for contributions opens in late February and will close on May 26, 2016.

<http://scg.ch/fallmeeting/2016>

NEWS

Professor Majed Chergui has been elected as Fellow of the European Physical Society.

The EPS is a major non-profit organization whose purpose is to promote physics and physicists in Europe. Founded in 1968, it includes members from 42 National Physical Societies in Europe, individuals from all fields of physics, and European research institutions, such as the Deutsche Physikalische Gesellschaft, the world's largest organization of physicists. The EPS also publishes *Europhysics Letters*, *Europhysics News*, and the *European Journal of Physics*.



Prof. Majed Chergui is Professor of Physics and

Chemistry at EPFL, where he pursues a variety of ultrafast UV and X-ray spectroscopic studies on chemical and biological systems. Since 2013, he has been Editor-in-chief of the open-access journal *Structural Dynamics*, created by the American Institute of Physics and the American Crystallographic Association.

With his election as Fellow, the EPS recognizes Professor Chergui "for his pioneering of novel ultrafast X-ray and ultraviolet spectroscopic tools, for the study of molecular and biomolecular dynamics in solutions, and for his engagement in promoting science in the developing world and in Europe."

Website of Prof. Chergui's Lab: <http://lsu.epfl.ch/>

Additional honors of Prof. Majed Chergui in 2015:

- Morino Lecturer, Morino Foundation for Molecular Sciences, Japan
- The Edward Stern Prize, International X-ray absorption Society-IXAS

Text: EPFL news channel, <http://actu.epfl.ch>

Prof. Petra Dittrich (ETHZ) wins Heinrich-Emanuel Merck Award for Analytical Science 2015



Prof. Petra Dittrich, a leading bioanalytical chemist, was awarded this year's Merck Award for her publication "Implementing enzyme-linked immunosorbent assays on a microfluidic chip to quantify intracellular molecules in single cells" in the journal *Analytical Chemistry*. The award is for chemists under the age of 45, working in particular

on developing new analytical methods and their applications in areas of human interest. Their work should be directed towards the improvement of our conditions of life, providing solutions to analytical problems in the areas of life sciences, material sciences or environment. The prize was awarded to Dittrich during the EuroAnalysis2015 Conference in Bordeaux, France, in September.

Prof. Dittrich received her education in Germany, in Bielefeld, and obtained top distinctions both for her undergraduate degree as well as for her PhD, which she completed in only slightly over 3 years in the group of Prof. P. Schuille at the Max Planck-Institute for Biophysical Chemistry (MPI Göttingen) in 2003, working on fluorescence correlation spectroscopy in microfluidic channels. Petra Dittrich then worked as a postdoc at the same institute until 2004, and subsequently became a project leader at the famous Institute for Analytical Sciences (ISAS) in Dortmund, where she was instrumental in a number of projects in the field of miniaturization and Lab-on-Chip-technology for single cell/single particle analysis and manipulation, and creation of artificial cells, biomimetic systems, and soft matter devices.

Petra Dittrich was appointed as an Assistant Professor for Bioanalytics to the Department of Chemistry and Applied Biosciences (D-CHAB) at ETH Zürich in 2008, where she rapidly built up an excellent and rather large research group. Because of her excellence both as a researcher and as a teacher, her non-tenure-track status was converted to tenure-track, and in 2014 she was promoted to be a tenured Associate Professor at ETH.

Petra Dittrich was a fellow of the Studienstiftung des Deutschen Volkes, the German Exchange Organization DAAD and the Christiane Nüsslein-Vollhard-foundation. In 2008 she received the Starting Grant from the European Research Commission (ERC) and in 2010, the Analytica Forschungspreis of the

CHIMIA

www.chimia.ch



SCS
Swiss Chemical
Society

Laureates: Junior Prizes, SCS Fall Meeting 2015



Cover picture by Anne-Clémence Corninboeuf, Riccardo Petraglia and Laurent Vannay, Institute of Chemical Sciences and Engineering, EPFL
Photos by Patrick Favre, Institute of Chemical Sciences and Engineering, EPFL

Editorial



Sandrine Gerber

As a sign of the vitality and variety of chemical research being carried out in Switzerland, the SCS Fall Meeting 2015, organized under the auspices of the SCS Division of Fundamental Research, gathered about 800 participants on the premises of the EPF Lausanne on September 4, 2015. The 507 scientific contributions (oral and poster presentations) and 12 invited lectures attracted collaborators from both academia and chemical/pharmaceutical industry to present, discuss and share recent scientific achievements which were presented in eight parallel sessions and two plenary sessions. The excitement of the young researchers disclosing the most important results of their research was palpable, and the social components of this large and lively annual event gave excellent opportunities to make new contacts and enlarge professional networks. What a sign of enthusiasm to see a full auditorium for the final lecture and plenary session until 6.30 pm!

The SCS Fall Meeting was again a perfect platform to honor scientists from academic institutions and industries for their outstanding contributions to chemical research and development. In particular, young researchers were honored for the scientific quality of their contributions by the SCS-Metrohm Awards for Best Oral Communications and the SCS-DSM Best Poster Awards. This issue of CHIMIA contains articles by these laureates and will give you a flavor of the research being developed in Switzerland in a wide range of chemical fields.

I would like to warmly congratulate all prize winners, thank the authors for their contributions, Metrohm and DSM for the generous sponsorship of the awards and their support to young talented chemists. My acknowledgements also go to the jury members for their excellent selections of laureates, from a considerable number of contributions.

Best Poster Award winner articles sponsored by DSM

- Jasmin Krismer, ETH Zurich
- Stefan Knecht, ETH Zurich
- Christoph Heinz, EPF Lausanne
- Lucas-Alexandre Stern, EPF Lausanne
- Anaëlle Dumas, University Paris-Sud
- Heiner Saßmannshausen, ETH Zurich

Best Oral Communication Award winner articles sponsored by Metrohm

- Andreas Riedo, University of Bern
- Mark Bispinghoff, ETH Zurich
- Adrian Najer, University of Basel
- Maximilian Moser, ETH Zurich
- Franziska A. Balmer, University of Bern

Finally, I sincerely thank the organizing team of the Institute of Chemical Sciences and Engineering (ISIC) at EPFL for their hard work and crucial contribution to the success of the SCS Fall Meeting 2015. We are looking forward to the 2016 edition, which will be held at the University of Zurich on September 15, 2016.

I hope that you will enjoy the content of this issue and I wish you all good reading.

Sandrine Gerber
Chair of the SCS Fall Meeting 2015
EPF Lausanne

Laureates: Junior Prizes of the SCS Fall Meeting 2015

EDITORIAL

233 S. Gerber

236 Single-cell MALDI Tandem Mass Spectrometry: Unambiguous Assignment of Small Biomolecules from Single *Chlamydomonas reinhardtii* Cells
J. Krismer, R. F. Steinhoff, R. Zenobi*

240 Efficient Water Electrolysis Using Ni₂P as a Bifunctional Catalyst: Unveiling the Oxygen Evolution Catalytic Properties of Ni₂P
L.-A. Stern, X. Hu*

244 New Approaches for *ab initio* Calculations of Molecules with Strong Electron Correlation
S. Knecht*, E. D. Hedegård, S. Keller, A. Kovyrshin, Y. Ma, A. Muolo, C. J. Stein, M. Reiher*

252 PLGA-PEG-supported Pd Nanoparticles as Efficient Catalysts for Suzuki-Miyaura Coupling Reactions in Water
A. Dumas*, A. Peramo, D. Desmaële, P. Couvreur

258 Total Synthesis of Fijiolide A
C. Heinz, N. Cramer*

263 Exotic Chemistry with Ultracold Rydberg Atoms
H. Saßmannshausen, J. Deiglmayr, F. Merkt*

268 Laser Ablation/Ionisation Mass Spectrometry: Sensitive and Quantitative Chemical Depth Profiling of Solid Materials
A. Riedo*, V. Grimaudo, P. Moreno-García, M. B. Neuland, M. Tulej, P. Broekmann, P. Wurz

274 Halogen Chemistry on Catalytic Surfaces
M. Moser, J. Pérez-Ramírez*

279 PH₃ as a Phosphorus Source for Phosphinidene–Carbene Adducts and Phosphinidene–Transition Metal Complexes.
M. Bispinghoff*, H. Grützmacher

284 Do Hydrogen Bonds Influence Excitonic Splittings?
F. A. Balmer, P. Ottiger, S. Leutwyler*

288 Giant Host Red Blood Cell Membrane Mimicking Polymersomes Bind Parasite Proteins and Malaria Parasites
A. Najer, S. Tamboo, C. G. Palivan, H.-P. Beck, W. Meier*

Single-cell MALDI Tandem Mass Spectrometry: Unambiguous Assignment of Small Biomolecules from Single *Chlamydomonas reinhardtii* Cells

Jasmin Krismer[§], Robert F. Steinhoff, and Renato Zenobi*

[§]SCS-DSM Award for best poster presentation in Analytical Sciences

Abstract: The analysis of compounds from single cells is a major challenge in analytical life science. Labeling strategies, for instance fluorescence detection, are well established for measuring proteins with single cell sensitivity, but they mostly fail to detect small molecules. More recently mass spectrometry has entered the realm of single cell sensitivity and enables the label-free and highly parallelized detection of small biomolecules from single cells. The assignment of signals detected in single cells, however, generally has to rely on measurements in whole cell culture extracts. Isobaric structures, contaminations, higher noise levels and the high variability in the abundance of peaks between single cells complicate the assignment of peaks in single-cell spectra. Tandem mass spectrometry would be very useful for compound identification *via* mass spectrometry directly in single-cell analyses. Here we present the first single cell tandem mass spectra collected using matrix-assisted laser-desorption/ionization. The spectra obtained allow the assignment of most compounds detected in the spectra. We also show that the fragmentation is not restricted to the most abundant peaks in the spectra, but over a dynamic range of more than one order of magnitude.

Keywords: Collision-induced-dissociation · Matrix-assisted laser-desorption/ionization · Single-cell mass spectrometry · Tandem mass spectrometry

Introduction

Individual cells are the smallest functioning unit of life and a key challenge in analytical life science. The analytical scientist is challenged by the high sensitivity and selectivity required for the analysis of single cells.^[1] The biologist, on the other hand, seeks to understand the individual cell within the biological context of its population or tissue, which adds high throughput to the list of challenges for analytical methods to overcome. There are plenty of single-cell techniques in the area of DNA,^[2,3] RNA^[4,5] and protein analysis^[6,7] that have found their way into biologists' labs. These techniques benefit from the amplification tools adopted from molecular biology and the high linear dynamic range and sensitivity of fluorescent probes.

However, few such tools exist for the analysis of small molecules from single cells,^[8] despite the fact that there is a great

need for phenotypic and metabolic characterization of single cells, especially since changes in genomes and transcriptomes are often poor predictors of cellular phenotypes.^[9] Mass spectrometry has made great progress with respect to sensitivity and resolution in the past decades. Matrix-assisted laser desorption/ionization (MALDI) mass spectrometry^[10] in particular can provide both the high throughput and the sensitivity needed for the analysis of large numbers of single cells.^[11] Analyzing complex and dynamic biological systems such as cells, however, requires not just detection of masses but also the assignment of the signals detected to functionally relate these to biological processes.

Tandem mass spectrometry is an important part of the methodological toolbox of a mass spectrometrist for several reasons.^[12] First, different constitutional isomers can be attributed to a single isobaric signal, which makes it possible to identify molecules using characteristic fragments. Second, contamination from different sources like solvents, the cell culture medium, cell manipulating devices or the MALDI-matrix can give rise to interferences that show the same or highly similar masses. This effect is especially important in single-cell mass spectrometry because

the weight of single cells is in the range of 10^{-12} – 10^{-15} grams.^[13,14] Third there is great variability in the relative abundance of molecules between single cells, which can complicate the peak assignment. Unfortunately the MS/MS capabilities of mass spectrometry approaches for single cell analysis have very much lagged behind.

Recently we reported a method for the high-throughput analysis of single cells for *Chlamydomonas reinhardtii*, a green freshwater algae and a well-studied model organism in photosynthesis and biofuel research.^[15] The method allowed the parallel detection and relative quantitation of more than 20 assigned peaks from different lipid classes with high throughput. MS/MS capabilities would greatly enhance the explanatory power based on higher confidence in peak assignment.

Here, we present the first ever MS/MS spectra collected from single cells using MALDI as an ionization method. The cells were analyzed using 2,5-dihydroxybenzoic acid (DHB) as a matrix, in positive ion mode. The method allowed us to assign about 15 compounds in our spectra belonging to different lipid and pigment classes. The assignments based on the single cell tandem mass spectra are in good agree-

*Correspondence: Prof. Dr. R. Zenobi
Department of Chemistry and Applied Biosciences
ETH Zurich
Vladimir-Prelog-Weg 3, CH-8093 Zurich
E-mail: zenobi@org.chem.ethz.ch

ment with spectra obtained by analyzing lipid extracts, as well as the relevant molecular biology literature.^[16–18]

Experimental Section

Chemicals

2,5-dihydroxybenzoic acid (DHB) was purchased from Sigma-Aldrich. Chlorophyll a (from *Anacystis nidulans*), chloroform (>99.8%), acetone (puriss. p.a., ≥99.5%) and 2-propanol (puriss., ≥99.5%) were purchased from Sigma Aldrich, Switzerland. Water (Optima® LC/MS grade) was purchased from Fisher-Chemicals. Hutners trace element solution for cell culture media preparation was obtained from the Chlamydomonas Resource Center (St. Paul, MN, USA)

MS/MS of Lipid Extracts

A lipid extract was performed with the Bligh-Dyer method^[19] using *C. reinhardtii* wild-type strain CC-125 obtained from the Chlamydomonas Resource Center, St Paul, MN. The cells were cultured in tris-acetate-phosphate medium.^[20] To aid the extraction the cells were sonicated for 30 seconds. The chloroform phase was collected and stored at -20°C . Then the chloroform was evaporated and the lipids solubilized in aqueous acetone (80 vol% acetone, 20 vol% water). The samples were mixed with DHB (10 mg/mL in 80% aqueous acetone) on the MALDI target (384 Opti-TOF 123 mm \times 61 mm SS, ABSciex, Toronto) in a sandwich fashion (0.5 μL DHB – 0.5 μL lipid extract – 0.5 μL DHB). The MS/MS method used for extracts was identical to the one described below.

Sample Preparation for Single-cell MS/MS

Wild-type *C. reinhardtii* cells (strain CC125) were centrifuged (3500 \times g for 5 min) three times and resuspended in water. The cells were placed on a microstructured array for MALDI mass spectrometry as reported previously.^[15] In short, the array consists of 55 \times 26 spots of 300 μm diameter each spaced by 720 μm on a stainless steel plate. A layer of matrix was added first, followed by deposition of the washed cells into the spots (Fig. 1A). Cellular metabolism was quenched immediately by immersing the entire array into liquid nitrogen. Extraction of analytes and co-crystallization with the matrix is achieved by recurrent extraction adding 5 \times 5 nL of 10 mg/mL of DHB dissolved in 80% aqueous acetone and letting the spots crystallize after each step. Fluorescence scans at 630 nm excitation and 670 nm emission were collected of the blank slide, of the cells after quenching, and after matrix application.

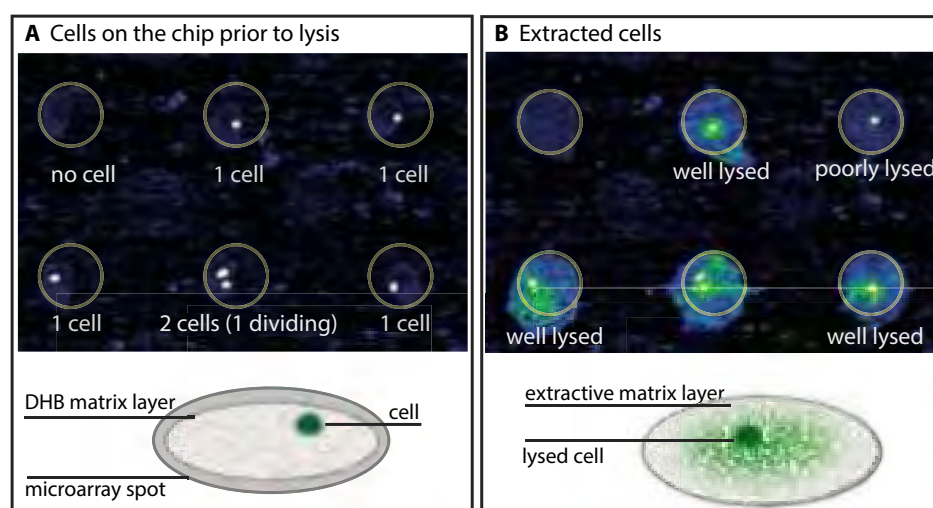


Fig. 1. Sample preparation procedure for single-cell MS/MS. Chlorophyll autofluorescence is measured at 630 nm excitation and 670 nm emission. Both of the images are scaled identically for better visibility (0–3000 instead of 0–65000) and falsely colored. The diameter of a spot is 300 μm . Cells are around 10 μm but appear larger due to over-scaling and scattering. A: The autofluorescent cells are imaged on the slide prior to lysis to determine the number of cells in each spot. As shown in the graphical abstract below a layer of matrix is applied prior to applying the cells. B: Scanning the slides after co-crystallization can monitor the success of cell lysis. Matrix autofluorescence is negligible. Only spots containing well-lysed cells should be used for single-cell MS/MS experiments.

Single-cell MS/MS

The tandem mass spectra were recorded on a reflectron MALDI-TOF instrument (AB Sciex 5800, Toronto, CA). The spots for MS/MS were selected from the plates based on the fluorescence scans. Spectra were collected from spots showing single cells in the fluorescence scan after quenching. To confirm the fact that the signal is produced only in the presence of cells MS/MS were recorded for the same precursor mass on spots showing no cells. In none of the cases did we detect fragments of cellular analytes in the absence of cells. The MALDI parameters used were: a delayed extraction time of 300 ns, a laser intensity of 5500 a.u. and a laser repetition rate of 1000 Hz. In all cases spectra were collected with and without metastable suppression. Precursors were isolated using a mass window of ± 1.5 Da, using the QuanTis timed ion selector of the reflectron TOF system operated with a TIS offset of 1.5 mm.

Data Analysis

Peak picking was performed according to a S/N ≥ 10 criterion. Spectra were calibrated externally using chlorophyll a as a reference. The spectra were smoothed using the default settings in the Data Explorer software (ABSciex, Toronto).

Results and Discussion

The tandem mass spectrometry method was optimized on a chlorophyll a standard and a lipid extract of *C. reinhardtii*. The lipid composition of *C. reinhardtii* is well

studied, since the species is both a model organism in photosynthesis and a candidate for biofuel production. From an experimental perspective one of the key advantages in using the algae as a model for optimizing and developing a single cell method is that due to its autofluorescent pigments in the form of chlorophylls it is possible to visualize cell lysis, a key step for successful single cell mass spectrometry.^[15] Two aspects are very important here: the first is to make sure that the actual measurement is taken on a single cell. In the current procedure the cells are placed on a microarray by spotting a cell culture at an optimized cell density. This procedure leaves most spots occupied with single cells, which can be identified, based on fluorescence scans (Fig. 1A). However, some spots remain empty while multiple cells occupy others. These spots are discarded for analysis. The second key step is lysis and co-crystallization (Fig. 1B). Only spots that show well-lysed cells as shown in Fig. 1 are considered for MS/MS. Poorly lysed cells may still show signals in MS mode, but these are generally too low in intensity to perform MS/MS experiments.

Relying on the sample preparation protocol for single-cell MALDI optimized for *C. reinhardtii* we were able to assign 16 compounds to 14 mass spectral peaks (Table 1) by performing single-cell MS/MS measurements. The assignments are backed up by literature. The most prominent signal in the single-cell spectra is the pigment chlorophyll a. However due to the presence of DHB, which is an acid, the extraction of the lipids is carried out under

low pH conditions. This leads to a release of the Mg^{2+} ion from the porphyrin macrocycle. Chlorophyll a is therefore detected as pheophytin a ($[M-Mg^{2+}+3H]^+$ = 871.57 Da) using DHB as a matrix.^[17,21] This is also true for chlorophyll b ($[M-Mg^{2+}+3H]^+$ = 885.55 Da). The single-cell MS/MS of chlorophyll a is dominated by the signal at 593.28 Da due to the loss of the phytol chain (Fig. 2A and 2D). Chlorophyll b fragmentation leads to the formation of 607.25 Da fragment due to phytol loss. Since chlorophylls are absorbing the wavelength of the MALDI laser at 355 nm both CID as well as in-source decay contribute to fragmentation. An increase in laser intensity was found to enhance fragmentation even in the absence of CID gas, which supports this interpretation (data not shown).

Furthermore, the spectra show all of the most abundant lipids, which can be detected in positive ion mode, both from the plastidic, *i.e.* of organellar origin and extraplastidic membrane systems. Plastidic membrane systems that include the thylakoid membranes, in which the photosynthetic complexes are embedded, mainly consist of the galactolipids mono- and digalactosyl-diacylglycerol (MGDG and DGDG) and sulfolipids in the form of sulfoquinovosyl-diacylglycerol (SQDG).^[18] Since the extraction protocol was optimized for chlorophyll, it is reasonable that the major membrane constituents are co-extracted. MGDG and DGDG can be detected in the form of sodium ($[M+Na]^+$) or potassium ($[M+K]^+$) adducts using MALDI-MS as

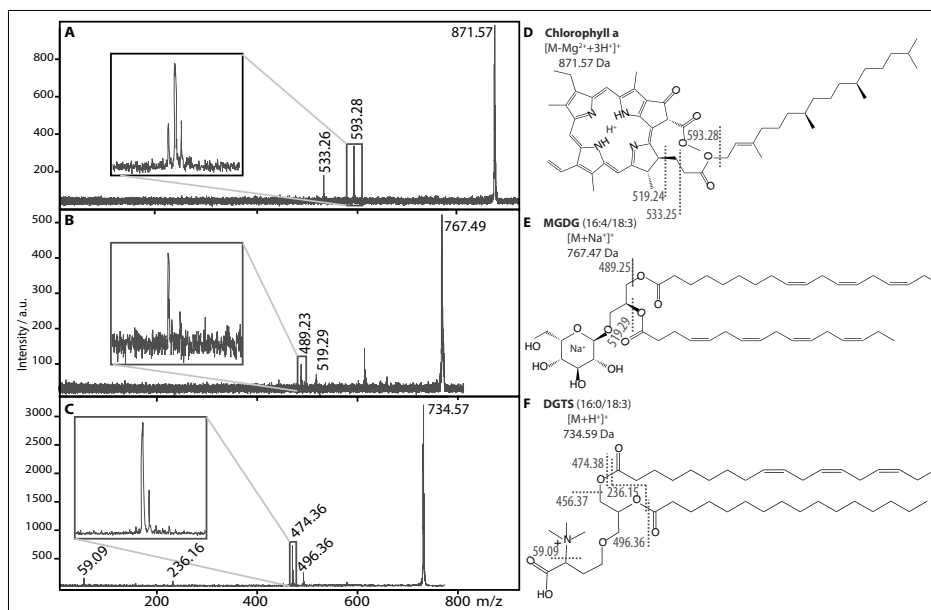


Fig. 2, Single-cell MS/MS and corresponding chemical structures of different compound classes detected in single cells. A/D: Single-cell MS/MS of chlorophyll a the structure showing the fragmentation explaining the most abundant signals in the MS/MS spectra. B/E: SC-MS/MS and the chemical structure of MGDG, a plastidic galactolipid. C/F: SC-MS/MS and chemical structure of a DGTS, an extraplastidic lipid. The highly stabilized charge leads to the detection of the lipid headgroup even in single-cell spectra. The positions of the two fatty acids (sn1 or sn2) cannot be determined using MS/MS but are adapted from literature.^[16]

previously reported by Vieler *et al.*^[21] In the single-cell mass spectra the sodium adducts are most prominent. The SC-MS/MS spectra of both MGDG (see Fig. 2B and 2E) and DGDG lipids are characterized by neutral loss of the fatty acid side chains.^[22] Despite the fact that MGDG (16:4/18:3) makes up for almost 80% of the MGDG

lipid, which in turn contributes about 50% of the total thylakoid lipid, the relative intensity of the peak is relatively low at 18%. This can be attributed to a lower ionization efficiency due to the sodium adduct formation.

The major extraplastidic lipid classes are the diacylglycerol-trimethylhomoser-

Table 1. List of compounds assigned by SC-MS/MS in *Chlamydomonas reinhardtii* using DHB in positive ion mode. Relative intensities relate to single-cell MS spectra collected from the same population. Numbers in brackets relate to the fatty acid composition (carbon number: number of double bonds) the position of the fatty acid or the position of the double bonds cannot be determined using single-cell MS/MS.

	metabolite name	rel. int.	species detected	parent mass	main fragment	other fragments
Pigments	Chlorophyll a	100	$[M-Mg^{2+}+3H]^+$	871.57	593.28	533.25, 519.30
	Chlorophyll b	34	$[M-Mg^{2+}+3H]^+$	885.55	607.25	547.24, 533.29
Galactolipids	MGDG (16:4/18:3)	18	$[M+Na]^+$	767.47	489.24	519.28
	DGDG (18:3/16:3)	19	$[M+Na]^+$	931.53	653.27	681.28
	DGDG (18:2/16:3)	15	$[M+Na]^+$	933.55	653.28	683.45
	DGDG (18:3/16:0)	9	$[M+Na]^+$	937.58	659.31	681.22
	DGDG (18:2/16:0)	9	$[M+Na]^+$	939.6	659.3	683.24
	Homoserine lipids	DGTS (16:0/18:4)	51	$[M+H]^+$	732.58	474.33
DGTS (16:0/18:3)		49	$[M+H]^+$	734.59	474.37	496.38, 236.16, 474.37, 456.34
DGTS (16:0/18:2)		21	$[M+H]^+$	736.61	474.36	498.33
DGTS (18:3/18:4)		19	$[M+H]^+$	754.55	496.42	494.42
DGTS (18:3/18:3), DGTS (18:4/18:2)		20	$[M+H]^+$	756.57	496.32	498.36, 494.29, 236.12
DGTS (18:2/18:3)		26	$[M+H]^+$	758.6	496.36	498.39
DGTS (18:2/18:2), DGTS (18:1/18:3)		18	$[M+H]^+$	760.61	498.36	496.45, 500.38

ines (DGTS) which functionally replace phosphatidylcholines in *C. reinhardtii*.^[18] The DGTS lipids show a great variety of fatty acid side chains in the single-cell spectra (Table 1, Fig. 2C and 2F). One reason for this lipid class to be readily observed might be the high ionization efficiency of the highly polar lipid headgroup. The trimethylhomoserine-headgroup itself as well as various fragments generated by the loss of fatty acid side chains can also be detected in single-cell MS/MS spectra (Fig. 3). In contrast to the galactolipids the side chain fragmentation leads both to the fatty acid neutral loss and the cleavage of the acyl group with the latter being more prominent in the single-cell MS/MS spectra. The relative abundance of the different DGTS species agrees well with previously reported values.^[16] A unique advantage of applying MS/MS is that fragmentation of the side chains allows the assignment of multiple isobaric species. We were able to assign multiple isobars for the signal at 756.57 Da (DGTS (18:2/18:2) and DGTS (18:1/18:3)) and 760.61 Da (DGTS (18:3/18:3) and DGTS (18:4/18:2)) respec-

tively. One explanation for the detection of multiple isobars in the case of 756.57 Da and 760.61 Da is the similar abundance of the two contributing DGTS species.^[16]

Conclusions

Peak assignment in single-cell spectra is a challenge for the advancement of single-cell mass spectrometry techniques. The certainty of the actual assignment based on fragment detection – despite all database searches and high mass accuracy – is unsurpassed. The successful implementation of MS/MS experiments on the single-cell level as shown here reflects the progress made with respect to sensitivity and reproducibility, and adds an important amendment to single-cell MALDI mass spectrometry.

Acknowledgement

We would like to thank the physics workshop of ETH Zurich and Dr. Rolf Brönnimann from EMPA Dübendorf for the help in producing the microarrays for MALDI-MS. We

would like to thank Dr. Jens Sobek from the Functional Genomics Center Zurich for the assistance using the microarrayer for the sample preparation and Prof. Dr. Julia Vorholt from the Microbiology Institute at ETH Zurich for allowing us to use their sterile bench.

Received: January 12, 2016

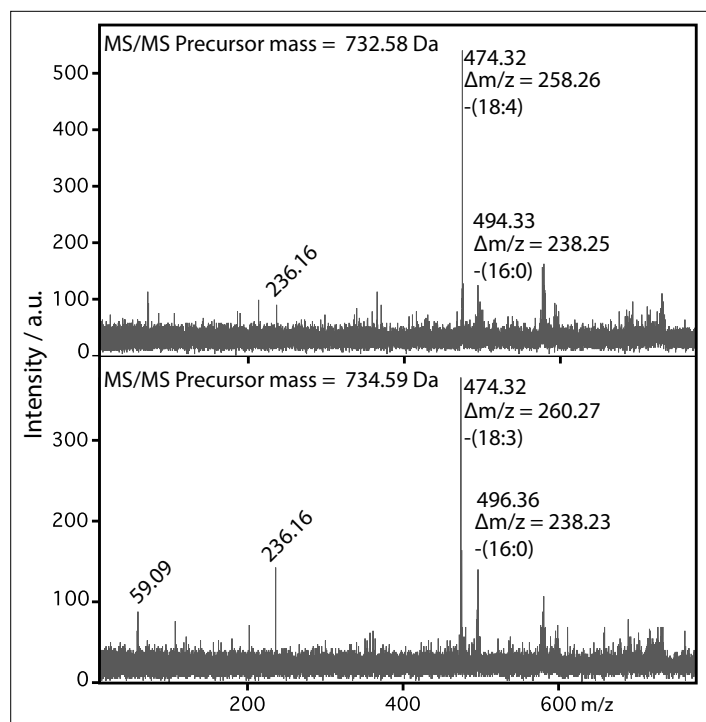


Fig. 3. Precursor ion suppressed single-cell MS/MS from two DGTS lipids. The DGTS at 732.58 Da (upper spectrum) fragments to 474.32 Da and 494.33 Da corresponding to the acyl loss of the fatty acids 18:4 and 16:0 respectively. DGTS at 734.59 Da (lower spectrum) fragments to 474.32 Da and 496.36 Da corresponding to the acyl loss of 18:3 and 16:0, respectively.

- [1] E. Strauss, *Nat. Chem. Biol.* **2010**, *6*, 873.
- [2] H. Li, U. B. Gyllensten, X. F. Cui, R. K. Saiki, H. A. Erlich, *Nature* **1988**, *335*, 414.
- [3] R. S. Lasken, *Curr. Opin. Microbiol.* **2007**, *10*, 510.
- [4] F. Tang, C. Barbacioru, Y. Wang, E. Nordman, C. Lee, N. Xu, X. Wang, J. Bodeau, B. B. Tuch, A. Siddiqui, K. Lao, M. A. Surani, *Nat. Meth.* **2009**, *6*, 377.
- [5] S. Islam, U. Kjällquist, A. Moliner, P. Zajac, J.-B. Fan, P. Lönnerberg, S. Linnarsson, *Nat. Protocols* **2012**, *7*, 813.
- [6] J. Lippincott-Schwartz, G. H. Patterson, *Science* **2003**, *300*, 87.
- [7] B. N. G. Giepmans, S. R. Adams, M. H. Ellisman, R. Y. Tsien, *Science* **2006**, *312*, 217.
- [8] R. Zenobi, *Science* **2013**, *342*, 1243259.
- [9] M. D. Ritchie, E. R. Holzinger, R. Li, S. A. Pendergrass, D. Kim, *Nat. Rev. Genet.* **2015**, *16*, 85.
- [10] M. Karas, D. Bachmann, U. Bahr, F. Hillenkamp, *Int. J. Mass Spectrom. Ion Proc.* **1987**, *78*, 53.
- [11] T. H. Ong, D. J. Kissick, E. T. Jansson, T. J. Comi, E. V. Romanova, S. S. Rubakhin, J. V. Sweedler, *Anal. Chem.* **2015**, *87*, 7036.
- [12] F. McLafferty, *Science* **1981**, *214*, 280.
- [13] T. P. Burg, M. Godin, S. M. Knudsen, W. Shen, G. Carlson, J. S. Foster, *Nature* **2007**, *446*, 1066.
- [14] G. Popescu, K. Park, M. Mir, R. Bashir, *Lab Chip* **2014**, *14*, 646.
- [15] J. Krismer, J. Sobek, R. F. Steinhoff, S. n R. Fagerer, M. Pabst, R. Zenobi, *Appl. Environ. Microbiol.* **2015**, *81*, 5546.
- [16] H. M. Nguyen, S. Cuiné, A. Beyly-Adriano, B. Légeret, E. Billon, Pa. Auroy, F. Beisson, G. Peltier, Y. Li-Beisson, *Plant Physiol.* **2013**, *163*, 914.
- [17] T. Suzuki, H. Midonoya, Y. Shioi, *Anal. Biochem.* **2009**, *390*, 57.
- [18] W. R. Riekhof, C. Benning, 'Glycerolipid Biosynthesis', in 'The Chlamydomonas Sourcebook' 2nd Ed., Chap. 2, Ed. E.H.H.B.S.B. Witman, **2009**, Academic Press: London. pp. 41-68.
- [19] E. G. Blish, W. J. Dyer, *Can. J. Biochem. Physiol.* **1959**, *37*, 911.
- [20] D. S. Gorman, R.P. Levine, *Proc. Nat. Acad. Sci. USA* **1965**, *54*, 1665.
- [21] A. Vieler, C. Wilhelm, R. Goss, R. Süß, J. Schiller, *Chem. Phys. Lipids* **2007**, *150*, 143.
- [22] L. Fouillen, B. Colsch, R. Lessire, 'The Lipid World Concept of Plant Lipidomics', in 'Advances in Botanical Research', Chap. 7, Ed. R. Dominique, **2013**, Academic Press. pp. 331-376.

Efficient Water Electrolysis Using Ni₂P as a Bifunctional Catalyst: Unveiling the Oxygen Evolution Catalytic Properties of Ni₂P

Lucas-Alexandre Stern[§] and Xile Hu*

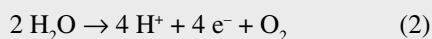
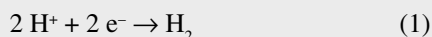
[§]SCS-DSM Award for best poster presentation in Catalysis Science and Engineering

Abstract: The excellent bifunctional catalytic activity of nickel phosphide (Ni₂P) for water splitting is reported. Ni₂P, an active hydrogen evolving catalyst, is shown to be highly active for oxygen evolution. Only 290 mV of overpotential is required to generate a current density of 10 mA cm⁻² in 1 M KOH. Under oxygen evolving conditions, Ni₂P undergoes structural modification to form a Ni₂P/NiO_x core-shell assembly, the catalytic active species. Ni₂P is applied on both electrodes of an alkaline electrolyser and a current density of 10 mA cm⁻² is generated at 1.63 V.

Keywords: Electrochemistry · Janus catalyst · Ni₂P · Oxygen evolution · Water splitting

1. Introduction

Global scale exploitation of renewable energy resources, such as wind and solar energy, demands efficient energy storage techniques. Electrochemical water splitting is one of the most attractive method for energy storage.^[1] Water splitting is subdivided in two half-reactions, namely, the hydrogen evolution reaction (HER, Eqn. (1)) and the oxygen evolution reaction (OER, Eqn. (2)).



Both reactions require electrocatalysts to proceed efficiently. State-of-the-art catalysts rely on the use of scarce and expensive noble metals, *e.g.* platinum.^[2] While promising Earth-abundant water-

splitting catalysts have been developed, only few materials are able to catalyse both HER and OER in the same media. Bifunctional catalysts made from Earth-abundant metals would facilitate production and implementation of electrolyser devices. The reported bifunctional systems include Co,^[2] Ni,^[3] Cu,^[4] NiFe LDH,^[5] NiFeO_x,^[6] NiCo₂S₄,^[7] Ni₅P₄,^[8] CoO_x,^[9] CoP,^[10] FeP.^[11] In this article, we show that Ni₂P, an active HER catalyst, is efficient for the oxygen evolution reaction in alkaline medium. Under OER conditions, the material forms a Ni₂P/NiO_x core-shell heterostructure. This assembly generates a current density of 10 mA cm⁻² at an overpotential of only 290 mV.^[12] The Janus behaviour of the material permits the fabrication of an efficient alkaline electrolyser using Ni₂P as catalyst for both the cathode and the anode.

2. Oxygen Evolution Activity of Ni₂P

The Ni₂P nanoparticles were prepared *via* a solid-state thermal reaction previously reported by our group.^[13] Briefly, a phosphorus source, NaH₂PO₂ (0.66 g, for analysis, Acros), and a nickel salt, NiCl₂·6H₂O (0.3 g, ReagentPlus®, Aldrich), were ground together at ambient atmosphere and then placed in a quartz boat. This was then transferred into a tubular furnace and heated at 250 °C under a constant flow of nitrogen. The obtained powder was further ground and the impurities were washed off from the product using copious amount of distilled water. The product was then dried in an oven at 50 °C for a few hours. X-ray diffraction of the obtained powder is shown in Fig. 1b. The diffraction signal was compared

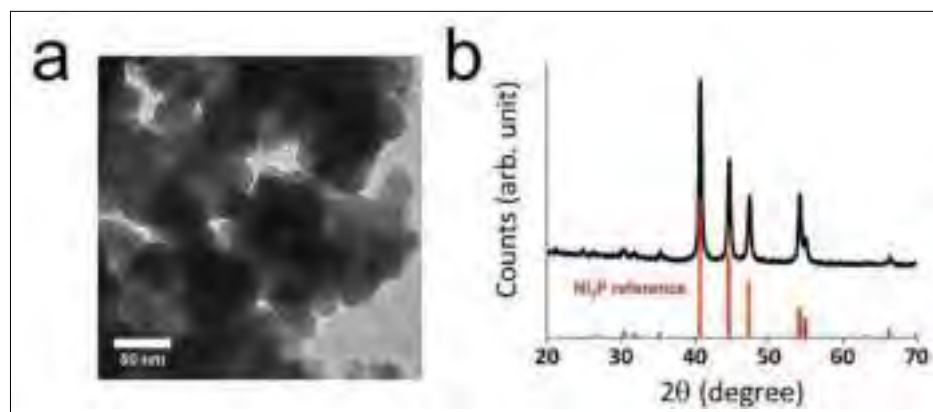


Fig. 1. a) TEM image of polycrystalline Ni₂P. b) Powder X-ray diffraction pattern of the Ni₂P nanoparticles. Adapted by permission of The Royal Society of Chemistry from ref. [12].

*Correspondence: Prof. Dr. X. Hu
Laboratory of Inorganic Synthesis and Catalysis
Institute of Chemical Sciences and Engineering
École Polytechnique Fédérale de Lausanne (EPFL)
ISIC-LSCI, BCH 3305
CH-1015 Lausanne
E-mail: xile.hu@epfl.ch

to the reference diffraction pattern obtained from the International Center of Diffraction Data. The overlapping signals indicated the successful synthesis of pure phase Ni_2P . The transmission electron microscopy (TEM) image shows that the Ni_2P nanoparticles have an averaged size of 50 nm and are coated with a thin amorphous layer (Fig. 1a).

To evaluate the catalytic activity of Ni_2P for the oxygen evolution reaction, linear sweep voltammetry scans were performed in 1 M KOH. The catalytic activity of nickel phosphide was measured and compared to various nanomaterials including IrO_2 , Ni, NiO_x and an electrodeposited $\text{Ni}(\text{OH})_2$ film (Fig. 2a). IrO_2 (99.9% Ir, abcr) and NiO_x (99.8% trace metals basis, Aldrich) were used as received, while Ni nanoparticles and $\text{Ni}(\text{OH})_2$ film preparation has been reported previously.^[14] The loading of IrO_2 , Ni, NiO_x applied on the glassy carbon electrode was identical to Ni_2P loading. Fig. 2a shows that Ni_2P nanoparticles catalytic activity is superior to that of the different catalysts evaluated. The overpotential to generate a current density of 10 mA cm^{-2} is only 290 mV for Ni_2P . To reach similar current density, IrO_2 and $\text{Ni}(\text{OH})_2$ requires an additional 40 mV of overpotential compared to Ni_2P . Ni and NiO_x drive a current density of 10 mA cm^{-2} at 365 mV of overpotential.

The electrochemical surface area (ESCA) of the materials was assessed and compared. For this purpose, the double-layer capacitance of the materials was calculated. Fig. 2b shows the ESCA of the nickel-based catalysts. The ESCA for the different materials were expressed in terms of surface averaged double layer capacitance. Ni_2P have higher surface area for similar loading than other nickel materials: $176.9 \mu\text{F cm}^{-2}$, followed by $\text{Ni}(\text{OH})_2$ $137.2 \mu\text{F cm}^{-2}$. NiO_x and Ni nanoparticles have smaller ESCA values 68 and $37 \mu\text{F cm}^{-2}$ respectively. The correlation determined between the ESCA of Ni, NiO_x , $\text{Ni}(\text{OH})_2$ and their respective catalytic activity at the fixed overpotential of 325 mV cannot be applied to Ni_2P . This indicates that high surface area is not the sole reason for the superior catalytic activity of nickel phosphide.

The stability of the nickel phosphide nanoparticles was probed by galvanostatic experiment. Fig. 2c shows that the overpotential to generate 10 mA cm^{-2} increased only of 10 mV over the course of 10 hours indicating high stability of the catalyst. The nickel phosphide oxygen evolution activity was also compared to several state-of-the-art materials (Table 1). It can be seen that Ni_2P is more active than many Ni and Co-based oxides, and even IrO_2 in base.

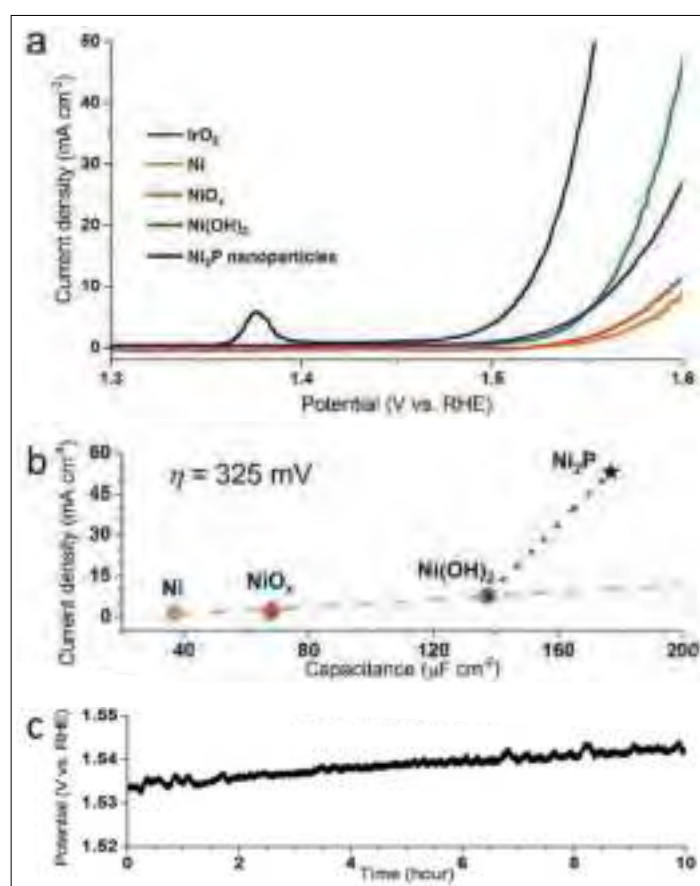


Fig. 2. a) Linear sweep voltammetric (LSV) curves of Ni_2P , Ni nanoparticles, NiO_x nanoparticles, electrodeposited $\text{Ni}(\text{OH})_2$, and IrO_2 in 1 M KOH. b) Correlation of the current density at an overpotential of 325 mV, with the electrochemical capacitance of the different nickel materials. c) Galvanostatic measurement on the Ni_2P nanoparticles in 1 M KOH at a constant current density of 10 mA cm^{-2} over 10 h. Conditions: pretreated working electrode, pre-activated Ni_2P catalysts, 5 mV s^{-1} , 0.14 mg cm^{-2} . Adapted by permission of The Royal Society of Chemistry from ref. [12].

Table 1. Comparison of the OER catalytic activity of state-of-the-art catalysts. Adapted by permission of The Royal Society of Chemistry from ref. [12].

Material	Loading [mg cm^{-2}]	η @ 10 mA cm^{-2} [mV]	Ref.
Ni	0.14	377	This work
NiO_x	0.14	364	This work
$\text{Ni}(\text{OH})_2$	0.14	331	This work
Ni_2P	0.14	290	This work
NiO_x	0.02	360	[15c]
$\alpha\text{-Ni}(\text{OH})_2$	0.20	331	[15d]
$\beta\text{-Ni}(\text{OH})_2$	0.20	444	[15d]
NiCo_2O_4	0.53	565	[15e]
NiFe-LDH	0.20	320	[16]
CoO_x @CN	0.42	410	[9]
BSCF82	0.25	320	[17]
IrO_2	-	320	[15b]
IrO_2^a	0.35	275	[18]

^aCatalytic activity measured in acidic conditions

3. $\text{Ni}_2\text{P}/\text{NiO}_x$ Core-shell Structure: The OER Catalytic Active Species

To identify the nature of the chemical modifications undergone by nickel phosphide during water oxidation, the

Ni_2P nanoparticles were characterized prior and after catalysis by high-resolution TEM, energy-dispersive X-ray element mapping and X-ray photoelectron spectroscopy (XPS) (Fig. 3). The data indicate that prior to catalysis crystalline

nanoparticles of Ni_2P are embedded in an amorphous matrix, which is oxygen-rich, contains phosphorus, and is free of any metallic content (Fig. 3a–e). This layer likely consists of residual P_2O_5 as a side product of the catalyst synthesis. Important structural change can be observed on the catalytic material after oxygen evolution for 1 h. The HRTEM image (Fig. 3g) shows that after OER, the layer surrounding the nanoparticles is composed of ultrafine particles of about 2–3 nm diameter. Closer inspection of the particles in the layer revealed the presence of lattice registry indicative of crystalline materials. Fast Fourier transform (FFT) (Fig. 3g inset) allowed measurement of the crystal lattice spacing of the fine particles. The distance between two crystal planes is characteristic of NiO_x material. A crystal lattice spacing of the material's core was also determined and it is characteristic of the (100) facet of Ni_2P . Elemental mapping images of the catalyst after OER (Fig. 3h–k) clearly show the $\text{Ni}_2\text{P}/\text{NiO}_x$ core-shell heterostructure that the material adopts under oxidative conditions. Nickel is present in both layers of the material. Oxygen coats homogeneously the particle surface. Phosphorus is present only in the core. The structure of the material was further corroborated by XPS measurements (Fig. 3l).^[19] Electrochemical measurements also validate the formation of a $\text{Ni}_2\text{P}/\text{NiO}_x$ core-shell heterostructure during OER. The oxidation peak observed is indicative of the $\text{Ni}^{2+}/\text{Ni}^{3+}$ oxidation in many nickel oxide hydroxide and bimetallic NiFeO_x OER catalysts.^[13,15a,15d,20] The pre-activation of the catalyst is, thus, hypothesized to allow the *in situ* formation of a stable $\text{Ni}_2\text{P}/\text{NiO}_x$ core-shell heterostructure with improved OER catalytic properties.

The enhanced catalytic activity of the $\text{Ni}_2\text{P}/\text{NiO}_x$ core-shell structure compared to other NiO_x catalysts for OER has two possible origins. On one hand the unique assembly provides significant improvement in electron conduction.^[21] Indeed, the metallic Ni_2P core might provide an efficient electron pathway to the insulating NiO_x shell. On the other hand, Ni_2P allows the *in situ* formation of ultrafine nanoparticles of NiO_x , which allows higher active site exposure. Synergistic effects, which warrant further investigation, may play a role as well.

4. Efficient and Inexpensive Alkaline Electrolyser Fabricated Using Ni_2P as Catalyst

The hydrogen evolving capabilities of Ni_2P have been reported recently.^[13,22] Given the presented OER catalytic activity, an alkaline electrolyser using Ni_2P as both

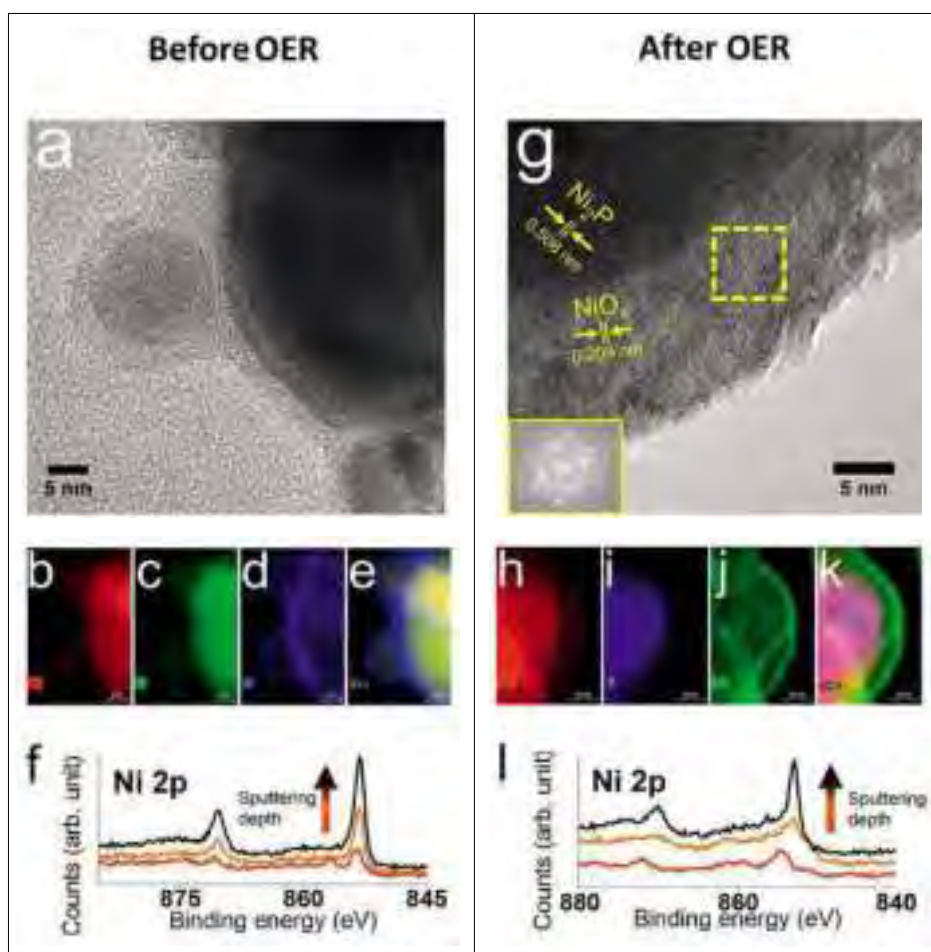


Fig. 3. a) High-resolution TEM (HRTEM) image of the Ni_2P nanoparticles prior to oxygen evolution catalysis. b–e) Corresponding energy dispersive X-ray (EDX) elemental maps of the system prior to catalysis (scale bar: 9 nm). b) Ni elemental mapping. c) Phosphorus elemental mapping. d) Oxygen elemental mapping. e) Combined elemental mapping. f) High-resolution depth-profiling XPS spectra of the Ni 2p area. As the profiling depth increases (arrow direction), the FWHM decreases, indicative of stronger metallic Ni content. g) HRTEM image of the Ni_2P nanoparticles after electrochemical pretreatment at 1.5 V vs. RHE for one hour. Inset (lower left): FFT of the framed area (middle). The spots observed on the FFT are indicative of registry order and so of crystallinity. The lattice fringes spacing of the materials were determined using FFT. They correspond to the characteristic (100) facet of Ni_2P and specific facets of nickel oxides/hydroxides species, NiO_x . h–k) Corresponding EDX maps of the elements on the sample region shown in (g) (scale bar: 20 nm). h) Nickel elemental mapping. i) Phosphorus elemental mapping. j) Oxygen elemental mapping. k) Combined elemental mapping of Ni, O, and P. l) High-resolution depth-profiling XPS spectra of the Ni 2p area after catalytic activity. As the profiling depth increases (arrow direction), the large FWHM, that is indicative of nickel oxide species, decreases, indicative of stronger metallic Ni content. This confirms the presence of a surface oxide layer around metallic nickel phosphide core. Adapted by permission of The Royal Society of Chemistry from ref. [12].

cathode and anode catalyst was fabricated. The catalyst support used for this device was nickel foam. The loading of catalyst applied on the two Ni foam was 10 mg cm^{-2} . Fig. 4 shows the measured catalytic activity of the alkaline electrolyser in 1 M KOH. The activity is compared with bare Ni foams as reference. To generate a current density of 10 mA cm^{-2} the alkaline electrolyser employing Ni_2P as catalyst only requires 400 mV of overpotential while bare Ni foams demands 560 mV of overpotential to reach the same value of current density.^[12] During water electrolysis, the cathode and the anode were separated using a glass frit membrane to avoid any undesirable

reactions. The stability of the alkaline electrolyser was tested *via* galvanostatic measurement. A constant current density of 10 mA cm^{-2} was applied for 10 h. Fig. 4 inset shows that the overpotential hardly increases during the course of the experiment and indicates high stability of the fabricated electrolyser. To confirm that all the current generated results from water splitting, the total pressure increase due to hydrogen and oxygen evolution was recorded using a pressure sensor during the electrochemical measurement. The pressure sensor data allows the amount of gas evolved to be calculated over the course of the water electrolysis. The

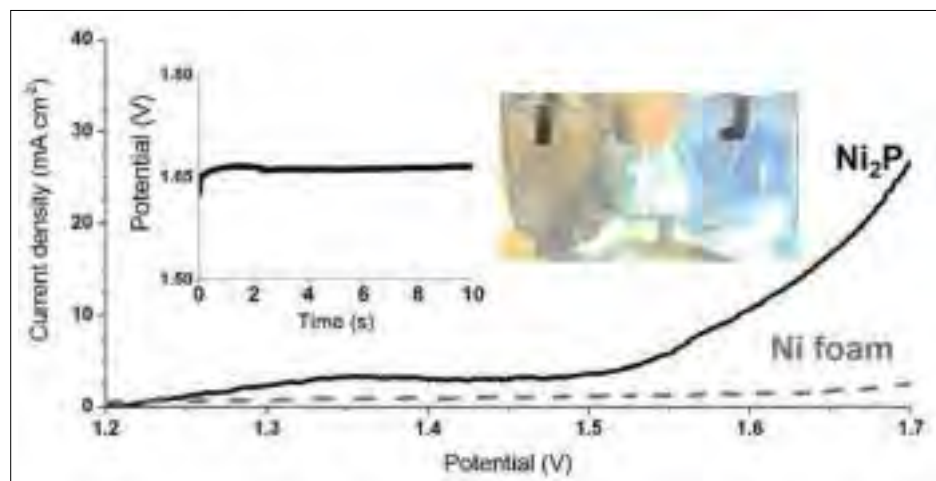


Fig. 4. LSV to evaluate the alkaline electrolyser activity under gas separating conditions. The Ni_2P system (loading 10 mg cm^{-2} , activated anode) necessitates only 400 mV to generate 10 mA cm^{-2} . The Ni foam support was evaluated under similar conditions (gas separation, activated anode but without catalyst) and required 560 mV to generate 10 mA cm^{-2} . A galvanostatic experiment on the Ni_2P alkaline electrolyser with glass frit separation was performed (inset) and indicates the good stability of the system over 10 hours of electrolysis at 10 mA cm^{-2} . An optical photograph illustrates the cell used for these experiments. Adapted by permission of The Royal Society of Chemistry from ref. [12].

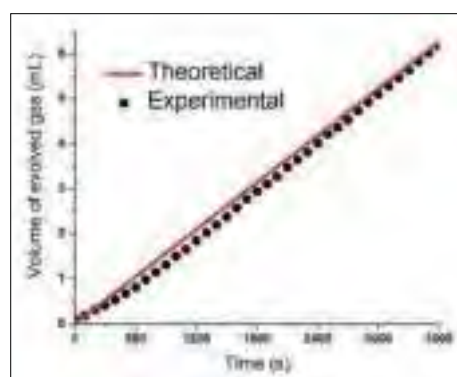


Fig. 5. Faraday yield measurement of the alkaline electrolyser fabricated from Ni_2P loaded Ni foams (loading 10 mg cm^{-2}). The quantity of gas evolved was determined by a pressure sensor. The overlapping lines between the theoretical and experimental values indicate a quantitative Faraday yield of the system, after an induction period of about 250 s . During this induction period, the gas generated are dissolved in the solution to reach an equilibrium. After the induction period, the gas generated can be measured by the pressure sensor. The galvanostatic experiment was performed over 1 h at a constant current density of 10 mA cm^{-2} . The anode was activated prior the galvanostatic experiment. The cathode was used as it is. Adapted by permission of The Royal Society of Chemistry from ref. [12].

theoretical volume of gas evolved can then be calculated by determining the charge passed over the course of the experiment. Comparison between experimental and theoretical volume of gas determines then

the Faradaic efficiency of the alkaline electrolyser. Fig. 5 illustrates that the experimental and theoretical amount of gas evolved overlaps indicative of a quantitative Faraday efficiency for the device. Ni_2P is thus an active and stable bifunctional catalyst for water splitting in alkaline media.

5. Conclusion

In summary, Ni_2P is an active catalyst for OER in alkaline conditions. The catalyst is prepared *via* a simple solid-state reaction from abundant and cheap reagents. The catalytic active species is a $\text{Ni}_2\text{P}/\text{NiO}_x$ core-shell heterostructure that is formed *in situ* under OER conditions. The catalytic activity is superior to several state-of-the-art catalysts. The Janus behaviour of the catalyst allows the fabrication of an efficient alkaline electrolyser who generates 10 mA cm^{-2} at an overpotential of only 400 mV . Ni_2P shows promise of potential applications for future devices and highlights the potential of Earth-abundant catalysts as viable electrocatalysts for energy conversion devices and fuel cell applications.

Acknowledgement

This work is supported by the EPFL. We thank Dr. Ligang Feng and Dr. Fang Song at EPFL for assistance in the experiments.

Received: December 1, 2015

- [1] N. S. Lewis, D. G. Nocera, *Proc. Natl. Acad. Sci. USA* **2006**, *103*, 15729.
- [2] S. Cobo, J. Heidkamp, P.-A. Jacques, J. Fize, V. Fourmond, L. Guetaz, B. Jusselme, V. Ivanova, H. Dau, S. Palacin, M. Fontecave, V. Artero, *Nat. Mater.* **2012**, *11*, 802.
- [3] C. He, X. Wu, Z. He, *J. Phys. Chem. C* **2014**, *118*, 4578.
- [4] X. Liu, H. Zheng, Z. Sun, A. Han, P. Du, *ACS Catal.* **2015**, *5*, 1530.
- [5] J. Luo, J.-H. Im, M. T. Mayer, M. Schreier, M. K. Nazeeruddin, N.-G. Park, S. D. Tilley, H. J. Fan, M. Graetzel, *Science* **2014**, *345*, 1593.
- [6] H. Wang, H.-W. Lee, Y. Deng, Z. Lu, P.-C. Hsu, Y. Liu, D. Lin, Y. Cui, *Nat. Commun.* **2015**, *6*, 7261.
- [7] D. Liu, Q. Lu, Y. Luo, X. Sun, A. M. Asiri, *Nanoscale* **2015**, *7*, 15122.
- [8] M. Ledendecjer, S. K. Calderón, C. Papp, H.-P. Steinrück, M. Antonietti, M. Shalom, *Angw. Chem. Int. Ed.* **2015**, *54*, 12361.
- [9] H. Jin, J. Wang, D. Su, Z. Wei, Z. Pang, Y. Wang, *J. Am. Chem. Soc.* **2015**, *137*, 2688.
- [10] a) N. Jiang, B. You, M. Sheng, Y. Sun, *Angw. Chem. Int. Ed.* **2015**, *54*, 6251; b) Y. Yang, H. Fei, G. Ruan, J. M. Tour, *Adv. Mater.* **2015**, *27*, 3175; c) J. Chang, Y. Xiao, M. Xiao, J. Ge, C. Liu, W. Xing, *ACS Catal.* **2015**, *5*, 6874.
- [11] Y. Yan, B. Y. Xia, X. Ge, Z. Liu, A. Fisher, X. Wang, *Chem. Eur. J.* **2015**, *21*, 18062.
- [12] L.-A. Stern, L. Feng, F. Song, X. Hu, *Energy Environ. Sci.* **2015**, *8*, 2347.
- [13] L. Feng, H. Vrubel, M. Bensimon, X. Hu, *Phys. Chem. Chem. Phys.* **2014**, *16*, 5917.
- [14] a) Y. Chen, D.-L. Peng, D. Lin, X. Luo, *nanotechnol.* **2007**, *18*, 505703; b) D. A. Corrigan, R. M. Bendert, *J. Electrochem. Soc.* **1989**, *136*, 723.
- [15] a) L. Trotochaud, J. K. Ranney, K. N. Williams, S. W. Boettcher, *J. Am. Chem. Soc.* **2012**, *134*, 17253; b) C. C. L. McCrory, S. H. Jung, J. C. Peters, T. F. Jaramillo, *J. Am. Chem. Soc.* **2013**, *135*, 16977; c) K. Fominykh, J. M. Feckl, J. Sicklinger, M. Doeblinger, S. Boecklein, J. Ziegler, L. Peter, J. Rathousky, E.-W. Scheidt, T. Bein, D. Fattakhova-Rohlfing, *Adv. Funct. Mater.* **2014**, *24*, 3123; d) M. Gao, W. Sheng, Z. Zhuang, Q. Fang, S. Gu, J. Jiang, Y. Yan, *J. Am. Chem. Soc.* **2014**, *136*, 7077; e) H. Shi, G. Zhao, *J. Phys. Chem. C* **2014**, *118*, 25939.
- [16] M. Gong, Y. G. Li, H. L. Wang, Y. Y. Liang, J. Z. Wu, J. G. Zhou, J. Wang, T. Regier, F. Wie, H. J. Dai, *J. Am. Chem. Soc.* **2013**, *135*, 8452.
- [17] K. J. May, C. E. Carlton, K. A. Stoerzinger, M. Risch, J. Suntivich, Y.-L. Lee, A. Grimaud, Y. Shao-Horn, *J. Phys. Chem. Lett.* **2012**, *3*, 3264.
- [18] L. Ouattara, S. Fierro, O. Frey, M. Koudelka, C. Comninellis, *J. Appl. Electrochem.* **2009**, *39*, 1361.
- [19] P. E. R. Blanchard, A. P. Grosvenor, R. G. Cavell, A. Mar, *J. Mater. Chem.* **2009**, *19*, 6015.
- [20] a) R. L. Doyle, I. J. Godwin, M. P. Brandon, M. E. G. Lyons, *Phys. Chem. Chem. Phys.* **2013**, *15*, 13737; b) L.-A. Stern, X. Hu, *Faraday Discuss.* **2014**, *176*, 363.
- [21] a) M. Gong, W. Zhou, M.-C. Tsai, J. Zhou, M. Guan, M.-C. Lin, B. Zhang, Y. Hu, D.-Y. Wang, J. Yang, S. J. Pennycook, B.-J. Hwang, H. Dai, *Nat. Commun.* **2014**, *5*, 4695; b) G. Elmaci, C. E. Frey, P. Kurz, B. Zumreoglu-Karan, *Inorg. Chem.* **2015**, *54*, 2734; c) L. Trotochaud, S. L. Young, J. K. Ranney, S. W. Boettcher, *J. Am. Chem. Soc.* **2014**, *136*, 6744.
- [22] E. J. Popczun, J. R. McKone, C. G. Read, A. J. Baciocchi, A. M. Wiltrout, N. S. Lewis, R. E. Schaak, *J. Am. Chem. Soc.* **2013**, *135*, 9267.

New Approaches for *ab initio* Calculations of Molecules with Strong Electron Correlation

Stefan Knecht^{§*}, Erik Donovan Hedegård, Sebastian Keller, Arseny Kovyrshin, Yingjin Ma, Andrea Muolo, Christopher J. Stein, and Markus Reiher^{*}

[§]SCS-DSM Award for best poster presentation in Computational Chemistry

Abstract: Reliable quantum chemical methods for the description of molecules with dense-lying frontier orbitals are needed in the context of many chemical compounds and reactions. Here, we review developments that led to our new computational toolbox which implements the quantum chemical density matrix renormalization group in a second-generation algorithm. We present an overview of the different components of this toolbox.

Keyword: *ab initio* quantum chemistry · DMRG · Matrix product operators · Strong electron correlation · Tensor network states

1. Introduction

Computational modeling has undoubtedly become an integral part of chemical research.^[1] For instance, understanding a (photo-)chemical process in atomistic detail – including all elementary reaction steps involved – calls for a reliable, but feasible and preferably black-box computational approach that provides a sufficiently accurate approximation to the exact solution of the electronic Schrödinger equation. A typical example for a complex chemical process is a reaction catalyzed by a transition-metal complex.^[2] A metal center can directly activate a reagent through bond formation and/or bond breaking or act as a photoacceptor for a subsequent energy transfer to the reagent from an electronically excited state. The common challenge is then to quantitatively describe open shells that will emerge in such processes, which is far from trivial to meet.^[3–7] The presence of open shells and/or activat-

ed bonds usually entails a multiconfigurational electronic structure where strong static electron correlation becomes sizable. Molecules with these features then exhibit many dense-lying orbitals in the frontier-orbital region.

Although by construction a single-configuration *ansatz*, to date, density functional theory (DFT)^[6] is by far the most popular approach to study photochemistry (see for example ref. [8] and references therein) and transition-metal chemistry^[4,9,10] because of its low computational cost, often at reasonable accuracy, and because of its favorable scaling with the size of a molecule. The standard approach to describe half-filled shells in molecules with small HOMO-LUMO gaps is to break a symmetry of the system within DFT, usually the total-spin symmetry.^[11,12] Besides known fundamental problems of single-configuration DFT in correctly describing strong static correlation^[13] all spin symmetries can be properly introduced in DFT leading to spin-state dependent functionals,^[14] but little work along these lines has been carried out so far.^[15]

A multiconfigurational *wave function* based-method tailored to recover static correlation is the complete active space (CAS) *ansatz*,^[16] often combined with a simultaneous self-consistent field (SCF) optimization of the orbital basis. Naturally, CASSCF-type approaches have been applied in theoretical photochemistry and transition-metal chemistry.^[17–19] The central idea of a CASSCF-type approach is the selection of an active space of N electrons in L orbitals to yield a CAS(N,L), on which a full configuration interaction

(FCI) expansion of the wave function is constructed,

$$|\Psi_{\text{CAS-CI}}\rangle = \sum_{n_1, \dots, n_L} c_{n_1 n_2 \dots n_L} |n_1 n_2 \dots n_L\rangle, \quad (1)$$

where $|n_1 n_2 \dots n_L\rangle$ is an occupation number vector corresponding to an orthonormal basis state, *e.g.* a Slater determinant. This procedure, however, does not yield an exact wave function as the orbital basis is restricted. Moreover, the underlying FCI expansion still scales exponentially with respect to the number of active electrons and orbitals so that the computational feasibility of traditional CAS methods reaches a limit at a CAS size of about CAS(18,18).^[19]

Originally developed to study the physics of spin chains, the density matrix renormalization group (DMRG)^[20,21] algorithm emerged as a viable alternative to traditional CAS methods. This is rooted in the fact that it is capable of iteratively converging to the exact solution in a given active orbital space with polynomial rather than exponential cost.^[22] In DMRG, CASs are accessible with up to about 100 orbitals exceeding by far the limits encountered by traditional CAS methods. Many quantum-chemical DMRG implementations, with (DMRG-SCF) and without (DMRG-CI) orbital optimization, have been developed since the late 1990s.

Here, we present an overview of our recent efforts to further develop methods that rely on the DMRG. They comprise features (i) to locate for a given molecule the minimum structure of its ground and

*Correspondence: Dr. S. Knecht, Prof. Dr. M. Reiher
E-mail: stefan.knecht@phys.chem.ethz.ch;
markus.reiher@phys.chem.ethz.ch
ETH Zürich
Laboratorium für Physikalische Chemie
Vladimir-Prelog-Weg 2,
CH-8093 Zürich

excited states, (ii) to take into account electron correlation effects beyond static correlation, (iii) to model a complex molecular system embedded in a structured environment, and (iv) to account for effects of Einstein's theory of special relativity, when needed. To this end, we developed the *second-generation* quantum-chemical DMRG program QCMAQUIS^[23] that unites these objectives in a unique framework.

In actual applications, the breakeven point for computational costs of a DMRG calculation compared to a traditional CASSCF calculation is reached for CAS(14,14) in QCMAQUIS.

2. Second-generation DMRG

DMRG,^[20,21] invented by White, was inspired by its predecessor, Wilson's numerical renormalization group, in which a Hilbert space is truncated by selecting the lowest-lying eigenstates of a Hamiltonian. By contrast, White proposed to select states according to their weight in the density matrix, which dramatically improved the performance of the renormalization group. To date, DMRG is the most successful numerical method to solve one- or quasi-one-dimensional systems in solid-state physics. In quantum chemistry, DMRG has been established as a powerful active-space method, allowing for much larger active spaces than a traditional CASSCF-type approach. The higher performance comes at a price, however. The truncation of the density matrix by only retaining the m states with the highest weight implies that the accuracy of the approximation is to be assessed *a posteriori*. The latter can be achieved by analyzing the weights of the discarded density matrix eigenstates and by performing calculations with different values for m (that may then be subjected to an extrapolation towards $m \rightarrow \infty$).

A few years after the introduction of DMRG, it was realized that the DMRG algorithm is equivalent to the variational optimization of a special class of *ansatz* states called matrix product states (MPSs),^[24,25]

$$|\Psi_{\text{MPS}}\rangle = \sum_{n_1, \dots, n_L} M^{n_1} M^{n_2} \dots M^{n_L} |n_1 n_2 \dots n_L\rangle, \quad (2)$$

where L is the total number of active orbitals as before and M^l are matrices for the l -th spatial orbital whose product yields the corresponding CI coefficients $C_{n_1 n_2 \dots n_L}$ (implying that M^{n_1} and M^{n_L} are actually vectors). Each local space n_l of the l -th spatial orbital is of dimension four corresponding to the possible orbital occupations $n_l = \uparrow\downarrow, \uparrow\uparrow, \downarrow\downarrow, |0\rangle$. The connection between DMRG and MPS provided the theoretical understanding of why DMRG

works well for one-dimensional systems but becomes less efficient in higher dimensions.^[26–28] Moreover, it allowed for very flexible implementations in which wave functions and operators can be combined arbitrarily in operations such as overlap and expectation value calculations, operator-wave function actions, and operator-operator actions.

In quantum chemical MPS-DMRG in conjunction with a Hamiltonian expressed as a matrix product operator (MPO), the main challenge is the efficient construction of the MPO, because the performance of the method depends critically on it. We demonstrated^[23] that the full quantum-chemical Hamiltonian MPO can be efficiently constructed so that the same computational scaling is achieved as in traditional, *i.e.* pre-MPO quantum-chemical DMRG. We refer to this MPO-based algorithm implemented in QCMAQUIS as second-generation DMRG.^[23]

Compared to traditional DMRG, second-generation DMRG is more versatile with respect to the decisive quantities, *i.e.* wave functions and operators, that can be handled independently of each other. As a consequence, for example, we were able to quickly implement relativistic Hamiltonians (see Section 4) by simply exchanging the MPO while re-using all contraction routines handling the application of the MPO to the MPS. Another example for the efficiency of a second-generation algorithm is the implementation of spin-adapted MPSs and MPOs.^[29]

3. Tensor Network Parameterizations

The MPS *ansatz* imposes a one-dimensional *ad hoc* ordering of molecular orbitals in the construction process of the total basis states and wave function. While for linear spin chains in solid-state physics this is a natural procedure, for chemical systems this is in general not the case and can give rise to convergence problems. To overcome these issues stimulated further developments and led to the formulation of a new family of states, the so-called Tensor Network States (TNS).^[30–33] The TNS approach tends to break down the high-dimensional CI coefficient tensor $C_{n_1 n_2 \dots n_L}$ of the FCI *ansatz* into a network of low-rank tensors. One of the latest developments in this field are Tree Tensor Network States (TTNS).^[34–36] For the quantum chemical Hamiltonian a TTNS variant has been developed by Nakatani and Chan^[37] that is essentially a generalization of the MPS concept. Interestingly, the Nakatani-Chan implementation was an MPO-based second-generation quantum-chemical DMRG program prior to QCMAQUIS with the cor-

rected scaling,^[38] and has been turned into the general MPO/MPS library MPSXX available on GitHub.^[39]

In the Nakatani-Chan approach, tensors are connected as a tree graph of degree z (any orbital has at most z neighbors) and depth Δ (number of edges/arcs from the root node to the leaf node of the tree). For a given orbital (site) i their TTNS *ansatz* reads

$$|\Psi_{\text{TTNS}}\rangle = \sum_{b_1^1 \dots b_i^z n_i} C_{b_1^1 \dots b_i^z}^{n_i} |b_1^1 \dots b_i^z n_i\rangle, \quad (3)$$

where $|b_i^\alpha\rangle$ ($\alpha = 1, \dots, z$) is the renormalized basis in the α -th branch of site n_i .^[37] Nakatani and Chan define this basis recursively contracting tensors in the branch from the leaves up to site i

$$|b_i^\alpha\rangle = \sum_{b_j^1 \dots b_j^{z-1} n_j} A_{b_j^1 \dots b_j^{z-1} n_j}^{n_j} |b_j^1 \dots b_j^{z-1} n_j\rangle, \quad (4)$$

where the sites j are adjacent to i in the branch.^[37] The absence of loops in the tree graph simplifies many mathematical properties of the TTNSs and makes them similar to MPSs.^[37] This allows Nakatani and Chan to use the DMRG optimization algorithm for TTNSs, where one site at a time is considered.

TTNSs approximate many-dimensional entanglement by a tree-entanglement structure, which can still be inappropriate for molecules with some extended two- and three-dimensional structure, give nonuniform entanglement, and lead to convergence problems. In general, molecular orbitals (even specially prepared ones) are delocalized over more than one atom, and hence they may not strictly follow the graph underlying a TTNS.

By contrast, the Complete Graph Tensor Network States (CGTNS) *ansatz*^[40] considers entanglement of all orbitals on equal footing by so-called correlators. The CGTNS approach factorizes the high-dimensional CI coefficient tensor $C_{n_1 n_2 \dots n_L}$ into a product of all possible 2-site ($2s$) correlators $C_{n_i n_j}^{[ij]}$.

$$|\Psi_{\text{CGTNS}}^{2s}\rangle = \sum_{n_1 n_2 \dots n_L} \prod_{i < j} C_{n_i n_j}^{[ij]} |n_1 n_2 \dots n_L\rangle. \quad (5)$$

The total number of correlators used in this *ansatz* is equal to $L(L+1)/2$, which makes the number of variational parameters in this *ansatz* equal to $L(L+1)q^2/2$, where q is the number of local states ($q = 2$ for spin orbitals and $q = 4$ for spatial orbitals). One can consider the CGTNS *ansatz* as a generalization of the Correlator Product States *ansatz* suggested by Changlani *et al.*,^[41] where correlators were

only used between nearest-neighbor sites. Higher accuracy can be achieved by invoking higher-order correlators (3-site correlators, 4-site correlators, and so forth).^[40–42] While we continue to investigate such general decompositions of CI coefficients,^[42] the advantage of the MPS ansatz is that it can be efficiently optimized by the DMRG algorithm.

4. Relativistic Hamiltonians and Symmetries

In 1928 C. G. Darwin wrote:^[43] *In a recent paper Dirac has brilliantly removed the defects before existing in the mechanics of the electron, and has shown how the phenomena usually called the ‘spinning electron’ fit into place in the complete theory.* Since the non-relativistic Schrödinger equation was spin-free, it was clear at that time that a new formalism was needed to combine quantum theory with Einstein’s theory of special relativity. Since the 1970s numerous unusual features have been recognized in heavy-element chemistry and spectroscopy that can only be explained considering a relativistic quantum description of electrons.^[44–47] The liquid state of mercury under ambient condition^[48] and the lead battery in cars^[49] are prominent examples for which these so-called ‘relativistic effects’ are in operation.

Today, relativistic electronic structure theory is a mature and well-understood field.^[47,50] Once a relativistic Hamiltonian is chosen, established electronic-structure methods can be employed to approximate the wave function. Our QCMAQUIS program package can handle the symmetry properties of the Dirac-Coulomb and Dirac-Coulomb-Breit Hamiltonians as well as of their two-component analogs.^[51] Whereas the first such implementation into a traditional DMRG program^[52] could only handle real double groups (DG), these limitations are overcome in QCMAQUIS.

In the molecular spinor basis significant computational savings can be achieved by adopting the symmetries that are obeyed by two- and four-component Hamiltonians. In non-relativistic quantum chemistry, one only needs to treat space inversions and rotations because all other symmetries can be generated by a successive application of these two. In the relativistic framework, time and space are tied together to the space-time, and hence the time reversal operator $\hat{\mathcal{K}}$ is to be addressed and double point groups need to be taken into account. The effect of $\hat{\mathcal{K}}$ on a wave function $\Psi(t)$ yields the time-reversed wave function $\bar{\Psi}(-t)$. It can be shown^[50] that the pair $\{\Psi, \hat{\mathcal{K}}\Psi = \bar{\Psi}\}$ corresponds to a doubly-degenerate fermionic state function which is called a *Kramers pair*

(loosely speaking, the relativistic analog of two degenerate non-relativistic α - and β -spin orbitals). Performing calculations in a Kramers basis reduces the possible number of two-electron integrals ($ijkl$) arising from all combinations of unbarred and barred indices, 16 in total, to only six symmetric non-redundant integrals.^[53]

Double groups are constructed from the direct product of point groups and the sub-group $\{E, \bar{E}\}$ where \bar{E} represents a rotation through 2π and E a rotation through 4π . Double groups are in general non-abelian, which gives rise to additional complications for symmetry multiplications in quantum chemistry programs. If time reversal symmetry can be considered (e.g. in the absence of an external magnetic field), it can be shown^[50] that certain classes of two-electron integrals are real, complex, or can be excluded *a priori*, because they are equal to zero. Finally, for systems of interest to chemists, the number of particles is conserved, which implies that the unitary one-dimensional group $U(1)$ can also be included along with all other symmetries introduced above. In our case, with DMRG as the post-Hartree-Fock method of choice, UIDG symmetry is employed to decrease the number of many-particle states for symmetry reasons. Characters and multiplication tables for C_{1v} , C_{2v} , C_{2h} , C_{6v} and C_{32h} double groups^[54] were implemented in QCMAQUIS.^[51]

The relativistic DMRG model in QCMAQUIS supports double group symmetries in order to assign to every site an irreducible representation corresponding to the spinor placed there. No assumptions are made with respect to the spinor basis which can be either a Kramers-restricted or Kramers-unrestricted basis. In addition, no formal distinction is made between barred and unbarred spinors but simplifications due to the selected symmetry may lead to an elimination of certain terms in the Hamiltonian. Finally, no explicit reference of two- or four-component quantities is made inside QCMAQUIS and the only input data for the calculations are the pre-computed relativistic one- and two-electron integrals from MOLCAS,^[19] DALTON,^[55] MOLPRO,^[56] DIRAC^[57] or BAGEL.^[58]

5. Set-up, Parameter Dependence, and Convergence Acceleration

The ability of DMRG to handle active orbital spaces that are much larger than those of conventional CASSCF approaches comes with an additional set of mainly technical parameters that can affect convergence and accuracy.^[59] Among these parameters are the ordering of the orbitals as sites on the one-dimensional lattice, the number of renormalized states m , the num-

ber of sweeps, and the initialization procedure of the MPS in the first sweep, the so-called warm-up sweep. This increase in the number of control parameters is a threat to the routine application of DMRG in standard computational chemistry. As our aim is to make DMRG a valuable and reliable tool for computational chemistry, easy usage as well as stable and fast convergence are of paramount importance for a ‘black-box’ set-up of such calculations.

While the number of sweeps required for convergence and the number of renormalized states necessary can be easily controlled, the ordering of the orbitals on the lattice and the initialization procedure need more sophisticated ideas. Both problems were addressed by Legeza and co-workers^[60,61] by making use of entanglement measures for the active orbitals expressed in terms of one- and two-orbital von Neumann entropies.^[62–64] Especially the mutual information matrix \mathbf{I} , which is a measure for the entanglement of pairs of orbitals, proved to be a valuable tool in the analysis of MPS wave functions and multi-reference wave functions in general. For fast convergence of a DMRG calculation, it is essential that highly entangled orbitals are close to each other on the lattice. This will be guaranteed if the orbitals are ordered according to the Fiedler vector,^[65,66] which is the eigenvector corresponding to the second smallest eigenvalue of the graph Laplacian L_g , defined in this case as $L_g = D - \mathbf{I}$, where D is a diagonal matrix, $D_{ii} = \sum_j I_{ij}$ (i and j are labels for the orbitals on the lattice, i.e. for the orbitals chosen to be in the CAS). The Fiedler vector minimizes the cost measure^[61]

$$\omega = \sum_{ij} I_{ij} |i - j|^2. \quad (6)$$

This Fiedler ordering significantly improves the convergence and is implemented in QCMAQUIS.

Convergence can further be improved by a suitable guess of the environment states in the warm-up sweep. While an obvious choice is to start from an MPS that contains a reference determinant (such as the Hartree-Fock determinant or the determinant with the largest weight in configuration-interaction language), it is possible to improve on this by including the *most important determinants* into the initial MPS. These most important determinants are selected by varying the occupation on those sites that have the highest one-orbital entropies. If these determinants are further limited to have a specific excitation level with respect to a reference determinant, this initialization procedure invented by Legeza^[67,68] is referred to as CI-DEAS. Calculations starting from a CI-DEAS

MPS are less prone to get stuck in local minima and show enhanced convergence behavior.^[61,69–71] The specific CI-DEAS procedure available in QCMAQUIS is described elsewhere.^[70]

Although the maximally possible size for an active space is enlarged by DMRG, the choice of a suitable set of active orbitals is still largely a matter of experience. It has already been pointed out in the context of traditional CASSCF methodologies that the selection of orbitals is a non-trivial problem and can lead to qualitatively wrong results.^[72–74] This problem is not in general solved by the possibility of including more orbitals. On the contrary, the distinction between non-dynamically and dynamically correlated orbitals is equally important in DMRG^[75] and requires a separate description of dynamical correlation by means of perturbation theory or short-range DFT (see Section 6). However, entropy-based entanglement measures can be of valuable help for the assessment of a chosen CAS.^[76]

Entanglement information can already be obtained from a preliminary calculation performed with a low number of renormalized states m .^[71] Combined with the fact that DMRG is an iterative algorithm that allows one to stop a calculation well before full (energy) convergence is reached, this enables us to quickly assess automatically constructed CASs.^[71] Moreover, such un-converged DMRG calculations can additionally be used for the optimized Fiedler ordering and the CI-DEAS initialization procedure,^[71] all at low additional cost.

6. Dynamical Correlation

Whereas static electron correlation effects can be well described by DMRG on the basis of sufficiently large active orbital spaces, a remaining, yet essential part of electron correlation, commonly referred to as *dynamical* correlation, cannot be accounted for. It originates from electronic interactions described between orbitals in the active space and external (inactive and secondary) orbitals as well as among inactive and secondary orbitals themselves. For quantitative results, it is mandatory to account for dynamical electron correlation.

Following the developments of multi-reference wave functions based on traditional multi-configurational wave function approaches such as CASSCF, internally-contracted multireference CI (MR-CI)^[77] and multireference perturbation theory (MR-PT) approaches – most importantly, N -electron valence perturbation theory to second-order (NEVPT2)^[78] and complete-active space perturbation theory to second order (CASPT2)^[79,80] – were combined with MPS reference wave functions.

The central idea of all of these methods is to describe dominating static correlation effects by a zeroth-order Hamiltonian, while capturing dynamical correlation in a subsequent step which follows a ‘diagonalize-then-perturb’^[81] strategy. The price to pay is the need to calculate n -particle reduced density matrices (n -RDMs, with $n > 2$ and up to 5) of the DMRG wave function and to carry out a four-index transformation of all two-electron integrals in the full molecular orbital basis. The computational cost of the former scales in a naïve implementation approximately as L^{2n} where L is the number of orbitals defining the active orbital space. A possible solution to this problem comprises a cumulant-based reconstruction scheme of higher-order n -RDMs, typically for $n = 3, 4$, from the knowledge of the 2-RDM alone (see ref. [82] for a comprehensive review). Although such a reconstruction is appealing, neglecting higher-order cumulants (required for the desired computational savings) results in a loss of the N -representability of the high-order RDM (meaning that the trace of the matrix does not yield a well-defined function of the number of active electrons N). The latter can in turn introduce unphysical solutions to the eigenvalue problem under consideration.^[77,80] For these reasons, our current NEVPT2 and CASPT2 implementations in QCMAQUIS^[78,83] avoid cumulant approximations, although the full elegance of our MPO-DMRG program for an efficient calculation of 3- and 4-RDMs has not been fully exploited yet.

In addition to perturbation theory-based methods, we also implemented a conceptually different approach based on short-range (sr) DFT^[84,85] that (i) does not require the evaluation of higher-order n -RDMs, (ii) is capable of simultaneously handling dynamic and static correlation, and (iii) combines wave function theory with DFT. As such, our DMRG-srDFT approach^[86] preserves all efficiency advantages of DMRG.

Hybrid methods between DFT and wave function theory often face the so-called ‘double-counting problem’ of electron-correlation effects because of the correlation energy functional that introduces correlation effects in a way unrelated to the multi-determinant *ansatz* for the wave function. This issue can be solved elegantly with a range-separation *ansatz*^[84,85] where the two-electron repulsion operator is separated into a short-range and a long-range part. While such an *ansatz* was explored for standard wave function methods,^[84,85,87–91] we introduced the DMRG-srDFT approach^[86] where long-range electron correlation is treated by MPSs in QCMAQUIS complemented with a short-range DFT description of the two-electron interaction in DALTON.^[55]

In contrast to two-step approaches (*vide supra*), the overall scaling of DMRG-srDFT does not exceed that of a DMRG calculation since it requires at maximum an additional evaluation of a 1-RDM. This feature is particularly advantageous for transition-metal complexes or large organic chromophores when combined, for example, with the embedding methods described in Section 7. Although DMRG-srDFT can, in its present formulation, only be used for state-specific optimization of excited states, a simultaneous state-average optimization of ground- and excited states is possible in an ensemble DFT *ansatz* (see, for example, ref. [92]). We are currently exploring the latter option based on a (long-range) DMRG wave function in our laboratory. The efficiency of srDFT originates from the description of the Coulomb hole of the electron-electron interaction. However, this does not account for long-range dynamical correlation effects, which are neglected.

7. Embedding in a Structured Environment

In appreciation of the fact that the majority of experimental investigations are carried out in some medium, such as a solvent or a protein environment, the QCMAQUIS program is coupled to schemes that can describe such a surrounding environment. We first focus on the coupling of DMRG to the frozen density embedding scheme (FDE)^[93–95] in QCMAQUIS.^[96]

The FDE scheme belongs to a group of sub-system approaches in which the total system is partitioned into smaller fragments, thereby reducing the total computational cost. Density-based subsystem approaches assume that the total density can be described as a sum of the densities of the individual subsystems, for instance,

$$\rho(\mathbf{r}) = \rho_{\text{act}}(\mathbf{r}) + \rho_{\text{env}}(\mathbf{r}), \quad (7)$$

where the environment density $\rho_{\text{env}}(\mathbf{r})$ itself can be described as a sum of densities of individual fragments, $\rho_{\text{env}}(\mathbf{r}) = \sum_j \rho_{\text{env}}^j(\mathbf{r})$.

The FDE scheme is typically employed as a *focused* model which has shown to be a very successful route to model local chemical phenomena such as a solute in a solvent or a chromophore within a protein.^[95] Traditionally, focused models employ a quantum mechanical (QM) method for a pre-defined *active region* and a more approximate model for the environment. Some models treat the environment as a structureless continuum, whereas others (such as FDE) use an explicit description.

An example of the former is a polarizable continuum model,^[97] while the most renowned explicit model is probably the quantum mechanics/molecular mechanics (QM/MM) coupling scheme.^[98,99] FDE strives for higher accuracy than QM/MM by moving beyond a purely classical description for the environment and by also allowing for a polarization of the environment.

The FDE approach was originally devised within DFT and then $\rho_{\text{env}}(\mathbf{r})$ is obtained from Kohn-Sham DFT calculations of the individual fragments constituting the environment. This density is used to construct an effective embedding operator which enters the Kohn-Sham equations of the active region, thereby including the effect of the surrounding environment. Originally, the environment density was kept frozen, which can be a severe approximation in cases of large mutual polarization of active region and environment. To handle such cases, the two regions can be allowed to polarize each other by iteratively exchanging the role of active and environment subsystems until convergence, known as ‘freeze-and-thaw’ cycles.^[100] The DMRG-FDE implementation builds upon an extension of the original DFT-in-DFT based scheme in order to treat the active region with a wave function method.^[101,102] The DMRG-FDE electronic energy reads^[96]

$$E_{\text{tot}} = E_{\text{act}}^{\text{DMRG}} + E_{\text{env}}^{\text{KS-DFT}} + E_{\text{int}}^{\text{OF-DFT}}, \quad (8)$$

where the first term is

$$E_{\text{act}}^{\text{DMRG}} = \langle \Psi_{\text{MPS}} | \hat{H}_{\text{MPO}} | \Psi_{\text{MPS}} \rangle. \quad (9)$$

In practice, this term is evaluated as the pseudo-energy

$$\mathcal{E}_{\text{act}}^{\text{DMRG}} = \langle \Psi_{\text{MPS}} | \hat{H}_{\text{MPO}} + \sum_{i=1}^N \hat{v}_{\text{emb}}^{\text{act}}[\rho_{\text{act}}, \rho_{\text{env}}](\mathbf{r}_i) | \Psi_{\text{MPS}} \rangle, \quad (10)$$

which can be optimized in an MPO-based formalism in a way that ensures that the embedding potential is obtained self-consistently.^[96] The sum in Eqn. (10) runs over the active electrons N and the MPS obtained from Eqn. (10) yields the energy in Eqn. (9) $E_{\text{env}}^{\text{KS-DFT}}$ in Eqn. (8) is the environment energy evaluated within DFT, while $E_{\text{int}}^{\text{OF-DFT}}$ is the interaction between active and environment subsystems. $E_{\text{int}}^{\text{OF-DFT}}$ also contains a so-called non-additive energy correction, arising from the exchange-correlation functional and the kinetic energy operator. This non-additive kinetic energy is most efficiently evaluated by orbital-free

DFT (OF-DFT), which requires accurate orbital-free kinetic energy functionals (see, e.g. ref. [95] and references cited therein).

Several other embedding schemes also build on a divide-and-conquer approach. Many of these schemes have complementary strengths and weaknesses. In addition to the FDE scheme, we have very recently combined^[103] QCMAQUIS with a polarizable embedding (PE) scheme^[104] that was shown^[105] to yield promising results in combination with multireference methods. In PE, environment fragment densities are represented by a classical multipole expansion with atom-centered multipoles and (anisotropic) polarizabilities.

8. Structure Optimization

A major area of research in computational chemistry encompasses the study and prediction of (photo-)chemical reaction mechanisms, in which the determination of stable intermediates, the location of transition states and the exploration of excited state reaction pathways are crucial tasks that necessitate access to a reliable potential energy surface (PES). Such stationary states can be determined by calculating the first (‘gradient’) and second (‘Hessian’) derivatives of the electronic energy with respect to all nuclear displacements at a fixed reference geometry, which makes a fast and computationally stable evaluation of gradients and Hessian elements an essential feature of *ab initio* methods.

Since the majority of structure optimization algorithms follow a gradient-only driven optimization scheme (with approximate Hessian evaluations) to find extremal points on the PES, we focus here on the derivative of a DMRG state $|\Psi_{\text{MPS}}\rangle$ in its orbital-optimized form from a DMRG-SCF calculation. In this case, the Hellmann-Feynman theorem holds such that no coupled-perturbed equation for the orbital relaxation part needs to be solved.^[106,107] An analytic energy gradient is readily obtained by taking the first derivative of the electronic energy $E^{\text{DMRG-SCF}}$ with respect to the nuclear displacement vector \mathbf{R} at a given reference geometry ($\mathbf{0}$),

$$\left. \frac{\partial E^{\text{DMRG-SCF}}}{\partial \mathbf{R}} \right|_{\mathbf{0}} = \left\langle \Psi_{\text{MPS}} \left| \frac{\partial \hat{H}_{\text{MPO}}}{\partial \mathbf{R}} \right| \Psi_{\text{MPS}} \right\rangle, \quad (11)$$

where \hat{H}_{MPO} is the electronic Hamiltonian in MPO format. It can then be shown^[70] that the gradient evaluation in Eqn. (11) reduces to a simple evaluation of 1- and 2-RDMs that are to be contracted with the derivatives of the one- and two-electron integrals in full analogy to CASSCF.^[106]

Although a majority of chemical reactions takes place on a single Born-Oppenheimer PES (adiabatic processes), in particular photo-chemical processes proceed through one or several conical intersections of two PES along a reaction pathway. Since the Born-Oppenheimer approximation breaks down in the vicinity of a conical intersection, non-adiabatic transitions (driven by non-zero non-adiabatic coupling elements between the intersecting states) are possible. A computationally sound description of such a case is therefore best achieved in a state-averaged wave function optimization approach which allows one to treat a number of (near-degenerate) electronic states simultaneously on equal footing.

In contrast to the state-specific case, where the wave function (and therefore the energy) is fully variational, this is no longer the case for the energy of a given target state in a state-averaged space of all states under consideration. The gradient evaluation for a target state requires therefore the use of the Lagrange technique,^[108,109] in which the wave function of the target state is further relaxed with respect to all variational parameters (orbital rotations and CI coefficient changes) in order to obtain a now fully variational (‘state-specific’) wave function. With the latter at hand, the gradient of the target state in a state-averaged wave function optimization can then be evaluated according to Eqn. (11).^[70]

Within QCMAQUIS, a target state can easily be tracked during the structure optimization by using the MPS of the preceding step as a starting guess for the current step.^[23,70] This procedure ensures a maximum overlap between both states. Additionally, each state is successively calculated^[23] which prevents state-flipping or state-crossing in case of near degeneracies. The latter task is less trivial within the framework of traditional DMRG, because in this case all states are calculated simultaneously. If state-flipping or crossing occurs, it will be more difficult to track the target root requiring particular tools such as the maximum overlap technique.^[107]

9. The Singlet-Triplet Gap of Methylene

As an example, we present results for the singlet-triplet (S-T) gap of methylene, CH_2 . Although CH_2 is a small molecule and clearly not a typical target for DMRG-based approaches, it is a benchmark molecule for new theoretical methods.^[110] Here, we select small active spaces to demonstrate that DMRG-SCF (with NEVPT2) yields the same results as traditional CASSCF-type approaches. Methylene has, in accordance with Walsh’s rules, a bent C_{2v} equilibrium

structure (see ref. [111] for a qualitative study on the angle dependence of the S-T gap). The HOMO of the singlet \tilde{a}^1A_1 state is doubly occupied and of symmetry a_1 . In the triplet \tilde{X}^3B_1 state this electron pair becomes unpaired with one electron now residing in an orbital of symmetry b_1 that corresponds to the LUMO in the singlet state.

Unlike its heavier valence-isoelectronic homologs silylene (SiH_2) and germylene (GeH_2), which feature ground states of singlet spin symmetry,^[112,113] methylene has a triplet degenerate ground state with the lowest-energy singlet state lying about 9.2 kcal/mol (9.0 kcal/mol including zero-point vibrational corrections) higher in energy.^[114] A qualitative explanation for this observation could be based on the magnitude of the HOMO-LUMO gap which increases from CH_2 to SiH_2 to GeH_2 , but as discussed in detail in ref. [115] other electronic and steric effects need to be taken into account to arrive at a quantitative understanding.

For the results presented in this work, we employed a cc-pVTZ basis set.^[116] The equilibrium structures of the triplet \tilde{X}^3B_1 ground state and the first excited singlet \tilde{a}^1A_1 state correspond to those determined by Sherrill and co-workers with an FCI/TZ2P approach.^[117] Adapting a C_{2v} structure, the HCH angle and C–H bond lengths are 133.29° (101.89°) and 1.0775 Å (1.1089 Å), respectively, in the triplet (singlet) state.

We carried out a series of state-specific CASSCF, CASSCF/CASPT2, DMRG-SCF, and DMRG-SCF/NEVPT2 calculations with increasing size of the active orbital space to study the S-T splitting in methylene. The CASSCF and CASSCF/CASPT2 calculations were performed with a developers' version of the MOLCAS 8^[19] software package with its default zeroth-order Hamiltonian for CASPT2. The DMRG-SCF and DMRG-SCF/NEVPT2 calculations were carried out with QCMAQUIS and our local NEVPT2 implementation.^[78c] For DMRG-SCF/NEVPT2 we report only data for the so-called partially contracted approach as the results for the strongly contracted approach are similar. The number of renormalized DMRG block states m was set to $m = 1024$ which is sufficient to reach CASSCF accuracy for those active orbital spaces where a comparison with traditional CASSCF data was possible. Our CAS(6,6) comprises three orbitals in symmetry a_1 , one in b_1 , and two in b_2 , while the CAS(6,12) comprises six orbitals in a_1 , two in b_1 , and four in b_2 and CAS(6,20) comprises eight orbitals in a_1 , four in b_1 , six in b_2 , and two in a_2 . For comparison, we also performed single-point DFT calculations with the PBE^[118] and PBE0^[119] density functionals (as im-

Table 1: Calculated adiabatic singlet-triplet gap, $E(\tilde{a}^1A_1) - E(\tilde{X}^3B_1)$ in kcal/mol, for methylene.

Method	singlet-triplet gap		
	CAS(6,6)	CAS(6,12)	CAS(6,20)
CASSCF	10.53	5.71	9.93
CASSCF/CASPT2	11.87	10.56	10.26
DMRG-SCF	10.53	5.71	9.93
DMRG-SCF/NEVPT2	11.71	9.13	10.17
PBE		16.03	
PBE0		17.72	
previous work			
CAS-BCCC4 (ref. [121])		9.60	
MR-CISD+Q (ref. [121])		9.68	
FCI ^a (ref. [117])		11.14	
MR(6,12)MP2 ^b (ref. [122])		9.9	
CCSDT (ref. [123])		9.0c	
Exp. (ref. [114])		8.99 ^d /9.37 ^d	

^aTZ2P basis set; one core and one virtual orbital frozen; ^bcc-pVTZ basis set; equilibrium structures taken from ref. [110]; ^cEquilibrium structures optimized with CCSD(T)/6-311++G(2d,2p); extrapolation to the complete basis set limit from CCSDT/cc-pVTZ and CCSDT/cc-pVQZ calculations; ^dModified for direct comparison with the electronic energy difference; see also refs. [114], [123].

plemented in the Turbomole 6.5 program package^[120]. All results are compiled in Table 1 for the S-T splitting in methylene along with previous theoretical results and the experimental reference value.

As expected, the deviations of our S-T splittings from the experimental reference decrease with an increasing active orbital space (with the exception of CAS(6,12) where clearly a poor reference yields accidentally a seemingly accurate DMRG-SCF/NEVPT2 result). Moreover, our calculated S-T splittings agree well with previous theoretical results obtained by various methods. Somewhat surprising is the excellent performance of the single-reference CCSDT model^[123] for the multi-configurational character of the singlet \tilde{a}^1A_1 state that is best described in a two-configuration model.^[110] However, our CASSCF calculation with a CAS(6,20) yields a distribution of 91% of configuration $2a_1^2 1b_2^2 3a_1^2$ and 3% of $2a_1^2 1b_2^2 1b_1^2$. Interestingly, CASPT2 (NEVPT2) does not improve on the CASSCF (DMRG-SCF) S-T splitting (again with the CAS(6,12) result for DMRG-SCF/NEVPT2 as an exception), but yields a result that deviates more from experiment. This observation was already made for CASPT2 in ref. [121]. In addition, we also observe a similar trend for DMRG-SCF/NEVPT2. A possible explanation might be a differential dynamical-correlation effect where less dynamical correlation is recovered for the singlet \tilde{a}^1A_1 state than for the triplet state by either variant of multi-reference

perturbation theory that in turn leads to an overstabilization of the triplet \tilde{X}^3B_1 ground state. Finally, note that the DFT S-T gaps are off by almost a factor of two.

10. Conclusions

A reliable computational exploration of complex chemical reactions requires sophisticated *ab initio* approaches that are capable of accurately describing an electronic structure dominated by strong static correlation. The quantum-chemical DMRG algorithm iteratively converges to the exact solution of the electronic Schrödinger equation within a given complete active (orbital) space. Unlike traditional CASSCF-based approaches, which suffer from an exponential scaling of the computational cost with respect to an increase in the number of active orbitals and electrons, DMRG with its polynomial scaling emerged as a new option to explore the spectroscopy and chemical reactivity of molecular complexes with active spaces comprising up to 100 orbitals. Different possibilities are available to take into account dynamical correlation effects based on a DMRG wave function. Structure optimizations in ground and electronically excited states are possible. Also an embedding in a structured environment can be efficiently modeled. Finally, relativistic DMRG models allow us to account for spin-orbit coupling and other 'relativistic effects' in a rigorous way. All these build-

ing blocks complete our new computational toolbox QCMAQUIS that is available free of charge from our webpage.^[124]

Acknowledgments

This work was supported by ETH Zurich (Research Grant ETH-34 12-2 and ETH Fellowship FEL-27 14-1) and by the Schweizerischer Nationalfonds (Project No. 200020 156598). CJS thanks the Fonds der Chemischen Industrie for a Kékule PhD fellowship. EDH thanks the Villum foundation for a post-doctoral fellowship.

Received: December 31, 2015

- [1] P. Pyykkö, J. F. Stanton, *Chem. Rev.* **2012**, *112*, 1.
- [2] E. Negishi, *Angew. Chem. Int. Ed.* **2011**, *50*, 6738.
- [3] M. Reiher, *Chimia* **2009**, *63*, 140.
- [4] C. J. Cramer, D. G. Truhlar, *Phys. Chem. Chem. Phys.* **2009**, *11*, 10757.
- [5] K. Boguslawski, C. R. Jacob, M. Reiher, *J. Chem. Theory Comput.* **2011**, *7*, 2740.
- [6] K. Burke, *J. Chem. Phys.* **2012**, *136*, 150901.
- [7] K. Boguslawski, K. H. Marti, Ö. Legeza, M. Reiher, *J. Chem. Theory Comput.* **2012**, *8*, 1970.
- [8] Y.-J. Liu, D. Roca-Sanjuan, R. Lindh, *Photochemistry* **2012**, *40*, 42.
- [9] C. Garino, L. Salassa, *Phil. Trans. Roy. Soc. London A* **2013**, 371.
- [10] V. Barone, M. Biczysko, I. Carmimeo, 'Computational Tools for Structure, Spectroscopy and Thermochemistry', Ed. V. P. Ananikov, Wiley-VCH, **2014**, chap. 10, pp. 249–320.
- [11] L. Noodleman, *J. Chem. Phys.* **1981**, *74*, 5737.
- [12] L. Noodleman, D. Post, E. Baerends, *Chem. Phys.* **1982**, *64*, 159.
- [13] A. J. Cohen, P. Mori-Sánchez, W. Yang, *Science* **2008**, *321*, 792.
- [14] C. R. Jacob, M. Reiher, *Int. J. Quantum Chem.* **2012**, *112*, 3661.
- [15] K. Boguslawski, C. R. Jacob, M. Reiher, *J. Chem. Phys.* **2013**, *138*, 044111.
- [16] J. Olsen, *Int. J. Quantum Chem.* **2011**, *111*, 3267.
- [17] K. Pierloot, *Mol. Phys.* **2003**, *101*, 2083.
- [18] D. Roca-Sanjuan, F. Aquilante, R. Lindh, *WIREs* **2012**, *2*, 585.
- [19] F. Aquilante, J. Autschbach, R. K. Carlson, L. F. Chibotaru, M. G. Delcey, L. De Vico, I. Fdez. Galvn, N. Ferr, L. M. Frutos, L. Gagliardi, M. Garavelli, A. Giussani, C. E. Hoyer, G. Li Manni, H. Lischka, D. Ma, P. Å. Malmqvist, T. Müller, A. Nenov, M. Olivucci, T. B. Pedersen, D. Peng, F. Plasser, B. Pritchard, M. Reiher, I. Rivalta, I. Schapiro, J. Segarra-Martí, M. Stenrup, D. G. Truhlar, L. Ungar, A. Valentini, S. Vancoillie, V. Veryazov, V. P. Vysotskiy, O. Weingart, F. Zapata, R. Lindh, *J. Comput. Chem.* **2016**, in press.
- [20] S. R. White, *Phys. Rev. Lett.* **1992**, *69*, 2863.
- [21] S. R. White, *Phys. Rev. B* **1993**, *48*, 10345.
- [22] U. Schollwöck, *Ann. Phys.* **2011**, *326*, 96.
- [23] S. Keller, M. Dolfi, M. Troyer, M. Reiher, *J. Chem. Phys.* **2015**, *143*, 244118.
- [24] S. Östlund, S. Rommer, *Phys. Rev. Lett.* **1995**, *75*, 3537.
- [25] F. Verstraete, D. Porras, J. I. Cirac, *Phys. Rev. Lett.* **2004**, *93*, 227205.
- [26] G. Vidal, J. Latorre, E. Rico, A. Kitaev, *Phys. Rev. Lett.* **2003**, *90*, 227902.
- [27] T. Barthel, M.-C. Chung, U. Schollwöck, *Phys. Rev. A* **2006**, *74*, 022329.
- [28] N. Schuch, M. M. Wolf, F. Verstraete, J. I. Cirac, *Phys. Rev. Lett.* **2008**, *100*, 030504.
- [29] S. Keller, M. Reiher, **2016**, arXiv:1602.01145.
- [30] T. Nishino, K. Okunishi, Y. Hieida, N. Maeshima, Y. Akutsu, *Nucl. Phys. B* **2000**, *575*, 504.
- [31] T. Nishino, Y. Hieida, K. Okunishi, N. Maeshima, Y. Akutsu, A. Gendiar, *Prog. Theor. Phys.* **2001**, *105*, 409.
- [32] A. Gendiar, T. Nishino, *Phys. Rev. E* **2002**, *65*, 046702.
- [33] A. Gendiar, N. Maeshima, T. Nishino, *Prog. Theor. Phys.* **2003**, *110*, 691.
- [34] Y. Shi, L. Duan, G. Vidal, *Phys. Rev.* **2006**, *74*, 022320.
- [35] V. Murg, F. Verstraete, O. Legeza, R. M. Noack, *Phys. Rev. B* **2010**, *82*, 205105.
- [36] G. Barcza, O. Legeza, K. H. Marti, M. Reiher, *Phys. Rev. A* **2011**, *83*, 012508.
- [37] N. Nakatani, G. K.-L. Chan, *J. Chem. Phys.* **2013**, *138*, 134113.
- [38] S. Sharma, **2014**, private communication.
- [39] G. K.-L. Chan, **2016**, private communication.
- [40] K. H. Marti, B. Bauer, M. Reiher, M. Troyer, F. Verstraete, *New J. Phys.* **2010**, *12*, 103008.
- [41] H. J. Changlani, J. M. Kinder, C. J. Umrigar, G. K.-L. Chan, *Phys. Rev. B* **2009**, *80*, 245116.
- [42] A. Kovyrshin, M. Reiher, **2016**, in preparation.
- [43] C. G. Darwin, *Proc. Roy. Soc. London A* **1928**, *118*, 654.
- [44] P. Pyykkö, *Adv. Quantum Chem.* **1978**, *11*, 353.
- [45] K. S. Pitzer, *Acc. Chem. Res.* **1979**, *12*, 271.
- [46] P. Pyykkö, *Chem. Rev.* **1988**, *88*, 563.
- [47] M. Reiher, A. Wolf, 'Relativistic Quantum Chemistry', 2nd ed., Wiley-VCH: Weinheim, **2015**.
- [48] F. Calvo, E. Pahl, M. Wormit, P. Schwerdtfeger, *Angew. Chem. Int. Ed.* **2013**, *52*, 7583.
- [49] R. Ahuja, A. Blomqvist, P. Larsson, P. Pyykkö, P. Zaleski-Ejgierd, *Phys. Rev. Lett.* **2011**, *106*, 018301.
- [50] K. Faegri, K. G. Dyall, 'Introduction to Relativistic Quantum Chemistry', Oxford UP, New York, **2007**.
- [51] S. Battaglia, S. Keller, S. Knecht, A. Muolo, M. Reiher, **2016**, in preparation.
- [52] S. Knecht, Ö. Legeza, M. Reiher, *J. Chem. Phys.* **2014**, *140*, 041101.
- [53] J. Thyssen, Dissertation, Department of Chemistry, University of Southern Denmark, **2001**.
- [54] G. F. Koster, 'Properties of the thirty-two point groups', M.I.T. Press, **1963**.
- [55] K. Aidas, C. Angeli, K. L. Bak, V. Bakken, R. Bast, L. Boman, O. Christiansen, R. Cimraglia, S. Coriani, P. Dahle, E. K. Dalskov, U. Ekström, T. Enevoldsen, J. J. Eriksen, P. Ettenhuber, B. Fernández, L. Ferrighi, H. Fliegl, L. Frediani, K. Hald, A. Halkier, C. Hättig, H. Heiberg, T. Helgaker, A. C. Hennum, H. Hettema, E. Hjertenes, S. Høst, I.-M. Høyvik, M. F. Iozzi, B. Jansík, H. J. Aa. Jensen, D. Jonsson, P. Jørgensen, J. Kauczor, S. Kirpekar, T. Kjærgaard, W. Klopper, S. Knecht, R. Kobayashi, H. Koch, J. Kongsted, A. Krapp, K. Kristensen, A. Ligabue, O. B. Lutnaes, J. I. Melo, K. V. Mikkelsen, R. H. Myhre, C. Neiss, C. B. Nielsen, P. Norman, J. Olsen, J. M. H. Olsen, A. Osted, M. J. Packer, F. Pawłowski, T. B. Pedersen, P. F. Provasi, S. Reine, Z. Rinkevicius, T. A. Ruden, K. Ruud, V. V. Rybkin, P. Salek, C. C. M. Samson, A. S. de Merás, T. Saue, S. P. A. Sauer, B. Schimmelpfennig, K. Sneskov, A. H. Steindal, K. O. Sylvester-Hvid, P. R. Taylor, A. M. Teale, E. I. Tellgren, D. P. Tew, A. J. Thorvaldsen, L. Thøgersen, O. Vahtras, M. A. Watson, D. J. D. Wilson, M. Ziolkowski, H. Ågren, *WIREs Comput. Mol. Sci.* **2013**, *4*, 269.
- [56] H.-J. Werner, P. J. Knowles, G. Knizia, F. R. Manby, M. Schütz, et al., MOLPRO, version 2010.1, a package of *ab initio* programs, www.molpro.com, **2010**.
- [57] DIRAC, a relativistic *ab initio* electronic structure program, Release DIRAC14 (**2014**), written by T. Saue, L. Visscher, H. J. Aa. Jensen, and R. Bast, with contributions from V. Bakken, K. G. Dyall, S. Dubillard, U. Ekström, E. Eliav, T. Enevoldsen, E. Faßhauer, T. Fleig, O. Fossgaard, A. S. P. Gomes, T. Helgaker, J. K. Lærdahl, Y. S. Lee, J. Henriksson, M. Iliáš, Ch. R. Jacob, S. Knecht, S. Komorovský, O. Kullie, C. V. Larsen, H. S. Nataraj, P. Norman, G. Olejniczak, J. Olsen, Y. C. Park, J. K. Pedersen, M. Pernpointner, R. di Remigio, K. Ruud, P. Salek, B. Schimmelpfennig, J. Sikkema, A. J. Thorvaldsen, J. Thyssen, J. van Stralen, S. Villau-me, O. Visser, T. Winther, and S. Yamamoto (see <http://www.diracprogram.org>).
- [58] T. Shiozaki et al., BAGEL, Brilliantly Advanced General Electronic-structure Library, <http://www.nubakery.org> under the GNU Public License, accessed December 16, **2015**.
- [59] S. Keller, M. Reiher, *Chimia* **2014**, *68*, 200.
- [60] Ö. Legeza, J. Sólyom, *Phys. Rev. B* **2003**, *68*, 195116.
- [61] G. Barcza, Ö. Legeza, K. H. Marti, M. Reiher, *Phys. Rev. A* **2011**, *83*, 012508.
- [62] Ö. Legeza, J. Sólyom, *Phys. Rev. B* **2004**, *70*, 205118.
- [63] Ö. Legeza, J. Sólyom, *Phys. Rev. Lett.* **2006**, *96*, 116401.
- [64] J. Rissler, R. M. Noack, S. R. White, *Chem. Phys.* **2006**, *323*, 519.
- [65] M. Fiedler, *Czech. Math. J.* **1973**, *23*, 298.
- [66] M. Fiedler, *Czech. Math. J.* **1975**, *25*, 619.
- [67] Ö. Legeza, J. Sólyom, Lorentz Center, Leiden University, The Netherlands, **2004**, International Workshop on Recent Progress and Prospects in Density-Matrix Renormalization.
- [68] Ö. Legeza, CECAM workshop for tensor network methods for quantum chemistry, ETH Zurich, **2010**.
- [69] E. Fertiitta, B. Paulus, G. Barcza, Ö. Legeza, *Phys. Rev. B* **2014**, *90*, 245129.
- [70] Y. Ma, S. Keller, C. J. Stein, S. Knecht, R. Lindh, M. Reiher, **2016**, in preparation.
- [71] C. J. Stein, M. Reiher, *J. Chem. Theory Comput.*, doi:10.1021/acs.jctc.6b00156.
- [72] M. W. Schmidt, M. S. Gordon, *Annu. Rev. Phys. Chem.* **1998**, *49*, 233.
- [73] P. Å. Malmqvist, K. Pierloot, A. R. M. Shahi, C. J. Cramer, L. Gagliardi, *J. Chem. Phys.* **2008**, *128*, 204109.
- [74] V. Veryazov, P. Å. Malmqvist, B. O. Roos, *Int. J. Quantum Chem.* **2011**, *111*, 3329.
- [75] S. Keller, K. Boguslawski, T. Janowski, M. Reiher, P. Pulay, *J. Chem. Phys.* **2015**, *142*, 244104.
- [76] K. Boguslawski, P. Tecmer, Ö. Legeza, M. Reiher, *J. Phys. Chem. Lett.* **2012**, *3*, 3129.
- [77] M. Saitow, Y. Kurashige, T. Yanai, *J. Chem. Phys.* **2013**, *139*, 044118.
- [78] a) S. Sharma, G. K.-L. Chan, *J. Chem. Phys.* **2014**, *141*, 111101; b) S. Guo, M. A. Watson, W. Hu, Q. Sun, G. K.-L. Chan, *J. Chem. Theory Comput.* doi:10.1021/acs.jctc.5b012225; c) S. Knecht, S. Keller, C. Angeli, M. Reiher, **2015**, unpublished.
- [79] Y. Kurashige, T. Yanai, *J. Chem. Phys.* **2011**, *135*, 094104.
- [80] Y. Kurashige, J. Chalupsky, T. N. Lan, T. Yanai, *J. Chem. Phys.* **2014**, *141*, 174111.
- [81] I. Shavitt, *Int. J. Mol. Sci.* **2002**, *3*, 639.
- [82] F. E. Harris, *Int. J. Quantum Chem.* **2002**, *90*, 105.
- [83] S. Knecht, S. Keller, A. Muolo, T. Shiozaki, M. Reiher, **2015**, unpublished.
- [84] A. Savin, 'Recent Developments and Applications of Modern Density Functional Theory', Elsevier, Amsterdam, **1996**, p. 327.
- [85] A. Savin, H.-J. Flad, *Int. J. Quantum Chem.* **1995**, *56*, 327.
- [86] E. D. Hedegård, S. Knecht, J. S. Kielberg, H. J. Aa. Jensen, M. Reiher, *J. Chem. Phys.* **2015**, *142*, 224108.
- [87] E. Fromager, J. Toulouse, H. J. Aa. Jensen, *J. Chem. Phys.* **2007**, *126*, 074111.
- [88] E. Goll, H.-J. Werner, H. Stoll, *Z. Phys. Chem.* **2010**, *224*, 481.

- [89] E. Fromager, R. Cimiraaglia, H. J. Aa. Jensen, *Phys. Rev. A* **2010**, *81*, 024502.
- [90] E. Fromager, S. Knecht, H. J. Aa. Jensen, *J. Chem. Phys.* **2013**, *138*, 084101.
- [91] E. Fromager, *Mol. Phys.* **2015**, *113*, 419.
- [92] B. Senjean, E. D. Hedegård, M. M. Alam, S. Knecht, E. Fromager, *Mol. Phys.* **2016**, <http://dx.doi.org/10.1080/00268976.2015.1119902>.
- [93] P. Cortona, *Phys. Rev. B* **1991**, *44*, 8454.
- [94] T. A. Wesolowski, A. Warshel, *J. Phys. Chem.* **1993**, *97*, 8050.
- [95] C. R. Jacob, J. Neugebauer, *WIREs Comput. Mol. Sci.* **2014**, *4*, 325.
- [96] T. Dresselhaus, J. Neugebauer, S. Knecht, S. F. Keller, Y. Ma, M. Reiher, *J. Chem. Phys.* **2015**, *142*, 044111.
- [97] J. Tomasi, B. Mennucci, R. Cammi, *Chem. Rev.* **2005**, *105*, 2999.
- [98] A. Warshel, M. Levitt, *J. Mol. Biol.* **1976**, *103*, 227.
- [99] H. M. Senn, W. Thiel, *Angew. Chem. Int. Ed.* **2009**, *48*, 1198.
- [100] T. A. Wesolowski, A. Warshel, *Chem. Phys. Lett.* **1996**, *248*, 71.
- [101] N. Govind, Y. A. Wang, A. J. R. da Silva, E. A. Carter, *Chem. Phys. Lett.* **1998**, *97*, 129.
- [102] N. Govind, Y. A. Wang, E. A. Carter, *J. Chem. Phys.* **1999**, *110*, 7677.
- [103] E. D. Hedegård, M. Reiher, **2016**, in preparation.
- [104] J. M. Olsen, K. Aidas, J. Kongsted, *J. Chem. Theory Comput.* **2010**, *6*, 3721.
- [105] E. D. Hedegård, J.M.H. Olsen, S. Knecht, J. Kongsted, H. J. Aa. Jensen, *J. Chem. Phys.* **2015**, *142*, 114113.
- [106] P. G. Szalay, T. Müller, G. Gidofalvi, H. Lischka, R. Shepard, *Chem. Rev.* **2012**, *112*, 108.
- [107] W. Hu, G. K.-L. Chan, *J. Chem. Theory Comput.* **2015**, *11*, 3000.
- [108] J. Stålring, A. Bernhardsson, R. Lindh, *Mol. Phys.* **2001**, *99*, 103.
- [109] M. G. Delcey, T. B. Pedersen, F. Aquilante, R. Lindh, *J. Chem. Phys.* **2015**, *143*, 044110.
- [110] J. C. W. Bauschlicher, P. R. Taylor, *J. Chem. Phys.* **1986**, *85*, 6510.
- [111] V. Staemmler, *Theoret. Chim. Acta* **1973**, *31*, 49.
- [112] A. Kasdan, E. Herbst, W. C. Lineberger, *J. Chem. Phys.* **1975**, *62*, 541.
- [113] O. M. Nefedov, S. P. Kolensnikov, I. A. Ioffe, *J. Organomet. Chem. Library* **1977**, *5*, 181.
- [114] P. Jensen, P. R. Bunker, *J. Chem. Phys.* **1988**, *89*, 1327.
- [115] Y. Apeloig, R. Pauncz, M. Karni, R. West, W. Steiner, D. Chapman, *Organometallics* **2003**, *22*, 3250.
- [116] T. H. Dunning Jr., *J. Chem. Phys.* **1989**, *90*, 1007.
- [117] C. D. Sherrill, M. L. Leininger, T. J. V. Huis, H. F. S. III, *J. Chem. Phys.* **1998**, *108*, 1040.
- [118] J. P. Perdew, K. Burke, M. Ernzerhof, *Phys. Rev. Lett.* **1996**, *77*, 3865.
- [119] J. Perdew, M. Ernzerhof, K. Burke, *J. Chem. Phys.* **1996**, *105*, 9982.
- [120] R. Ahlrichs, M. Bär, M. Häser, H. Horn, C. Kölmel, *Chem. Phys. Lett.* **1989**, *162*, 165.
- [121] T. Fang, J. Shen, S. Li, in 'Block correlated coupled cluster theory with a complete active-space self-consistent-field reference function: the general formalism and applications', 'Recent Progress in Coupled Cluster Methods', Eds. P. Carsky, J. Paldus, J. Pittner, Springer Science+Business Media B.V., **2010**, pp. 145–174.
- [122] H. Nakano, T. Nakajima, T. Tsuneda, K. Hirao, 'Recent advances in ab initio, density functional theory, and relativistic electronic structure theory', in 'Theory and Applications of Computational Chemistry: The First Forty Years', Eds. C. Dykstra, G. Frenking, K. Kim, Elsevier B.V., **2005**, pp. 507–557.
- [123] A. Perera, J. R. W. Molt, V. F. Lotrich, R. J. Bartlett, *Theor. Chem. Acc.* **2014**, *133*, 1514.
- [124] www.reiher.ethz.ch/software/maquis.html, **2015**.

PLGA-PEG-supported Pd Nanoparticles as Efficient Catalysts for Suzuki-Miyaura Coupling Reactions in Water

Anaëlle Dumas^{§*}, Arnaud Peramo, Didier Desmaële, and Patrick Couvreur

[§]SCS-DSM Award for best poster presentation in Chemical Biology

Abstract: Chemical transformations that can be performed selectively under physiological conditions are highly desirable tools to track biomolecules and manipulate complex biological processes. Here, we report a new nanocatalyst consisting of small palladium nanoparticles stabilized on the surface of PLGA-PEG nanoparticles that show excellent catalytic activity for the modification of biological building blocks through Suzuki-Miyaura cross-coupling reactions in water. Brominated or iodinated amino acids were coupled with aryl boronic acids in phosphate buffer in good yields. Interestingly, up to 98% conversion into the coupled amino acid could be achieved in 2 h at 37 °C using the stable, water-soluble cyclic triolborate as organometallic partner in the presence of only 1 mol% of palladium. These results pave the way for the modification of biomolecules in complex biological systems such as the intracellular space.

Keywords: Amino acid chemistry · Palladium nanoparticles · Suzuki-Miyaura cross-coupling

Introduction

The tracking and manipulation of individual cellular components provide unprecedented opportunities to understand complex cellular processes and may open new avenues for the treatment of human disease.^[1] Among the functional tools available for the manipulation of biological systems, ‘bioorthogonal reactions’ offer versatile platforms for the selective and controlled modification of biomolecules of interest.^[1] These transformations involve covalent bond formation between non-native chemical tags that react highly chemoselectively together under physiological conditions, while remaining inert towards the myriad of other functional groups found in biological environments. The major difficulty resides in finding non-perturbing chemical handles that react rapidly, while generating no or non-toxic side products.^[2] As a result, only a hand-

ful of reactions have been developed that fulfil all of these criteria.^[3] Among them, the Staudinger ligation (azide-phosphine), copper-catalysed or strain-promoted azide-alkyne cycloadditions and tetrazine ligation approaches are the most widely utilised bioorthogonal reactions to date.^[4] While these transformations have been helpful addressing a number of fundamental biological questions,^[1b,5] toxicity, cross-reactivity with endogenous thiols or other biomolecules, and poor stability of the reagents in biological environments, complicate their application in a number of settings.^[6] Therefore, the design of truly bioorthogonal reactions, involving stable, selective and synthetically accessible reaction partners remains an area of active investigation in chemical biology.^[3,7]

Palladium-mediated cross-coupling reactions provide new possibilities for chemical reporter strategies.^[8] The reactive groups associated with these processes are rarely found in natural systems and cross-coupling reactions proceed with high specificity and broad functional group tolerance. However, the poor stability under aerobic conditions of most palladium(0) complexes used as catalysts, and the high temperatures required for activation, have restricted these reactions to the conventional organic synthesis of small molecules. In the last decade, efforts to develop water- and air-stable catalytic systems active within the narrow biologically-relevant pH and temperature windows, have enabled the use of palladium reactions in bio-

logical settings.^[6d,9] Palladium-catalysed cross-coupling reactions involving protein substrates suffered from low yields until Davis and coworkers reported the 2-amino-4,6-dihydropyrimidine (ADHP)-based catalyst [Pd(OAc)₂(ADHP)₂] enabling efficient Suzuki-Miyaura reaction of halogenated amino acids and peptides with boronic acids.^[10] This system proved its efficacy in the preparation of structurally-defined protein-conjugates with excellent conversions at chemically-installed or genetically-encoded aryl iodides on purified proteins and on the surface of bacteria.^[10,11] In parallel, the analogue *N,N'*-dimethyl ADHP-palladium(II) complex was reported by Li *et al.* to promote copper-free Sonogashira cross-coupling reactions on alkyne-labelled proteins inside bacterial cells.^[12]

These results propelled palladium-mediated reactions in the very demanding bioorthogonal chemistry toolbox. However, these transformations still suffer from drawbacks as the non-specific interactions of the homogenous palladium complexes with nitrogen-, sulphur-, or oxygen-containing biological building blocks may cause cytotoxicity^[12] and require the removal of the palladium catalyst after reaction using metal scavengers.^[11] The use of heterogeneous palladium catalysts could overcome these problems by reducing non-specific binding to biomolecules.^[8] Palladium nanoparticles (Pd NPs) stabilised by organic polymers, or inorganic supports have already demonstrated their

*Correspondence: Dr. A. Dumas
Institut Galien Paris-Sud
UMR 8612, CNRS, Univ. Paris-Sud
Université Paris-Saclay
Faculté de Pharmacie
5 rue JB Clément
92296 Châtenay-Malabry, France
E-mail: anaëlle.dumas@u-psud.fr

activity in Suzuki-Miyaura coupling with small molecules. In this context, they present attractive alternatives to homogenous catalysts owing to their facile separation from final products, possible reusability and cost-effectiveness as no elaborate ligand is necessary for their stabilisation.^[13] However, most reported Pd NPs-mediated reactions require the use of organic co-solvents, surfactants, strong bases and/or high temperatures, which are not compatible with biological applications.^[14] In our continued effort to develop efficient nanotechnologies to promote biologically compatible reactions, we report here the elaboration of palladium nanoparticles (*ca.* 5.6 nm diameter) stabilized on the surface of larger poly(D,L-lactide-*co*-glycolide)-*block*-poly(ethylene glycol) copolymer nanoparticles (PLGA-PEG NPs, *ca.* 158 nm diameter) as catalysts for the Suzuki-Miyaura cross-coupling reaction between halogenated amino acids and aryl-boron reagents under physiologically-relevant conditions. The prepared palladium-PLGA-PEG (Pd-PLGA-PEG) nanoassemblies (176 nm mean diameter) were found to be good catalysts for the coupling of brominated or iodinated amino acids with aryl boronic acids in phosphate buffer. Interestingly, the coupling with a stable water-soluble cyclic triolborate was even more efficient, yielding up to 98% conversion in 2 h at 37 °C in the presence of only 1 mol% of palladium, even at slightly acidic pH. The remarkable activity of these palladium-loaded nanoassemblies even in the absence of added base, the stability and the water-solubility of the cyclic triolborate^[15] make these reaction conditions a potential tool for the modification of biological systems through carbon-carbon bond formation.

Results and Discussion

Preparation of Palladium-loaded Nanoassemblies

The palladium-loaded PLGA-PEG nanoparticles were assembled according to a straightforward two-step process. Stable PLGA-PEG nanoparticles (157.9 nm ± 7.8 nm hydrodynamic diameter, as revealed by dynamic light scattering (DLS) analysis) were prepared according to the emulsion-evaporation method. These polymeric nanoparticles were then incubated with an aqueous solution of K₂PdCl₄. The mixture was stirred vigorously for 15 h at 25 °C. Excess palladium was then removed from the stable palladium-loaded nanoassemblies by ultracentrifugation. Cryogenic transmission electron microscopy (cryo-TEM) images of the Pd-PLGA-PEG nanoassemblies (Fig. 1A and B) showed palladium nanoparticles of 5.6 ± 1.2 nm diam-

eter (Fig. 1D) positioned on the surface of the polymeric nanoparticles. Inductively-coupled plasma mass spectrometry (ICP-MS) quantified the presence of 4.8 atoms of palladium/polymer chain (Pd/polymer mass ratio = 0.01). DLS analysis revealed that palladium loading resulted in an increase in diameter going from 157.9 ± 7.8 nm for PLGA-PEG NPs to 176.3 ± 6.8 nm for Pd-PLGA-PEG nanoassemblies. Reduction of the negative surface charge (Zeta potential) from -14.32 ± 0.45 mV to -7.68 ± 5.71 mV was also observed upon palladium loading (Table 1).

Despite their low absolute surface charge, the Pd-PLGA-PEG nanoassemblies showed reasonable stability, with no significant aggregation at least 3 days after

preparation (Fig. 1C). Macroscopic aggregation was, however, observed after six days of storage.

Catalytic Activity of Pd-PLGA-PEG Nanoassemblies in Suzuki-Miyaura Cross-coupling

The catalytic activity of the prepared assemblies was tested on model Suzuki-Miyaura reactions involving halogenated phenylalanine and tyrosine analogues in the presence of 1 mol% palladium in the form of Pd-PLGA-PEG nanoassemblies and in pH 8.0 phosphate buffer at 37 °C (Table 2). In these conditions, the reaction of *N*-Boc-4-iodo-L-phenylalanine (**1**) with phenyl boronic acid reached 42% and 68% conversion after 2 and 18 h respec-

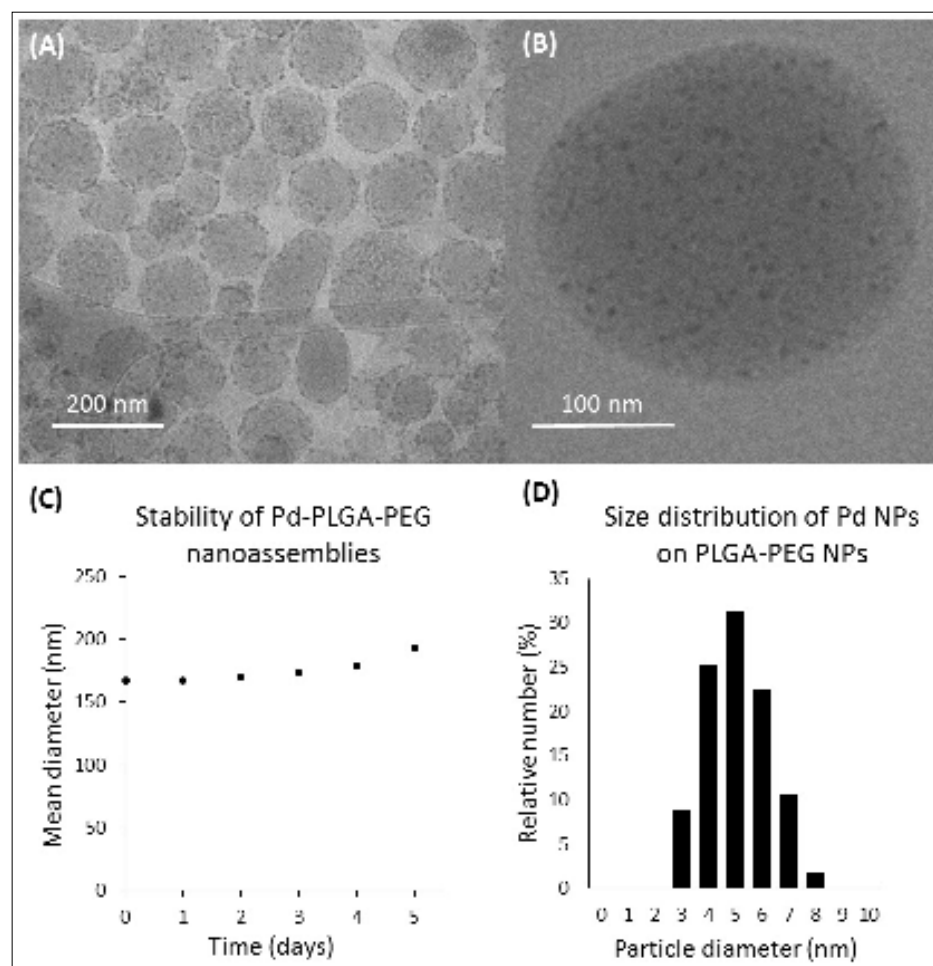


Fig. 1. Cryo-TEM images of (A) a representative sample and (B) a zoom of Pd-PLGA-PEG nanoassemblies. (C) Evolution of the mean diameter of Pd-PLGA-PEG nanoassemblies upon incubation at 25 °C in water for several days after resuspension (PLGA-PEG concentration = 0.2 mg/mL). (D) Size distribution of the palladium nanoparticles on the PLGA-PEG (304 randomly chosen samples on cryo-TEM images, mean diameter: 5.59 nm ± 1.17nm)

Table 1. Physicochemical characterisation of PLGA-PEG NPs and Pd-PLGA-PEG nanoassemblies (NAs). Each value represents the average of more than six experiments ± standard deviation.

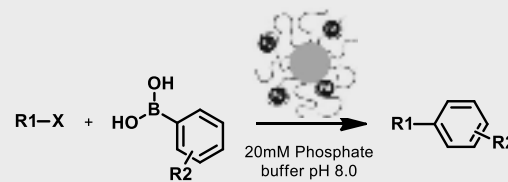
	Hydrodynamic diameter [nm]	Polydispersity index	Zeta potential [mV]
PLGA-PEG NPs	157.9 ± 7.8	0.094 ± 0.016	-14.32 ± 0.45
Pd-PLGA-PEG NAs	176.3 ± 6.8	0.113 ± 0.039	-7.68 ± 5.71

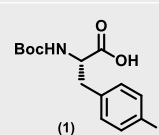
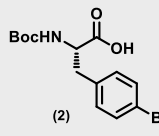
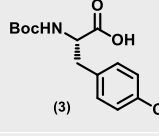
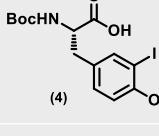
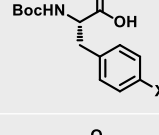
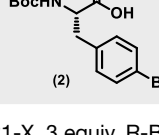
tively as determined by $^1\text{H-NMR}$ (Table 2, entry 1). Surprisingly, reaction with the 4-bromo-analog (**2**) showed 43% and 98% conversion efficiency after 2 and 18 h respectively under the same conditions (Table 2, entry 2). Although aryl bromides are usually less reactive than their iodinated analogues in the Suzuki-Miyaura reaction,^[16] the poor solubility of *N*-Boc-4-iodo-*L*-phenylalanine in phosphate buffer might explain the reversed reactivity pattern observed here. However, coupling of the chlorinated analogue (**3**) did not give the desired product under the mild conditions used here (Table 2, entry 3). When applied to *N*-Boc-3-iodo-*L*-tyrosine (**4**), our standard conditions yielded the expected coupling product in 67% and 70% conversion after 2 and 18 h respectively (Table 2, entry 4).

Exploring the electronic effect of substituents on the phenyl boronic acid revealed that, as expected, substitution on the 3-position of the phenyl ring with an electron-withdrawing nitro group, significantly slowed down the reaction rate, probably due to a decreased nucleophilicity of the boron reagent, disfavoring the transmetallation step. In this case, no reaction was observed with *N*-Boc-4-bromo-*L*-phenylalanine (**2**) whereas, the coupling with *N*-Boc-4-iodo-*L*-phenylalanine (**1**) afforded the corresponding adduct in 35% conversion in 2 h (Table 2, entry 5). By contrast, an electron-donating methoxy group on the 4-position of the phenyl boronic acid facilitated the reaction. Thus, as expected from an increased nucleophilicity of the boron coupling partner, coupling of *N*-Boc-4-bromo-*L*-phenylalanine (**2**) with 4-methoxyphenylboronic acids was found more efficient than in the absence of substituent, giving 62% conversion in 2 h (Table 2, entry 6).

Aryl boronic acids are the most widely used coupling partners in the Suzuki-Miyaura cross-coupling reaction, nevertheless they can suffer from a poor stability and give side reactions such as protodeboronation, di- and trimerization leading to the formation of byproducts, reducing yields and demanding laborious purification processes.^[17] Alternative organoboron reagents, such as pinacol esters, potassium trifluoroborates, or boronates, display improved physico-chemical properties providing clear advantages over standard boronic acids under specific Suzuki-Miyaura coupling conditions. To investigate the effect of the boron species on the reaction outcome, different water-soluble boronic coupling partners were tested in a model system involving the halogenated *N*-Boc-*L*-phenylalanine derivatives **1–3** with phenyl-boron reagents **5–7** in the presence of 1 mol% of PLGA-PEG-supported palladium. Aryltrifluoroborate salts and

Table 2. Suzuki-Miyaura cross-coupling reactions between halogenated amino acid and phenyl boronic acid derivatives catalyzed by Pd-PLGA-PEG nanoassemblies.



No	R1-X	R2	Time [h]	Conversion [%] ^a
1		H	2	42
			18	68
2		H	2	43
			18	98
3		H	2	0
			18	0
4		H	2	67
			18	70
5		3-NO ₂	X = Br 18	0
			X = I 2	35
6		4-OMe	2	62

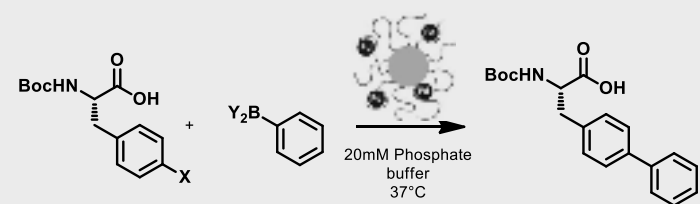
1 equiv. R1-X, 3 equiv. R-B(OH)₂, 1 mol% Pd on PLGA-PEG nanoparticles. ^aThe conversion was determined by $^1\text{H-NMR}$ spectroscopy on the crude reaction mixture.

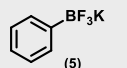
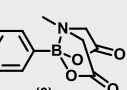
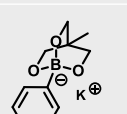
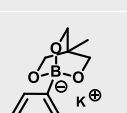
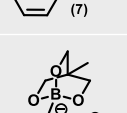
6-methyl-2-phenyl-1,3,6,2-dioxaborocane-4,8-dione (phenyl boronic MIDA esters) are known partners of the Suzuki-Miyaura cross-coupling reaction with the advantage of being monomeric, crystalline and air- and moisture-stable reagents.^[18] Although usually more efficient than the corresponding boronic acids in some reaction settings,^[15a] little or no reaction was observed with our system after 18 h (Table 3, entry 1 & 2).

The air- and moisture-stable tetracoordinated boronate complex **7** was then tested. These reagents were reported as useful reaction partners in Suzuki-Miyaura cross-couplings as the quaternization of the boron centre with the anionic ligand enhanced significantly the nucleophilicity of the organic groups attached, facilitating transmetallation on the metal centre.^[15] As a result, such reagents have been reported

to react in the Suzuki-Miyaura cross-coupling reaction even in the absence of added base. The phenyl cyclic triolborate derivative (**7**) was prepared from phenyl boronic acid following a reported procedure.^[15b] Interestingly, the reaction of this compound with *N*-Boc-4-iodo-*L*-phenylalanine (**1**) in the presence of the catalytic Pd-PLGA-PEG nanoassemblies led to excellent conversion in 2 h in pH 8.0 phosphate buffer at 37 °C (Table 3, entry 3). The reaction with the less reactive 4-bromo-phenylalanine analogue (**2**) led to 90% and 98% conversion in 2 and 18 h respectively (Table 3, entry 4). However, by analogy with the observation made with the arylboronic acids, no reaction was observed with *N*-Boc-4-chloro-*L*-phenylalanine (**3**) (Table 3, entry 5). Remarkably, although Suzuki-Miyaura cross-couplings with aryl boronic acids usually require the addition of an exoge-

Table 3. Suzuki-Miyaura cross-coupling reactions between halogenated phenylalanine and various organoboron reagents catalysed by Pd-PLGA-PEG nanoassemblies



No.	X	Y ₂ -B-Ph	pH	Time [h]	Conversion [%] ^a
1	I		8.0	18	4
2	I		8.0	18	0
3	I		8.0	2 18	98 100
4	Br		8.0	2 18	90 98
5	Cl		8.0	18	0
6	I		7.0	2	97
7	I		6.0	2	97

1 equiv. R1-X, 3 equiv. Y₂B-Ph, 1 mol% Pd on PLGA-PEG nanoparticles. ^aThe conversion was determined by ¹H-NMR spectroscopy on the crude reaction mixture.

nous base, the reaction between *N*-Boc-4-iodo-*L*-phenylalanine (**1**) and the triolborate (**7**) catalysed by the palladium-assemblies gave excellent conversions in 2 h even in neutral and slightly acidic buffers (97% conversion at pH 7.0 and 6.0) (Table 3, entries 6 & 7). The remarkable activity of these palladium-loaded nanoassemblies in the absence of added bases represents a significant advantage over standard Suzuki-Miyaura coupling conditions for reactions involving base-sensitive reaction partners or where little control over the pH is possible.

Interestingly, the process is not limited to the micromolar scale but could be scaled to afford milligram quantities. The reaction of 33 mg of *N*-Boc-4-iodo-*L*-phenylalanine (**1**) with **7** in the presence of

Pd-PLGA-PEG nanoassemblies (1mol% palladium) showed complete conversion after 2 h at 37 °C in phosphate buffer. The coupled product was isolated by column chromatography in 81% yield validating the usefulness of our process for synthetic transformations of polyfunctional, water-soluble substrates under mild conditions.

Conclusion and Perspectives

The Pd-PLGA-PEG nanoassemblies reported here showed excellent catalytic activities for the coupling of halogenated amino acid analogues *via* Suzuki-Miyaura reaction in water and mild conditions without the need for additional co-solvents or

surfactants. Noteworthy is the remarkable efficiency of the coupling process when using cyclic triolborate reagents as boron partners. Indeed, the reaction of *N*-Boc-4-iodo-*L*-phenylalanine (**1**) with a phenyl cyclic triolborate derivative **7** led to 98% conversion in 2 h in the presence of 1 mol% palladium in aqueous phosphate buffer at 37 °C, near-physiological pH and on a synthetically relevant scale.

The Suzuki-Miyaura cross-coupling variant reported here works even at slightly acidic pH. This will present a significant advantage compared to the original version of the reaction in environments where the pH cannot be controlled, such as in the intracellular space. In addition, the chelating effect of the polymer chains stabilising the metal may reduce non-specific interactions with surrounding biomolecules, and thus minimize toxicity as compared to small-molecule-stabilized homogenous catalysts. In this context, we believe that the present approach will contribute to the design of a catalytic system able to selectively achieve an irreversible carbon-carbon bond formation in complex biological systems.

Material and Methods

Materials

Unless otherwise stated, all reagents and solvents were purchased from Sigma-Aldrich. Potassium tetrachloropalladate (II) (K₂PdCl₄) 99.99% trace metal basis (Sigma-Aldrich, Lot N° MKBL2083V) was used as a palladium source.

N-Boc-4-iodo-*L*-phenylalanine, *N*-Boc-4-bromo-*L*-phenylalanine and *N*-Boc-4-chloro-*L*-phenylalanine were purchased from Alfa Aesar. *N*-Boc-3-iodo-*L*-tyrosine was prepared as reported elsewhere.^[19] PLGA-PEG (poly(ethylene glycol)-poly(DL-lactide-co-glycolide) 50:50 Resomer® PEG type RGP d 50105 (MW 50000 g/mol) (diblock, 10% PEG with 5000 Dalton, Evonik Industries AG, Essen, Germany) was generously donated by the group of Prof. Elias Fattal, Université Paris-Saclay. Deionized MilliQ purified water was used for all chemical reactions and for nanoparticles synthesis. Proton nuclear magnetic resonance (¹H NMR) spectra were recorded on a Bruker AV500 (500 MHz) or Bruker AV400 (400 MHz). All chemical shifts are quoted on the δ scale in ppm using residual solvent as the internal standard. Ultracentrifugation was achieved using Optima LE-80K Ultracentrifuge Beckman Coulter apparatus.

PLGA-PEG Nanoparticle (PLGA-PEG NPs) Preparation

Plain PLGA-PEG nanoparticles were prepared by emulsion-evaporation.

Practically, PLGA-PEG (50 mg) was dissolved into CH_2Cl_2 (4 mL). The organic phase was emulsified into 10 mL of 1.5% sodium cholate (w/v) aqueous solution using a vortex for 1 min and then a vibrating metallic tip at 180V, at 30% amplitude for 1 min at 0 °C. The organic solvent was evaporated by magnetic stirring for 4 h. The nanoparticles were recovered by ultracentrifugation (1 h, 27 440 g, 4 °C) and the pellet was resuspended in MilliQ water to form a stock suspension of 5 mg PLGA-PEG / mL.

Pd-loading on PLGA-PEG Nanoparticles (Pd-PLGA-PEG NPs)

PLGA-PEG NPs stock suspension (200 μL , 1 mg PLGA-PEG, 0.02 μmol) was diluted with 990 μL MilliQ water. K_2PdCl_4 stock solution (10 μL , 100 mM, 1 μmol) was added and the mixture was briefly vortexed and then incubated on a thermostated shaker (bioSan TS-100) at 25 °C and 800 rpm for 15 h. The resulting nanoassemblies were recovered by ultracentrifugation (1 h, 24 696 g, 4 °C), the supernatant was removed and the pellet was resuspended in 450 μL MilliQ water.

Size and Zeta Potential

The hydrodynamic diameter (dH) and polydispersity index (PDI) of the PLGA-PEG NPs and Pd-PLGA-PEG nanoassemblies were measured by quasi elastic light scattering, using a Zetasizer Nano ZS instrument (Malvern, France). Suspensions were diluted in water and filtered over a 1 μm -pore glass filter. Measurements were performed in triplicate at 20 °C, at an angle of 173° to avoid multiple scattering. The counting time was set at 60 s. Zeta potential measurements were carried out with the same instrument, at 25 °C, in 1 mM NaCl. The average palladium nanoparticle size and size distribution on the surface of the PLGA-PEG NPs were obtained from randomly chosen particles on Cryo-TEM images using imageJ software.

Cryogenic Transmission Electron Microscopy (cryo-TEM)

For cryogenic transmission electron microscopy (cryo-TEM) analysis, 5 μL of nanoassembly suspension at 5mg/mL were deposited onto a Lacey Formvar/carbon 300 Mesh Copper grid (Ted Pella). Most of the drop was removed with a blotting filter paper and the residual thin film remaining was vitrified by plunging into a bath of liquid ethane slush. The grids were stored under liquid nitrogen temperature until transfer to a 626 Single Tilt Cryotransfer System (Gatan Inc.) and observed with a JEOL 2100HC microscope operated at 200KV (JEOL Europe SAS). Images were recorded under low dose conditions on a Gatan Ultrascan 4k x 4k Digital (CCD)

Camera System Camera at a nominal magnification of 80x at a defocus level of 2 μm .

Determination of Pd Encapsulation Efficacy by ICP-MS

The association of Pd to PLGA-PEG nanoparticles (*i.e.* encapsulation efficacy) was determined by inductively coupled plasma-mass spectrometry (ICP-MS) by Antellis (Parc technologique du Canal, 3 rue des satellites, 31400 Toulouse).

Potassium 4-methyl-1-phenyl-2,6,7-trioxa-1-borate-bicyclo[2.2.2]octane (7)

A mixture of phenylboronic acid (1 mmol, 121.9 mg, 1 equiv.) and 1,1,1-tris(hydroxymethyl)ethane (1 mmol, 120.1 mg, 1 equiv.) in toluene (2 mL) was heated under reflux with azeotropic distillation using a Dean-Stark apparatus for 4 h. The solvent was removed under reduced pressure and the residue taken up into toluene (2 mL) and solid KOH (0.9 mmol, 50.4 mg, 0.9 equiv.) was added. The reaction mixture was heated at reflux with removal of the water by the Dean-Stark method for 4 h. The solid that precipitated was filtered, washed with acetone and dried under reduced pressure to afford the expected salt **7** (219.6 mg, 90% yield). ^1H NMR (300 MHz, DMSO) δ 7.30 (d, $J = 7.2$ Hz, 2H), 6.92 (m, 3H), 3.56 (s, 6H), 0.47 (s, 3H). ^{13}C NMR (75 MHz, DMSO) δ 132.61, 125.86, 124.31, 74.19, 16.76, (C-B signal was not detected).

General Method for Suzuki-Miyaura Coupling on Small Scale

In an Eppendorf tube, the arylhalide (0.008 mmol, 1 equiv.) and the boronic acid (0.024 mmol, 3 equiv.) were suspended in phosphate buffer pH 8.0 (200 mM, 50 μL). The suspension of Pd-PLGA-PEG nanoassemblies (0.00008 mmol Pd, 0.01 equiv., 450 μL) was added and the reaction was mixed and shaken on a thermostated shaker (bioSan TS-100) at 800rpm at 37 °C. After 2/18h, the reaction was frozen in liquid nitrogen and the solution lyophilised. The crude product was dissolved in MeOD and analysed by ^1H -NMR.

Synthesis of N-Boc-4-phenyl-L-phenylalanine via Suzuki-Miyaura coupling involving cyclic triol-borate **7**

N-Boc-4-iodo-L-phenylalanine (0.08 mmol, 31.3 mg, 1 equiv.) and potassium 4-methyl-1-phenyl-2,6,7-trioxa-1-borate-bicyclo[2.2.2]octane (**7**) (0.240 mmol, 58.5 mg, 3 equiv.) were dissolved in phosphate buffer (200 mM, 500 μL). Then Pd-PLGA-PEG nanoassemblies (0.0008 mmol Pd, 0.01 equiv., 4500 μL) were added and the reaction was stirred at 37 °C. After 2 h, the solution was acidified with a

citric acid solution 10% (5 mL). The aqueous solution was extracted with EtOAc (5 x 5 mL). The combined organic layers were then washed with brine (10 mL), dried over MgSO_4 , filtered and concentrated. The residue was purified by chromatography on silica gel column (100/0 to 95/5 DCM/MeOH) to provide the expected N-Boc-4-phenyl-L-phenylalanine (22.1 mg, 81%). ^1H NMR (500 MHz, MeOD) δ 7.47 (d, $J = 7.3$ Hz, 2H), 7.40 (d, $J = 7.7$ Hz, 2H), 7.30 (t, $J = 7.6$ Hz, 2H), 7.20 (d, $J = 7.4$ Hz, 3H), 4.21 (m, 1H), 3.11 (dd, $J = 13.6, 4.8$ Hz, 1H), 2.86 (dd, $J = 13.6, 8.0$ Hz, 1H), 1.24 (s, 9H). MS (ESI+) m/z (%): 364.1 (100%) [M+Na] $^+$.

Acknowledgements

This work is supported by a public grant overseen by the French National Research Agency (ANR) as part of the 'Investissements d'Avenir' program (Labex NanoSaclay, reference: ANR-10-LABX-0035). We thank Jean-François Gallard (Institut de Chimie des Substances Naturelles, CNRS-ICSN UPR 2301, Université Paris-Sud) and Camille Dejean (BioCIS, UMR-CNRS-8076, Université Paris-Sud) for technical assistance on NMR measurements; The Service d'Analyse des Médicaments et Métabolites (SAMM) and Stéphanie Nicolay for technical assistance on mass spectrometry measurements; Ghislaine Frébourg (Service de Microscopie Electronique de l'IFR de Biologie Intégrative, la FRM 2006, SESAME 2005 et le CNRS-INSB) and Julie Mougou (Institut Galien, UMR CNRS 8612, Université Paris-Sud) for technical assistance on cryo-TEM measurements. AD thanks the Swiss National Science Foundation for funding.

Received: January 15, 2016

- [1] a) J. A. Prescher, C. R. Bertozzi, *Nat. Chem. Biol.* **2005**, *1*, 13; b) M. Grammel, H. C. Hang, *Nat. Chem. Biol.* **2013**, *9*, 475.
- [2] a) E. M. Sletten, C. R. Bertozzi, *Angew. Chem. Int. Ed.* **2009**, *48*, 6974; b) K. Lang, J. W. Chin, *Acc. Chem. Biol.* **2014**, *9*, 16.
- [3] M. King, A. Wagner, *Bioconjugate Chem.* **2014**, *25*, 825.
- [4] a) E. M. Sletten, C. R. Bertozzi, *Acc. Chem. Res.* **2011**, *44*, 666; b) A. C. Knall, C. Slugovc, *Chem. Soc. Rev.* **2013**, *42*, 5131.
- [5] a) L. I. Willems, W. A. Van der Linden, N. Li, K. Y. Li, N. Liu, S. Hoogendoorn, G. A. Van der Marel, B. I. Florea, H. S. Overkleeft, *Acc. Chem. Res.* **2011**, *44*, 718; b) Z. Q. Li, D. Y. Wang, L. Li, S. J. Pan, Z. K. Na, C. Y. J. Tan, S. Q. Yao, *J. Am. Chem. Soc.* **2014**, *136*, 9990; c) J. Li, S. Jia, P. R. Chen, *Nat. Chem. Biol.* **2014**, *10*, 1003.
- [6] a) R. Ekkebus, S. I. van Kasteren, Y. Kulathu, A. Scholten, I. Berlin, P. P. Geurink, A. de Jong, S. Goerdalay, J. Neeffjes, A. J. R. Heck, D. Komander, H. Ovaa, *J. Am. Chem. Soc.* **2013**, *135*, 2867; b) M. F. Debets, S. S. Van Berkel, J. Dommerholt, A. J. Dirks, F. P. J. T. Rutjes, F. L. Van Delft, *Acc. Chem. Res.* **2011**, *44*, 805; c) M. T. Taylor, M. L. Blackman, O. Dmitrenko, J. M. Fox, *J. Am. Chem. Soc.* **2011**, *133*, 9646; d) J. Li, P. R. Chen, *ChemBioChem* **2012**, *13*, 1728; e) H. E. Murrey, J. C. Judkins, C. W. A. Ende, T. E. Ballard, Y. Z. Fang, K. Riccardi, L. Di, E.

- R. Guilmette, J. W. Schwartz, J. M. Fox, D. S. Johnson, *J. Am. Chem. Soc.* **2015**, *137*, 11461.
- [7] H. W. Shih, D. N. Kamber, J. A. Prescher, *Curr. Opin. Chem. Biol.* **2014**, *21*, 103.
- [8] S. V. Chankeshwara, E. Indrigo, M. Bradley, *Curr. Opin. Chem. Biol.* **2014**, *21*, 128.
- [9] a) R. M. Yusop, A. Unciti-Broceta, E. M. V. Johansson, R. M. Sanchez-Martin, M. Bradley, *Nat. Chem.* **2011**, *3*, 239; b) K. Kodama, S. Fukuzawa, H. Nakayama, K. Sakamoto, T. Kigawa, T. Yabuki, N. Matsuda, M. Shirouzu, K. Takio, S. Yokoyama, K. Tachibana, *ChemBioChem* **2007**, *8*, 232.
- [10] J. M. Chalker, C. S. C. Wood, B. G. Davis, *J. Am. Chem. Soc.* **2009**, *131*, 16346.
- [11] C. D. Spicer, B. G. Davis, *Chem. Commun.* **2011**, *47*, 1698.
- [12] N. Li, R. K. V. Lim, S. Edwardraja, Q. Lin, *J. Am. Chem. Soc.* **2011**, *133*, 15316.
- [13] a) M. Pérez-Lorenzo, *J. Phys. Chem. Lett.* **2012**, *3*, 167; b) P. Taladriz-Blanco, P. Herves, J. Perez-Juste, *Top. Catal.* **2013**, *56*, 1154.
- [14] a) B. J. Gallon, R. W. Kojima, R. B. Kaner, P. L. Diaconescu, *Angew. Chem. Int. Ed.* **2007**, *46*, 7251; b) S. W. Kim, M. Kim, W. Y. Lee, T. Hyeon, *J. Am. Chem. Soc.* **2002**, *124*, 7642; c) Y. Li, X. M. Hong, D. M. Collard, M. A. El-Sayed, *Org. Lett.* **2000**, *2*, 2385; d) C. Liu, Q. J. Ni, P. P. Hu, J. S. Qiu, *Org. Biomol. Chem.* **2011**, *9*, 1054; e) Y. Z. Piao, Y. J. Jang, M. Shokouhimehr, I. S. Lee, T. Hyeon, *Small* **2007**, *3*, 255; f) A. Prastaro, P. Ceci, E. Chiancone, A. Boffi, R. Cirilli, M. Colone, G. Fabrizi, A. Stringaro, S. Cacchi, *Green Chem.* **2009**, *11*, 1929; g) H. Veisi, A. R. Faraji, S. Hemmati, A. Gil, *Appl. Organomet. Chem.* **2015**, *29*, 517.
- [15] a) A. J. J. Lennox, G. C. Lloyd-Jones, *Chem. Soc. Rev.* **2014**, *43*, 412; b) Y. Yamamoto, M. Takizawa, X. Q. Yu, N. Miyaura, *Angew. Chem. Int. Ed.* **2008**, *47*, 928.
- [16] J. K. Stille, K. S. Y. Lau, *Acc. Chem. Res.* **1977**, *10*, 434.
- [17] D. G. Hall, in 'Boronic Acids', Wiley-VCH Verlag GmbH & Co. KGaA, **2006**, pp. 1–99.
- [18] a) D. M. Knapp, E. P. Gillis, M. D. Burke, *J. Am. Chem. Soc.* **2009**, *131*, 6961; b) G. A. Molander, B. Canturk, *Angew. Chem. Int. Ed.* **2009**, *48*, 9240.
- [19] A. Dumas, C. D. Spicer, Z. H. Gao, T. Takehana, Y. Y. A. Lin, T. Yasukohchi, B. G. Davis, *Angew. Chem. Int. Ed.* **2013**, *52*, 3916.

Total Synthesis of Fijiolide A[‡]

Christoph Heinz[§] and Nicolai Cramer^{*}

[§]SCS-DSM Award for best poster presentation in Organic Chemistry

Abstract: Fijiolide A is a secondary metabolite isolated from a marine-derived actinomycete of the genus *Nocardioopsis*. It was found to significantly reduce the TNF- α induced activity of the transcription factor NF κ B, which is considered a promising target for the treatment of cancer and inflammation-related diseases. We disclose an enantioselective synthesis of fijiolide A enabled by a fully intermolecular, yet regioselective cyclotrimerization of three unsymmetrical alkynes to construct its tetra-substituted arene core. An atropselective macroetherification enables the assembly of the strained [2.6]paracyclophane motif. A late-stage glycosylation of the macrocyclic aglycone at its tertiary alcohol position allowed for the first total synthesis of fijiolide A.

Keywords: [2+2+2] Cycloaddition · Fijiolide · Glycosylation · Paracyclophane formation · Total synthesis

Fijiolides A (**1**) and B were first isolated in 2010 by Fenical and coworkers from a marine-derived actinomycete of the genus *Nocardioopsis*, discovered in a sediment sample of the Beqa Lagoon, Fiji.^[1] Both secondary metabolites display inhibitory activity against TNF- α induced activation of nuclear factor kappa-light-chain-enhancer of activated B cells (NF κ B). Due to its pivotal role in immunological processes, NF κ B has been termed ‘central mediator of the human immune response’.^[2] As a rapid acting primary transcription factor, it regulates the expression of nearly 500 genes,^[3] many of whom encode tumorigenesis and inflammation-relevant proteins including cyclooxygenase (COX-2), matrix metalloproteinase (MMP-9), inducible nitric oxide synthase (iNOS) or anti-apoptotic proteins bcl-2 and bcl-xl.^[4]

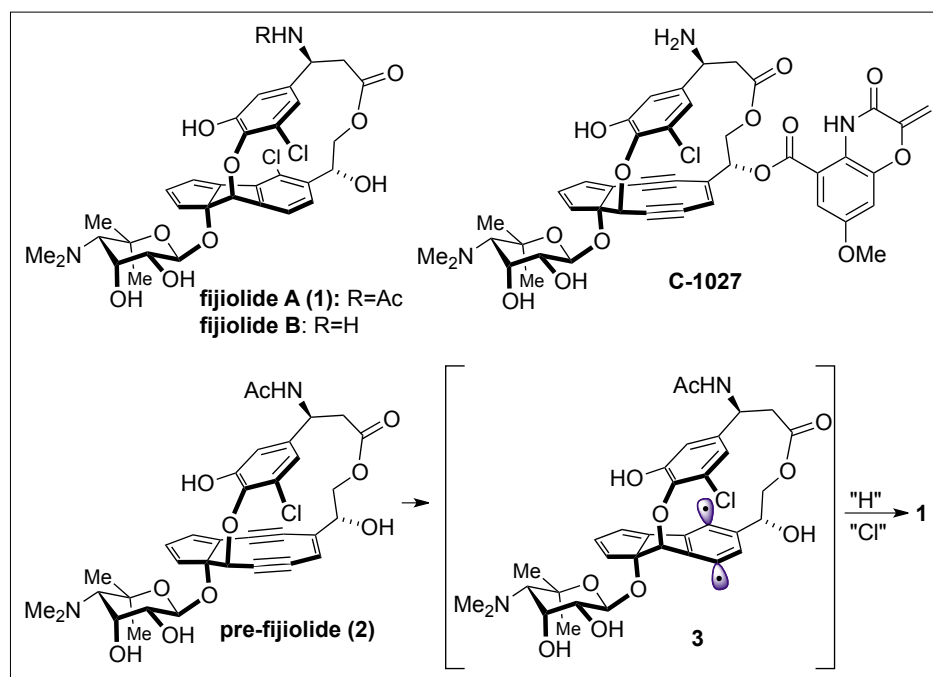
The structures of fijiolides A and B bear close resemblance to the Bergman-cyclization product of the enediyne C-1027 (Scheme 1).^[5,6] Consequently, a common biosynthetic origin from the 9-membered enediyne precursor pre-fijiolide (**2**) has been suggested.^[7] Recently, a supporting piece of evidence has been provided by Oh *et al.* who reported the isolation of fijiolides A and B together with the cycloaromatized C-1027 chromophore from an actinomycete strain, collected at the East Siberian continental margin.^[8] In analogy to the sporolides and cyanosporasides,^[9,10] the ex-

clusively mono-chlorinated cyclopenta[*a*]indene core of the fijiolides is believed to result from a regioselective ionic trapping of the intermediate *p*-benzyne biradical of the intermediate *p*-benzyne biradical species **3**.^[11]

The inhibitory properties of fijiolide A with respect to the TNF- α induced NF κ B activity renders **1** of pharmacological interest. Concomitant with an intriguing molecular architecture, fijiolide A represents a formidable target for total synthesis. From a synthetic point of view, **1** appears particularly challenging due to its rotationally restricted [2.6]paracyclophane core giving rise to planar chirality and non-biaryl atropisomerism. The strained structural motif is embedded into the fijiolide A aglycone which is glycosylated at its cyclopenta-

dieneol moiety. A synthesis of **1** requires the challenging installation of an amino ribopyranose unit at a hindered tertiary alcohol.

Retrosynthetically, fijiolide A was envisioned to be accessed from precursor **4** via a late-stage elimination of an allylic alcohol to install the cyclopentadienyl motif and a glycosylation of the tertiary allylic alcohol with the known Schmidt donor **5** (Scheme 2).^[12] An atropselective assembly of the rotationally restricted [2.6]paracyclophane core could be realized by a cyclization reaction forming the phenol ether bond rather than a more obvious macro-lactonization approach. An additional strategic fission of the six-atom paracyclophane bridge at the ester functionality dis-



Scheme 1. Structures of fijiolide A and B and related enediyne natural products.

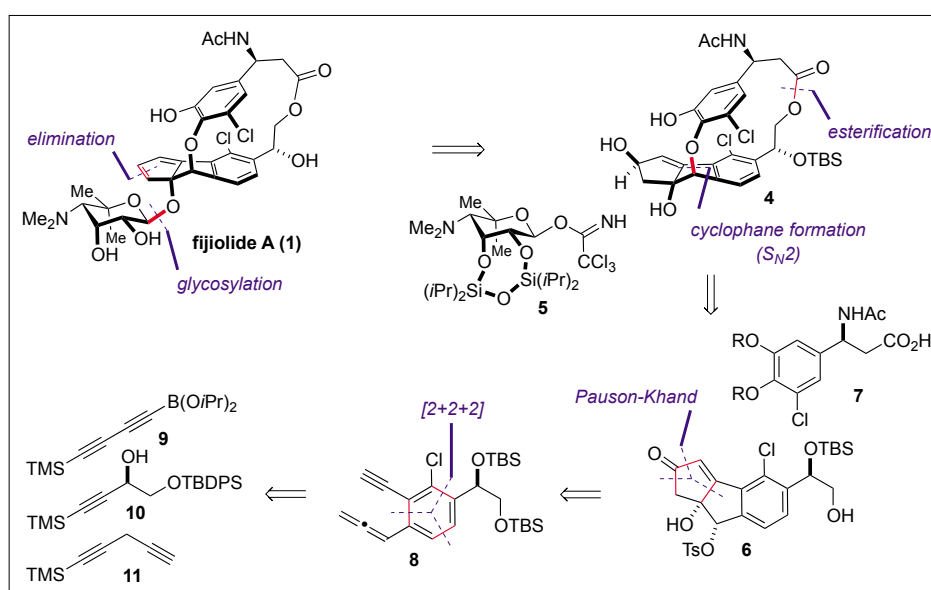
^{*}Correspondence: Prof. Dr. N. Cramer
Ecole Polytechnique Fédérale de Lausanne
EPFL SB ISIC LCSA
BCH 4305
CH-1015 Lausanne
E-mail: nicolai.cramer@epfl.ch

[‡]An original report on this work has been published previously: C. Heinz, N. Cramer, *J. Am. Chem. Soc.* **2015**, *137*, 11278.

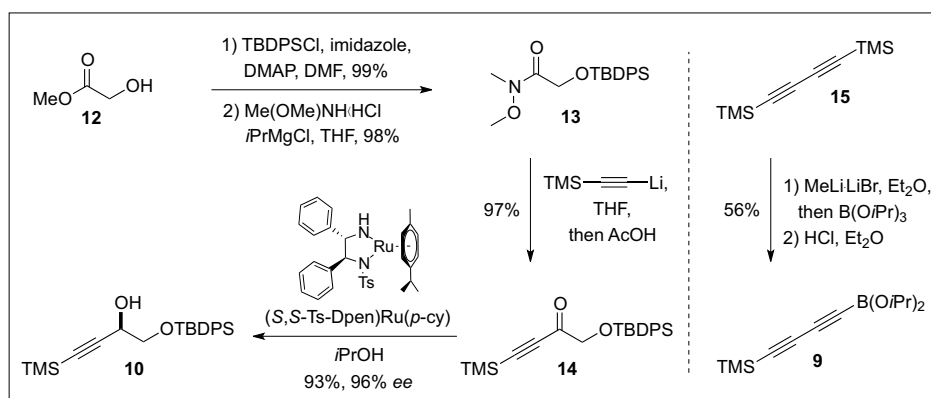
assembles **4** into indanyl cyclopentenone **6** and β -amino acid fragment **7**. In turn, the carbocyclic skeleton of **6** was envisaged to result from a Pauson-Khand reaction of allene-yne **8**. The *de novo* synthesis of benzene derivative **8** from alkynes **9**, **10** and **11** via an intermolecular [2+2+2] cycloaddition was considered to provide a higher step-economy than more conventional arene functionalizations.

Our synthesis of fijiolide A commenced with the preparation of enantioenriched propargylic alcohol **10** via Weinreb amide **13** (Scheme 3).^[13,14] Although commercially available, **13** was prepared in two steps and excellent yield by TBDPS-protection of methyl glycolate, followed by treatment with *N*-methoxy-*N*-methylamide hydrochloride in the presence of *i*PrMgCl. In turn, treatment of **13** with lithium trimethylsilylacetylide afforded ynone **14**. Noteworthy, quenching the reaction with acetic acid turned out to be key for high purity of **14**, and thus for direct employment of the crude product in the ensuing transfer hydrogenation step. Other work-up procedures, *e.g.* the addition of aqueous ammonium chloride led to partial silyl cleavage. The terminal ynone, thus formed, proved to be a strong poison of Noyori's (Ts-Dpen) Ru(*p*-cymene) catalyst.^[15] The acetic acid quench furnished a clean ynone **14** and allowed for the direct asymmetric reduction to propargyl alcohol **10** in 93% yield and 96% *ee*. Diynylboronate **9** was synthesized from TMS acetylene dimer **15** according to a modified literature procedure involving isolation of the intermediate lithium triisopropoxydiynylborate.^[16]

With **9** and **10** in hand, realization of the envisioned [2+2+2] cycloaddition became the paramount synthetic endeavor (Scheme 4). Intermolecular cyclotrimerizations of unsymmetrical alkynes allow for the rapid construction of highly substituted benzene derivatives. However, the difficulty in attaining satisfactory levels of chemo- and regioselectivity to produce a single isomer strongly limits its application in organic synthesis.^[17] In 2004, Yamamoto and coworkers reported a ruthenium-catalyzed regioselective cyclotrimerization enabled by a dynamic temporary boron tether between an alkynylboronate species and a propargylic alcohol component.^[18] Accordingly, alkynes **9** and **10** were mixed *in vacuo* in order to remove the released isopropanol and shift the equilibrium to the transesterified boronate **17**. Upon addition of Cp^{*}Ru(cod)Cl in DCE, the tethered 1,6-diyne moiety of **17** acts as a competent substrate for oxidative cyclization, giving ruthenacycle **18**. Coordination of terminal alkyne **11** to the metal center occurs preferentially with an orientation avoiding steric repulsion between its silylated propargyl moiety and the bulky, yet removable TMS



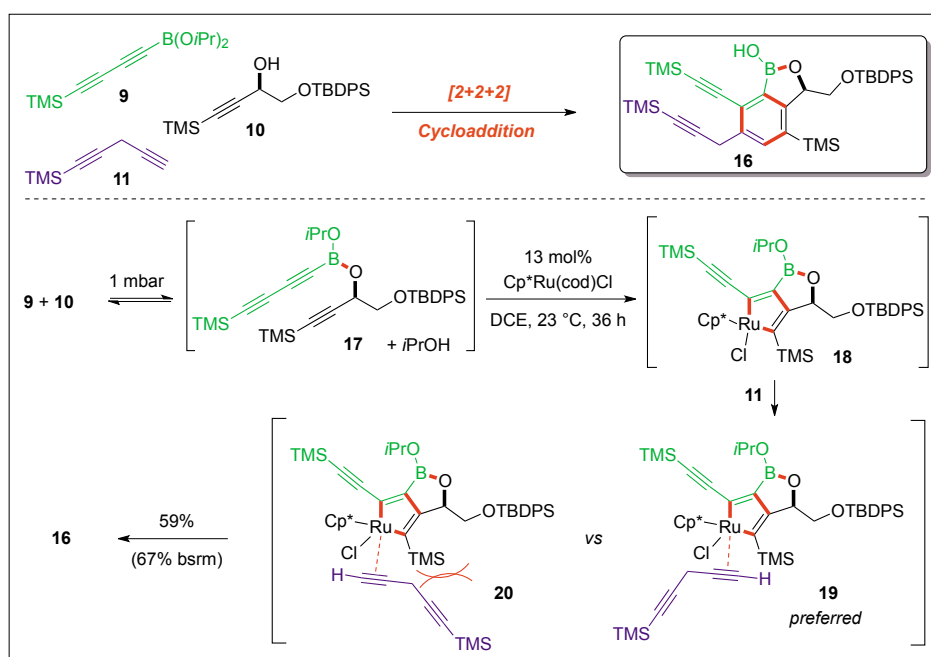
Scheme 2. Retrosynthetic analysis of fijiolide A.



Scheme 3. Synthesis of propargyl alcohol **10** and diynylboronate **9**.

group adjacent to the ruthenium atom (**19** preferred over **20**). Thus, insertion of the third alkyne proceeds in a productive man-

ner and allows for isolation of desired arylboronic acid derivative **16** in 59% yield (67% brsm of **10**) as a single regioisomer.

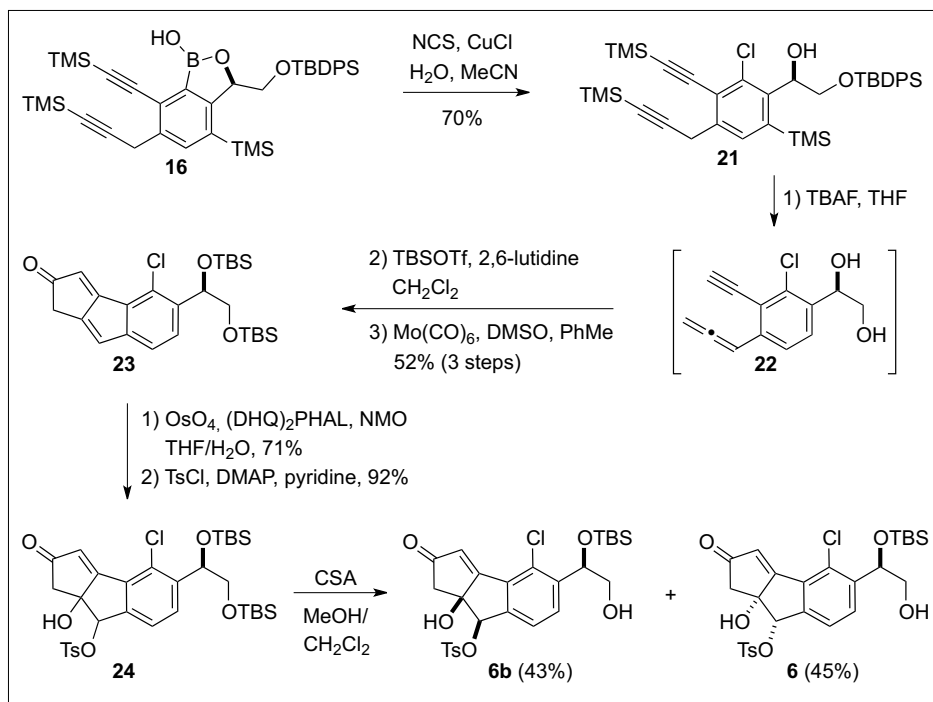
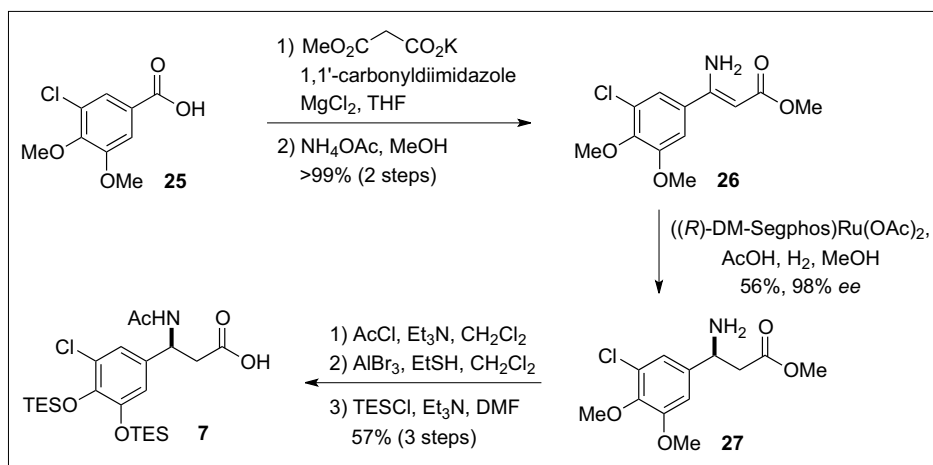
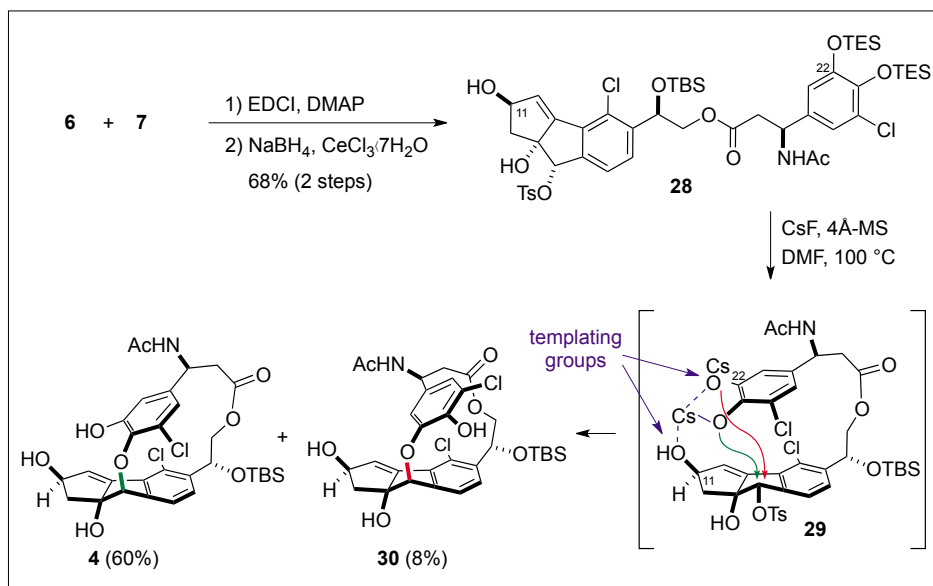


Scheme 4. Intermolecular [2+2+2] cycloaddition to assemble the fijiolide arene core.

Taking further advantage of the dynamic boron substituent as a chlorine atom synthon, oxidative halodeboronation of **16** could be realized in the presence of NCS/CuCl.^[19] Subsequent exposure of **21** to excess TBAF resulted in global desilylation and triggered the anticipated isomerization of the propargyl group, generating the required terminal allene.^[20] Intermediate diol **22** was protected as its corresponding *bis*-TBS ether. Ensuing subjection to a Mo(CO)₆ mediated allenic Pauson-Khand reaction afforded indenyl cyclopentenone **23**.^[21] Due to its inherent base-sensitivity, dihydroxylation of **23** could not be performed under classical Sharpless conditions (AD-mix).^[22] Consequently, a modified dihydroxylation procedure was employed proceeding with high chemoselectivity for the more electron-rich indenyl double bond. However, almost no facial selectivity could be attained. Selective activation of the secondary benzylic hydroxyl group with TsCl (**24**) over the tertiary alcohol, and cleavage of the primary TBS ether under acidic conditions (CSA) provided fragment **6** (Scheme 5). The separation of the desired diastereomer **6** was conveniently realized at this stage by flash chromatography.

The synthesis of the second building block, β -amino acid **7**, proceeded smoothly starting from 5-chloroveratric acid (**25**) (Scheme 6). A decarboxylative Claisen condensation afforded the corresponding β -keto ester,^[23] which was further converted into enamine **26** by treatment with ammonium acetate. Subsequent enantioselective enamine reduction in the presence of ((*R*)-DM-Segphos)RuOAc₂ produced β -amino ester **27** in 98% *ee*.^[24] Acetylation, followed by global demethylation with AlBr₃/EtSH,^[25] and TES protection of the intermediate catechol moiety furnished β -amino acid **7** in a total of six steps.

Ester formation of building blocks **6** and **7** was performed using EDCI (Scheme 7). The enone was diastereoselectively reduced to the secondary alcohol **28** under Luche conditions.^[26] Subsequent exposure of **28** to CsF in DMF at ambient temperature cleaved first both phenolic silyl groups. Heating the reaction mixture to 100 °C then enabled an ensuing macrocyclization *via* intramolecular nucleophilic displacement. Remarkably, the macroetherification proceeded in an atrop- and regioselective manner, allowing for isolation of desired [2.6]paracyclophane **4** in 60% yield. We attained this selectivity in the paracyclophane formation step by using an unprotected C(11) hydroxyl group and an *in situ* deprotected C(22) phenolic hydroxyl group. These groups are assumed to coordinate the cesium cation, resulting in preorganized intermediate **29**. The fa-

Scheme 5. Completion of carbocyclic fragment **6**.Scheme 6. Synthesis of β -amino acid **7**.

Scheme 7. Regio- and atropselective synthesis of the fijiolide [2.6]paracyclophane core.

avorable templating interactions in **29** are believed to facilitate nucleophilic substitution of the tosylate by the proximate phenolate, resulting in formation of the desired atrop- and regioisomer **4**.

Having overcome the crucial macrocyclization hurdle, our focus shifted towards installation of the cyclopentadiene moiety by elimination of C(11)-OH. Of the numerous dehydration reagents examined, only methyltriphenoxyphosphonium iodide (MTPI)^[27] allowed for isolation of the targeted unstable cyclopentadiene, although in unsatisfactory and non-reproducible yields. In accordance with additional model studies, the free cyclopentadienol moiety was identified as the main cause for the poor stability, particularly towards acid conditions. Therefore, glycosylation of any cyclopentadienol containing precursor with trichloroacetimidate **5** under common Schmidt conditions (TMSOTf/BF₃·OEt₂) was deemed inauspicious. Consequently, we built on a stepwise dehydration approach comprising a selective Mitsunobu-type substitution of the secondary allylic hydroxyl group by an *o*-nitrophenyl selenide to produce **31** (Scheme 8). From the outset, late-stage glycosylation of the sterically encumbered tertiary C(9) hydroxyl group was considered a key challenge and was expected to necessitate a preceding protection of the free phenol. However, silylation of **31** (TBSOTf, 2,6-lutidine, CH₂Cl₂) was found to occur selectively at C(9)-OH without the expected silyl aryl ether being formed. The observed reluctance of the phenol to engage in the silylation reaction prompted us to employ **31** directly as the glycosyl acceptor. Initial attempts on glycosylation with Schmidt donor **5** under standard conditions (TMSOTf/

CH₂Cl₂) predominantly led to silylation of the tertiary alcohol. This result was attributed to glycosyl donor **5**, carrying a basic amino group. In order to suppress the parasitic C(9)-OH silylation various solvents and Lewis acidic glycosylation promoters were screened. TBSOTf in toluene was found to efficiently activate the glycosyl donor, whereas the undesired silylation reaction could be entirely suppressed. The glycosylation proceeded with complete selectivity for the desired β -anomer and in a remarkable yield of 49% considering the complexity and steric hindrance of the glycosyl acceptor.

With the blocked C(9) hydroxyl group, installation of the cyclopentadiene motif was re-investigated. Direct exposure of the glycosylation product to H₂O₂/Et₃N in THF afforded a 1:1 mixture of the Grieco elimination product^[28] and a compound tentatively assigned as the seleno-Mislow-Evans [2,3]-sigmatropic rearranged allylic alcohol.^[29] TES protection of the free phenolic hydroxyl group solved this issue. Thus, treatment of **32** with a biphasic mixture of H₂O₂/Et₃N and toluene in a sonicator afforded the desired cyclopentadiene in 67% yield. Finally, global desilylation with HF·py proceeded smoothly and provided targeted fijiolide A in 84% isolated yield.

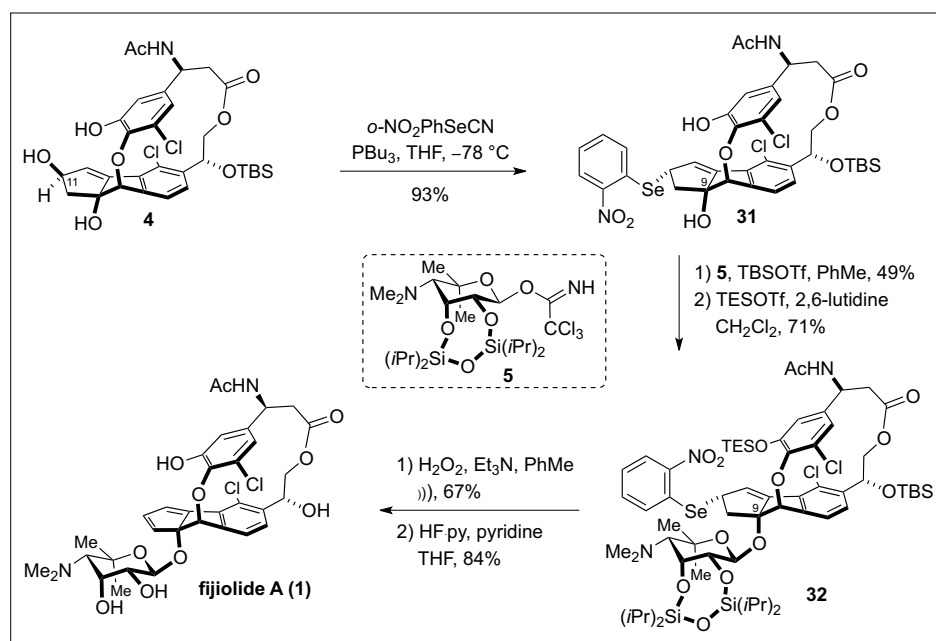
In summary, we disclose an enantio- and atropselective first total synthesis of fijiolide A. Our strategy encompasses a ruthenium-catalyzed cycloaddition of three unsymmetrical alkynes to construct the heavily substituted arene core with complete regioselectivity. An atropselective macroetherification gives access to the strained paracyclophane framework and is followed by glycosylation of a sterically

encumbered tertiary alcohol to assemble the entire carbon backbone. Our concise synthesis of fijiolide A in only 18 steps in the longest linear sequence allows now for the synthesis of analogues and their biological evaluation, which is a current subject of research in our laboratory.

Acknowledgments

Christoph Heinz is grateful to DSM and the Swiss Chemical Society for being awarded with the SCS-DSM best poster presentation award. We thank Professor William Fenical for sharing the NMR FID data of fijiolide A and the Ecole Polytechnique Fédérale de Lausanne for financial support.

Received: January 20, 2016



Scheme 8. Completion of the synthesis.

- [1] S.-J. Nam, S. P. Gaudêncio, C. A. Kauffman, P. R. Jensen, T. P. Kondratyuk, L. E. Marler, J. M. Pezzuto, W. Fenical, *J. Nat. Prod.* **2010**, *73*, 1080.
- [2] H. L. Pahl, *Oncogene* **1999**, *18*, 6853.
- [3] S. C. Gupta, C. Sundaram, S. Reuter, B. B. Aggarwal, *Biochim. Biophys. Acta* **2010**, *1799*, 775.
- [4] R. J. Anto, A. Mukhopadhyay, S. Shishodia, C. G. Gairola, B. B. Aggarwal, *Carcinogenesis* **2002**, *23*, 1511.
- [5] a) J. Hu, Y.-C. Xue, M.-Y. Xie, R. Zhang, T. Otani, Y. Minami, Y. Yamada, T. Marunaka, *J. Antibiot.* **1988**, *41*, 1575; For a synthesis of the C-1027 core, see b) M. Inoue, I. Ohashi, T. Kawaguchi, M. Hirama, *Angew. Chem. Int. Ed.* **2008**, *47*, 1777.
- [6] For a review on enediyne antibiotics, see: I. A. Maretina, B. A. Trofimov, *Russ. Chem. Rev.* **2006**, *75*, 825.
- [7] a) M. Jean, S. Tomasi, P. van de Weghe, *Org. Biomol. Chem.* **2012**, *10*, 7453; b) W. Liu, S. D. Christenson, S. Standage, B. Shen, *Science* **2002**, *297*, 1170; c) J. Zhang, S. G. Van Lanen, J. Ju, W. Liu, P. C. Dorrestein, W. Li, N. L. Kelleher, B. Shen, *Proc. Natl. Acad. Sci. USA* **2008**, *105*, 494.
- [8] K. Moon, C.-H. Ahn, Y. Shin, T. Won, K. Ko, S. Lee, K.-B. Oh, J. Shin, S.-I. Nam, D.-C. Oh, *Marine Drugs* **2014**, *12*, 2526.
- [9] G. O. Buchanan, P. G. Williams, R. H. Feling, C. A. Kauffman, P. R. Jensen, W. Fenical, *Org. Lett.* **2005**, *7*, 2731.
- [10] D.-C. Oh, P. G. Williams, C. A. Kauffman, P. R. Jensen, W. Fenical, *Org. Lett.* **2006**, *8*, 1021.
- [11] C. L. Perrin, B. L. Rodgers, J. M. O'Connor, *J. Am. Chem. Soc.* **2007**, *129*, 4795.
- [12] I. Sato, Y. Akahori, T. Sasaki, T. Kikuchi, M. Hirama, *Chem. Lett.* **1999**, 867; b) Y. Tamura, I. Sato, M. Hirama, *Synlett* **2010**, 2156; c) M. F. Semmelhack, Y. Jiang, D. Ho, *Org. Lett.* **2001**, *3*, 2403; d) K.-i. Iida, T. Ishii, M. Hirama, T. Otani, Y. Minami, K.-i. Yoshida, *Tetrahedron Lett.* **1993**, *34*, 4079.
- [13] C. Heinz, N. Cramer, *J. Am. Chem. Soc.* **2015**, *137*, 11278.
- [14] a) S. Nahm, M. Weinreb, *Tetrahedron Lett.* **1981**, *22*, 3816; b) H. Nemoto, M. Nagamochi, H. Ishibashi, K. Fukumoto, *J. Org. Chem.* **1994**, *59*, 74.
- [15] K. Matsumura, S. Hashiguchi, T. Ikariya, R. Noyori, *J. Am. Chem. Soc.* **1997**, *119*, 8738.
- [16] A. M. McAnoy, S. Dua, D. Schröder, J. H. Bowie, H. Schwarz, *J. Phys. Chem. A* **2004**, *108*, 2426.
- [17] For reviews, see: a) P. R. Chopade, J. Louie, *Adv. Synth. Catal.* **2006**, *348*, 2307; b) D. L. J. Broere, E. Ruijter, *Synthesis* **2012**, *44*, 2639.

- [18] For seminal reports on ruthenium-catalyzed [2+2+2] cycloadditions, see: a) C. Ernst, O. Walter, E. Dinjus, *J. Prakt. Chem.* **1999**, 341, 801; b) Y. Yamamoto, R. Ogawa, K. Itoh, *Chem. Commun.* **2000**, 549; c) Y. Yamamoto, T. Arakawa, R. Ogawa, K. Itoh, K. *J. Am. Chem. Soc.* **2003**, 125, 12143; For [2+2+2] cycloadditions of temporarily boron-tethered alkynes, see: d) Y. Yamamoto, J. Ishii, H. Nishiyama, K. Itoh, *J. Am. Chem. Soc.* **2004**, 126, 3712; e) Y. Yamamoto, J. Ishii, H. Nishiyama, K. Itoh, *J. Am. Chem. Soc.* **2005**, 127, 9625; f) Y. Yamamoto, J. Ishii, H. Nishiyama, K. Itoh, *Tetrahedron* **2005**, 61, 11501.
- [19] H. Wu, J. Hynes, *Org. Lett.* **2010**, 12, 1192.
- [20] K.-S. Masters, M. Wallesch, S. Bräse, *J. Org. Chem.* **2011**, 76, 9060.
- [21] a) J. L. Kent, H. Wan, K. M. Brummond, *Tetrahedron Lett.* **1995**, 36, 2407; b) J. L. Kent, H. Wan, K. M. Brummond, *J. Org. Chem.* **1998**, 63, 6535.
- [22] a) E. N. Jacobsen, I. Marko, W. S. Mungall, G. Schroeder, K. B. Sharpless, *J. Am. Chem. Soc.* **1988**, 110, 1968; b) K. B. Sharpless, W. Amberg, Y. L. Bennani, G. A. Crispino, J. Hartung, K. S. Jeong, H. L. Kwong, K. Morikawa, Z. M. Wang, D. Xu, X. L. Zhang, *J. Org. Chem.* **1992**, 57, 2768; c) H. C. Kolb, M. S. VanNieuwenhze, K. B. Sharpless, *Chem. Rev.* **1994**, 94, 2483.
- [23] D. W. Brooks, L. D. L. Lu, S. Masamune, *Angew. Chem. Int. Ed.* **1979**, 18, 72.
- [24] K. Matsumura, X. Zhang, K. Hori, T. Murayama, T. Ohmiya, H. Shimizu, T. Saito, N. Sayo, *Org. Process Res. Dev.* **2011**, 15, 1130.
- [25] M. Node, K. Nishide, K. Fuji, E. Fujita, *J. Org. Chem.* **1980**, 45, 4275.
- [26] A. L. Gemal, J. L. Luche, *J. Am. Chem. Soc.* **1981**, 103, 5454.
- [27] J.-R. Dormoy, B. Castro, in 'Encyclopedia of Reagents for Organic Synthesis', John Wiley & Sons, Ltd, **2001**.
- [28] a) M. Nishizawa, S. Gilman, P. A. Grieco, *J. Org. Chem.* **1976**, 41, 1485; b) K. B. Sharpless, M. W. Young, R. F. Lauer, *Tetrahedron Lett.* **1973**, 14, 1979; c) H. J. Reich, S. Wollowitz, J. E. Trend, F. Chow, D. F. Wendelborn, *J. Org. Chem.* **1978**, 43, 1697.
- [29] a) H. J. Reich, *J. Org. Chem.* **1975**, 40, 2570; b) D. A. Evans, G. C. Andrews, *Acc. Chem. Res.* **1974**, 7, 147; c) K. B. Sharpless, R. F. Lauer, *J. Am. Chem. Soc.* **1972**, 95, 7154.

Exotic Chemistry with Ultracold Rydberg Atoms

Heiner Saßmannshausen[§], Johannes Deiglmayr, and Frédéric Merkt*

[§]SCS-DSM Award for best poster presentation in Physical Chemistry

Abstract: We review recent experiments carried out with dense (10^{12} cm^{-3}) ultracold ($T = 40 \text{ } \mu\text{K}$) samples of Cs atoms which have the goal to characterize, by high-resolution spectroscopy, the interactions between Cs atoms, Cs⁺ ions and electrons that lead to the formation of metastable long-range molecules. The types of molecules observed in these experiments and the mechanisms leading to the aggregation of atoms in weakly bound molecules are very different from those encountered in warmer samples. In particular, we present results on molecules with binding energies of less than 0.05 J/mol and discuss their properties in the context of a new category of molecular states arising from slow-electron-atom scattering and their relation to atomic and molecular Rydberg states. One of the astonishing aspects of these types of molecules is that they can still be treated in good approximation in the realm of the Born-Oppenheimer approximation despite a huge electronic-state density. Non-Born-Oppenheimer effects are revealed by the decay of the molecules into neutral and charged fragments.

Keywords: Dipole-dipole interactions · Long-range Rydberg molecules · Rydberg states · Singlet and triplet electron-Cs scattering length · Ultracold Rydberg gases

1. Rydberg States and Long-range Rydberg Molecules

Powerful methods to cool down atomic samples to ultracold temperatures,^[1–4] *i.e.* temperatures below 1 mK, offer chemists the opportunity to study atom/atom interactions and molecule formation in a regime previously not accessible. This regime is characterized, in our experiments, by a typical temperature of 40 μK corresponding to a thermal energy of $h \cdot 800 \text{ kHz}$ or 0.3 mJ/mol and to an extremely low average velocity of 0.05 m/s in the case of Cs atoms. Such conditions enable the investigation of fragile molecules bound by much less than the thermal energy at room temperature. Such molecules can be formed and studied by high-resolution photoassociation spectroscopy starting from ultracold atomic samples. Using ultracold samples in spectroscopic experiments has the additional advantages of negligible Doppler widths (200 kHz in the UV and for Cs atoms at 40 μK) and long interaction times, resulting in small energy uncertainties, relevant,

e.g. for the spectroscopic determination of binding energies. These advantages are currently exploited in an increasing range of applications in atomic and molecular physics and in chemistry focusing on the fundamental understanding of interatomic and intramolecular long-range interactions (see *e.g.* refs [5,6]) and precision measurements of atomic and molecular properties (see *e.g.* refs [7–10]).

Rydberg states of atoms and molecules are at the heart of the research presented in this contribution. These states consist of a positively charged ion core and an excited electron (the Rydberg electron) located in a large orbit of dimension given approximately by the Bohr radius $a_0 n^2$, where n

is the principal quantum number. At sufficiently high values of n , the Rydberg electron is insensitive to the structure of the positively charged ion core, and the Rydberg level structure becomes similar to that of the hydrogen atom. High Rydberg states of all atoms and molecules can be described in good approximation by Rydberg's empirical formula^[11,12]

$$E(n) = E_I(\alpha^+) - \frac{hcR_M}{(n-\delta_l)^2}, \quad (1)$$

where h , c , $E_I(\alpha^+)$, R_M , and δ_l are Planck's constant, the speed of light in vacuum, the energy of the ionic state α^+ relative to the

Table 1. Scaling of selected properties of atoms in high Rydberg states of principal quantum number n . Numerical values correspond to the $33p_{3/2}$ state of Cs.

Property	n scaling	Cs ($33p_{3/2}$)
Binding energy	n^{-2}	127 cm^{-1} , 16 meV, 3.8 THz
Orbital radius	n^2	70 nm
Radiative lifetime	n^3	> 50 μs
Induced dipole moment	n^2	3000 Debye
Local electron density	n^{-6}	
Polarizability	n^7	
C_6 van der Waals coefficient	n^{11}	

*Correspondence: Prof. Dr. F. Merkt
Laboratory of Physical Chemistry
ETH Zurich
Vladimir-Prelog-Weg 2
CH-8093 Zürich
E-mail: feme@xuv.phys.chem.ethz.ch

neutral ground state, the mass-dependent Rydberg constant and the quantum defect, which, in any non-hydrogenic atom or molecule, depends on the orbital angular momentum quantum number l and deviates from zero in penetrating low- l states.

The scaling with n of the physical properties of Rydberg atoms and molecules most relevant to our studies are summarized in Table 1. This Table illustrates that high Rydberg states have a large orbital radius, are weakly bound, long lived, highly polarisable, and easily perturbed by ground-state or Rydberg atoms in their vicinity. The physical properties of atoms or molecules in high Rydberg states are primarily determined by their quantum state and are thus universal.

The experiments summarized below rely on the combination of ultracold samples of Cs atoms prepared in a magneto-optical trap (MOT) and the unusual properties of Rydberg states at high n values. These experiments have been described in more detail in refs [10,13–16].

2. Experimental

The experiments were performed under ultrahigh vacuum using ultracold samples of Cs atoms released from a MOT at a density of 10^{12} atoms/cm³ and a temperature of 40 μ K. All atoms were prepared in either the $F = 3$ or the $F = 4$ hyperfine component of the $6s_{1/2}$ ground state, from which they were photoexcited to high $np_{3/2}$ Rydberg states in single-photon transitions in the ultraviolet (UV) at a wavelength of ~ 319 nm. The UV radiation driving the transitions is either obtained by doubling the frequency of the continuous-wave output of a single-mode ring dye laser at ~ 639 nm resulting in a bandwidth of 1 MHz in the UV, or by pulse amplification of the 639 nm radiation in dye cells, followed by frequency doubling in a BBO crystal, resulting in 5 ns long UV pulses with a bandwidth of 140 MHz at a repetition rate of 10 Hz. The frequency of the laser is calibrated with a wavemeter and with a frequency comb.^[10] The Rydberg atoms or molecules are detected by applying pulsed electric potentials to a pair of electrodes surrounding the photoexcitation region, causing pulsed field ionisation and extraction of the ions towards a charged-particle detector through an ion time-of-flight mass spectrometer. The resulting Cs⁺ and Cs²⁺ ions are detected in separate channels, which enables us to detect molecular products resulting from the interaction of Cs Rydberg atoms with other Cs atoms located in their vicinity. Before photoexcitation, we turn off all optical and magnetic trapping fields and carefully compensate remaining electric and magnetic stray fields.

3. Precision Measurements of Rydberg States of Cs

When we carry out precision measurements of atomic properties we i) operate the trap at low atom densities to avoid broadening by interactions of the Rydberg atoms with ground-state atoms, ii) use low laser intensities to avoid AC Stark shifts of the transitions, and, more importantly, to avoid van-der-Waals interactions between Rydberg atoms, and iii) minimize the temperature of the trapped sample to reduce Doppler broadening. Under these conditions, we can record transitions from the $6s_{1/2}$ ground state to np Rydberg states of Cs with a resolution (full width at half maximum) of 1 MHz as illustrated in Fig. 1a. When the laser frequency is calibrated with a frequency comb, the line centers can be determined at an absolute accuracy of 60 kHz. Extrapolation of the measured Rydberg series using Rydberg's formula (Eqn. (1)), taking into account the energy dependence of the quantum defect up to the term linear in energy, enabled us to determine the first ionization energy of Cs ($E_1 = hc \cdot 31406.4677325(14)$ cm⁻¹) to extreme precision and to extract improved values of the quantum defects of the p Rydberg series and their energy dependence.^[10] Such a high precision and accuracy can only be achieved by careful compensation of stray magnetic and electric fields. We accomplish this by monitoring and minimizing the frequency shifts of the microwave transition between the $F = 3$ and $F = 4$ hyperfine components of the $6s_{1/2}$ ground state and of the $np_{3/2} \leftarrow 6s_{1/2}$ transitions using solenoids and electrodes designed for this purpose. An exemplary measurement of the stray electric field along one spatial coordinate is presented in Fig. 1b. The measured $70p_{3/2} \leftarrow 6s_{1/2}$ transition is

shifted almost exclusively by the quadratic Stark effect of the $70p_{3/2}$ Rydberg state. The externally applied electric-field strengths are given on the y axis of Fig. 1b. At the point of maximal frequency (*i.e.* minimal quadratic Stark shift) the stray electric field in the direction of the externally applied field is compensated.^[17] This point lies at the apex of the parabola presented as a dashed black line. Measuring the Stark effect of high Rydberg states by applying electric fields in all three spatial dimensions enables us to reduce a background electric stray field of ~ 0.3 V/cm to below 1 mV/cm. This level of compensation is necessary to avoid asymmetric line broadenings and shifts in precision measurements of Rydberg transitions and to achieve the afore-mentioned precision and accuracy. A full account of this investigation is given in ref. [10].

4. Pressure Shift, Fermi Pseudo-potential and Long-range Rydberg Molecules

At the maximal atom density in our MOT, the average distance between neighbouring atoms is on the order of 1 μ m and the probability that ground-state atoms are located within the large Rydberg orbit (diameter of about 140 nm at $n = 33$, see Table 1) becomes significant. We can therefore study interactions between Rydberg and ground-state atoms in detail by observing how the Rydberg spectrum is affected by the increased atom density, ultimately leading to the well-known pressure shift of Rydberg transitions. This shift was first measured by Amaldi and Segré in 1934^[18] and interpreted by Fermi^[19] as arising from the scattering of the Rydberg electron with atoms located within the electron orbit.

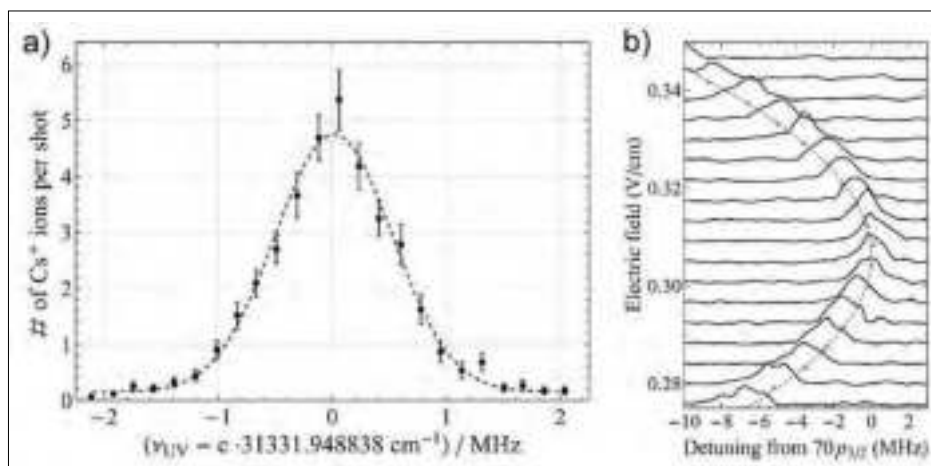


Fig. 1. a) Example of a high-resolution recording of the $42p_{1/2} \leftarrow 6s_{1/2}$ transition. b) Example for the spectroscopic determination of the electric stray field along the lab-frame z axis. The figure contains several spectra of the $70p_{3/2} \leftarrow 6s_{1/2}$ transition measured in various externally applied electric fields. The values of the applied electric-field strengths correspond to the vertical offset of the spectra. The line centers are marked by orange dots and the dashed line indicates the parabolic curve fitted to the observed quadratic Stark shifts.

This scattering can be treated using what is now known as a Fermi-contact-type pseudo-potential

$$V(R) = 2\pi A_0 |\Psi(R)|^2. \quad (2)$$

In this model, the interaction between the Rydberg and the ground-state atoms is reduced to the ‘local’ interaction between the electron, with the electron density at the position R of the ground-state atom relative to the Rydberg ion core given by the square of the Rydberg electron wavefunction $|\Psi(R)|^2$. In Eqn. (2), A_0 is the zero-energy s -wave scattering length of the electron-atom collision. Because the Rydberg electron has a very small kinetic energy at the distance of high probability around the classical outer turning point, the model considers s -wave scattering only, and all higher partial waves do not contribute because the energy of the collision is assumed to be lower than the centrifugal barrier in the electron-atom scattering for $l > 0$. Fermi showed that Eqn. (2) adequately describes the pressure shifts and broadenings of Rydberg lines arising from the presence of many ground-state atoms inside the Rydberg-electron orbit.^[19]

In the limit of a single ground-state atom within the Rydberg-electron orbit and for a negative scattering length A_0 , the Fermi pseudo-potential leads to the existence of a shallow oscillating molecular potential $V(R)$, proportional to the Rydberg electron density.^[20] Greene and coworkers^[21] pointed out that $V(R)$ can actually bind the Rydberg atom to the ground-state atom, giving rise to long-range Rydberg molecules with rovibrational levels that could be observed by high-resolution spectroscopy in ultracold gases. The size of these long-range Rydberg molecules is given by the size of the Rydberg-electron orbit and is enormous, about 50 nm at $n=30$. The existence of these long-range molecules was confirmed experimentally in studies of $ns_{1/2}$ ($n = 32\text{--}36$) Rydberg states of Rb in an ultracold sample by Pfau and coworkers.^[22] The molecular potential can be refined by considering a linear energy dependence of the scattering length on the electron quasi-classical momentum k ^[23]

$$A(k) = A_0 + \frac{\pi}{3} \alpha k(R), \quad (3)$$

where α is the polarisability of the ground-state atom. The kinetic energy $k^2/2$ of the Rydberg electron corresponds to the difference between the total energy and the Coulomb potential energy using the relation (in atomic units)

$$\frac{1}{2} k^2 = -\frac{1}{2n^2} + \frac{1}{R}. \quad (4)$$

In this model, the only parameter needed to describe the molecular states is the zero-energy electron-atom scattering length A_0 , for which calculations exist for many different elements. The calculated values of A_0 for the rare-gas atoms and the alkali-metal atoms are presented in Fig. 2 as a function of the polarisability of the atom in its ground state. In the case of the rare-gas atoms with completely filled subshells, only one scattering channel exists. The alkali-metal atoms with a single valence electron in the ns atomic orbit ($n = 2, 3, 4, 5$, and 6 for Li, Na, K, Rb, and Cs, respectively) exhibit a singlet ($S = 0$) and a triplet ($S = 1$) scattering channel depending on the relative orientation of the spins of the valence electron and the scattered (Rydberg) electron. Fig. 2 reveals a surprisingly simple, linear scaling of the scattering lengths with the polarisabilities α of the ground-state atoms. It also reveals a stronger binding interaction in the long-range molecules resulting from triplet scattering than for singlet scattering channels. This difference can be attributed to the exchange interaction between the Rydberg electron and the valence electron of the ground-state atom.

High-resolution photoassociation spectroscopy of long-range Rydberg molecules and a fit of their binding energies on the basis of Eqn. (2) have yielded the first

experimental determination of the singlet scattering length of electron-Cs collisions,^[13] and later, following the same model, also for electron-Rb collisions.^[29] The experimental observations confirmed the calculations and also the linear scaling of A_0 with α . Our contribution to the studies of these rather unusual molecular states came from the realization that the hyperfine interaction in the ground state of Cs (and of the lighter alkali-metal atoms) is larger than the interaction described by Eqn. (2) for the Rydberg states with n in the range 25–40 studied experimentally (see discussion in refs [13,30]). The hyperfine interaction of the ground-state atom thus couples the electron spin to its own nuclear spin, which effectively mixes singlet and triplet channels and gives rise to a second class of long-range molecular states with mixed singlet-triplet scattering character and even weaker molecular binding energies than the first class of purely triplet scattering character.^[13] An example for the resulting potential-energy curves and vibrational eigenstates is given in Fig. 3a for $33p_{3/2}$.

In the Rydberg spectra, the molecular states appear on the low-frequency side of the atomic resonances, see Fig. 3b for a measurement in the vicinity of the $33p_{3/2} \leftarrow 6s_{1/2}$ transition. The spectrum reveals among several other lines two strong lines. The first one, marked with a thick blue assignment bar at the top of Fig. 3b, appears at larger detuning from the atomic transition and arises from pure triplet

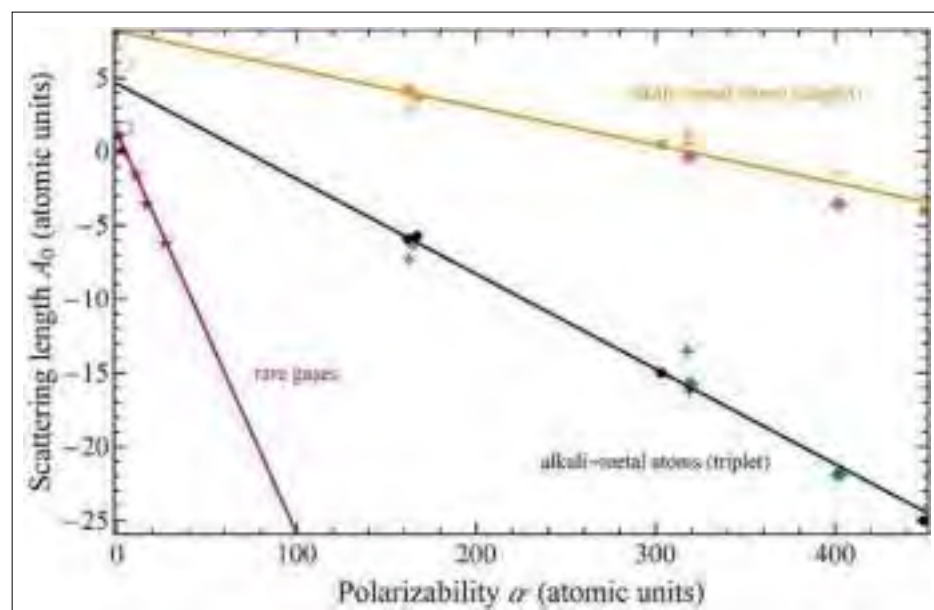


Fig. 2. Electron-atom scattering lengths A_0 as a function of the polarisability α for different elements and scattering channels. Values for the rare gases He, Ne, Ar, Kr and Xe are taken from ref [24] and are indicated by purple five-pointed stars. For the alkali-metal atoms Li, Na, K, Rb and Cs, the singlet and triplet scattering lengths are presented in orange and black, respectively (data taken from refs [25–27]). The singlet and triplet electron-H scattering lengths (data taken from ref [28]) are indicated by open squares. The values determined from a fit to high-resolution long-range Rydberg photoassociation spectroscopy are shown in green (triplet) and magenta (singlet) for Rb^[29] and Cs^[13]. Solid lines represent linear fits to the data of the different groups of elements.

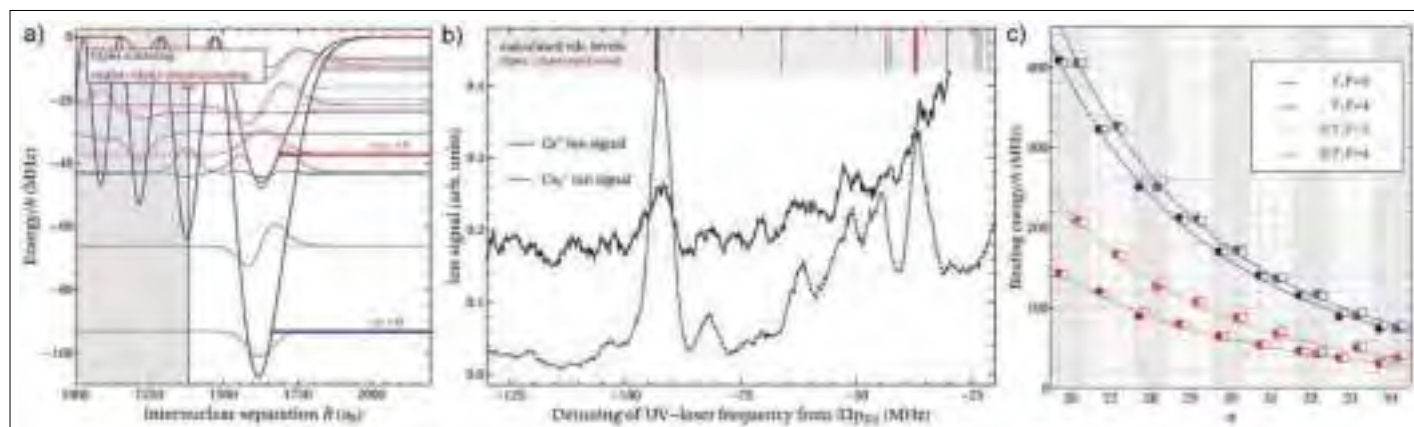


Fig. 3. a) Born-Oppenheimer (BO) potential energy curves calculated for the long-range Cs₂ Rydberg molecular states resulting from pure triplet scattering (blue line) and mixed singlet-triplet scattering located near the Cs 6s_{1/2} (F = 4) + Cs 33p_{3/2} dissociation asymptote. The wavefunctions of the vibrational states are indicated by thin, the binding energies of the vibrational ground states by thick lines. b) Experimental spectra recorded on the low-frequency side of the atomic 33p_{3/2} ← 6s_{1/2} (F = 4) transition. The Cs⁺ and Cs₂⁺ ion signals are displayed as full and dashed lines, respectively. The spectra were measured with a 0.5 μs long 150 mW UV pulse, and a delay of 5 μs between photoexcitation and pulsed-field ionisation. The spectral positions of vibrational levels calculated on the basis of the BO potentials displayed on the left-hand side of the figure are indicated by vertical lines at the top of the panel. c) Comparison of the binding energies (solid symbols) of all measured long-range molecules in their vibrational ground states in the range of principal quantum numbers between 26 and 34 with the calculated values (open symbols).

scattering. The second one, marked with a thick red assignment bar, is observed at smaller detuning and results from mixed singlet-triplet scattering. At the positions of the molecular resonances, we actually photoassociate two ultracold Cs atoms and form a long-range metastable Cs₂ molecule. When we detect the molecules by pulsed field ionisation, we predominantly observe Cs₂⁺ ions (see Fig. 3b). The calculated positions of the vibrational ground states agree well with our experimental results over a wide range of *n* values (*n* = 26–34), as illustrated by Fig. 3c.

For a chemist it may seem extraordinary that potential functions of the type represented in Fig. 3a can at all faithfully describe molecules in an energy region where the electronic-state density

is enormous and the Born-Oppenheimer approximation would be expected to fail. The reason why this is not the case is that, although the electronic motion is slow, the nuclear motion is still much slower at the low temperature of the atom sample and the large distances where photoassociation into these molecules takes place. A full account of this investigation is given in ref. [13].

5. Rydberg-atom Dimers Interacting Through the van der Waals Interaction

A final example illustrating the unusual properties of Rydberg atoms and their interactions is presented in Fig. 4, which shows

the formation of molecular resonances resulting from the interaction between two Cs Rydberg atoms. Because of the scaling of the van der Waals coefficients with *n*¹¹ (see Table 1), the long-range interactions between two ultracold atoms in high-*n* Rydberg states can dominate the dynamics of the system. To treat the long-range van der Waals interaction theoretically, one usually expresses it as a multipole expansion, the leading and often dominating term being the dipole-dipole interaction, which results formally in configuration interactions between near-degenerate levels of the atom pair, such as

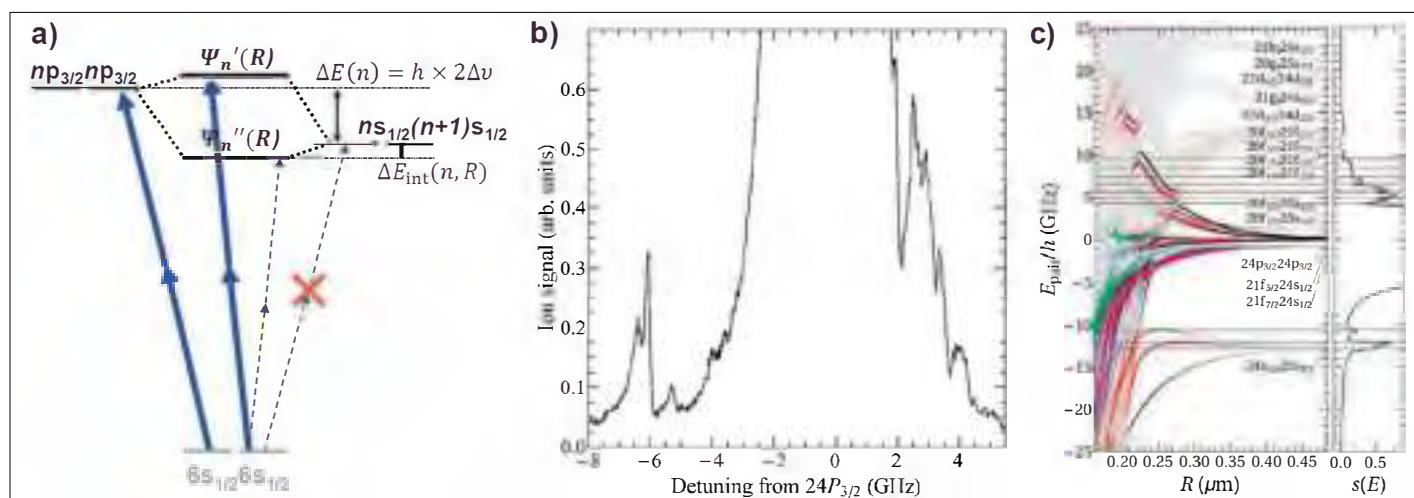
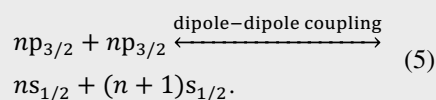


Fig. 4. a) Simplified and schematic configuration-interaction diagram describing the interactions between two Rydberg atoms at long range. Laser excitation is symbolized by blue arrows. The excitation of non-interacting atoms is only allowed to *np* states (thick arrows), and forbidden, e.g., to *ns*_{1/2} states (dashed thin arrows). Ψ(*R*) are the molecular states resulting from the long-range interactions. b) Spectrum recorded in the vicinity of the 24p_{3/2} ← 6s_{1/2} transition with a 5-ns-long pulsed UV laser. c) Calculated potential-energy curves of interacting Rydberg-atom-pair states. The colour coding refers to the *np* character of the molecular states. The spectrum displayed on the right-hand side was simulated on the basis of the potential-energy functions, as explained in detail in ref [16].



This interaction is schematically depicted in the simplified energy-level diagram of Fig. 4a. The long-range interaction between the two Rydberg atoms leads to an R -dependent configuration mixing and to ‘bonding’ Ψ'_n and ‘anti-bonding’ Ψ''_n molecular eigenstates. These two molecular eigenstates $\Psi(R)$ have mixed $np_{3/2}np_{3/2}$ and $ns_{1/2}(n+1)s_{1/2}$ character and are shifted in energy by ΔE_{int} compared to the pair-dissociation asymptotes constituted by the sum of the two Rydberg levels of the non-interacting atoms.

The dipole-dipole interaction mixes the optically accessible p Rydberg states with Rydberg states of s character that are not accessible in single-photon transitions from the 6s ground state. The intensity of the transitions to the mixed molecular states, formed by the interacting Rydberg atoms, is proportional to the p-character of the mixed states.

The observation of such resonances^[6,31–34] requires the simultaneous excitation of two Cs atoms to interacting Rydberg states. With a single monochromatic laser this corresponds to a two-photon excitation. The laser frequency at the position of the two-photon resonances is detuned from the $np_{3/2} \leftarrow 6s_{1/2}$ resonances of the isolated atoms (see Fig. 4a). Because the strength of the two-photon transition rapidly decreases with increasing detuning from the atomic transition, we observe these molecular Rydberg-atom pairs only when the ultracold sample of Cs is illuminated with very intense UV laser pulses.

A typical spectrum recorded with a 5 ns long pulsed, intense (~ 10 MW/cm²) UV laser is presented in Fig. 4b. The laser frequency is calibrated with a wavemeter and is referenced to the atomic $24p_{3/2} \leftarrow 6s_{1/2}$ transition, which is strongly saturated under the conditions where the Rydberg-atom-pair states are observed. Next to the saturated atomic resonance, we observe the density-dependent appearance of additional, sharp (~ 300 MHz FWHM) resonances at negative and positive detunings from the atomic resonance. To assign the molecular resonances observed experimentally it is necessary to consider several interacting Rydberg-atom-pair states and to carefully model the R -dependent interactions. To this end, we set up a Hamiltonian matrix describing the relevant long-range interactions, primarily dipole-dipole interactions,

with weaker contributions from dipole-quadrupole^[15] and quadrupole-quadrupole^[16] interactions. Determining the eigenvalues of this interaction matrix as a function of the internuclear distance leads to sets of potential-energy functions, as illustrated in Fig. 4c for the spectral region near the $24p_{3/2}24p_{3/2}$ dissociation asymptote.

Some spectral positions correspond closely to the energy of pair-dissociation asymptotes, e.g. the resonance at a detuning of ~ -6 GHz in the spectrum depicted in Fig. 4b, which results from molecular states correlated at long range to the $23s_{1/2}24s_{1/2}$ asymptote. The resonances on the high-frequency side result from quadrupole-quadrupole interactions between $np_{3/2}np_{3/2}$ and $nf n'f$ Rydberg-atom pair states.^[16]

The shift of the line observed at a detuning of -6 GHz from the position of the $23s_{1/2}24s_{1/2}$ dissociation asymptote corresponds to the interaction-induced shift ΔE_{int} introduced in Fig. 4a. The resonance exhibits an asymmetric broadening and a red-degraded line shape. The line shape and the magnitude and sign of the interaction-induced shift can be almost perfectly modeled by our numerical calculations based on the potential curves presented in Fig. 4c, taking into account the fact that it is the p-character of the final state that gives rise to observable intensities. A full account of these studies is given in ref. [16].

6. Conclusion

In this short overview of our research on Cs Rydberg atoms in ultracold samples we have studied unusual electronically excited states of Cs₂ with extremely weak binding energies. Because in these states the nuclear motion is still much slower than the slow electronic motion, the treatment of the energy-level structure based on the Born-Oppenheimer approximation remains approximately valid. The states we have observed include long-range Rydberg molecules bound by a Fermi-contact-type interaction of the electron with the Cs neutral atoms. The binding is weaker than the hyperfine interaction in the ground state of Cs, which results in two classes of states, one of which we have observed for the first time. The second type of molecules consists of two atoms both excited to high Rydberg states and interacting at long range *via* the dipole-dipole and higher order multipole-multipole interactions. The very large internuclear distances and the

extremely weak bonds observed in these molecules make them fascinating objects of scientific investigations.

Received: December 30, 2015

- [1] T. Hänsch, A. Schawlow, *Opt. Commun.* **1975**, *13*, 68.
- [2] D. J. Wineland, W. M. Itano, *Phys. Rev. A* **1979**, *20*, 1521.
- [3] E. L. Raab, M. Prentiss, A. Cable, S. Chu, D. E. Pritchard, *Phys. Rev. Lett.* **1987**, *59*, 2631.
- [4] C. Monroe, W. Swan, H. Robinson, C. Wieman, *Phys. Rev. Lett.* **1990**, *65*, 1571.
- [5] K. M. Jones, E. Tiesinga, P. D. Lett, P. S. Julienne, *Rev. Mod. Phys.* **2006**, *78*, 483.
- [6] S. M. Farooqi, D. Tong, S. Krishnan, J. Stanojevic, Y. P. Zhang, J. R. Ensher, A. S. Estrin, C. Boisseau, R. Côté, E. E. Eyler, P. L. Gould, *Phys. Rev. Lett.* **2003**, *91*, 183002.
- [7] A. Marte, T. Volz, J. Schuster, S. Dürr, G. Rempe, E. G. M. van Kempen, B. J. Verhaar, *Phys. Rev. Lett.* **2002**, *89*, 283202.
- [8] L. Carr, J. Ye, *New J. Phys.* **2009**, *11*, 055009.
- [9] M. Mack, F. Karlewski, H. Hattermann, S. Höckh, F. Jessen, D. Cano, J. Fortágh, *Phys. Rev. A* **2011**, *83*, 052515.
- [10] J. Deiglmayr, H. Herburger, H. Saßmannshausen, P. Jansen, H. Schmutz, F. Merkt, *Phys. Rev. A* **2016**, *93*, 013424.
- [11] J. R. Rydberg, *Z. Phys. Chem.* **1890**, *5*, 227.
- [12] T. F. Gallagher, ‘Rydberg Atoms’, Cambridge University Press, Cambridge, **1994**.
- [13] H. Saßmannshausen, F. Merkt, J. Deiglmayr, *Phys. Rev. Lett.* **2015**, *114*, 133201.
- [14] H. Saßmannshausen, F. Merkt, J. Deiglmayr, *Phys. Rev. A* **2013**, *87*, 032519.
- [15] J. Deiglmayr, H. Saßmannshausen, P. Pillet, F. Merkt, *Phys. Rev. Lett.* **2014**, *113*, 193001.
- [16] H. Saßmannshausen, F. Merkt, J. Deiglmayr, *Phys. Rev. A* **2015**, *92*, 032505.
- [17] A. Osterwalder, F. Merkt, *Phys. Rev. Lett.* **1999**, *82*, 1831.
- [18] E. Amaldi, E. Segrè, *Il Nuovo Cimento* **1934**, *11*, 145.
- [19] E. Fermi, *Il Nuovo Cimento* **1934**, *11*, 157.
- [20] V. Kokoouline, O. Dulieu, R. Kosloff, F. Masnou-Seeuws, *J. Chem. Phys.* **1999**, *110*, 9865.
- [21] C. H. Greene, A. S. Dickinson, H. R. Sadeghpour, *Phys. Rev. Lett.* **2000**, *85*, 2458.
- [22] V. Bendkowsky, B. Butscher, J. Nipper, J. P. Shaffer, R. Löw, T. Pfau, *Nature* **2009**, *458*, 1005.
- [23] A. Omont, *J. Phys. (Paris)* **1977**, *38*, 1343.
- [24] K. Rupnik, U. Asaf, S.P. McGlynn, *J. Chem. Phys.* **1990**, *92*, 2303.
- [25] E. Karule, *Phys. Lett.* **1965**, *15*, 137.
- [26] D. W. Norcross, *J. Phys. B: At. Mol. Phys.* **1971**, *4*, 1458.
- [27] C. Bahrim, U. Thumm, I. I. Fabrikant, *J. Phys. B: At. Mol. Opt. Phys.* **2001**, *34*, L195.
- [28] C. Schwartz, *Phys. Rev.* **1961**, *124*, 1468.
- [29] F. Böttcher, A. Gaj, K. M. Westphal, M. Schlagmüller, K. S. Kleinbach, R. Löw, T. Cubel Liebisch, T. Pfau, S. Hofferberth, *arXiv:1510.01097*, **2015**.
- [30] D. A. Anderson, S. A. Miller, G. Raitel, *Phys. Rev. A* **2014**, *90*, 062518.
- [31] J. Stanojevic, R. Côté, D. Tong, S. M. Farooqi, E. E. Eyler, P. L. Gould, *Eur. Phys. J. D* **2006**, *40*, 3.
- [32] J. Stanojevic, R. Côté, D. Tong, E. E. Eyler, P. L. Gould, *Phys. Rev. A* **2008**, *78*, 052709.
- [33] K. R. Overstreet, A. Schwettmann, J. Tallant, J. P. Shaffer, *Phys. Rev. A* **2007**, *76*, 011403.
- [34] K. R. Overstreet, A. Schwettmann, J. Tallant, D. Booth, J. P. Shaffer, *Nat. Phys.* **2009**, *5*, 581.

Laser Ablation/Ionisation Mass Spectrometry: Sensitive and Quantitative Chemical Depth Profiling of Solid Materials

Andreas Riedo^{§a*}, Valentine Grimaudo^b, Pavel Moreno-García^b, Maike B. Neuland^a, Marek Tulej^a, Peter Broekmann^b and Peter Wurz^a

[§]SCS-Metrohm Award for best oral presentation in Analytical Sciences

Abstract: Direct quantitative and sensitive chemical analysis of solid materials with high spatial resolution, both in lateral and vertical direction is of high importance in various fields of analytical research, ranging from *in situ* space research to the semiconductor industry. Accurate knowledge of the chemical composition of solid materials allows a better understanding of physical and chemical processes that formed/alterd the material and allows *e.g.* to further improve these processes. So far, state-of-the-art techniques such as SIMS, LA-ICP-MS or GD-MS have been applied for chemical analyses in these fields of research. In this report we review the current measurement capability and the applicability of our Laser Ablation/Ionisation Mass Spectrometer (instrument name LMS) for the chemical analysis of solids with high spatial resolution. The most recent chemical analyses conducted on various solid materials, including *e.g.* alloys, fossils and meteorites are discussed.

Keywords: Chemical depth profiling · Chemical mapping of heterogeneous materials · High spatial resolution analysis · Laser ablation · Laser ionisation mass spectrometry

1. Introduction

Sensitive chemical analysis of solid materials with high spatial resolution in the micro- and nanometre regime is of considerable interest and importance in various fields of academic and industrial research. These include *e.g.* the chemical analysis of layered solar panels,^[1,2] the analysis of space-weathered samples,^[3] the investigations of contaminants embedded within electrodeposited Cu interconnects^[4,5] and extensive chemical analyses of corroded glass,^[6] ancient celadon^[7] or geological samples,^[8] among many others. In comparison to bulk analyses, measurement techniques with high spatial resolution enable detailed chemical insights into the sample material and provide better understanding of physical and chemical processes that may have fashioned or modified the analyte of interest.

Various sensitive and high-resolution measurement techniques available nowadays on the market, such as Auger Electron Spectroscopy (AES),^[9,10] X-ray Photoelectron Spectroscopy (XPS),^[9,11] Secondary Ion Mass Spectrometry (SIMS)^[5,9] and Secondary Neutron Mass Spectroscopy (SNMS),^[12] Glow Discharge Time-of-Flight Mass Spectrometry (GD-TOF-MS)^[1,9] or Laser Ablation Inductively Coupled Plasma Mass Spectrometry (LA-ICP-MS)^[2,6,9] are widely applied for the understanding of the above listed questions concerning the chemical composition of solid materials. Each analytical technique differs in its measurement capabilities and limitations, including *e.g.* its detection sensitivity (*e.g.* mass spectroscopic versus mass spectrometric), quantitative nature of conducted measurements (*e.g.* SIMS versus LA-ICP-MS), lateral profiling capabilities (*e.g.* SIMS versus GD-TOF-MS), vertical profiling capabilities (SIMS versus LA-ICP-MS), measurement speed acquisition (*e.g.* XPS versus GD-TOF-MS), time for data interpretation (GD-TOF-MS versus AES), or limitations concerning the suitable sample shape.^[9,12] Therefore, typically a combination of diverse measurement techniques is required to provide detailed insights into the sample material and hence, to answer the scientific questions of interest.

With advances in vacuum technology, improved high speed electronics (*e.g.* data acquisition system) and laser systems with significantly increased performance, Laser Ablation/Ionisation Mass Spectrometry (LIMS) has proved, in the last decade, to be a truly alternative measurement technique for the sensitive and quantitative chemical investigation of solid materials with high spatial resolution and figures of merit comparable to state-of-the-art measurement techniques, such as SIMS, LA-ICP-MS or GD-TOF-MS.^[4,7,13–16] The implementation of ultrafast pulsed laser systems used as ablation and ionisation source with pulse widths within the femtosecond regime and pulse to pulse energy stability better than the % level (*e.g.* CPA system, Clark-MXR Inc., USA) has allowed the measurement performance and capabilities of LIMS to be significantly increased.^[4,14,17] In comparison to laser systems providing longer pulses the application of a femtosecond laser ablation/ionisation source has various analytical advantages, including *e.g.* minimised elemental fractionation due to reduced thermal heating of the sample material (heat affected zone, HAZ)^[18] and the lack of interaction between the ejected plasma during the laser ablation process and the laser pulse.^[19,20] Another important advantage concerns the improved stoichiometry and ionisation efficiency of

*Correspondence: Dr. A. Riedo^a

E-mail: andreas.riedo@space.unibe.ch

^aPhysics Institute, Space Research and Planetary Sciences
University of Bern,

Sidlerstrasse 5, CH-3012 Bern, Switzerland

^bDepartment of Chemistry and Biochemistry
Interfacial Electrochemistry Group
University of Bern

Freiestrasse 3, CH-3012 Bern, Switzerland

the elements,^[14,17] which together with the ability of clean material ablation^[19–22] and high pulse-to-pulse reproducibility enable a laser ablation in a highly controlled manner.^[4,17]

So far, various LIMS systems have been designed and constructed specifically to investigate different scientific questions and for the application in variable environments, ranging from elemental mapping^[8,23] to depth profiling analyses,^[4,16] from laboratory^[7,8,12,14–16,24,25] instruments to instruments with the capability to operate on planetary objects.^[17,26–31] However, and to our best current knowledge, only the designs from the research groups of Huang,^[8,14,15,24] Cui *et al.*,^[16] and Wurz,^[4,13,17,23,32] have reached the measurement capabilities and performance comparable to the state-of-the-art measurement techniques for chemical analysis with high spatial resolution. All these systems consist of a TOF mass analyser, a sophisticated detector system and are equipped with a femtosecond laser ablation/ionisation source and differ only in their technical realisation. In the following the LIMS systems from Cui *et al.*^[16] and the Huang group^[8,14,15,24] are discussed only briefly. Readers should consult the listed references for further information. To introduce the reader in more detail to the LIMS measurement technique, the performance and principles of operation of the LIMS system developed in our group are discussed in more detail afterwards.

The LIMS system from the Huang group (MCP detector system in chevron configuration, dynamic range of about 6–7 orders of magnitude, lateral resolution of about 40 μm) is based on an orthogonal ion source design (the principal axis of the laser ablation/ionisation ion source is orthogonal to the principal ion optical axis of the mass spectrometer) and consists of a reflectron-type time-of-flight (TOF) mass spectrometer.^[8,14,15,24] In comparison to the other LIMS systems, inert buffer gas such as He or Ar is used for collisional cooling of energetic ions from the ablation process as well as charge reduction of multiple charged ions produced during the laser ablation process.^[15,33] The system has a detection sensitivity down to 30 ppb (g/g, Li) but due to contaminants within the buffer gas sensitivities for a few elements, *e.g.* C, N or O, rises to few hundreds of ppm.^[8,24] So far, the system has been used for chemical mapping of solids with high lateral resolution^[8] and no depth profiling studies were carried out, to the best of our knowledge. In the LIMS system from Cui *et al.* (MCP detector system in chevron configuration), laser ablation is realised by the laser hitting the sample at a 60° incident angle, instead of perpendicular incidence, which results in an elliptical ablation spot

and crater.^[16] Depending on the applied laser irradiance the dimension of the crater in one direction is about 5 μm , and shows an increased dimension in the other axis. An integrated ion funnel and a differential pumping system allow the ion source to be operated at pressures up to about 0.3 mbar. This latter LIMS system can be used for elemental imaging with a lateral resolution on the μm -scale but also for chemical depth profiling studies with a resolution of about 6 nm.^[8]

The LIMS system developed by the group of Wurz (instrument name LMS) was originally designed for *in situ* investigation of the chemical composition of solids on planetary objects, for a lander platform on-board ESA's BepiColombo space mission for the detailed exploration of Mercury's surface.^[26] Unfortunately, the lander platform was cancelled later on due to budgetary reasons but since its first design in 2003 LMS has been continuously further developed.^[4,13,17,32–42] Today, LMS represents the most powerful and versatile LIMS system ever designed for *in situ* space investigations and exhibits top performing figures of merit. The system has the capability to conduct quantitative measurements with high detection sensitivity (10 ppb, atomic fraction) and with a dynamic range of about eight orders of magnitude.^[17,37] It allows measurements of element isotopes with high accuracy,^[38] enables the elemental imaging of heterogeneous materials with micrometre resolution,^[23,32,35,36] and provides high vertical depth profiling capabilities with sub-nanometre resolution.^[4,13] The measurement capabilities of LMS for elemental imaging and depth profiling of solid materials are presented in more detail in section 3, where most recent and current measurements conducted on different sample materials, including the chemical mapping of an Allende meteorite sample, depth profiling of Si-supported Cu layers, chemical analysis of micrometre fossils embedded in an argonite matrix, and capabilities towards 3D elemental imaging of bronze-alloy samples are presented.

2. Experimental Setup

LMS is a reflectron-type time-of-flight (RTOF) mass spectrometer and was originally designed for *in situ* measurements on planetary objects. The principles of operation and technical scheme of LMS are briefly discussed in the following. Detailed information of the current setup can be found in recent publications.^[4,17,26,37]

Since parameters such as size, power consumption and mass are highly limited on a spacecraft the LMS mass analyser has the dimensions of only 160 mm \times 60 mm.

In the current setup an ultrafast pulse laser system ($\lambda = 775 \text{ nm}$, $\tau \sim 190 \text{ fs}$, repetition rate $\leq 1 \text{ kHz}$, intensity $\leq 1 \text{ mJ/pulse}$, CPA system, Clark-MXR Inc., USA) is used as ablation/ionisation source and is positioned outside the vacuum chamber.^[17] Laser pulses are guided towards the vacuum chamber by dielectric mirrors, pass the entrance window of the vacuum chamber and are focused through the mass analyser towards the sample surface using a lens system installed right on top of the mass analyser. The current lens system allows circular laser ablation generating a crater diameter in the range of about 10–15 μm .^[4] Samples are positioned about 1 mm away from the entrance of the LMS by using a high resolution xyz-micro translational stage with a position accuracy of about 2 μm . Only positively charged ions, generated during the ablation/ionisation process, can enter the ion optical system of LMS where they are subsequently accelerated, focussed and confined in the field free drift tube. The ions are finally reflected by the ion mirror towards the detector system by passing the field free drift tube a second time. In Fig. 1 the scheme and principles of operation of LMS are shown. Mass separation occurs along the ion trajectory because of the different velocity of different mass ions, having the same energy and the ions arrive at the detector system in sequence of their mass-to-charge ratio (m/z). A multi-readout multi-channel plate

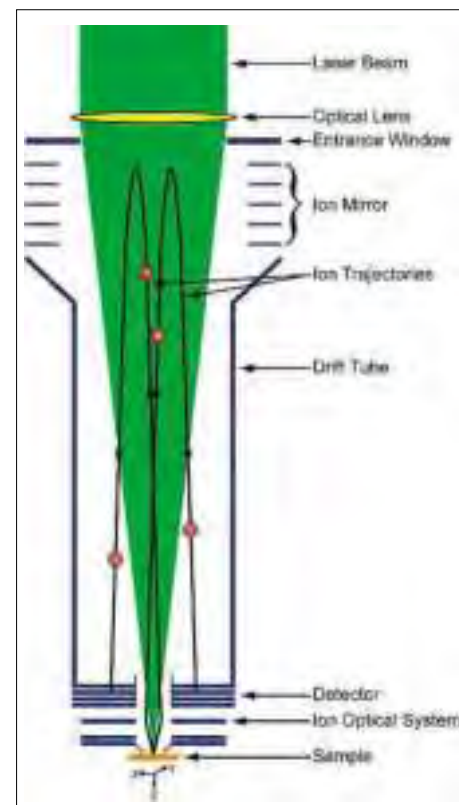


Fig. 1. Simplified schematic drawing of our LMS instrument showing briefly its principle of operation.

(MCP) detector system in chevron configuration (stack of 2 MCP plates) is used for the detection of the incoming ions. The special design of the detector system and the multi-readout of signals allow measurements to be conducted with a high dynamic range of about eight orders of magnitude and hence, allow signals from major to trace elements to be measured simultaneously. Two high speed ADC cards (8 bit, 2 channels each, up to 4 GS/s) are used to record the electrical signals generated by the MCP detector system.

The laser system (initiation, energy/pulse, number of single laser shots), the micro translational stage and the acquisition system are controlled fully remotely by a custom-made software package. The remote access to these units allows measurements with specific needs to be conducted, such as single spot measurements or rastering over a complete sample surface stepwise or continuously, including the acquisition of single laser shot mass spectra.^[4,13,17,23,32,36]

3. Measurement Examples and Discussions

The studies presented in the following are a set of examples of what has been achieved so far with the LMS. Additionally, current research on a wide variety of materials is being carried out to further demonstrate the capabilities and versatility of LMS.

3.1 Two-dimensional Elemental Imaging of an Allende Meteorite Fragment

Fig. 2 shows a composite microscope image of an Allende meteorite sample, a highly heterogeneous extra-terrestrial material, composed of matrix material and various chondrules and inclusions.^[23] The Allende sample was selected for mass spectrometric investigations using LMS to demonstrate the performance of the instrument for *in situ* chemical analysis of heterogeneous samples on planetary objects, such as planets, moons, and asteroids. The measurements demonstrate the capability of LMS to provide chemical maps of highly heterogeneous materials. Chemical analyses were conducted using two different laser systems, a nanosecond laser system ($\lambda = 266$ nm, $\tau \sim 3$ ns, pulse repetition rate of 20 Hz, ablation crater of ~ 20 μm in diameter, $\leq 1\text{GW}/\text{cm}^2$)^[23] and a femtosecond laser system ($\lambda = 775$ nm, $\tau \sim 190$ fs, pulse repetition rate of 1 kHz, ablation crater of ~ 12 μm in diameter, $\sim 30\text{TW}/\text{cm}^2$). Mass spectrometric measurements were conducted on 138 single surface positions with a horizontal and vertical spacing of 600 μm and 426 μm respectively, using

the nanosecond laser system. In this measurement campaign 500 single waveforms per analysed location were acquired, each an accumulation of 100 single laser shot mass spectra (50'000 single laser shots were applied). Detailed information on the measurements can be found in ref. [23]. Subsequently, a dense raster of 63×13 single surface positions (spacing of 50 μm) using the femtosecond laser system was conducted (black rectangle in Fig. 2). On each surface position 30 waveforms were acquired, each an accumulation of 2'000 single laser shot mass spectra (60'000 single laser shots were applied), and analysed.



Fig. 2. Composite microscope image of an Allende meteorite sample. The surface area surrounded by the black rectangle was investigated spot-wise in detail by LMS using the femtosecond laser system (see Fig. 3).

Fig. 3 presents the high resolution elemental mapping (preliminary analysis) of the selected Allende surface area (black frame) conducted using the femtosecond laser system. In panel a) the investigated surface area (Fig. 2) is magnified and several inclusions are visible; the three most distinct inclusions are marked in black (A1 and A2). Panels b) – d) illustrate the abundance distribution for Cr, S, and Fe, respectively. While within the areas A1 and A2 Fe and S are less abundant, a higher abundance of Cr was measured at the boundary of area A1. In general, mass spectrometric investi-

gations of Allende, so far, were conducted separately on specifically selected sample material, such as chondrules or CAIs (Ca-Al-rich inclusions) that were mechanically extracted by dedicated tools for the purpose of measurement.^[e.g.43,44] The elemental mapping using LMS, however, allows the chemical composition of Allende to be quantified without any dedicated sample preparation. Furthermore, by knowing the chemical composition of many surface positions on any geological sample, a mineralogical bulk analysis of the sample can be provided. Fig. 4 presents the mineralogical analysis resulting from the LMS measurements on Allende conducted with the nanosecond laser system. The measurements are in good agreement with the expected elemental composition of the meteorite. In this campaign most measurements represent mixtures of known minerals, which can be explained by the small size of mineral grains and the comparably larger size of the laser spot. Therefore, the collectivity of the 138 measurement points is in good agreement with the literature Allende bulk composition.^[23]

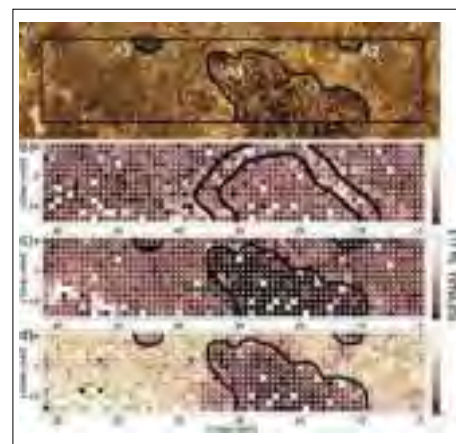


Fig. 3. Spot-wise chemical investigation (13×63 single surface positions) of a sample of Allende meteorite using LMS. a) Detail of rectangular section from Fig. 2, element map of b) Cr, c) S, and d) Fe.

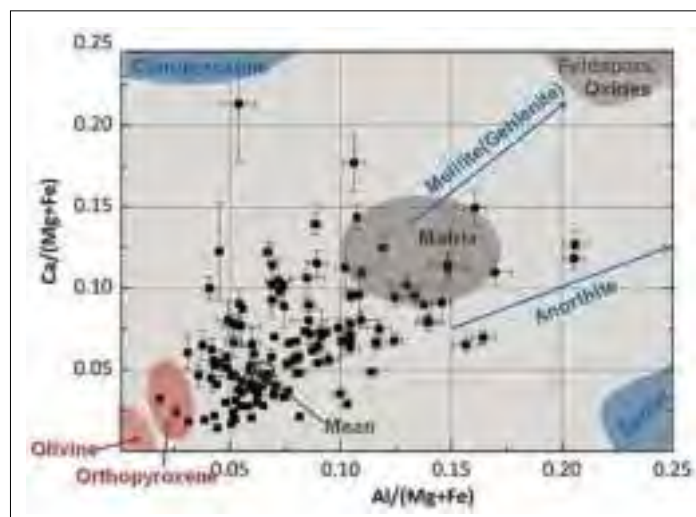


Fig. 4. Mineralogical analysis of Allende as a result of measurements conducted with the nanosecond laser system. Literature mean (in green) from Stracke *et al.*^[45] and McSween and Huss.^[46] Reprinted from Neuland *et al.*^[23] Copyright (2016), with permission from Elsevier.

3.2 Chemical Analysis with Sub-nanometre Vertical Resolution

Single laser shot mass spectrometric measurements were conducted on Cu samples with defined thickness (typically 10 μm) to investigate the correlation between laser pulse energies (laser irradiances) and resulting mean ablation rate, that is the ratio between layer thickness and number of applied single laser shots needed to perforate the layer.^[4] The Cu was electrochemically deposited on a Si-supported Cu seed layer under galvanostatic conditions in the presence of different plating additives (SPS, Imep, PEI, and PAG).^[4] The femtosecond laser system was used as ablation/ionisation source and laser pulses were focussed onto the sample surface with a diameter of about 14 μm . For the first time quantitative mass spectrometric depth profiles with a mean ablation rate at the sub-nanometre regime were achieved by applying the LIMS measurement technique (Fig. 5).

Fig. 6 demonstrates the quantitative depth profiling capability of LMS. It shows a depth profile section of a multi-layered Cu film (sample S4), where the abundances of the major contaminant C, N and O, mainly originating from the electroplating additives SPS and Imep, are monitored with sub-nanometre resolution.^[4] These additives are applied to improve the copper electrodeposition of interconnects. However, under specific electrochemical conditions they can form quasi-periodic embedded contamination layers inside the Cu film.^[4,5,47–50] The sharp increase and subsequent decrease of the C, N and O signals are in phase and exhibit anti-correlated intensity oscillations with the recorded Cu signal, as was expected from previous depth profiling experiments obtained with the SIMS technique. However, in contrast to traditional SIMS measurements, the LMS measurements neither showed attenuation nor broadening of these oscillations with increasing material erosion, indicating a smoother ablation procedure and negligible roughening effects at the crater bottom.

3.3 Micrometre-size Fossils Embedded in an Argonite Matrix

Fig. 7 shows microscope images of a geological sample with embedded fossils within an argonite matrix. Mass spectrometric measurements were conducted within the square M1 (200 \times 200 μm^2), marked in panel a) and enlarged in panel b). The area of interest was investigated spot-wise by a raster of 10 \times 10 surface positions with a spacing of 20 μm . From each single surface position 20 waveforms were recorded, each an accumulation of 2'000 single laser shot mass spectra (40'000 single laser shot mass spectra in total), which corresponds to a depth resolution of about

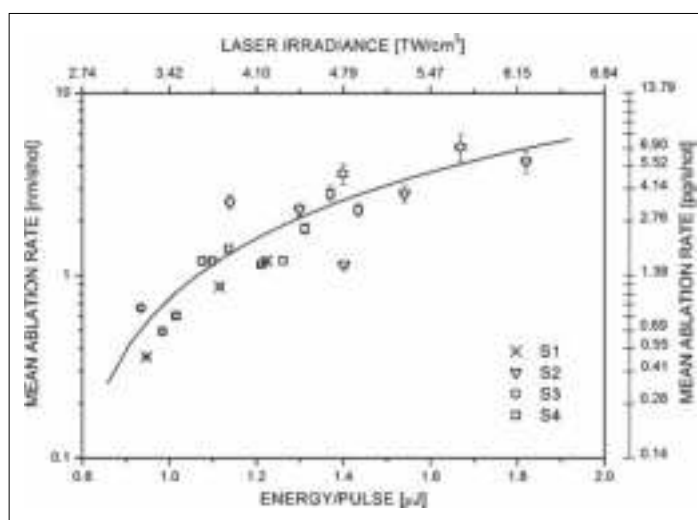


Fig. 5. Correlation between mean ablation rate and applied pulse energy (laser irradiance). For the first time quantitative mass spectrometric measurements with sub-nanometre resolution per single laser shot were realized using the LIMS measurement technique.^[4] Reprinted with permission from Grimaudo *et al.*^[4] Copyright (2016) American Chemical Society.

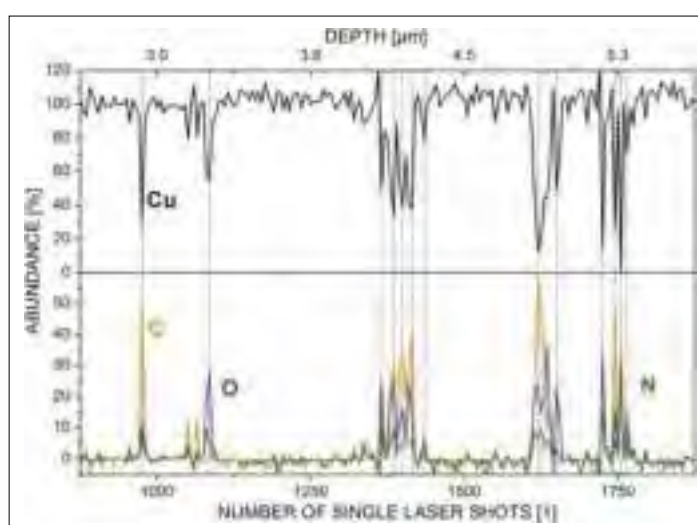


Fig. 6. Depth profiling section of the Cu film (sample S4) showing the anti-correlation between the major contaminants C, N, and O and Cu.^[4] Reprinted with permission from Grimaudo *et al.*^[4] Copyright (2016) American Chemical Society.

200 nm per waveform.^[32] In this campaign the depth resolution was electronically limited, by the accumulation of 2'000 single laser shot mass spectra to one waveform. Accumulation of a reduced number of mass spectra would increase the depth resolution. The femtosecond laser system was used as ablation/ionisation source and

a laser irradiance of about 5.5 TW/cm^2 was applied for this measurement campaign (laser ablation crater with a diameter of about 15 μm).

The current measurement performance of LMS, including the used depth profiling measurement protocol, allowed the localisation of fossil veins even within the sam-

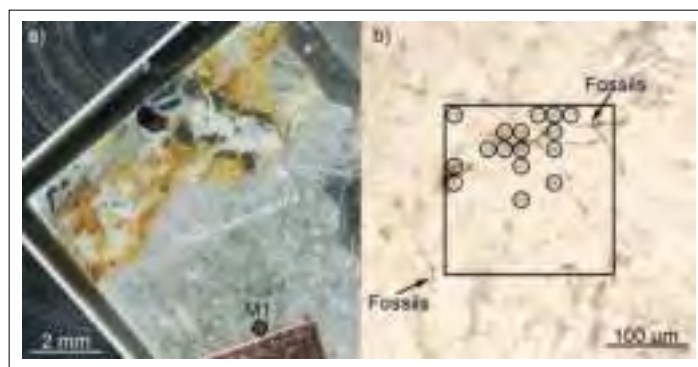


Fig. 7. Microscope image of a geological sample containing fossils of micrometre dimensions. The area marked by a black square (M1) in panel a) is shown enlarged in b). The black veins correspond to fossils embedded in the sample matrix. M1 was spot-wise investigated (100 single surface positions) using LMS. Image adapted with permission from Tulej *et al.*^[32] Copyright (2016) Mary Ann Liebert, Inc.

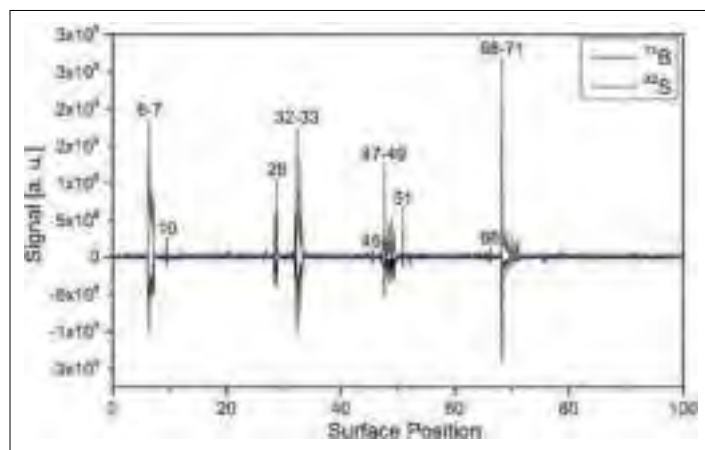


Fig. 8. The accumulation of all mass spectrometric measurements conducted on one surface position allowed to identify embedded fossils veins by monitoring bio-relevant elements, here B and S. Image adapted with permission from Tulej *et al.*^[32] Copyright (2016) Mary Ann Liebert, Inc.

ple matrix where optical microscopes find their limitations. In Fig. 8 the signals from bio-relevant elements, B and S, are presented for the different surface positions. For this analysis all waveforms from each single surface position were accumulated to build one single mass spectrum and special attention was devoted to the B and S signals. Surface positions 45 and 66 turned out to contain bio-relevant elements (see Fig. 8), but no fossil veins were visible on these positions in the microscope image. Furthermore, the depth profiling procedure with LMS allowed these fossil signatures to be localised in the matrix within the depth profiling accuracy.^[32]

3.4 Three-dimensional Elemental Imaging of Bronze Alloys

Alloys are used in various fields of research, ranging from applications within the microchip industry to technologies for energy conversion.^[51–55] Most recent measurements using the LMS instrument were conducted on Cu-Pb-Sn alloys containing different abundances of these three major elements. Mass spectrometric measurements with a lateral and vertical resolution within the micrometre and sub-micrometre regime, respectively, were conduct-

ed to provide a 3D chemical record of the elemental distribution of Cu, Sn, and Pb within the alloys. For these measurements the femtosecond laser system was used as ablation/ionisation source whereas laser pulses of a few TW/cm² were focussed onto a surface area of about 10–15 μm in diameter. The alloy surfaces were investigated by a 4 × 4 single-spot raster and up to 1'000 waveforms were recorded from each surface position, each an accumulation of 200 single laser shot mass spectra.^[56]

In Fig. 9 preliminary analyses of the chemical depth profile (the first 500 waveforms, top of profile corresponds to the sample surface) are presented showing the spatial distribution of the elements Pb, Sn and Cu at three different surface positions.^[56] While green indicates the expected elemental abundances according to the empirical formula (Cu₈₀Sn₁₀Pb₁₀ alloy), blue and red show decreased or enriched elemental abundances, respectively. The accumulation over all mass spectrometric information from one raster experiment resulted in mean elemental abundances of about (73 ± 11) wt%, (8 ± 4) wt% and (19 ± 10) wt%, respectively for Cu, Sn and Pb. The latest results illustrate the possibility of applying LMS to investigate not only

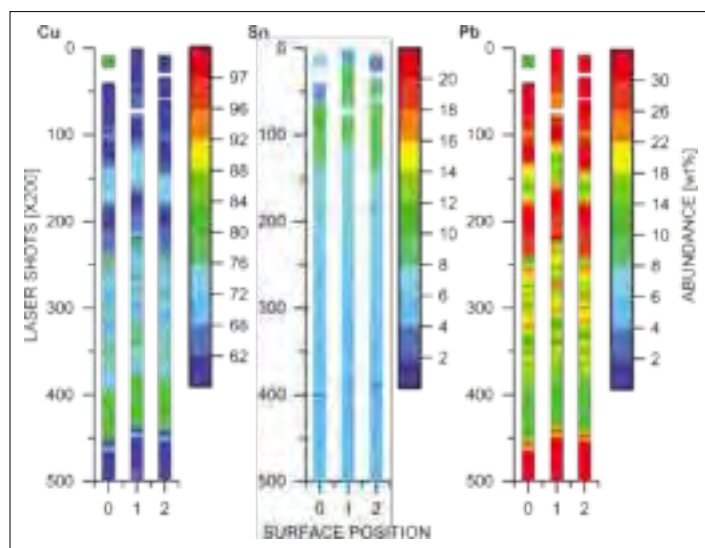


Fig. 9. Preliminary depth profiling studies of bronze alloys are shown. By averaging all individual mass spectrometric measurements the nominal abundances of Pb, Sn and Cu in wt% is derived. However, in certain applications the spatial distribution of incorporated elements are of high interest.

the elemental distribution at the surface of a material but also to get an insight into the homogeneity in all three dimensions giving evidence about the quality of the alloying material.^[56]

4. Conclusions

Chemical analysis with high spatial resolution in the micro- and nanometre regime is of high interest in various fields of research, where detailed chemical insights within the solid material are necessary to *e.g.* further improve production processes. So far, measurement techniques such as SIMS, LA-ICP-MS and GD-MS have been used to conduct measurements with high spatial resolution. However, with the advances in the last decades regarding laser systems, electronics, and vacuum technology, LIMS has emerged as a truly alternative direct measurement technique with measurement capabilities comparable to the state-of-the-art techniques. Nowadays LIMS instruments can conduct sensitive (ppb level) and quantitative mass spectrometric analyses of solid materials with a lateral resolution in the micrometre regime and a vertical resolution at the sub-nanometre level, both of considerable importance to provide a 3D chemical insight into the analyte of interest.

Acknowledgments

This work is supported by the Swiss National Science Foundation.

Received: January 15, 2016

- [1] J. Pisonero, N. Bordel, C. Gonzalez de Vega, B. Fernández, R. Pereiro, A. Sanz-Medel, *Anal. Bioanal. Chem.* **2013**, *405*, 5655.
- [2] A. Gutiérrez-González, C. González-Gago, J. Pisonero, N. Tibbetts, A. Menéndez, M. Vélez, N. Bordel, *J. Anal. At. Spectrom.* **2015**, *30*, 191.
- [3] T. Noguchi, T. Nakamura, M. Kimura, M. E. Zolensky, M. Tanaka, T. Hashimoto, M. Konno, A. Nakato, T. Ogami, A. Fujimura, M. Abe, T. Yada, T. Mukai, M. Ueno, T. Okada, K. Shirai, Y. Ishibashi, R. Okazaki, *Science* **2011**, *333*, 1121.
- [4] V. Grimaudo, P. Moreno-García, A. Riedo, M. B. Neuland, M. Tulej, P. Broekmann, P. Wurz, *Anal. Chem.* **2015**, *87*, 2037.
- [5] N. T. M. Hai, D. Lechner, F. Stricker, J. Furrer, P. Broekmann, *ChemElectroChem* **2015**, *2*, 664.
- [6] S. J. M. Van Malderen, J. T. Van Elteren, F. Vanhaecke, *Anal. Chem.* **2015**, *87*, 6125.
- [7] M. He, Y. Xiao, S. Zhang, R. Liu, W. Hang, B. Huang, *Appl. Surf. Sci.* **2015**, *351*, 624.
- [8] R. Huang, B. Zhang, D. Zou, W. Hang, J. He, B. Huang, *Anal. Chem.* **2011**, *83*, 1102.
- [9] J. S. Becker, 'Inorganic Mass Spectrometry - Principles and Applications', John Wiley & Sons Ltd., England, **2007**.
- [10] J. Pantoja-Enríquez, E. Gómez-Barojas, R. Silva-González, U. Pal, *Sol. Energy Mater. Sol. Cells* **2007**, *91*, 1392.
- [11] M. Duta, S. Mihaiu, C. Munteanu, M. Anastasescu, P. Osiceanu, A. Marin, S. Preda, M. Nicolescu, M. Modreanu, M. Zaharescu, M. Gartner, *Appl. Surf. Sci.* **2015**, *344*, 196.

- [12] P. Le Coustumer, P. Chapon, A. Tempez, Y. Popov, G. Thompson, I. Molchan, N. Trigoulet, P. Skeldon, A. Licciardello, N. Tuccitto, I. Delfanti, K. Fuhrer, M. Gonin, J. Whitby, M. Hohl, C. Tanner, N. Bordel Garcia, L. Lobo Revilla, J. Pisonero, R. Pereiro, C. Gonzalez Gago, A. Sanz Medel, M. Ganciu Petcu, A. Surmeian, C. Diplasu, A. Groza, N. Jakubowski, R. Dorka, S. Canulescu, J. Michler, P. Belenguer, T. Nelis, A. Zahri, P. Guillot, L. Thérèse, A. Littner, R. Vaux, J. Malherbe, F. Huneau, F. Stevie, H. François-Saint-Cyr, 'Analysis of thin and thick Films', in 'Mass Spectrometry Handbook', Ed. M.S. Lee, **2012**, John Wiley & Sons, Inc., Hoboken, NJ, USA.
- [13] A. Riedo, V. Grimaudo, P. Moreno-García, M. B. Neuland, M. Tulej, P. Wurz, P. Broekmann, *J. Anal. At. Spectrom.* **2015**, *30*, 2371.
- [14] B. Zhang, M. He, W. Hang, B. Huang, *Anal. Chem.* **2013**, *85*, 4507.
- [15] Q. Yu, R. Huang, L. Li, L. Lin, W. Hang, J. He, B. Huang, *Anal. Chem.* **2009**, *81*, 4343.
- [16] Y. Cui, J. F. Moore, S. Milasinovic, Y. Liu, R. J. Gordon, L. Hanley, *Rev. Sci. Instr.* **2012**, *83*, 093702.
- [17] A. Riedo, M. Neuland, S. Meyer, M. Tulej, P. Wurz, *J. Anal. At. Spectrom.* **2013**, *28*, 1256.
- [18] R. E. Russo, X. Mao, J. J. Gonzales, J. Yoo, *Spectroscopy* **2013**, *28*, 24.
- [19] R. Hergenröder, O. Samek, V. Hommes, *Mass Spectrom. Rev.* **2006**, *25*, 551.
- [20] X. Zeng, X. L. Mao, R. Greif, R. E. Russo, *Appl. Phys. A: Mater. Sci. Process.* **2005**, *80*, 237.
- [21] R. E. Russo, X. Mao, J. J. Gonzales, S. S. Mao, *Anal. At. Spectrom.* **2002**, *17*, 1072.
- [22] D. J. Hwang, H. Jeon, C. P. Grigoropoulos, J. Yoo, R. E. Russo, *App. Phys. Lett.* **2007**, *91*, 251118.
- [23] M. B. Neuland, S. Meyer, K. Mezger, A. Riedo, M. Tulej, P. Wurz, *Planet. Space Sci.* **2014**, *101*, 196.
- [24] R. Huang, Q. Yu, L. Li, Y. Lin, W. Hang, J. He, B. Huang, *Mass Spectrom. Rev.* **2011**, *30*, 1256.
- [25] W. Hang, *J. Anal. At. Spectrom.* **2005**, *20*, 301.
- [26] U. Rohner, J. A. Whitby, P. Wurz, *Meas. Sci. Technol.* **2003**, *14*, 2159.
- [27] W. B. Brinckerhoff, G. G. Managadze, R. W. McEntire, A. F. Cheng, W. J. Green, *Rev. Sci. Instr.* **2000**, *71*, 536.
- [28] W.B. Brinckerhoff, *Planet. Space. Sci.* **2005**, *53*, 817.
- [29] X. Li, W. B. Brinckerhoff, G.G. Managadze, D.E. Pugel, C.M. Corrigan, J.H. Doty, *Int. J. Mass Spectrom.* **2012**, 323 63.
- [30] W. B. Brinckerhoff, *Appl. Phys. A*, **2004**, *79*, 953.
- [31] G. G. Managadze, P. Wurz, R. Z. Sagdeev, A. E. Chumikov, M. Tulej, M. Yakovleva, N. G. Managadze, A. L. Bondarenko, *Sol. Sys. Res.* **2010**, *44*, 376.
- [32] M. Tulej, A. Neubeck, M. Ivarsson, A. Riedo, M. B. Neuland, S. Meyer, P. Wurz, *Astrobiol.* **2015**, *15*, 669.
- [33] Y. Lin, Q. Yu, R. Huang, W. Hang, J. He, B. Huang, *Spectrochim. Acta Part B* **2009**, *64*, 1204.
- [34] M. Tulej, M. Iakovleva, I. Leya, P. Wurz, *Anal. Bional. Chem.* **2011**, *399*, 2185.
- [35] A. Neubeck, M. Tulej, M. Ivarsson, C. Broman, A. Riedo, S. McMahon, P. Wurz, S. Bengtsson, *Int. J. Astrobiol.* **2016**, *15*, 133.
- [36] M. Tulej, A. Riedo, M. B. Neuland, S. Meyer, P. Wurz, N. Thomas, V. Grimaudo, P. Moreno-García, P. Broekmann, A. Neubeck, M. Ivarsson, *Geostand. Geoanal. Res.* **2014**, *38*, 441.
- [37] A. Riedo, A. Bieler, M. Neuland, M. Tulej, P. Wurz, *J. Mass Spectrom.* **2013**, *48*, 1.
- [38] A. Riedo, S. Meyer, B. Heredia, M. B. Neuland, A. Bieler, M. Tulej, I. Leya, M. Iakovleva, K. Mezger, P. Wurz, *Planet. Space Sci.* **2013**, *87*, 1.
- [39] M. Tulej, A. Riedo, M. Iakovleva, P. Wurz, *Int. J. Spec.* **2012**, *2012*, 234949-1.
- [40] A. Bieler, K. Altwegg, L. Hofer, A. Jäckel, A. Riedo, T. Sémon, P. Wurz, *J. Mass Spectrom.* **2011**, *46*, 1143.
- [41] A. Riedo, P. Wahlström, J. A. Scheer, P. Wurz, M. Tulej, *J. Appl. Phys.* **2010**, *108*, 114915-1.
- [42] P. Moreno-García, V. Grimaudo, A. Riedo, M. Tulej, P. Wurz, P. Broekmann, *Rapid Commun. Mass Spectrom.* **2016**, *30*, 1031.
- [43] Y. Liu, C. Chai, *Chem. Geol.* **1997**, *141*, 105.
- [44] R. M. Housley, E. H. Cirilin, 'On the alteration of Allende chondrules and the formation of matrix', in 'Chondrules and their origins (A85-26528 11-91)', Houston, TX, Lunar and Planetary Institute, **1983**, pp. 145-161.
- [45] A. Stracke, H. Palme, M. Gellissen, C. Münker, T. Kleine, K. Birbaum, D. Günther, B. Bourdon, J. Zipfel, *Geochim. Cosmochim. Acta* **2012**, *85*, 114.
- [46] H. Y. McSween Jr., G. R. Huss, 'Cosmochemistry', **2010**, Cambridge University Press.
- [47] N. T. M. Hai, K. W. Krämer, A. Fluegel, M. Arnold, D. Mayer, P. Broekmann, *Electrochim. Acta* **2012**, *83*, 367.
- [48] N. T. M. Hai, J. Odermatt, V. Grimaudo, K.W. Krämer, A. Fluegel, M. Arnold, D. Mayer, P. Broekmann, *J. Phys. Chem. C* **2012**, *116*, 6913.
- [49] K. Krischer, N. Mazouz, P. Grauel, *Angew. Chem. Int. Ed.* **2001**, *40*, 850.
- [50] P. Strasser, M. Eiswirth, M. T. M. Koper, *J. Electroanal. Chem.* **1999**, *478*, 50.
- [51] H.-A. Kuhn, I. Altenberger, A. Käufler, H. Hölzl, M. Fünfer, 'Properties of High Performance Alloys for Electromechanical Connectors (CH3)', in 'Copper Alloys – Early Applications and Current Performance – Enhancing Processes', Ed. L. Collini, InTech, **2012**.
- [52] G. Zangari, *Coatings* **2015**, *5*, 195.
- [53] C. Gütz, M. Selt, M. Bänziger, C. Bucher, C. Römelt, N. Hecken, F. Gallou, Tomás R. Galvão, S.R. Waldvogel, *Chem. Eur. J.* **2015**, *21*, 13878.
- [54] C. Edinger, S. R. Waldvogel, *Eur. J. Org. Chem.* **2014**, *2014*, 5144.
- [55] C. Edinger, V. Grimaudo, P. Broekmann, S. R. Waldvogel, *ChemElectroChem* **2014**, *1*, 1018.
- [56] V. Grimaudo, P. Moreno-García, A. Riedo, M. Tulej, P. Broekmann, P. Wurz, *Anal. Chem.*, to be submitted, **2016**.

Halogen Chemistry on Catalytic Surfaces

Maximilian Moser[§] and Javier Pérez-Ramírez*

[§]SCS-Metrohm Award for best oral presentation in Catalysis Science and Engineering

Abstract: Halogens are key building blocks for the manufacture of high-value products such as chemicals, plastics, and pharmaceuticals. The catalytic oxidation of HCl and HBr is an attractive route to recover chlorine and bromine in order to ensure the sustainability of the production processes. Very few materials withstand the high corrosiveness and the strong exothermicity of the reactions and among them RuO₂ and CeO₂-based catalysts have been successfully applied in HCl oxidation. The search for efficient systems for HBr oxidation was initiated by extrapolating the results of HCl oxidation based on the chemical similarity of these reactions. Interestingly, despite its inactivity in HCl oxidation, TiO₂ was found to be an outstanding HBr oxidation catalyst, which highlighted that the latter reaction is more complex than previously assumed. Herein, we discuss the results of recent comparative studies of HCl and HBr oxidation on both rutile-type (RuO₂, IrO₂, and TiO₂) and ceria-based catalysts using a combination of advanced experimental and theoretical methods to provide deeper molecular-level understanding of the reactions. This knowledge aids the design of the next-generation catalysts for halogen recycling.

Keywords: Ceria-zirconia · Hydrogen halides · Oxidation · Prompt gamma activation analysis · Rutile-type oxides.

Introduction

Halogens are widely applied as reactive intermediates in the synthesis of various commodities in the chemical, pharmaceutical, and plastics industry.^[1] However, about half of the halogens are reduced to undesired hydrogen halides and halide salts. The copious formation of HCl or HBr by-products is a serious challenge, since options to deal with this waste stream such as marketing or neutralization are unattractive.^[1] The recovery of Cl₂ and Br₂ from HCl and HBr has been recognized as the most appealing route in order to maintain an economically feasible and environmentally friendly process design. Amongst the available options, catalytic oxidation has been shown to be the most waste- and cost-efficient method to achieve this.^[1,2]

The study of HCl oxidation dates back to the 1860s, when Henry Deacon invent-

ed the process to recover chlorine for the Leblanc process.^[1a,b] The corrosiveness and the high exothermicity of the reaction was detrimental to the CuCl₂-based catalyst, which suffered from volatilization of its active phase. The Deacon process was eventually abandoned in the 1890s due to substitution of the Leblanc process by the Solvay process.^[1a,b] Still, various companies and researchers attempted throughout the 20th century to improve the Cu-based catalysts or to identify new systems.^[1a,b] At the turn of the millennium, RuO₂-based catalysts, developed independently by Sumitomo Chemicals and Bayer MaterialScience, were implemented as the new generation of highly active and stable HCl oxidation catalysts for chlorine recycling within the manufacture of polyurethanes and polycarbonates.^[1a] In the continuous search for more alternative catalysts, other metal oxides such as CeO₂, U₃O₈, and CuCrO₂, have been discovered.^[3] In particular, ceria has received considerable attention, which peaked in the formulation of a technical CeO₂/ZrO₂ catalyst with stable performance in pilot studies.^[4]

The development of an analogue catalytic HBr oxidation process was first attempted in the 1930s by George Hooker, who adopted the original Deacon concept.^[5] HBr oxidation has been investigated by different companies in the past decades, but the implementation was inhibited due to the difficulties of identifying stable catalysts and a safe process.^[2b] Research in bromine recovery was re-

vised when the increased production of unconventional natural gas prompted the potential use of Br₂ to functionalize the inert alkanes into alkyl bromides for further conversion into fuels and chemicals.^[1c,2a] The search for a cost-efficient bromine recovery process logically led to the investigation of HCl oxidation catalysts for HBr oxidation. CeO₂-based and rutile-type (*i.e.* RuO₂ and IrO₂) materials have been shown to catalyze HBr oxidation, corroborating the anticipated chemical similarities of both reactions.^[6] However, the unexpected activity of TiO₂ in HBr oxidation, despite its inactivity in HCl oxidation, underlined that the mechanism of HBr oxidation has features distinct from that of HCl oxidation.^[7] To close this gap in understanding, dedicated studies are needed to rationalize the relationship between the state of the surface and the apparent performance over both rutile-type and ceria-based catalysts in HBr oxidation.

In this article, we discuss the strategy for an integrated approach to halogen chemistry and present advanced methods, *i.e.* temporal analysis of products (TAP) and prompt gamma activation analysis (PGAA), as key techniques to experimentally analyze mechanistic aspects and the state of the catalyst surface under working conditions. We outline the interplay between the surface chemistry and the performance in HCl and HBr oxidation over rutile-type and ceria-based catalysts. We highlight the necessity to individually optimize the catalyst formulation for either HCl or HBr oxidation.

*Correspondence: Prof. Dr. J. Pérez-Ramírez
E-mail: jpr@chem.ethz.ch

Institute for Chemical and Bioengineering
Department of Chemical and Applied Biosciences
ETH Zurich
Vladimir-Prelog-Weg 1
CH-8093 Zurich

Integrated Approach to Halogen Chemistry

Throughout the research on HCl and HBr oxidation, the study of the surface chemistry under working conditions has been hampered by the corrosiveness of the reactants. Mechanistic studies mostly emphasized on *ex situ* characterization such as X-ray diffraction (XRD), X-ray photoelectron spectroscopy (XPS), and high-resolution transmission electron microscopy (HRTEM), as well as molecular modeling.^[8] Further, ultra-high vacuum (UHV) methods, such as the high-resolution core-level shift, enables the study of surface processes under reaction atmosphere over single RuO₂ crystals.^[9] However, to connect the molecular-level studies on model surfaces to the apparent performance of real-life catalysts the pressure and materials gaps have to be closed.^[10] For this purpose, an integrated approach was developed by combining different characterization techniques (Fig. 1a). The key methods of this strategy are theoretical studies using density functional theory (DFT), transient mechanistic studies using temporal analysis of products (TAP),^[11] and the quantification of the halogen uptake under working conditions with *operando* prompt gamma activation analysis (PGAA).^[4,8c,12]

TAP is a highly advanced technique to study mechanisms of experimentally demanding reactions over industrially relevant catalysts.^[10] Small amounts (10⁶ molecules) of the reactants are pulsed over the catalyst bed and are analyzed by quadrupole mass spectroscopy (QMS) as shown in Fig. 1b. The reactants can be pulsed individually, simultaneously, or in pump-probe fashion, *i.e.* with distinct time delay between individual reactant pulses. Key advantages of TAP comprise (i) a millisecond time resolution, (ii) the use of practical catalysts, (iii) excellent temperature control, and (iv) safe operation. These aspects

make TAP a unique technology to bridge the pressure and material gap between UHV and real-life catalytic conditions.^[10]

PGAA has been shown to be a direct and reliable method to determine the elemental composition of the catalysts under reaction conditions.^[4,8c,12] The working principle is based on radiative neutron capture, or (*n, γ*) reaction upon irradiation of the sample with cold neutrons (Fig. 1c). The nuclei capture the neutrons and promptly emit typically 2 to 4 gamma rays in a cascade before returning to the ground state. The gamma radiation is characteristic, *i.e.* the energy values of the gamma rays identify the nuclide, and their intensities are proportional to the number of atoms present in the analyzed volume. The sensitivity and the detection limit of PGAA differ from element to element, and depend on the partial gamma-ray production cross-section, the detector efficiency and the level of the baseline at the analytical line. The dynamic range of the method is limited by either the too low sensitivity, such as for oxygen, or by the too high counting rate that overloads the counting system, *e.g.* with iridium.^[13]

Surface Chemistry and Performance of Rutile-type Catalysts for Halogen Production

RuO₂-based materials are the current state-of-the-art catalysts for HCl oxidation and have received widespread attention amongst researchers, who aimed to understand the reaction mechanism and to lower the amount of precious ruthenium required in the catalyst composition.^[14] Besides RuO₂, also IrO₂ was discovered to be active in HCl oxidation.^[15] Both metal oxides comprise a dense rutile-type structure that inhibits the penetration of chlorine atoms into the subsurface layers. IrO₂ operates, however, at much higher temperature compared to RuO₂ due to its larger chlorine

evolution barrier. With respect to the catalyst scale up, both metal oxides can be dispersed in the form of small nano layers or clusters on TiO₂-rutile, which is due to lattice matching (RuO₂) or electronic effects (IrO₂). Owing to their robustness in HCl oxidation, both catalysts were considered potential candidates for a stable oxidation of HBr. In fact, the comparison of their activities in HCl and HBr oxidation revealed that they oxidize HBr at much lower temperature (Fig. 2a).^[6] The activity of TiO₂ for HBr oxidation^[7] was not expected due to the inactivity in HCl oxidation which led to the commonly accepted theory that TiO₂ cannot catalyze hydrogen halide oxidation due to its inability to adsorb and dissociate molecular oxygen.^[16]

In-depth studies were undertaken to assess and compare the rutile-type catalysts in HCl and HBr oxidation. Despite its stability in HCl oxidation, RuO₂ brominates in contrast to TiO₂, which led to changes in the crystallinity observed by HRTEM and supported by *ab initio* thermodynamics, suggesting that the replacement of lattice oxygen is more exothermic in RuO₂ than TiO₂, facilitating a strong bromination of the surface and subsurface (Fig. 2b).^[17]

To shed light on the reaction mechanism, the surface of TiO₂ was studied with XPS, which evidenced the formation of Ti³⁺ sites during the HBr oxidation;^[7] an indication of the formation of surface defects. Theoretical calculations on this defect formation ultimately proposed that the replacement of the bridge oxygen with a bromine atom is a self-doping mechanism that eventually enables the adsorption of molecular oxygen due to the smaller energetic barrier to transfer the electrons from the bromide to the oxygen (Fig. 2c).^[7] In contrast to that, the energetic barrier of the chlorine doped surface is too large to enable the activation of molecular oxygen on the surface.

DFT indicated that the reaction mech-

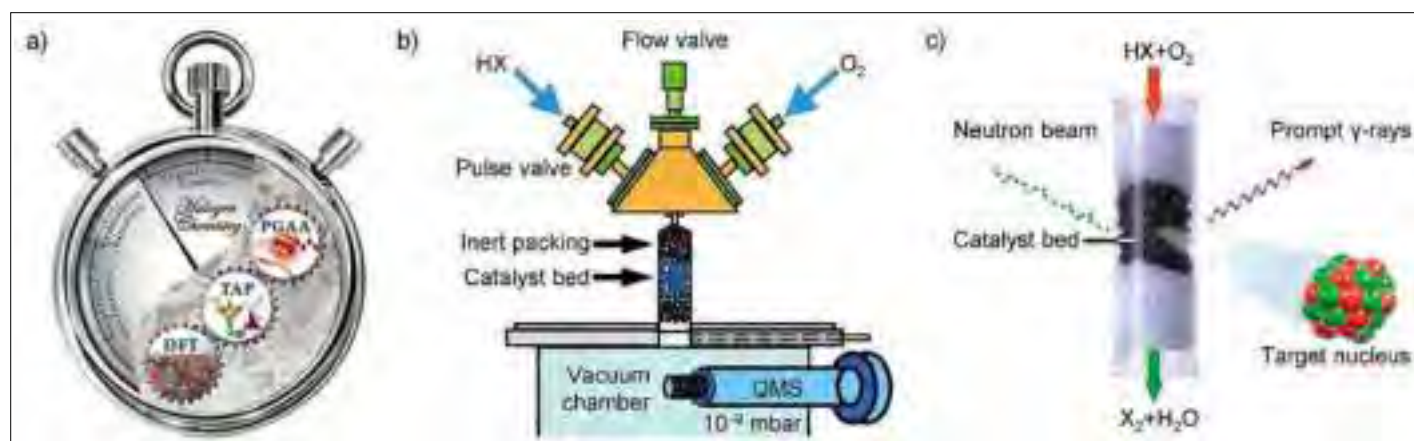


Fig. 1. The synchronization of advanced techniques bridges the pressure and materials gap between molecular studies and catalytic evaluation under working conditions (a). Transient mechanistic studies on real-life catalysts are conducted using TAP at millisecond time resolution (b). The uptake of halogens on the catalysts under working conditions is quantified using PGAA (c).

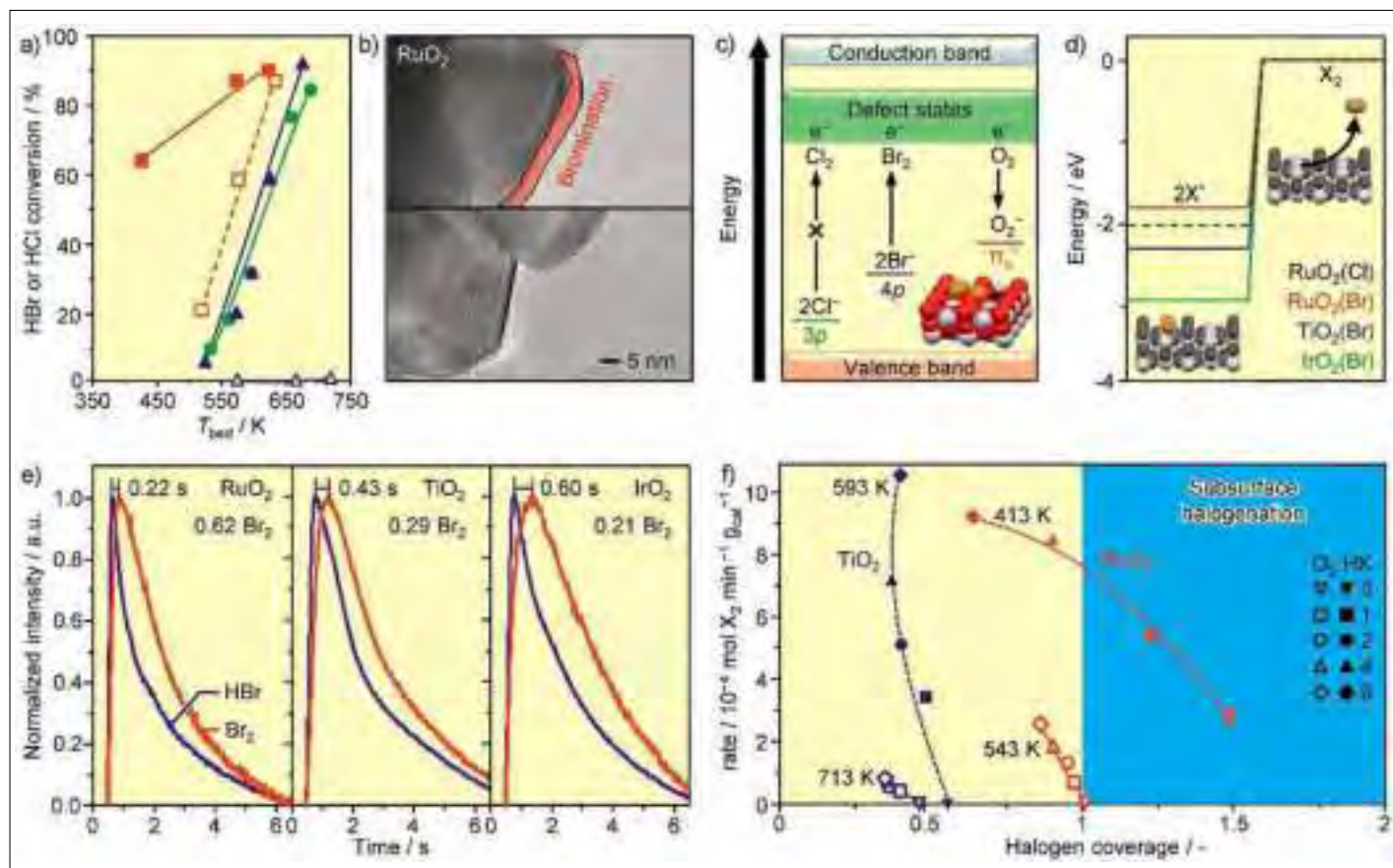


Fig. 2. Activity versus temperature for RuO_2 (red), IrO_2 (green) and TiO_2 (blue) in HCl (dashed line) and HBr (solid lines) oxidation (a). HRTEM micrographs of RuO_2 (b) treated in HBr (top) and HCl (bottom). Illustration of the band gap of the semiconductor TiO_2 (c). DFT calculation for the halogen evolution on halogenated rutile-type surfaces (d). Normalized HBr and Br_2 responses after simultaneous HBr and O_2 pulsing for rutile-type catalysts (e). Activity versus halogen coverage over TiO_2 and RuO_2 in HCl (open symbols) and HBr (solid symbols) oxidation at different oxygen partial pressures (f).

anism follows the same path with bromine evolution as the most energy demanding step (Fig. 2d).^[7] The calculations were corroborated by TAP studies, which showed that the bromine evolution from the surface is the slowest step. Furthermore, the time delay between the HBr and the Br_2 pulse increases in the order: $\text{RuO}_2 < \text{TiO}_2 < \text{IrO}_2$, which is in agreement with the increase in the calculated energy barriers (Fig. 2e)^[17] This also supports that bromine evolution is easier on TiO_2 than IrO_2 and explains that the apparently similar activity of both catalysts in HBr oxidation results from a compensation effect between the surface coverage and the reaction kinetics.^[7,17]

The quantitative determination of the halogen uptake under working conditions using PGAA demonstrates that RuO_2 suffers from extensive subsurface bromination, at low O_2 :HBr ratios and temperatures, which agrees with the microscopic studies and *ab initio* thermodynamics. TiO_2 exhibits inherently low halogen coverage (30–50%) at all conditions due to its unique defect-driven mechanism (Fig. 2f).^[17] In HCl oxidation, TiO_2 is inactive and the chlorination of the active RuO_2 is limited to the surface. Correlating the halogen uptake to the apparent performance ev-

idenced the completely different behavior of the rutile materials under working conditions, which points to the need for further optimization of the stability of RuO_2 if an application at low reaction temperatures is desired. One way could be the formulation of mixed Ru-Ti oxides to decrease the surface bromination and inhibit the penetration of bromine into the subsurface.

Stability and Activity of Mixed Ce-Zr Oxides in HCl and HBr Oxidation

Similar stability issues, as seen for RuO_2 in HBr oxidation, were already known from the case of CeO_2 in HCl oxidation.^[3a] CeO_2 suffers from subsurface chlorination under harsh reaction conditions as evidenced by *operando* PGAA, forming stable and inactive cerium chloride.^[12] In an attempt to stabilize the CeO_2 different support materials were investigated, which led to the discovery of the supported $\text{CeO}_2/\text{ZrO}_2$ systems.^[4] It was shown that the ZrO_2 support reduced the chlorine uptake and increased the activity of CeO_2 significantly, which was suggested to be linked to stabilization of CeO_2 nanostruc-

tures and the formation of Ce-Zr mixed oxides.^[4] The formation of mixed Ce-Zr oxides positively affects the performance in HCl oxidation due to improved redox properties and higher thermal stability.^[13] However, the impact of the catalyst's morphology, *i.e.* how well Ce and Zr have to be intermixed at an atomic or particle level to achieve these properties, was unknown.

To study the impact of zirconia on the performance of ceria, different ceria-zirconia mixed oxides were prepared exhibiting distinct morphologies that are either homogeneous or non-homogeneous mixed Ce-Zr oxides as shown by energy-dispersive X-ray spectroscopy (EDS) mapping (Fig. 3a). The catalytic performance in HCl oxidation of both materials is very comparable.^[13] However, in HBr oxidation distinctions became evident as the catalytic activity of non-homogeneous materials dropped more strongly within 40 h compared to the homogeneous mixed oxide (Fig. 3b).

PGAA studies on the different mixed Ce-Zr oxides indicated that CeO_2 -based catalysts are more prone to bromination than chlorination (Fig. 3c,d), which is detrimental to their stability. The chlorine uptake under different reaction conditions

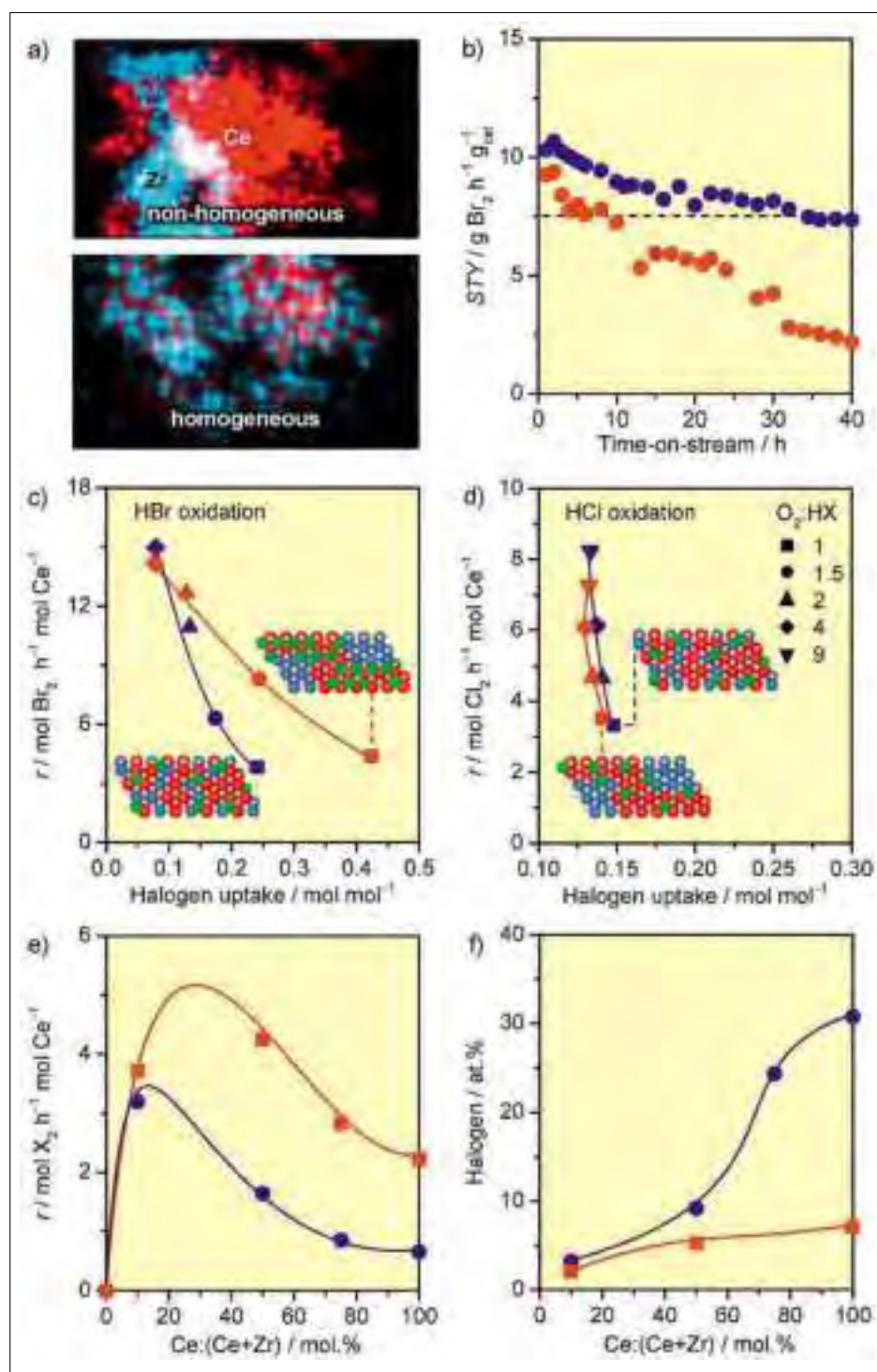


Fig. 3. EDS mapping of different mixed Ce-Zr oxides (a). Activity versus time on stream (b) and halogen uptake at different oxygen partial pressures (c,d) for homogeneous (blue) and non-homogeneous (red) mixed Ce-Zr oxides. Activity (e) and halogen content (f) versus Ce content of the homogeneous catalysts in HCl (red) and HBr (blue) oxidation.

was comparable over both materials and did not significantly change when reducing oxygen partial pressures. The bromine uptake of the non-homogeneous sample was up to 50% higher compared to the homogeneous counterpart (Fig. 3c).^[13] This indicates that the stability can be optimized by the atomic-level intermixing of the Ce and Zr phases apart from tuning the reaction conditions.

In order to assess the influence of the

composition of the homogeneous ceria-zirconia solid solution on the catalytic performance, CeO₂-ZrO₂ mixed oxides with variable Zr content were tested in HCl and HBr oxidation.^[13] The highest reaction rate over ceria-zirconia in both HBr and HCl oxidation was achieved with Zr contents between ca. 90 and 70 mol.% (Fig. 3e) at which point the halogen content reaches a minimum (Fig. 3f). For pure CeO₂ (*i.e.* 100 mol.%), the bromine content is about

four times higher than that of chlorine, due to the stronger tendency for bromination than chlorination. As the bromine content is higher than that of chlorine, the optimum for the HBr oxidation seems to have further shifted towards a higher Zr content (Fig. 3e), which underlines the distinctions in the optimal design of Ce-Zr catalysts for application in either HCl or HBr oxidation. In this respect, the Ce:Zr ratio is the key optimization parameter to tune the stability of the CeO₂-based catalysts.

Conclusions

The study of catalytic hydrogen halide oxidation is experimentally challenging, which presents significant demands for the mechanistic analysis and characterization of catalysts under working conditions. The combination of advanced techniques such as TAP and *operando* PGAA with theoretical calculations comprise an optimal approach to understand halogen chemistry on catalytic materials. This strategy enabled the rationalization of the exceptional activity of TiO₂ and the stability issues of RuO₂- and CeO₂-based catalysts in HBr oxidation. The comparison between HBr and HCl oxidation indicated that the catalyst design criteria applied in HCl oxidation cannot be directly extrapolated to the recycling of Br₂. Thus, catalyst design should be tailored for each reaction. The investigation showed that the halogen coverage under working conditions is the best parameter to assess the catalytic performance, which also highlights the significance of PGAA for this research. The surface halogenation can be tuned by optimizing the reaction conditions or the catalyst formulation which provides the foundation for future work on developing more stable and active catalysts not only for halogen recovery, but also for other halogen-based reactions such as the oxyhalogenation of hydrocarbons.

Acknowledgements

The Swiss National Science Foundation (SNF project number 200021-156107) and the European Union's 7th Framework Programme (NMI3-II grant number 283883) are thanked for financial support. Dr. Detre Teschner and Prof. Núria López are thanked for the long-standing and fruitful collaboration on the halogen field.

Received: December 18, 2016

- [1] J. Pérez-Ramírez, C. Mondelli, T. Schmidt, O. F.-K. Schlüter, A. Wolf, L. Mleczko, T. Dreier, *Energy Environ. Sci.* **2011**, *4*, 4786; b) C. Mondelli, A. P. Amrute, M. Moser, T. Schmidt, J. Pérez-Ramírez, *Chimia* **2012**, *9*, 66; c) E. McFarland, *Science* **2012**, *338*, 340.
[2] a) G. A. Olah, B. Gupta, M. Farina, J. D. Felberg, W. M. Ip, A. Husain, R. Karpeles,

- K. Lammertsma, A. K. Melhotra, N. J. Trivedi, *J. Am. Chem. Soc.* **1985**, *107*, 7097; b) P. F. Schubert, R. D. Beatty, S. Mahajan, 'Catalytic Bromine Recovery from HBr Waste', *Environmental Catalysis*, American Chemical Society, Washington DC, **1994**, p. 405.
- [3] a) A. P. Amrute, C. Mondelli, M. Moser, G. Novell-Leruth, N. López, D. Rosenthal, R. Farra, M. E. Schuster, D. Teschner, T. Schmidt, J. Pérez-Ramírez, *J. Catal.* **2012**, *286*, 287; b) A. P. Amrute, F. Krumeich, C. Mondelli, J. Pérez-Ramírez, *Chem. Sci.* **2013**, *4*, 2209; c) A. P. Amrute, G. O. Larrazábal, C. Mondelli, J. Pérez-Ramírez, *Angew. Chem., Int. Ed.* **2013**, *3*, 657.
- [4] M. Moser, C. Mondelli, T. Schmidt, F. Girgsdies, M. E. Schuster, R. Farra, L. Szentmiklósi, D. Teschner, J. Pérez-Ramírez, *Appl. Catal. B* **2013**, *132–133*, 123.
- [5] G. W. Hooker, US Patent 2163877, **1939**.
- [6] M. Moser, L. Rodríguez-García, A. P. Amrute, J. Pérez-Ramírez, *ChemCatChem* **2013**, *5*, 3520.
- [7] M. Moser, I. Czekaj, N. López, J. Pérez-Ramírez, *Angew. Chem., Int. Ed.* **2014**, *53*, 8628.
- [8] a) N. López, J. Gómez-Segura, R. P. Marín, J. Pérez-Ramírez, *J. Catal.* **2008**, *255*, 29; b) D. Teschner, R. Farra, L.-D. Yao, R. Schlögl, H. Soerijanto, R. Schomäcker, T. Schmidt, L. Szentmiklósi, A. P. Amrute, C. Mondelli, J. Pérez-Ramírez, G. Novell-Leruth, N. López, *J. Catal.* **2012**, *285*, 273; c) D. Teschner, G. Novell-Leruth, R. Farra, A. Knop-Gericke, R. Schlögl, L. Szentmiklósi, M. G. Hevia, H. Soerijanto, R. Schomäcker, J. Pérez-Ramírez, N. López, *Nat. Chem.* **2012**, *4*, 739.
- [9] a) D. Crihan, M. Knapp, S. Zweidinger, E. Lundgren, C. J. Weststrate, J. N. Andersen, A. P. Seitsonen, H. Over, *Angew. Chem., Int. Ed.* **2008**, *47*, 2131; b) S. Zweidinger, D. Crihan, M. Knapp, J. P. Hofmann, A. P. Seitsonen, C. J. Weststrate, E. Lundgren, J. N. Andersen, H. Over, *J. Phys. Chem. C* **2008**, *112*, 9966.
- [10] J. Pérez-Ramírez, E. V. Kondratenko, *Catal. Today* **2007**, *121*, 160.
- [11] a) M. A. G. Hevia, A. P. Amrute, T. Schmidt, J. Pérez-Ramírez, *J. Catal.* **2010**, *276*, 141; b) A. P. Amrute, C. Mondelli, M. A. G. Hevia, J. Pérez-Ramírez, *J. Phys. Chem. C* **2011**, *115*, 1056; c) A. P. Amrute, C. Mondelli, M. A. G. Hevia, J. Pérez-Ramírez, *ACS Catal.* **2011**, *1*, 583.
- [12] R. Farra, M. García-Melchor, M. Eichelbaum, M. Hashagen, W. Frandsen, J. Allan, F. Girgsdies, L. Szentmiklósi, N. López, D. Teschner, *ACS Catal.* **2013**, *3*, 2256.
- [13] M. Moser, G. Vilé, S. Colussi, F. Krumeich, D. Teschner, L. Szentmiklósi, A. Trovarelli, J. Pérez-Ramírez, *J. Catal.* **2015**, *331*, 128.
- [14] a) K. Seki, *Catal. Surv. Asia* **2010**, *14*, 168; b) C. Mondelli, A. P. Amrute, F. Krumeich, T. Schmidt, J. Pérez-Ramírez, *ChemCatChem* **2011**, *3*, 657.
- [15] M. Moser, C. Mondelli, A. P. Amrute, A. Tazawa, D. Teschner, M. Schuster, A. Klein-Hoffman, N. López, T. Schmidt, T. J. Pérez-Ramírez, *ACS Catal.* **2013**, *3*, 2813.
- [16] A. Toftelund, I. C. Man, H. A. Hansen, F. Abild-Pedersen, T. Bligaard, J. Rossmeisl, F. Studt, *ChemCatChem* **2012**, *4*, 1856.
- [17] M. Moser, V. Paunović, Z. Guo, L. Szentmiklósi, M. G. Hevia, M. Higham, N. López, D. Teschner, J. Pérez-Ramírez, *Chem. Sci.* **2016**, doi:10.1039/C5SC04247J.

PH₃ as a Phosphorus Source for Phosphinidene–Carbene Adducts and Phosphinidene–Transition Metal Complexes.

Mark Bispinghoff^{§*} and Hansjörg Grützmacher

[§]SCS-Metrohm Award for best oral presentation in Inorganic and Coordination Chemistry

Abstract: The parent phosphinidene–carbene adduct NHC=PH is a versatile synthon in main group chemistry and can act as an electronically flexible ligand for transition metals. Previously, it could only be synthesized with sterically demanding *N*-aryl substituents. This paper describes simple methods for the synthesis of NHC=PH adducts with varying steric demand from elemental phosphorus or easily accessible phosphorus sources. Furthermore, the reactivity of NHCs towards PH₃ was investigated. It was shown how a NHC inserts into the P–H bond of PH₃, which opens up a route to NHC=PH adducts from an imidazolium salt and PH₃. The adducts were used in the simple syntheses of bis(phosphinidene) mercury(II) and group 6 pentacarbonyl parent phosphinidene complexes. Their electronic and structural properties were investigated to elucidate the influence of the NHC on the phosphinidene and identify possible applications.

Keywords: Carbene insertion · N-Heterocyclic carbenes · Phosphine gas PH₃ · Phosphinidene complexes · Transition metal complexes

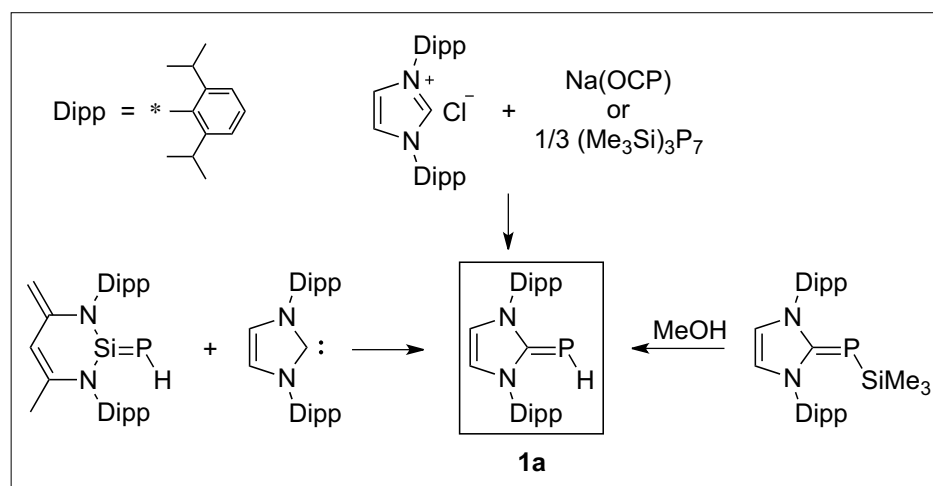
1. Introduction

Phosphinidenes are a highly reactive class of low-coordinate main group compounds, which easily oligomerize to cyclophosphanes.^[1] Free phosphinidenes have eluded isolation so far. However, they can be stabilized in the presence of Lewis bases or in the coordination sphere of a metal.^[2] Since their first preparation, *N*-heterocyclic carbenes (NHC) have been used for the stabilization of numerous main group species,^[3] including substituted phosphinidenes PR.^[4] Recently, the NHC-stabilized parent phosphinidene NHC=PH has been isolated using three different synthetic protocols (Scheme 1).^[5–7]

The parent phosphinidene–carbene adduct ^{Dipp}NHC=PH **1a** (^{Dipp}NHC = bis(2,6-diisopropylphenyl)imidazol-2-ylidene) can be prepared from a phosphasilene and the corresponding carbene by H–P transfer.^[5] It is also accessible from sodium phosphoethynolate, Na(OCP) or the substituted heptaphosphide (Me₃Si)₃P₇ and the corresponding imidazolium salt.^[6] Furthermore, it can be obtained by methanolysis of ^{Dipp}NHC=PSiMe₃.^[7]

The adduct **1a** has been used for the synthesis of carbene-supported P₃ and

PA₃P cations and radicals.^[6] The reaction of **1a** with chlorophosphanes in presence of DABCO gives rise to NHC-substituted chlorodiphosphanes ^{Dipp}NHC=P–PClR and their cationic derivatives, [^{Dipp}NHC=P–PR]⁺, which depending on the steric bulk of their substituents, can be isolated in monomeric or dimeric form.^[8] Bertrand and co-workers have isolated the carbene-stabilized parent phosphonium cation [NHC–PH₂]⁺ by treating a NHC=PH adduct featuring very bulky *N*-substituents with trifluorosulfonic acid.^[9] These results indi-



Scheme 1. Several routes to parent phosphinidene–carbene adducts are described in literature.^[5–7] However, they are limited to the use of the sterically demanding ^{Dipp}NHC.

*Correspondence: M. Bispinghoff
Laboratory of Inorganic Chemistry
ETH Zürich
Vladimir-Prelog-Weg 1
CH-8093 Zürich
E-mail: bispinghoff@inorg.chem.ethz.ch

cate that NHC=PH adducts can be used as versatile synthons for the preparation of a variety of organophosphorus compounds.

Furthermore, NHC=PH adducts can act as versatile one- or two-electron ligands in transition metal complexes. Upon reaction with metal halogenide precursors, the carbene-stabilized phosphinidene unit NHC=P can bind covalently to metal centers and thus act as a one-electron ligand. By this method, the ruthenium and rhodium phosphinidene complexes [(DippNHC=P)RuClL] (L = η^6 -*p*-cymene) and [(DippNHC=P)RhClL] (L = η^5 -C₅Me₅) were prepared from DippNHC=PSiMe₃ and the corresponding dichloride precursors.^[7]

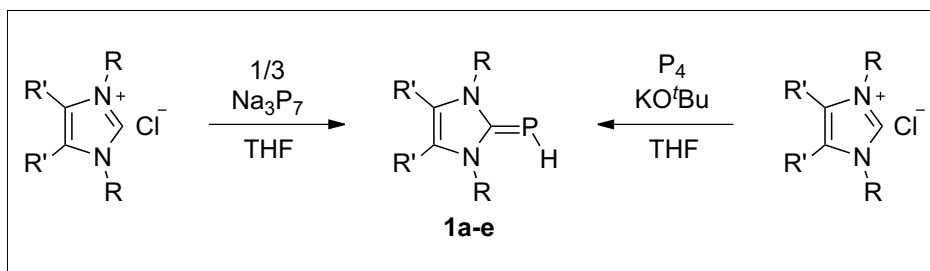
The phosphorus lone pair can also coordinate metal centers in a dative fashion, so that the NHC=PH unit acts as a two-electron ligand. Bertrand and co-workers have reacted a NHC=PH adduct with Fe₂(CO)₉, yielding the iron complex [(NHC=PH)Fe(CO)₄], in which the geometry around the phosphorus atom is trigonal pyramidal. Even though the natural bond analysis (NBO) analysis of the complex revealed a second lone pair on the P center, addition of excess Fe₂(CO)₉ did not lead to further coordination. This was assumed to be due to steric hindrance caused by the bulky Fe complex in conjugation with the very bulky NHC. Indeed, the second lone pair is accessible. If two equivalents of the linear gold complex [AuCl(tht)] (tht = tetrahydrothiophene) are added to the NHC=PH adduct, the bis-metal complex [(NHC=PH)(AuCl)₂] is formed.^[9]

In this article, we review our work on versatile, direct routes to parent phosphinidene-NHC adducts and their use as transition metal ligands. Furthermore, we report on the synthesis and characterization of NHC=PH group 6 pentacarbonyl complexes.

2. Results and Discussion

The synthetic routes to NHC=PH adducts described above are limited to the use of NHCs with sterically demanding *N*-aryl substituents. Exposure of Na(OCP) or (Me₃Si)₃P₇ to *N*-alkylated imidazolium salts (e.g. 1,3-dimethylimidazolium chloride or 1,3-diisopropylimidazolium chloride) did not lead to NHC=PH adducts. As the large steric bulk of the *N*-aryl substituents can lead to steric hindrance of some reactions, we were interested in finding a more versatile access to NHC=PH adducts.

We have thus investigated different phosphorus sources and have shown that the NHC=PH adducts **1a-e** with *N*-substituents of varying steric bulk can be prepared from sodium heptaphosphide Na₃P₇ and even from elemental phosphorus, P₄ (Scheme 2).^[10] Even though these



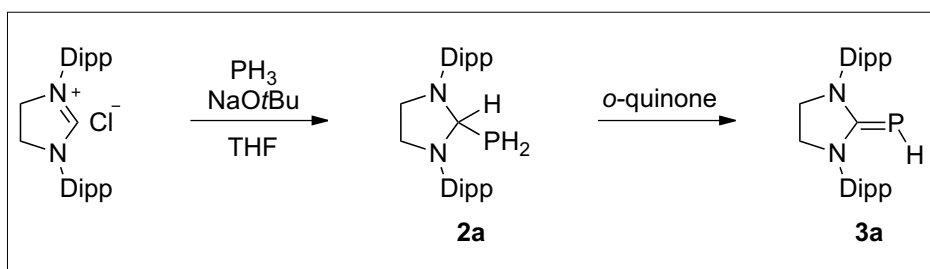
Scheme 2. NHC=PH adducts **1a-e** with NHCs of varying steric bulk are easily accessible from Na₃P₇ or P₄ and KOtBu. a: R = Dipp, R' = H, b: R = Mes, R' = H, c: R = *i*Pr, R' = H, d: R = Me, R' = H, e: R = Me, R' = Me.^[10]

phosphorus sources are easily accessible, they suffer from rather poor atom efficiency, as only one (in case of P₄) or three (in case of Na₃P₇) phosphorus atoms are incorporated into the NHC=PH adduct, whereas the others form bis(carbene) stabilized P(I) cations or insoluble polyphosphides.

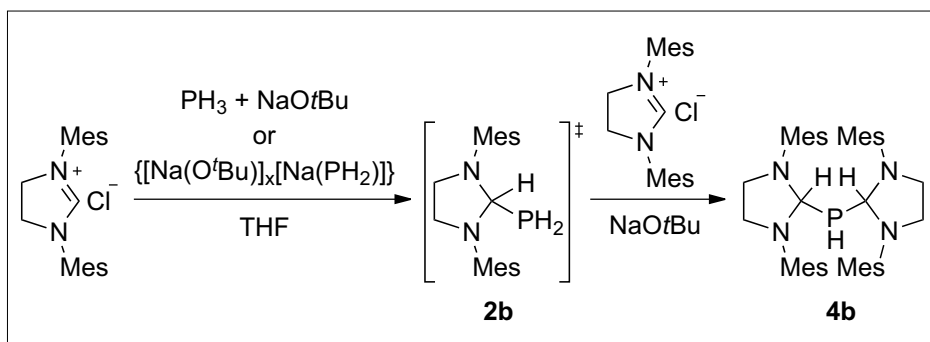
To find a more atom efficient route, we envisioned the use of a mononuclear phosphorus source. Monophosphine (PH₃) has been employed as a versatile precursor to organophosphorus compounds.^[11] Despite its limited usability in laboratories due to its high toxicity, it is considered a cheap and rather easy to handle phosphorus source industrially. Even though the reactivity of NHCs towards main group compounds has been studied extensively, their reactivity towards PH₃ remained unknown. We have shown that the saturated analogue of **1a**, DippNHC*=PH **3a** (DippNHC* =

1,3-bis(2,6-diisopropylphenyl)imidazolin-2-ylidene) can be synthesized from the corresponding imidazolium salt and PH₃ (Scheme 3). The *in situ* generated NHC inserts into the P-H bond of PH₃, giving rise to the phosphanyl-imidazolidine [DippNHC*-H]-[PH₂] **2**. This can subsequently be dehydrogenated with an *ortho*-quinone to the phosphinidene **3a**.^[12]

This reaction is highly sensitive to the electronic properties of the NHC. Whereas the saturated DippNHC* reacts readily with PH₃, the unsaturated analogue DippNHC does not show any reaction. Furthermore, it is also sensitive to the steric properties of the NHC. If the related *N*-mesityl substituted MesNHC* is exposed to PH₃, the bis(imidazolidine) phosphanyl species [MesNHC*-H]₂-[PH] (**4b**) is formed selectively (Scheme 4). The ³¹P-NMR spectrum exhibits a doublet of triplets at δ =



Scheme 3. The *in situ* generated carbene inserts into the P-H bond of PH₃, giving rise to a phosphanyl-imidazolidine **2a**, which can be subsequently dehydrogenated to the NHC=PH adduct **3a**.^[12]



Scheme 4. If the mesityl-substituted imidazolium salt is used instead of the Dipp-substituted, the phosphanyl-imidazolidine **2b** reacts further to the bis(imidazolidine) phosphanyl **4b**, which cannot be dehydrogenated.

–40.9 ppm ($^1J_{\text{PH}} = 203$ Hz, $^3J_{\text{PH}} = 18$ Hz). As opposed to **2a**, which is easily dehydrogenated to **3a**, **4b** is stable against dehydrogenation.

We have shown previously that **2a** can be obtained by either exposing the *in situ* generated $^{\text{Dipp}}\text{NHC}^*$ to PH_3 or by the reaction between the imidazolium salt [$^{\text{Dipp}}\text{NHC}^*\text{-H}$]-[Cl] and the sodium *tert*-butoxide/sodium dihydrogenphosphide aggregate $\{[\text{Na}(\text{O}^t\text{Bu})]_x[\text{Na}(\text{PH}_2)]\}$ ($x \approx 2.5$).^[12] In order to investigate the mechanism of the formation of **4b**, we monitored the reaction of [$^{\text{Mes}}\text{NHC}^*\text{-H}$]-[Cl] with the $\text{Na}(\text{PH}_2)$ aggregate by ^{31}P -NMR spectroscopy. After 15 min, the spectrum exhibited two sets of signals in an approximately 1:1 intensity ratio. One corresponded to **4b**, the other one, a triplet of doublets at $\delta = -144.1$ ppm ($^3J_{\text{PH}} = 186$ Hz, $^1J_{\text{PH}} = 18$ Hz), can be attributed to the related phosphanyl-imidazolidine [$^{\text{Mes}}\text{NHC}^*\text{-H}$]-[PH_2] **2b**. Over the course of 24 h, the mixture was converted quantitatively to the bis(imidazolidine) phosphanyl species **4b**. This suggests that the formation of **4b** from PH_3 or the $\text{Na}(\text{PH}_2)$ aggregate proceeds *via* the formation of the phosphanyl-imidazolidine **2b**, which then reacts further with a second equivalent of [$^{\text{Mes}}\text{NHC}^*\text{-H}$]-[Cl] under deprotonation with excess $\text{Na}(\text{O}^t\text{Bu})$ to **4b** (Scheme 4). It is noted that the exposure of **2a** to $\text{Na}(\text{O}^t\text{Bu})$ does not result in any reaction, which can be accounted for by the larger steric bulk of the *N*-substituents.

Single crystal X-ray diffraction was used to unambiguously identify the bis(imidazolidine) **4b** (Fig. 1). Its bond distances and angles are similar to those of the imidazolidine **2a** (Table 1). The C1–P1 as well as the N1–C1 and N2–C1 bond distances of **4b** do not differ significantly from those of **2a**. The C2–C3 distance in **4b** (1.487(5) Å) is shorter than in **2a** (1.526(2) Å) and the N1–C1–N2 bond angle (102.2(2) °) larger than in **2a** (101.5(1) °).

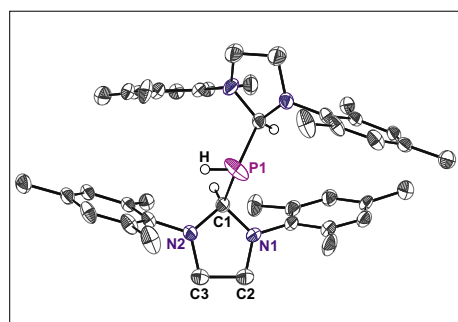
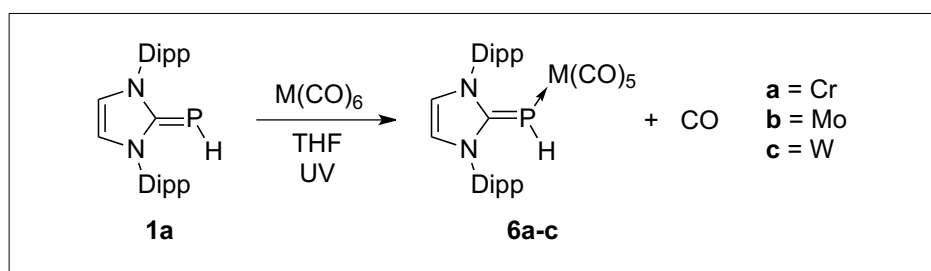


Fig. 1. ORTEP plot of the bis(imidazolidine) phosphanyl **4b**. Hydrogen atoms apart from the phosphorus and the carbene–C bound hydrogen atoms have been omitted for clarity. Thermal ellipsoids are shown at 50% probability.



Scheme 5. Group 6 pentacarbonyl complexes of the $\text{NHC}=\text{PH}$ unit are easily accessible through CO replacement. Upon exposure of mixtures of **1a** and metal hexacarbonyls to UV radiation, the complexes **6a–c** are formed.

We have recently reported the reaction between the adducts $^{\text{Dipp}}\text{NHC}=\text{PH}$ and $^{\text{Dipp}}\text{NHC}^*=\text{PH}$ and mercury dichloride in presence of a strong base to obtain the bis(carbene-phosphinidene)mercury(II) complexes [$(^{\text{Dipp}}\text{NHC}=\text{P})_2\text{Hg}$] (**5a**) and [$(^{\text{Dipp}}\text{NHC}^*=\text{P})_2\text{Hg}$] (**5b**), in which the mercury centers are coordinated linearly by two phosphinidene–carbene units. A comparison of the structural properties of the adducts **1a** and **3a** and the mercury complexes **5a** and **5b** revealed that the different electronic properties of the unsaturated versus saturated NHCs are not reflected in the structures.^[12]

In addition to these findings, here we describe group 6 pentacarbonyl parent phosphinidene complexes of the structure [$(^{\text{Dipp}}\text{NHC}=\text{PH})\text{M}(\text{CO})_5$] (**6a–c**, $\text{M} = \text{Cr}, \text{Mo}, \text{W}$), in which the $\text{NHC}=\text{PH}$ unit acts as a two-electron ligand. These complexes are easily accessible from the metal hexacarbonyls and the adduct **1a** (Scheme 5). Upon exposure of a THF solution of **1a** and the metal hexacarbonyl $\text{M}(\text{CO})_6$ ($\text{M} = \text{Cr}, \text{Mo}, \text{W}$) to UV light at room temperature, one CO molecule is replaced by the $^{\text{Dipp}}\text{NHC}=\text{PH}$ unit. The conversion strongly depends on the CO-pressure in the reaction vessel. If the reaction is carried out in closed flask, the conversion of **1a** does not exceed 20%, whereas if it is connected to an argon Schlenk line with an overpressure valve, nearly-quantitative conversion

is observed. Excess $\text{NHC}=\text{PH}$ and $\text{M}(\text{CO})_6$ were removed by washing with *n*-hexane, yielding the pentacarbonyl complexes as pale yellow powders in 65 to 82% yield.

The complexes exhibit doublets between –120.6 and –161.9 ppm ($^1J_{\text{PH}} = 214$ to 217 Hz) in the ^{31}P -NMR spectra. Comparing the ^{31}P -NMR resonances of the free $\text{NHC}=\text{PH}$ ($\delta = -136.7$ ppm) to the resonances of the group 6 complexes, the coordination to chromium has a deshielding effect ($\delta = -120.6$ ppm, $\Delta\delta = -16.1$ ppm), whereas the coordination to molybdenum ($\delta = -147.3$ ppm, $\Delta\delta = -10.6$ ppm) and tungsten ($\delta = -161.9$ ppm, $\Delta\delta = -25.2$ ppm) has a shielding effect. The ^{31}P -NMR chemical shift is influenced by a local diamagnetic term, a paramagnetic term, the neighbor anisotropy effect and interatomic currents. The local diamagnetic term depends on the electron density around the phosphorus atom.^[13] Coordination to a metal center leads to a lower electron density at the phosphorus atom and thus, a deshielded resonance is expected, as observed for chromium. However, heavy atoms can exhibit a strong neighbor anisotropy effect and thus a shielding influence on the ^{31}P -NMR resonance.^[14,15] In case of molybdenum and tungsten, this effect appears to be stronger than the deshielding influence of the coordination of the lone pair. The same trend was observed in group 6 pentacarbonyl phosphine complexes, in which the

Table 1. Comparison of selected bond lengths and angles of [$^{\text{Dipp}}\text{NHC}^*\text{-H}$]-[PH_2] (**2a**),^[12] [$^{\text{Mes}}\text{NHC}^*\text{-H}$]-[PH] (**4b**), $^{\text{Dipp}}\text{NHC}=\text{PH}$ (**1a**),^[6] and the metal complexes [$(^{\text{Dipp}}\text{NHC}=\text{PH})\text{M}(\text{CO})_5$] (**6a** = Cr, **6b** = Mo, **6c** = W) determined by single crystal X-ray diffraction.

	2a	4b	1a	6a	6b	6c
C1–P1 ^a	1.885(2)	1.896(3)	1.752(1)	1.821(3)	1.804(3)	1.807(3)
P1–M ^a	---	---	---	2.470(1)	2.619(1)	2.608(1)
N1–C1 ^a	1.454(2)	1.466(3)	1.373(1)	1.357(3)	1.360(3)	1.360(4)
N2–C1 ^a	1.456(2)	1.454(3)	1.373 (1)	1.357(3)	1.357(3)	1.359(4)
C2–C3 ^a	1.526(2)	1.486(4)	1.341 (2)	1.337(5)	1.337(4)	1.339(4)
N1–C1–N2 ^b	101.5(1)	102.1(2)	104.3(1)	105.7(3)	105.6(2)	105.5(2)
C1–P1–M ^b	---	---	---	110.6(1)	114.5(1)	114.0(1)

^aBond length given in Å. ^bBond angle given in °.

^{31}P -NMR resonances become more shielded from chromium to tungsten.^[14,15]

The ^{31}P -NMR spectrum of the tungsten complex **6c** exhibits ^{183}W -satellites (^{183}W : 14.3% abundant, $I = 1/2$) with a coupling constant of $^1J_{\text{PW}} = 48$ Hz. The $^{183}\text{W}^{31}\text{P}$ coupling constant was shown to be a sensitive measure for the electronic properties of phosphine ligands and increases with the electronegativity of the phosphorus substituents.^[16] For tungsten pentacarbonyl phosphine complexes $[\text{W}(\text{CO})_5\text{PR}_3]$ coupling constants between 142 Hz ($R = \text{Me}_3\text{Sn}$) and 485 Hz ($R = \text{F}$) have been reported.^[16,17] The exceptionally small coupling constant observed here suggests that the NHC unit in **1a** serves as a strong electron donor. That is, the dipolar resonance structure NHC^+-PH strongly contributes to the electronic ground state.

The solid-state structures of the complexes **6a–c** were determined by single crystal X-ray diffraction. Fig. 2 depicts the structure of the tungsten complex **6c** as an example. Selected bond lengths and angles are listed in comparison to those of **1a** in Table 1. The significant contraction of the C1–P1 bond and the widening of the N1–C1–N2 bond angle upon coordination of **1a** to the metal pentacarbonyls can be attributed to the large steric demand of the pentacarbonyls. The P1–M distances of the molybdenum and tungsten complexes **6b** (2.619 Å) and **6c** (2.608 Å) are about 0.15 Å longer than the distance of the chromium complex **6a** (2.470 Å). Furthermore, the C1–P1–M bond angles of **6b** and **6c** are about 4° wider than the angle of **6a**. Both effects can be attributed to the larger atomic radii and larger steric demand of molybdenum and tungsten versus chromium. The P–M distances observed here are longer than typical distances of group 6 metal phosphines M-PR_3 (Cr: 2.31–2.33 Å, Mo:

2.52 Å, W: 2.54 Å for M-PPh_3) and phosphides M-PR_2 (Cr: 2.32 Å, Mo: 2.39 Å).^[18]

In order to quantify the steric demand of NHC ligands, Cavallo and Nolan proposed the use of the ‘percent buried volume’ $\%V_{\text{Bur}}$, which is defined as the percent of potential coordination sphere around a metal occupied by the ligand and calculated from crystallographic data.^[19] For the $\text{DippNHC}=\text{PH}$ ligand **1a** a percent buried volume of $\%V_{\text{Bur}} = 30.4\%$ was obtained. This value is smaller than that of PPh_3 ($\%V_{\text{Bur}} = 34.5\%$) and corresponds to the value of PnBu_3 ($\%V_{\text{Bur}} = 30.4\%$). It is considerably smaller than that of the corresponding DippNHC in the complex $[\text{DippNHC}=\text{PH}]\text{M}(\text{CO})_5$ ($\%V_{\text{Bur}} = 39.0\%$).^[20] This lower steric hindrance of the metal center despite the bulky substituents on the NHC can be attributed to the larger distance between the metal and the NHC. Correspondingly, metal complexes with $\text{NHC}=\text{PH}$ ligands could be interesting candidates for homogenous catalysis as their metal centers suffer from less steric hindrance than their NHC counterparts.

3. Conclusion

Parent phosphinidene–carbene adducts $\text{NHC}=\text{PH}$ with varying steric bulk have been synthesized from elemental phosphorus P_4 or the easily accessible phosphorus sources Na_3P_7 , $(\text{Me}_3\text{Si})_3\text{P}_7$ and $\text{Na}(\text{OCP})$. Furthermore, *N*-heterocyclic carbenes were shown to insert into a P–H bond of PH_3 , giving rise to a phosphanyl–imidazolidine, which can be dehydrogenated to the $\text{NHC}=\text{PH}$ adduct. The interaction between PH_3 and *N*-heterocyclic carbenes strongly depends on the steric and electronic properties of the NHC. The $\text{NHC}=\text{PH}$ adducts can act as electronically flexible ligands and can be used to generate bis(phosphinidene) mercury(II) complexes of the structure $[(\text{NHC}=\text{P})_2\text{Hg}]$. Moreover, group 6 pentacarbonyl complexes of the structure $[(\text{DippNHC}=\text{PH})\text{M}(\text{CO})_5]$ are easily obtained by photolysis of solutions containing $\text{NHC}=\text{PH}$ and metal hexacarbonyls. Calculations of the percent buried volume revealed only low coverage of the metal center by the $\text{NHC}=\text{PH}$ ligand despite its sterically demanding substituents. This might prove useful for the application in homogenous catalysis, as the ligand keeps the metal sufficiently free for catalytic interaction and still provides kinetic stabilization to the complexes. Accordingly, further investigations of metal complexes with $\text{NHC}=\text{PH}$ ligands, which can be used in homogeneously catalyzed reactions, are planned.

4. Experimental

4.1 Materials and Methods

All reactions were carried out under argon using either standard Schlenk techniques or an argon-filled glove box. Solvents were purified using an Innovative Technology PureSolv MD 7 solvent purification system. All reagents were used as received from commercial suppliers unless otherwise stated. The compounds $[\text{DippNHC}=\text{PH}]\text{M}(\text{CO})_5$ (**1a**),^[10] $[\text{MesNHC}^+-\text{H}]\text{M}(\text{CO})_5$ (**1b**)^[21] and $[\text{Na}(\text{OtBu})]_x[\text{Na}(\text{PH}_2)]_x$ ($x \approx 2.5$)^[22] were synthesized following literature procedures. Reactions involving PH_3 gas were carried out in a setup and following a procedure described by Pringle and co-workers^[23] and PH_3 electronic grade, > 99.9995% was used.

UV irradiation was carried out with a mercury vapor pressure lamp (Heraeus TQ 150, 150 W) inside a quartz dip tube in a temperature-controlled water bath. X-ray single crystal diffraction studies were performed on a Bruker Smart APEX or an Oxford XCalibur S diffractometer, both equipped with a molybdenum X-ray tube ($\lambda = 0.7107$ Å).

Percent buried volume $\%V_{\text{Bur}}$ was calculated using the user friendly online tool SambVca available at www.molnac.unisa.it/OMtools/sambvca.php with the default parameters as suggested by Cavallo and co-workers (sphere radius $R = 3.5$ Å, M–P distance $d = 2.10$ Å, Bondi radii^[24] scaled by 1.17, mesh spacing $s = 0.05$ Å, including H-atoms).^[25]

4.2 Synthetic Procedures

4.2.1 Synthesis of $[\text{MesNHC}^+-\text{H}]_2\text{-[PH]}$ (**4b**)

A suspension of the imidazolium salt $[\text{MesNHC}^+-\text{H}]\text{M}(\text{CO})_5$ (257 mg, 0.75 mmol) and sodium *tert*-butoxide (96 mg, 1.0 mmol) in THF (15 mL) was treated with PH_3 as described previously for the synthesis of $[\text{DippNHC}^+-\text{H}]\text{M}(\text{CO})_5$.^[12] Volatiles were removed under reduced pressure from the yellow suspension and the product extracted with *n*-hexane (3 x 3 mL). Removal of the solvent under reduced pressure and recrystallization from *n*-hexane yielded **4b** as a pale yellow, crystalline solid (280 mg, 0.433 mmol, 57%). Single crystals suitable for X-ray diffraction were obtained from a saturated *n*-hexane solution at -30°C .

4.2.2 Synthesis of the Complexes

$[(\text{DippNHC}=\text{PH})\text{M}(\text{CO})_5]$ (**6a–c**, $M = \text{Cr}, \text{Mo}, \text{W}$)

In a 200 mL Schlenk tube, **1a** (210 mg, 0.500 mmol) and the equimolar amount of the corresponding metal hexacarbonyl were dissolved in THF (20 mL). The flask was connected to an argon Schlenk line fitted with an overpressure valve set to 0.1 bar overpressure and exposed to UV radiation.

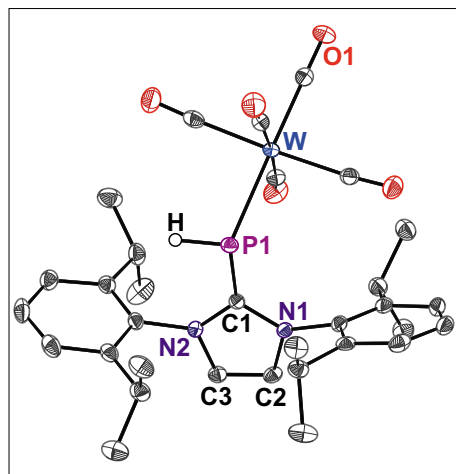


Fig. 2. ORTEP plot of the $\text{DippNHC}=\text{PH}$ tungsten pentacarbonyl complex **6c**. Hydrogen atoms apart from the phosphorus bound hydrogen atoms have been omitted for clarity. Thermal ellipsoids are shown at 50% probability.

The reaction was monitored by ^{31}P -NMR spectroscopy. After radiation times of 5 to 10 h, maximum conversions of 90–95% were observed. The solvent was removed under reduced pressure and the residue washed with *n*-hexane (5x 5 mL) to remove excess starting materials. Recrystallization from boiling toluene gave the complexes as yellow crystalline solids in 65–82 % yield. Single crystals suitable for X-ray diffraction were obtained from saturated toluene solutions at $-30\text{ }^{\circ}\text{C}$ ($\text{M} = \text{Cr}$) or from saturated toluene solutions layered with *n*-hexane ($\text{M} = \text{Mo}, \text{W}$).

Supplementary Information

The structures discussed here have been deposited with the Cambridge Structural Database under the numbers CCDC 1446562, 1446676, 1446858, 1446859.

Acknowledgements

We thank the European Union (Marie Curie ITN SusPhos, Grant Agreement No. 317404) for financial support. Furthermore, M.B. thanks the Swiss Chemical Society and Metrohm for the SCS-Metrohm Award for the best oral presentation in Inorganic and Coordination Chemistry.

Received: January 18, 2016

- [1] a) K. Lammertsma in 'New Aspects in Phosphorus Chemistry III', Ed.: J.-P. Majoral, Springer, Berlin Heidelberg, **2003**; b) Z. Benko, R. Streubel, L. Nyulaszi, *Dalton Trans.* **2006**, 4321.
- [2] H. Aktaş, J. C. Slootweg, K. Lammertsma, *Angew. Chem. Int. Ed.* **2010**, *49*, 2102.
- [3] a) L. J. Murphy, K. N. Robertson, J. D. Masuda, J. A. Clyburne in 'N-Heterocyclic Carbenes', Ed.: S. P. Nolan, Wiley-VCH Verlag GmbH & Co. KGaA, Weinheim, **2014**; b) C. D. Martin, M. Soleilhavoup, G. Bertrand, *Chem. Sci.* **2013**, *4*, 3020; c) D. J. D. Wilson, S. A. Couchman, J. L. Dutton, *Inorg. Chem.* **2012**, *51*, 7657; d) Y. Wang, G. H. Robinson, *Inorg. Chem.* **2011**, *50*, 12326; e) O. Back, B. Donnadiou, P. Parameswaran, G. Frenking, G. Bertrand, *Nat. Chem.* **2010**, *2*, 369.
- [4] a) A. J. Arduengo, J. C. Calabrese, A. H. Cowley, H. V. R. Dias, J. R. Goerlich, W. J. Marshall, B. Riegel, *Inorg. Chem.* **1997**, *36*, 2151; b) A. J. Arduengo, H. V. R. Dias, J. C. Calabrese, *Chem. Lett.* **1997**, *26*, 143; c) A. J. Arduengo III, J. Carmalt, Claire, A. C. Clyburne, Jason, H. Cowley, Alan, R. Pyati, *Chem. Commun.* **1997**, 981.
- [5] K. Hansen, T. Szilvási, B. Blom, E. Irran, M. Driess, *Chem. Eur. J.* **2014**, *20*, 1947.
- [6] A. M. Tondreau, Z. Benkő, J. R. Harmer, H. Grützmacher, *Chem. Sci.* **2014**, *5*, 1545.
- [7] A. Doddi, D. Bockfeld, T. Bannenberg, P. G. Jones, M. Tamm, *Angew. Chem. Int. Ed.* **2014**, *53*, 13568.
- [8] A. Beil, R. J. Gilliard, H. Grützmacher, *Dalton Trans.* **2016**, DOI: 10.1039/C5DT03014E.
- [9] L. Liu, D. A. Ruiz, F. Dahcheh, G. Bertrand, *Chem. Commun.* **2015**, *51*, 12732.
- [10] M. Cicač-Hudi, J. Bender, S. H. Schlindwein, M. Bispinghoff, M. Nieger, H. Grützmacher, D. Gudat, *Eur. J. Inorg. Chem.* **2015**, DOI: 10.1002/ejic.201501017.
- [11] B. A. Trofimov, S. N. Arbuzova, N. K. Gusarova, *Russ. Chem. Rev.* **1999**, *68*, 215.
- [12] M. Bispinghoff, A. M. Tondreau, H. Grützmacher, C. A. Faradji, P. G. Pringle, *Dalton Trans.* **2015**, DOI: 10.1039/C5DT01741F.
- [13] K. J. Packer, *J. Chem. Soc.* **1963**, 960.
- [14] S. O. Grim, D. A. Wheatland, W. McFarlane, *J. Am. Chem. Soc.* **1967**, *89*, 5573.
- [15] M. F. Guns, E. G. Claeys, G. P. van der Kelen, *J. Mol. Struct.* **1979**, *54*, 101.
- [16] E. O. Fischer, L. Knauss, R. L. Keiter, J. G. Verkade, *J. Organomet. Chem.* **1972**, *37*, C7.
- [17] H. Schumann, H.-J. Kroth, *Z. Naturforsch., B: Chem. Sci.* **1977**, *32*, 768.
- [18] F. H. Allen, O. Kennard, D. G. Watson, L. Brammer, Orpen, A. Guy, R. Taylor, *J. Chem. Soc., Perkin Trans. 2* **1987**, S1.
- [19] A. C. Hillier, W. J. Sommer, B. S. Yong, J. L. Petersen, L. Cavallo, S. P. Nolan, *Organometallics* **2003**, *22*, 4322.
- [20] H. Clavier, S. P. Nolan, *Chem. Commun.* **2010**, 46, 841.
- [21] K. M. Kuhn, R. H. Grubbs, *Org. Lett.* **2008**, *10*, 2075.
- [22] M. Podewitz, J. D. van Beek, M. Wörle, T. Ott, D. Stein, H. Rüegger, B. H. Meier, M. Reiher, H. Grützmacher, *Angew. Chem. Int. Ed.* **2010**, *49*, 7465.
- [23] J. H. Downing, J. Floure, K. Heslop, M. F. Haddow, J. Hopewell, M. Lusi, H. Phetmung, Orpen, A. Guy, P. G. Pringle, R. I. Pugh, D. Zambrano-Williams, *Organometallics* **2008**, *27*, 3216.
- [24] A. Bondi, *J. Phys. Chem.* **1964**, *68*, 441.
- [25] A. Poater, B. Cosenza, A. Correa, S. Giudice, F. Ragone, V. Scarano, L. Cavallo, *Eur. J. Inorg. Chem.* **2009**, 1759.

Do Hydrogen Bonds Influence Excitonic Splittings?

Franziska A. Balmer[§], Philipp Ottiger, and Samuel Leutwyler*

[§]SCS-Metrohm Award for best oral presentation in Physical Chemistry

Abstract: The excitonic splitting and vibronic quenching of the inversion-symmetric homodimers of benzonitrile, (BN)₂, and *meta*-cyanophenol, (mCP)₂, are investigated by two-color resonant two-photon ionization spectroscopy. These systems have very different hydrogen bond strengths: the OH⋯N≡C bonds in (mCP)₂ are ~10 times stronger than the CH⋯N≡C hydrogen bonds in (BN)₂. In (BN)₂ the S₀(¹A_g) → S₁(¹A_g) transition is electric-dipole forbidden, while the S₀(¹A_g) → S₂(¹B_u) transition is allowed. The opposite holds for (mCP)₂ due to the different transition dipole moment vector alignment. The S₀ → S₁/S₂ spectra of the dimers are compared and their excitonic splittings and vibronic quenchings are investigated by measuring the ¹³C-substituted heterodimer isotopomers, for which the centrosymmetry is broken and both transitions are allowed. The excitonic splittings are determined as Δ_{exc} = 2.1 cm⁻¹ for (BN)₂ and Δ_{exc} = 7.3 cm⁻¹ for (mCP)₂. The latter exhibits a much stronger vibronic quenching, as the purely electronic splitting resulting from *ab initio* calculations is determined to be Δ_{calc} = 179 cm⁻¹, while in (BN)₂ the calculated splitting is Δ_{calc} = 10 cm⁻¹. The monomer site-shifts upon dimerization and comparing certain vibrations that deform the hydrogen bonds confirm that the OH⋯N≡C hydrogen bond is much stronger than the CH⋯N≡C bond. We show that the H-bonds have large effects on the spectral shifts, but little or no influence on the excitonic splitting.

Keywords: Benzonitrile · *meta*-Cyanophenol · Excitonic splitting · Hydrogen bonds · Vibronic coupling

1. Introduction

Hydrogen-bonded molecular dimers are model systems to investigate excitonic interactions, which are of great importance in many photochemical and biological systems such as conjugated polymers, molecular crystals and photosynthetic light-harvesting complexes.^[1] Such dimers of benzene derivatives are small enough to allow detailed experimental, theoretical and computational investigations and are at the same time representative of larger systems. Our group has been studying the excitonic S₀ → S₁/S₂ splittings in rigid, doubly hydrogen-bonded dimers such as (2-pyridone)₂, (2-aminopyridine)₂, (benzoic acid)₂, (benzonitrile)₂ and (*ortho*-cyanophenol)₂.^[2–6]

They are centrosymmetric, meaning that the electronically excited S₁ (and higher S_n) states of monomers *A* and *B* are degenerate and excitonically coupled.^[2–8] Upon dimerization the transition dipole moment (TDM) vectors of the monomers combine in a parallel and antiparallel manner, giving rise to an antisymmetric (A_u, B_u) and a symmetric (A_g) excited state combination.^[9] Thus, either the S₀ → S₁ or the S₀ → S₂ transition is electric-dipole (g↔u) allowed, while the other is electric-dipole (g↔g) forbidden. The inversion symmetry can be broken by isotopic substitution of even a single atom, *e.g.* ¹²C/¹³C or H/D, rendering the forbidden transition slightly allowed.^[2–6] This enables us to experimentally determine the S₁/S₂ splitting, denoted Δ_{obs}.

We have previously shown that the displacements along the intra- and intermolecular vibrational coordinates Q_i that occur upon electronic excitation and which are quantified by the Huang-Rhys factors S_i have a major impact on the magnitude of the experimental splittings.^[3,6] The observed splittings are up to a factor 40 smaller than the purely electronic (Davydov) exciton splittings Δ_{calc} that are predicted by high-level *ab initio* calculations. This so-called ‘vibronic quenching’ of the excitonic splitting Δ_{calc} can be obtained^[3–10] by taking the Huang-Rhys factors S_i into account within Förster’s perturbation theory

approach^[7] or the Fulton-Gouterman model.^[11,12] Applying the resulting quenching factor Γ to the calculated exciton splitting Δ_{calc} results in vibronic splittings Δ_{vibron} that are very close to the experimentally observed S₁/S₂ splittings.

$$\Delta_{\text{vibron}} = \Gamma \cdot \Delta_{\text{calc}} \quad (1)$$

The strength of hydrogen bonds is dependent on the atoms involved and on structural aspects. The shift in absorption energy of the dimer relative to the monomer allows us to draw conclusions on the stabilization gained upon dimerization. Further, vibrations deforming the hydrogen bond also give us information on the H-bond strength. Here, we investigate if hydrogen bond strength has a direct influence on the excitonic splitting and vibronic coupling on the examples of the benzonitrile dimer, (BN)₂, with two CH⋯N≡C hydrogen bonds, and the *meta*-cyanophenol dimer, (mCP)₂, with two OH⋯N≡C hydrogen bonds.

2. Structural Aspects

The ground-state structures of (BN)₂ and (mCP)₂ were optimized by the spin-component-scaled variant of the approxi-

*Correspondence: Prof. Dr. S. Leutwyler
E-mail: leutwyler@dcb.unibe.ch
Universität Bern
Departement für Chemie und Biochemie
Freiestrasse 3
CH-3012 Bern

mate second-order coupled-cluster (SCS-CC2) method using the aug-cc-pVTZ basis set and are shown in Fig. 1. $(\text{BN})_2$ is a planar, C_{2h} -symmetric dimer,^[13,14] while $(\text{mCP})_2$ is C_i -symmetric, with the monomers slightly out of plane.^[9,15]

The calculated intermonomer distance between the centers of mass in $(\text{mCP})_2$ is $R_{\text{AB}} = 5.34 \text{ \AA}$ with an $\text{H}\cdots\text{N}$ distance of 2.04 \AA ; the center-of-mass distance in $(\text{BN})_2$ is $R_{\text{AB}} = 6.46 \text{ \AA}$ and the $\text{H}\cdots\text{N}$ distance is 2.36 \AA . The presence of the OH group in $(\text{mCP})_2$ changes the transition dipole moment (TDM) orientation: In $(\text{BN})_2$ the angle of the monomer TDM relative to the \vec{R}_{AB} vector is $\theta = 63^\circ$, which is larger than the 'magic angle' for which the magnitude of the dipole-dipole interaction goes to zero, *i.e.* $\arccos(1/\sqrt{3}) = 54.7^\circ$.

Thus, the TDMs are oriented parallel/antiparallel, the $S_0 \rightarrow S_1$ transition is forbidden and the $S_0 \rightarrow S_2$ transition is allowed. For $(\text{mCP})_2$, the angle is $\theta = 11^\circ$, which is smaller than the magic angle. In this case, the $S_0 \rightarrow S_1$ transition is allowed and the $S_0 \rightarrow S_2$ transition is forbidden.^[9]

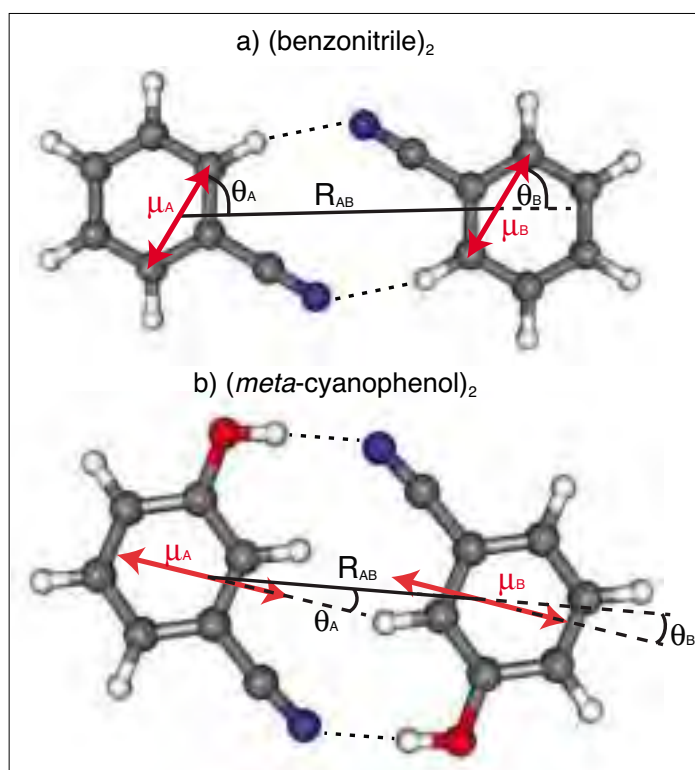


Fig. 1. a) $(\text{Benzonitrile})_2$ and b) $(\text{meta-cyanophenol})_2$ with indicated monomer transition dipole moments (μ), intermonomer distance R_{AB} and TDM alignment angle θ .

3. Two-Color Resonant Two-Photon Ionization Spectra

The dimers were produced and cooled in pulsed supersonic jet expansions. BN was heated to 75°C in an external vaporizer and seeded into the neon carrier gas (backing pressure 1.2 bar), while mCP was heated inside the pulsed nozzle to 80°C . Two-color resonant two-photon ionization (2C-R2PI) spectra were recorded by overlapping the excitation and ionization lasers in the source of a time-of-flight mass spectrometer. The spectra are shown in Fig. 2 with both electronic origins set to zero for comparison. The 0_0^0 transition energies are indicated next to the corresponding band, namely 36420 cm^{-1} for $(\text{BN})_2$ and 33255 cm^{-1} for $(\text{mCP})_2$.^[9,13] These energies correspond to spectral shifts of $\delta\nu = -92 \text{ cm}^{-1}$ for $(\text{BN})_2$ and $\delta\nu = -1094 \text{ cm}^{-1}$ for $(\text{mCP})_2$ relative to the respective monomer $S_0 \rightarrow S_1$ transition energies. The much larger shift for $(\text{mCP})_2$ indicates a stronger hydrogen bond of $(\text{mCP})_2$ relative to that of $(\text{BN})_2$. This will be discussed in Section 5.

The intramolecular normal modes are denoted according to the Wilson notation,^[16] while for the intermolecular normal modes we employ the nomenclature introduced in ref. [17]. The $(\text{BN})_2$ spectrum is dominated by intramolecular vibronic bands. Only one intermolecular vibration is observed, the shear vibration χ_0^1 ; otherwise the spectrum is very similar to that of BN.^[13] By contrast, the spectrum of $(\text{mCP})_2$ shows many excitations of intermolecular vibrations (δ , β , θ , σ , χ) as well as several intramolecular vibrations.^[9,15]

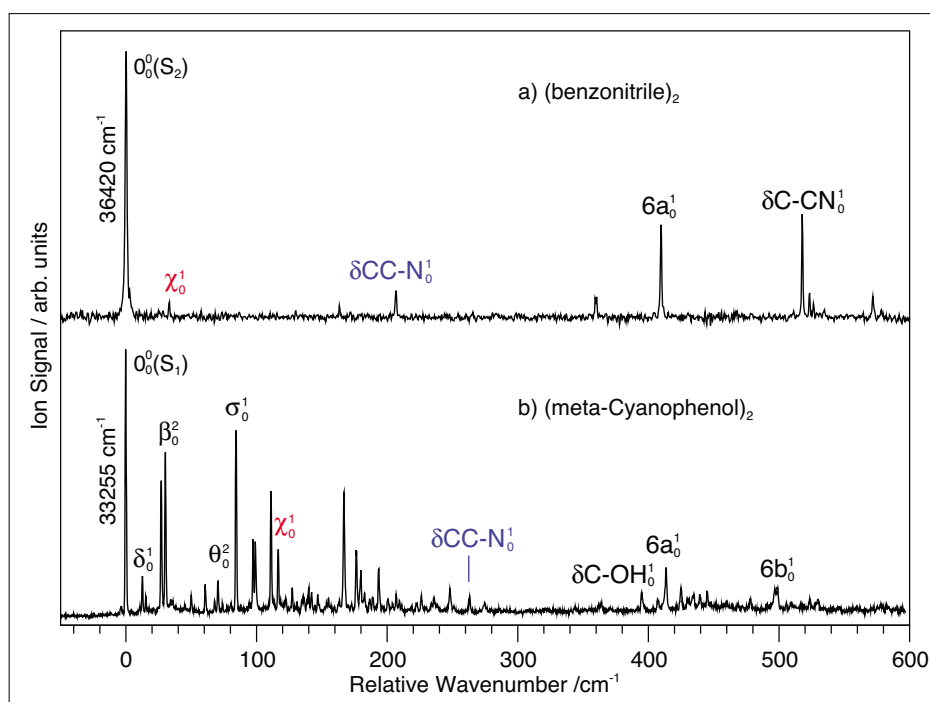


Fig. 2. Two-color resonant two-photon ionization spectra of a) $(\text{benzonitrile})_2$ and b) $(\text{meta-cyanophenol})_2$ with assignments. Vibrations appearing in both spectra are color-coded.

Inter- and intramolecular vibrations that involve large motions of the H-bonded atoms and that appear in the spectra of both $(\text{BN})_2$ and $(\text{mCP})_2$ allow to draw conclusions on H-bond strength. The intermolecular shear vibration χ and the in-plane cyano-group bend δCCN appear in both spectra. The respective fundamental excitations exhibit lower frequencies in $(\text{BN})_2$ compared to $(\text{mCP})_2$: χ_0^1 has an experimental frequency of 33 cm^{-1} in $(\text{BN})_2$ and 117 cm^{-1} in $(\text{mCP})_2$; the δCCN_0^1 is at 206 cm^{-1} in

$(\text{BN})_2$ and 263 cm^{-1} in $(\text{mCP})_2$. This shows that the $\text{OH}\cdots\text{N}\equiv\text{C}$ H-bond is much stronger compared to the $\text{CH}\cdots\text{N}\equiv\text{C}$ bond, because more energy is required to deform it. This is confirmed by the SCS-CC2/aVTZ calculated and counterpoise-corrected intermolecular S_0 binding energies, which are $D_e^{\text{CPC}} = -57.9 \text{ kJ/mol}$ for $(\text{mCP})_2$ and $D_e^{\text{CPC}} = -23.1 \text{ kJ/mol}$ for $(\text{BN})_2$, with corresponding basis-set superposition errors of 9.5 kJ/mol and 4.3 kJ/mol , respectively.

4. Excitonic Splitting and Vibronic Coupling

Isotopic $^{12}\text{C}/^{13}\text{C}$ substitution at a single atom breaks the inversion symmetry of the dimers and the symmetry descent, which is $C_{2h} \rightarrow C_s$ for $(\text{BN})_2$ and $C_i \rightarrow C_1$ for $(\text{mCP})_2$, renders the forbidden transition allowed. We take advantage of the natural abundance of ^{13}C . Fig. 3 shows the mass-selective 2C-R2PI spectra of $(\text{BN})_2$ and $(\text{mCP})_2$ in the 0_0^0 region, where the top panels display the all- ^{12}C mass channel and the lower panels the ^{13}C -trace. In the case of $(\text{BN})_2$ - ^{13}C the $S_0 \rightarrow S_1$ 0_0^0 transition appears at 36418.9 cm^{-1} , red-shifted by 1.2 cm^{-1} relative to $(\text{BN})_2$, and with an S_1/S_2 splitting of $\Delta_{\text{obs}} = 3.9 \text{ cm}^{-1}$,^[13] see Fig. 3(a). The $S_0 \rightarrow S_2$ transition of $(\text{BN})_2$ - ^{13}C is blue-shifted by 2.7 cm^{-1} relative to the $(\text{BN})_2$ S_2 origin, which is due to changes in the zero-point vibrational energy (ZPVE) by isotopic substitution Δ_{iso} . The observed S_1/S_2 splitting thus comprises an excitonic contribution Δ_{exc} and an isotopic contribution Δ_{iso} . According to degenerate perturbation theory, these combine as:^[4,13]

$$\Delta_{\text{obs}} = \sqrt{\Delta_{\text{exc}}^2 + \Delta_{\text{iso}}^2}. \quad (2)$$

From monomer 2C-R2PI spectra of ^{12}C -BN and ^{13}C -BN we have determined the purely isotopic contribution to be $\Delta_{\text{iso}} = 3.3 \text{ cm}^{-1}$, leading to an excitonic splitting of $\Delta_{\text{exc}} = 2.1 \text{ cm}^{-1}$.^[13]

In the case of $(\text{mCP})_2$ the forbidden S_2 0_0^0 band appears very weakly in the $(\text{mCP})_2$ - ^{13}C spectrum at 8.0 cm^{-1} above the S_1 origin, see Fig. 3(b). The S_1 0_0^0 band of $(\text{mCP})_2$ - ^{13}C is hardly shifted compared to that of $(\text{mCP})_2$, indicating smaller changes in ZPVE.^[9] The $S_0 \rightarrow S_1$ spectra of mCP and $\text{mCP}-^{13}\text{C}$ were used to determine the isotopic contribution $\Delta_{\text{iso}} = 3.3 \text{ cm}^{-1}$ as well. Employing Eqn. (2) with $\Delta_{\text{obs}} = 8.0 \text{ cm}^{-1}$ yields an excitonic splitting of $\Delta_{\text{exc}} = 7.3 \text{ cm}^{-1}$.

The vertical excitation energies calculated at the optimized SCS-CC2/aVTZ ground-state structures predict purely electronic splittings of $\Delta_{\text{calc}} = 10 \text{ cm}^{-1}$ for $(\text{BN})_2$ and $\Delta_{\text{calc}} = 179 \text{ cm}^{-1}$ for $(\text{mCP})_2$. However, these splittings do not take the redistribution of the electronic TDM into vibronic TDMs into account, and can therefore not be directly compared to the determined excitonic splittings Δ_{exc} .^[3-7,9,10] To calculate the vibronic quenching factor $\Gamma = \prod_i \exp(-S_i) = \exp(-\sum_i S_i)$, we employed the Huang-Rhys factors $S_i = l_i/2\mu_i\hbar\omega_i^3$, where i numbers the totally-symmetric intramolecular vibrations of the BN or mCP monomer.^[3-6] The experimental S_i yielded $\Gamma_{\text{exp}} = 0.213$ for $(\text{BN})_2$ and $\Gamma_{\text{exp}} = 0.043$ for $(\text{mCP})_2$.^[9,13] The vibronic coupling hence

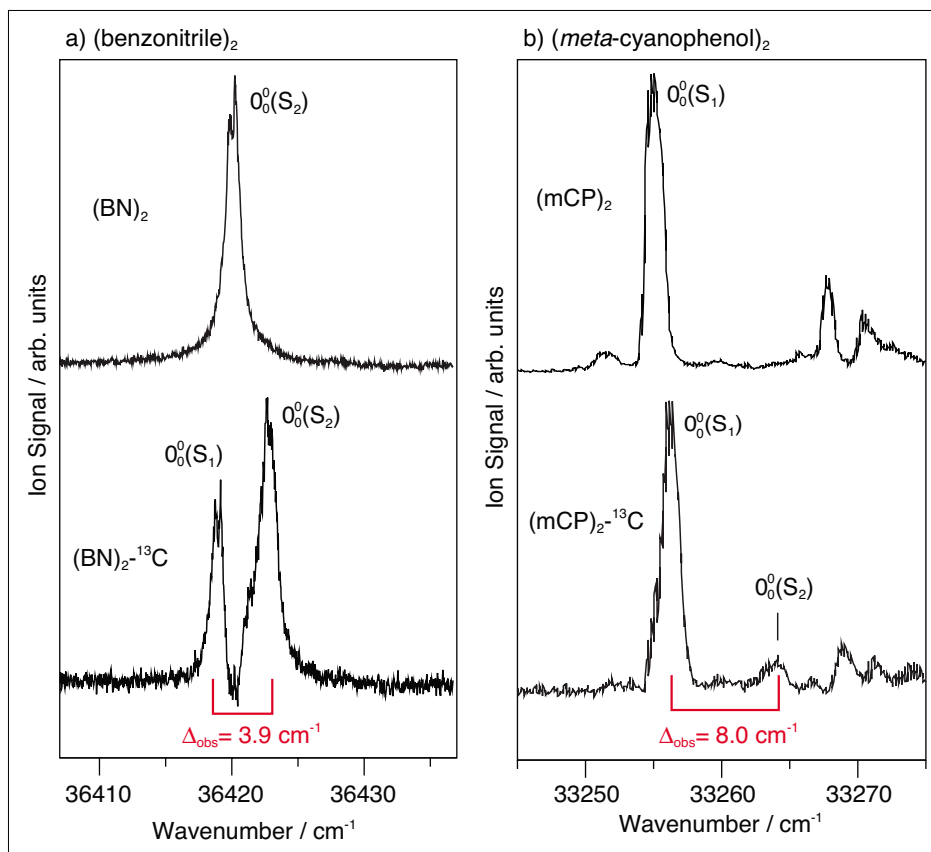


Fig. 3. 2C-R2PI spectra in the origin region of a) $(\text{benzonitrile})_2$ and b) $(\text{meta-cyanophenol})_2$ in the ^{12}C -mass channel (top) and the ^{13}C -mass channel (bottom) with observed S_1/S_2 splitting in red.

quenches the Davydov splittings by factors of $\Gamma^{-1} = 5$ and 23 , respectively, leading to vibronic S_1/S_2 splittings of $\Delta_{\text{vibron}} = 2.1 \text{ cm}^{-1}$ for $(\text{BN})_2$ and $\Delta_{\text{vibron}} = 7.7 \text{ cm}^{-1}$ for $(\text{mCP})_2$. This is in excellent agreement with the excitonic splittings determined above; all the splittings are summarized in Table 1. We note that these splittings arise from properties of the monomers: The excitonic splitting results due to coupling of the monomer TDMs and the vibronic quenching is largely dependent on intramolecular monomer vibrations Q_i and Huang-Rhys factors S_i . This implies that the H-bond strength of the dimer does not affect the excitonic splitting or vibronic quenching.

Table 1. Excitonic S_1/S_2 splitting (Δ_{exc}), Davydov splitting (Δ_{calc}), quenching factor (Γ), resulting vibronic splitting ($\Delta_{\text{vibron}} = \Gamma \cdot \Delta_{\text{calc}}$) and site-shift ($\delta\nu$).

	(benzonitrile)₂	(m-cyanophenol)₂
Δ_{exc}	2.0 cm^{-1}	7.3 cm^{-1}
Δ_{calc}	10 cm^{-1}	179 cm^{-1}
Γ	0.213	0.043
Δ_{vibron}	2.1 cm^{-1}	7.7 cm^{-1}
$\delta\nu$	-92 cm^{-1}	-1094 cm^{-1}

5. Spectral Site-Shifts

The intermolecular interactions that occur upon dimerization act on the constituent monomers and result in changes of the monomer geometry as well as energy (the so-called deformation energy). The geometry deformation of the monomer leads to a change of its electronic structure. This change is different in the S_0 and S_1 states, leading to a shift of the adiabatic $S_0 \rightarrow S_1$ absorption frequency. Thus the dimerization causes an electronic spectral site-shift. The site-shift can be evaluated from the average of spectral shifts of the dimer S_1/S_2 0_0^0 bands relative to the monomer $S_0 \rightarrow S_1$ 0_0^0 band, see Fig. 4.

Fig. 4 shows that the excitonic splitting discussed above is relatively small and does not depend on the H-bond strength. In contrast, the site-shift leads to much larger spectral effects and largely depends on the H-bond strength. The BN $S_0 \rightarrow S_1$ 0_0^0 band is observed at 36513 cm^{-1} ^[18] and the average of the dimer $S_0 \rightarrow S_1/S_2$ transitions is 36420 cm^{-1} .^[13] This result corresponds to a small site-shift of $\Delta_{\text{site}} = -92 \text{ cm}^{-1}$, which is 5% of the binding energy. The mCP monomer origin lies at 34354 cm^{-1} while the average of the dimer $S_0 \rightarrow S_1/S_2$ origins is at 33260 cm^{-1} , resulting in a much larger site-shift of $\Delta_{\text{site}} = -1094 \text{ cm}^{-1}$. Here, the site-stabilization is 23% of the dimer binding energy. This shows that the $\text{CH}\cdots\text{N}\equiv\text{C}$

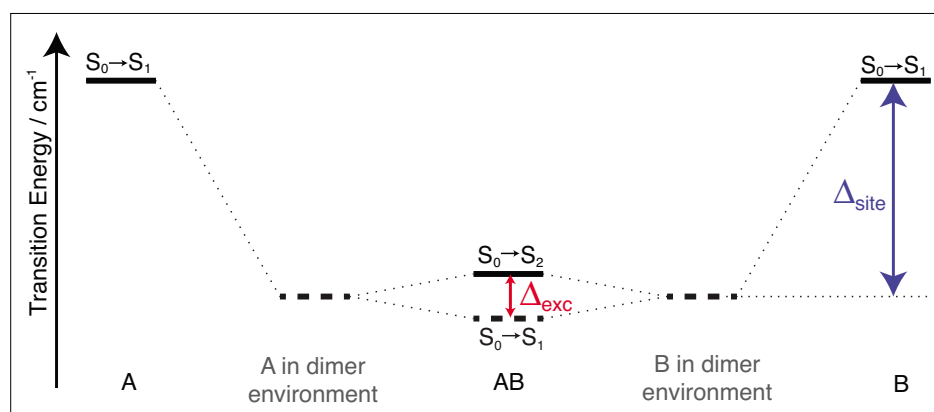


Fig. 4. Schematic representation of site- and excitonic splitting in a homodimer, where the $S_0 \rightarrow S_1$ transition is forbidden. Experimentally accessible values are marked in full lines, while calculated or indirectly determined transitions are dashed.

bonds have a much smaller influence than the $\text{OH} \cdots \text{N}=\text{C}$ bonds, as the stabilization is much larger in $(\text{mCP})_2$.

6. Conclusions

Jet-cooled two-color resonant two-photon ionization spectra of $(\text{benzotrifluoride})_2$ and $(\text{meta-cyanophenol})_2$ and their ^{13}C -isotopomers revealed excitonic splittings of $\Delta_{\text{exc}} = 2.1 \text{ cm}^{-1}$ and $\Delta_{\text{exc}} = 7.3 \text{ cm}^{-1}$, respectively. The vibronic quenching factor derived from monomer fluorescence spectra was much smaller for $(\text{mCP})_2$ ($\Gamma = 0.043$) than for $(\text{BN})_2$ ($\Gamma = 0.213$), since 2C-R2PI spectrum of mCP exhibits many more vibronic bands than BN. This leads to a much stronger quenching of the electronic exciton splitting by a factor $\Gamma^{-1} = 23$, while in $(\text{BN})_2$ $\Gamma^{-1} = 5$. The hy-

drogen bonds in $(\text{mCP})_2$ are much stronger compared to $(\text{BN})_2$, which is reflected in (i) the binding energy D_e of the complexes, (ii) the site-stabilization δv of the dimer relative to the corresponding monomer units and (iii) the shifts of inter- and intramolecular vibrational frequencies of dimer modes such as the shear and the in-plane nitrogen bend, where the frequency is much lower in $(\text{BN})_2$ compared to $(\text{mCP})_2$. Yet, the strength of the hydrogen bond only affects site-shift of the monomers upon dimerization, but not excitonic interaction. The latter arises due coupling of the monomer TDMs and the vibronic quenching is well reproduced by only including intramolecular monomer modes. One sees that while the excitonic splitting is of great importance, it is energetically a comparatively weak interaction. The electronic spectral site-shifts are 15–150 times

larger than the excitonic splittings and are heavily influenced by the hydrogen bond strengths. Thus the H-bonds have large effects on the spectral shifts, but little or no influence on the exciton splitting.

Received: January 21, 2016

- [1] F. C. Spano, *Annu. Rev. Phys. Chem.* **2006**, *57*, 4563.
- [2] P. Ottiger, S. Leutwyler, H. Köppel, *J. Chem. Phys.* **2009**, *131*, 204308.
- [3] P. Ottiger, S. Leutwyler, H. Köppel, *J. Chem. Phys.* **2012**, *136*, 174308.
- [4] P. Ottiger, S. Leutwyler, *J. Chem. Phys.* **2012**, *137*, 204303.
- [5] S. Kopec, P. Ottiger, S. Leutwyler, H. Köppel, *J. Chem. Phys.* **2015**, *142*, 084308.
- [6] P. Ottiger, S. Leutwyler, H. Köppel, *Chem. Sci.* **2015**, *6*, 6059.
- [7] T. Förster, in 'Modern Quantum Chemistry', Ed. O. Sinanoglu, Academic, New York and London, **1965**, Chap. IIIB, p. 93.
- [8] A. Witkowski, W. Moffitt, *J. Chem. Phys.* **1960**, *33*, 872.
- [9] F. A. Balmer, P. Ottiger, S. Kopec, H. Köppel, S. Leutwyler, to be submitted.
- [10] S. Kopec, P. Ottiger, S. Leutwyler, H. Köppel, *J. Chem. Phys.* **2012**, *137*, 184312.
- [11] R. L. Fulton, M. Gouterman, *J. Chem. Phys.* **1961**, *35*, 1059.
- [12] R. L. Fulton, M. Gouterman, *J. Chem. Phys.* **1964**, *41*, 2280.
- [13] F. A. Balmer, P. Ottiger, S. Leutwyler, *J. Phys. Chem. A* **2014**, *118*, 11253.
- [14] T. Kobayashi, K. Honma, O. Kajimoto, S. Tsuchiya, *J. Chem. Phys.* **1987**, *86*, 1111.
- [15] N. Seurre, K. Le Barbu-Débus, F. Lahmani, A. Zehnacker-Rentien, J. Sepiol, *Chem. Phys.* **2003**, *295*, 21.
- [16] E. B. Wilson, *Phys. Rev.* **1934**, *45*, 706
- [17] A. Müller, F. Talbot, S. Leutwyler, *J. Am. Chem. Soc.* **2002**, *124*, 14486.
- [18] P. Imhof, D. Krügler, R. Brause, K. Kleinermanns, *J. Chem. Phys.* **2004**, *121*, 2598.

Giant Host Red Blood Cell Membrane Mimicking Polymersomes Bind Parasite Proteins and Malaria Parasites

Adrian Najer^{§abc}, Sagana Thamboo^a, Cornelia G. Palivan^a, Hans-Peter Beck^{bc}, and Wolfgang Meier^{a*}

[§]SCS-Metrohm Award for best oral presentation in Polymers, Colloids and Interfaces

Abstract: Malaria is an infectious disease that needs to be addressed using innovative approaches to counteract spread of drug resistance and to establish or optimize vaccination strategies. With our approach, we aim for a dual action with drug- and ‘vaccine-like’ activity against malaria. By inhibiting entry of malaria parasites into host red blood cells (RBCs) – using polymer vesicle-based (polymersome) nanomimics of RBC membranes – the life cycle of the parasite is interrupted and the exposed parasites are accessible to the host immune system. Here, we describe how host cell-sized RBC membrane mimics, formed with the same block copolymers as nanomimics, also bind the corresponding malaria parasite ligand and whole malaria parasites, similar to nanomimics. This was demonstrated using fluorescence imaging techniques and confirms the suitability of giant polymersomes (GUVs) as simple mimics for RBC membranes.

Keywords: Giant polymersomes · GUV · Malaria · Membrane mimics · *Plasmodium*

Introduction

Block copolymer-based vesicles, called polymersomes^[1] due to their increased mechanical stability compared to liposomes and broad chemical versatility to introduce *e.g.* stimuli-responsiveness – are considered ideal candidates for drug delivery purposes, as nanoreactors, as artificial organelles inside cells, or as simple cell mimics.^[2,3] Our recently developed nanomimic strategy against infectious diseases is based on such polymer vesicles imitating a host cell membrane at the nanoscale (nanomimics), which was achieved by mixing two distinct block copolymers: vesicle-forming poly(2-methyl-2-oxazoline)-*block*-poly(dimethylsiloxane)-*block*-poly(2-methyl-2-oxazoline) (PMOXA-*b*-PDMS-*b*-PMOXA), and PDMS-*b*-heparin.^[4,5] Giant polymersomes (giant unilamellar vesicles, GUVs), several micrometers in diameter, are increasingly acknowledged as interesting model systems of very simplified cell mimics.^[6]

Malaria, a disease caused by *Plasmodium* spp. parasites that are transmitted by *Anopheles* mosquitoes – killing more than 600'000 people each year^[7] – is our current target. When reaching the blood stage cycle, the malaria parasite form called merozoite attaches to and enters red blood cells (RBCs), where the parasite asexually divides to form more parasites, which egress from the infected RBC (iRBC) after about 48 hours and infect more RBCs.^[8] Heparan sulphate (very similar to heparin) on RBCs is considered as being responsible for the initial attachment of merozoite to the RBC by interaction with *Plasmodium falciparum* merozoite surface protein 1-42 (*Pf*MSP1₄₂).^[9] With our approach we block the malaria blood stage life cycle using RBC-membrane-mimicking polymersomes, which block the parasite after egress from iRBCs, inhibit invasion, and expose the infective merozoites to the immune system. If successful *in vivo*, this artificial inhibition of merozoite invasion could lead to an immune boost against extracellular merozoites.^[4]

Here, we demonstrate that RBC membrane mimics formed at a larger size, but with similar hollow sphere architecture (heparin GUVs), can also bind the parasite protein *Pf*MSP1₄₂ and the whole *Plasmodium* parasite (merozoite form) in a similar fashion as their nano-sized counterparts, the nanomimics.^[4,5] This indicates that GUVs indeed represent a suitable model of small polymersomes,

with the advantage of a size close to that of RBCs. Certain aspects, *e.g.* binding of *Pf*MSP1₄₂ to polymersomes can be studied with GUVs using methods that would not be suitable for the nanostructure (*e.g.* confocal laser scanning microscopy (CLSM) to study protein binding).

Experimental

Materials

PDMS-*b*-heparin, PMOXA-*b*-PDMS-*b*-PMOXA, and *Pf*MSP1₄₂-OG488 synthesis and characterization can be found in our previous publications.^[4,5]

Giant Polymersome Formation

Giant polymersome (GUV) formation was accomplished according to the standard electroformation technique^[10] using a Nanion Vesicle Prep Pro setup (Nanion Technologies, Munich, Germany). A freshly cleaned ITO-coated glass slide was first plasma-treated (Plasma Cleaner, PDC-002, Harrick Plasma, Ithaca, New York, USA), and then, a thin polymer film was deposited on it. For control GUVs (only PMOXA-*b*-PDMS-*b*-PMOXA) a solution of PMOXA-*b*-PDMS-*b*-PMOXA in ethanol (6 mg/mL, 40 μ L) was dispersed on the ITO-coated side of the glass slide and ethanol was subsequently evaporated using a vacuum chamber for 30 min (Plasma Cleaner, PDC-002, Harrick Plasma, Ithaca, New York, USA). For the heparin GUVs a mixture of PMOXA-*b*-PDMS-

*Correspondence: Prof. Dr. W. Meier^a

E-mail: wolfgang.meier@unibas.ch

^aDepartment of Chemistry

University of Basel

Klingelbergstrasse 80

CH-4056 Basel

^bSwiss Tropical and Public Health Institute

Socinstrasse 57 Postfach

CH-4002 Basel

^cUniversity of Basel

Petersgraben 2, CH-4002 Basel

b-PMOXA in ethanol (6 mg/mL, 40 μ L) and PDMS-*b*-heparin in ethanol (4 mg/mL, 10 μ L) corresponding to a ratio of wt/wt 85:15 was used. Afterwards, a greased O-ring was put around the polymer film on the glass slide to form a chamber and then an aqueous sucrose solution (300 mM, 600 μ L) was added to hydrate the polymer film. After covering by another ITO-coated glass slide, the sample was exposed to an ac current (3.0 V, 3.0 Hz) at room temperature. For control GUVs we performed electroformation overnight and for heparin GUVs electroformation was conducted for one hour. Finally, the GUV solutions were transferred to Eppendorf tubes and stored at 4 $^{\circ}$ C.

Fluorescence Microscopy

Fluorescence imaging of protein interaction with giant polymersomes was performed on a confocal laser scanning microscope (Zeiss CLSM 510-META/Confocor2, Carl Zeiss, Jena, Germany). A freshly plasma-cleaned 8-well microscopy chamber (Nunc Lab-Tek Chamber Slide System, Thermo Fisher Scientific) was filled with PBS (200 μ L, pH 7.2), GUVs (20 μ L in 300 mM sucrose), Bodipy630 (10 μ L, 72 μ M) in PBS, and *Pf*MSP1₄₂-OG488 in PBS (5 μ L, 2.5 μ M). For the CLSM measurements a water immersion objective (C-Apochromat, 40 x magnification, NA of 1.2) was used. The OG488 signal was obtained by excitation with an Ar laser (λ = 488 nm) with dichroic mirrors HFT (main beam splitter) 488 and NFT (secondary beam splitter) 490 with the band-pass BP 500-550 filter. HFT 488/543/633, NFT 545 and the long-pass LP 650 filters were used to collect the fluorescence signal of Bodipy630. The pinhole size was set to 70 μ m for the green channel, and 90 μ m for the red channel, respectively. All settings (including laser power, detector gains) were kept constant for imaging of positive and negative samples.

Fluorescence imaging of heparin GUVs with merozoites was performed on a Leica DM 5000B fluorescence microscope using the appropriate filters.

Study Interaction of Giants and Merozoites

Plasmodium falciparum 3D7 parasite culturing and merozoite isolation was performed as described elsewhere.^[4,11] Briefly, a 30 mL petri dish filled with human RBCs at 5% haematocrit and 5–6% parasitemia (iRBC late stages) was used for merozoite isolation. First, late stage iRBCs were separated from RBCs and young iRBCs by Percoll density gradient. After maturation to schizont stage parasites, they were concentrated to 1 mL in malaria culture medium, and viable merozoites were mechanically released using 1.2 μ m syringe

filters. They were immediately mixed with 300 μ L of a heparin GUV solution in 300 mM sucrose, gently shaken, and incubated under static conditions at 37 $^{\circ}$ C for 15 min. Subsequently, 2 μ L of 1 mg/mL Hoechst (DNA stain) was added and merozoite/giant mixture was fixed in 2% paraformaldehyde/0.2% glutaraldehyde in 150 mM phosphate buffer (pH 7.4) overnight. After gentle centrifugation (3500 RCF) for 5 min, 10 μ L of the pellet was mounted on a microscopy slide.

Results and Discussion

Recently, we demonstrated that polymersome-based nanomimics of host RBC membranes efficiently block malaria parasite invasion into host RBCs *in vitro*; nanomimics were more than two orders of magnitude more potent invasion inhibitors compared to soluble receptor-like molecules (heparin), when IC₅₀ values were compared based on the heparin concentration in the assays.^[4,5] Furthermore, we measured that several heparin chains on a single nanomimic bound parasite ligands *Pf*MSP1₄₂-OG488 with a high affinity (K_d of 12.1 \pm 1.6 nM) using fluorescence cross-correlation spectroscopy (FCCS) of green labelled ligand and red labelled nanomimics.^[5] This multiple binding with high affinity is the basis for a strong multivalent interaction of nanomimic and merozoite, explaining the potent invasion inhibition by nanomimics.^[5]

Herein, host RBC membrane-mimick-

ing polymersomes were formed at a larger size (micrometer scale, heparin GUVs) to study malaria protein and whole parasite interaction with RBC-sized polymersome-based mimics (Fig. 1). The same two block copolymers previously used for nanomimic formation were also used to form these giant mimics. PDMS₆₅-*b*-heparin₁₂ was mixed with PMOXA₅-*b*-PDMS₅₈-*b*-PMOXA₅ (or PMOXA₉-*b*-PDMS₆₇-*b*-PMOXA₉) using 15 wt% of the first block copolymer and subsequent electroformation, yielding heparin GUVs. GUVs made from PMOXA₅-*b*-PDMS₅₈-*b*-PMOXA₅ without the heparin-functionalized copolymer were used as controls.

Giant Host Red Blood Cell Membrane Mimicking Polymersomes Bind Plasmodium Proteins

Formation of GUVs and heparin GUVs was successfully achieved in both cases using electroformation. Usually, a large number of mainly unilamellar, univesicular polymersomes were formed, whereas only few giants with multivesicular structures were found. Interestingly, these artificial and flexible membranes possess a thickness of about 11 nm,^[4] whilst all the membrane components can laterally diffuse within the membrane,^[12,13] but still form stable vesicles with several tens of micrometers in diameter. We performed CLSM to study the interaction of fluorescently labelled *Plasmodium* ligand *Pf*MSP1₄₂-OG488 and heparin, the receptor-like molecule known to bind *Pf*MSP1₄₂,^[9] on the surface

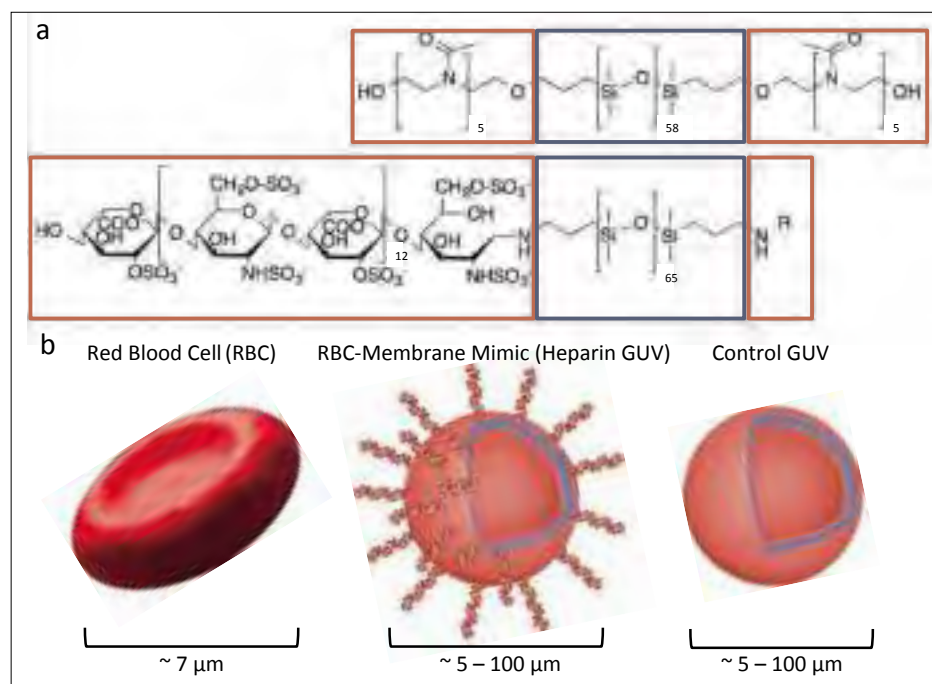


Fig. 1. a) Representation of the chemical structure of the two used block copolymers: PMOXA₅-*b*-PDMS₅₈-*b*-PMOXA₅ and PDMS₆₅-*b*-heparin₁₂. R is either another heparin chain or hydrogen. b) Schematic representation of a red blood cell (RBC), a RBC-membrane-mimetic giant polymer (heparin GUV), and a control GUV without the heparin-containing copolymer.

of heparin GUVs. This is only possible with GUVs and not with the nanomimics, because of resolution limitations. The membrane of control GUVs and heparin GUVs were labelled with the hydrophobic dye Bodipy630 for visualizing all the membranes in the red channel (Fig. 2). The hydrophobic dye spontaneously incorporates into the hydrophobic part of the membranes (PDMS).

The receptor-ligand interaction was followed after mixing control GUVs and heparin GUVs with green-labelled *PfMSP1*₄₂-OG488, respectively. In the control experiments, where GUVs without the receptor-like polysaccharide were used, no significant interaction with the parasite protein was observed as expected (Fig. 2c,d). Only the heparin GUVs, which mimic the host RBC membrane, were covered with *PfMSP1*₄₂-OG488 proteins on the surface, which appeared as green rings, whilst the exact same imaging settings as in the experiments with GUVs were used (Fig. 2a,b). Therefore, we could successfully observe the interaction of heparin on GUVs with the *Plasmodium* ligands *PfMSP1*₄₂ using conventional CLSM imaging. This confirms measurements performed using nanomimics and fluorescence-based diffusion measurements (fluorescence correlation spectroscopy (FCS), and FCCS) with the same *PfMSP1*₄₂-OG488 ligands of merozoites.^[4,5] This indicates that the membrane-bound receptor-like molecules (heparin) were also exposed on the large heparin GUVs after electroformation, similarly to the nano-scaled versions thereof (nanomimics). Therefore, GUVs are well suited to study certain biophysical aspects of the interaction between the parasite proteins and membrane mimics with a size relevant biologically, which support the conclusions already reported for the corresponding nanoversion system (nanomimics).^[4,5]

Giant Host Red Blood Cell Membrane Mimicking Polymersomes Bind Plasmodium Merozoites

Successful binding of parasite proteins to heparin GUVs encouraged us to perform experiments with whole *Plasmodium* merozoites to check for binding of viable parasites to heparin GUVs. This was studied using fluorescence microscopy after incubation of heparin GUVs with purified, viable *Plasmodium falciparum* merozoites, which is the most aggressive, life-threatening species of malaria parasites. The membrane of heparin GUVs was again visualized by red, hydrophobic dye (Bodipy630). Fluorescence images clearly demonstrate that merozoites also bind to RBC-sized host membrane-mimetic polymersomes (Fig. 3). In both examples shown, the

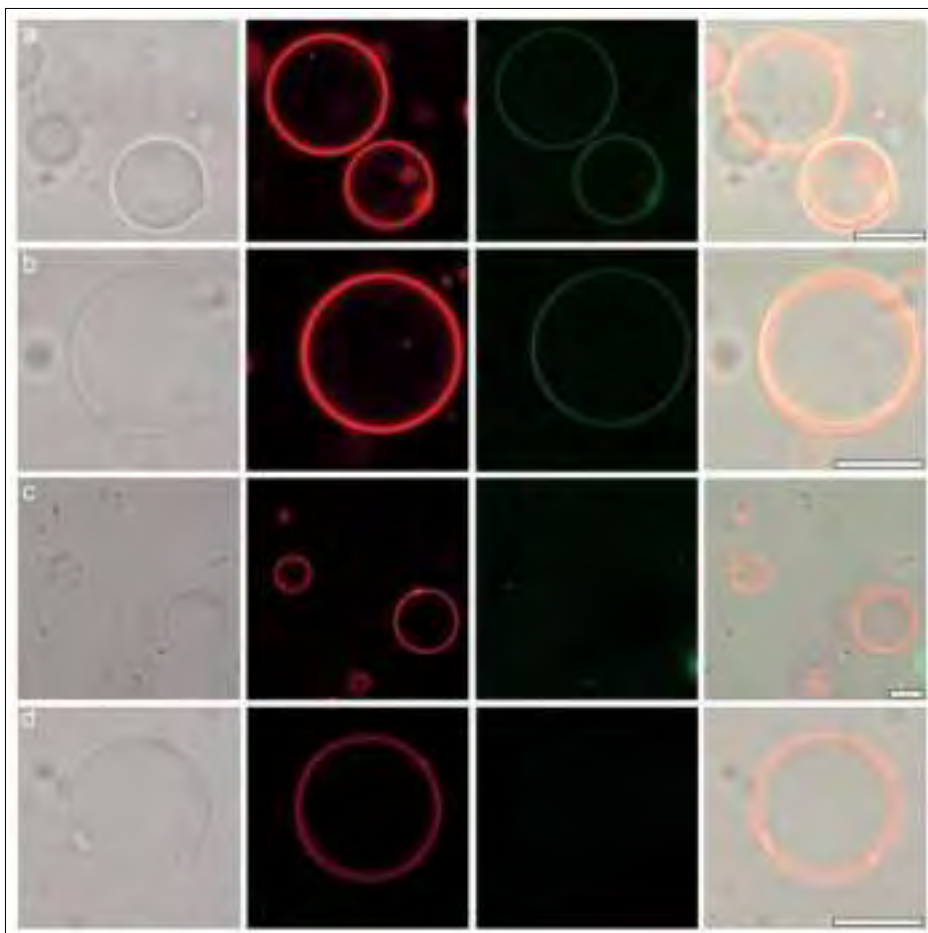


Fig. 2. CLSM images of heparin GUVs (a, b) and control GUVs (c, d), which were mixed with the *Plasmodium* parasite ligand *PfMSP1*₄₂-OG488 to investigate the ligand-receptor interaction; only when the receptor was presented on the surface (heparin GUVs), the parasite ligand bound to the GUVs, control GUVs showed no non-specific interaction with the protein. Left: DIC image. Middle left: Bodipy630 in the hydrophobic part of the GUV membranes. Middle right: OG488 on *PfMSP1*₄₂. Right: Merge. Scale bars: 10 μ m.

merozoites slightly indented the membrane of heparin GUVs upon binding. This deformation of the polymersome structure upon merozoite binding was also seen with nanomimics as previously demonstrated by electron microscopy of ultrathin slices of merozoite-nanomimic complexes.^[4]

This confirms that large-scaled poly-

mer vesicles can mimic – at a very primitive stage – the membrane of the host RBC to such an extent that binding of *Plasmodium* proteins and whole malaria parasites is achieved. The large size of GUVs allows the analysis of certain aspects by conventional imaging methods. Naturally, for a real *in vivo* application the nano-scaled

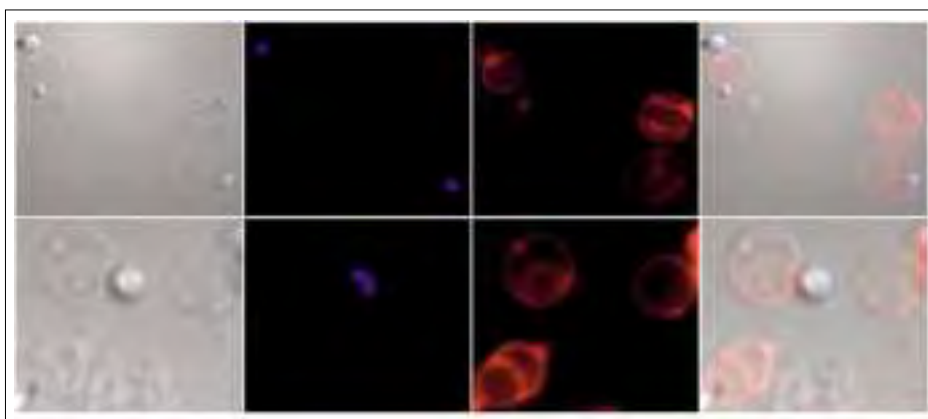


Fig. 3. Fluorescence microscopy images of giant host RBC-mimicking polymersomes (red) that bound *Plasmodium* merozoites (blue, DNA stain). Left: DIC image. Middle left: Hoechst, DNA stain. Middle right: Bodipy630, staining polymersome membranes. Right: Merge. Merozoites are about 1.5 μ m long.

versions are preferable, but certain aspects are difficult to analyze using only nano-sized structures.

Conclusion

Host RBC-membrane-mimicking polymersomes (heparin GUVs) were successfully formed at a corresponding RBC size (about 7 μm disk diameter) using two block copolymers and electroformation technique. Only when the second copolymer, containing the receptor-like molecule (heparin), was present in the GUV membrane, the parasite ligand PfMSP1₄₂ bound to the GUVs. Furthermore, whole, viable, and RBC-infecting *Plasmodium falciparum* merozoites interacted and deformed these large-sized RBC membrane mimics (heparin GUVs). These are important steps towards understanding and de-

fining this concept and to advance closer to a real biomedical application.

Acknowledgements

The Swiss National Science Foundation, NCCR 'Molecular Systems Engineering', and the University of Basel are acknowledged for financial support. A.N. gratefully acknowledges Metrohm Schweiz AG and the Swiss Chemical Society for the award. Authors thank S. Kasper for synthesizing PMOXA-*b*-PDMS-*b*-PMOXA and E. Angov (Division of Malaria Vaccine Development, Walter Reed Army Institute of Research, Silver Spring, MD, USA) is kindly acknowledged for providing PfMSP1₄₂.

Received: December 27, 2015

- [1] B. M. Discher, *Science* **1999**, 284, 1143.
- [2] A. Feng, J. Yuan, *Macromol. Rapid Commun.* **2014**, 35, 767.
- [3] C. G. Palivan, R. Goers, A. Najer, X. Zhang, A. Car, W. Meier, *Chem. Soc. Rev.* **2016**, 42, 377.
- [4] A. Najer, D. Wu, A. Bieri, F. Brand, C. G. Palivan, H.-P. Beck, W. Meier, *ACS Nano* **2014**, 8, 12560.
- [5] A. Najer, S. Thamboo, J. T. Duskey, C. G. Palivan, H.-P. Beck, W. Meier, *Macromol. Rapid Commun.* **2015**, 36, 1923.
- [6] M. Marguet, C. Bonduelle, S. Lecommandoux, *Chem. Soc. Rev.* **2012**, 42, 512.
- [7] World Health Organization, 'World Health Statistics 2014', Geneva, **2014**.
- [8] A. F. Cowman, D. Berry, J. Baum, *J. Cell Biol.* **2012**, 198, 961.
- [9] M. J. Boyle, J. S. Richards, P. R. Gilson, W. Chai, J. G. Beeson, *Blood* **2010**, 115, 4559.
- [10] M. I. Angelova, D. S. Dimitrov, *Faraday Discuss. Chem. Soc.* **1986**, 81, 303.
- [11] M. J. Boyle, D. W. Wilson, J. S. Richards, D. T. Riglar, K. K. Tetteh, D. J. Conway, S. A. Ralph, J. Baum, J. G. Beeson, *Proc. Natl. Acad. Sci. USA* **2010**, 107, 14378.
- [12] F. Itel, M. Chami, A. Najer, S. Lörcher, D. Wu, I. A. Dinu, W. Meier, *Macromolecules* **2014**, 47, 7588.
- [13] F. Itel, A. Najer, C. G. Palivan, W. Meier, *Nano Lett.* **2015**, 15, 3871.